Confinement of Nematic and Chiral Nematic Systems and Their Response to External Stimuli

Jack Kaufman

Submitted for the degree of Doctor of Philosophy

Lancaster University

Department of Chemistry

December 2022

i. Abstract

In this thesis, several examples of responsive liquid crystal elastomer microparticles are reported, as well as chiral nematic films. Bipolar nematic liquid crystal elastomer particles were of significant interest due their reversible shape change at the liquid crystal to isotropic phase transition. Furthermore, a spontaneous deformation of spherical droplets into spindle shaped particles upon irradiation with UV light was investigated. The spontaneous deformation and resulting particle surface morphology was studied to elucidate the phenomenon. Droplets and particles were subjected to external stimuli such as temperature and magnetic fields to produce samples with polar alignment not seen before in the literature.

In addition, a microfluidic method is reported for the introduction of nanoparticles into bipolar nematic droplets with greater control of both droplet diameter as well as the number of nanoparticles within droplets compared to methods previously reported. To achieve this, polymer nanoparticles were dyed with fluorescent dye and suspended in organic solvent so that they were compatible with the microfluidic inner phase containing nematic monomer, photoinitiator and crosslinker in chloroform, to which they were added. After photopolymerisation, yielding nanoparticle infiltrated elastomer microparticles, we demonstrated, for the first time, a reversible shape change response to temperature of nematic elastomer microparticles with localised nanoparticles, an initial step for applications of these materials within areas such as micromechanics and soft robotics.

Finally, doped chiral nematic systems were produced in the form of elastomer film and microparticle optical reflectors, and in some cases the dopant was extracted to produce chiral imprinted elastomers. Chiral doped monomer systems with tuneable selective reflection colours across the whole visible spectrum at room temperature are reported along with their responsiveness to temperature and pressure. Elastomer microparticles exhibited high quality optical properties after polymerisation, due to preserved internal mesogen alignment stemming from the particle size, monodispersity and overall quality of the droplets produced using our microfluidic method.

ii. Table of Contents

iii. Table of Equations

iv. Table of Figures and Schemes

v. Table of Tables

vi. List of Abbreviations

%v/v Percent volume per volume

%w/v Percent weight per volume

3D Three dimensional

5CB 4-Cyano-4′-pentylbiphenyl

60CB 4′-Hexyloxy-4-cyanobiphenyl

AR Aspect ratio

BP Blue phase

Ca Capillary number

CB15 (S)-4'-(2-Methylbutyl)-4-cyanobiphenyl

c_d Chiral dopant concentration

CE Chiral elastomer

CF Chiral film

cm Centimetre

CM Chiral mixture

cont. Continued

CV Coefficient of variation

d Distance

D Tube diameter

DMF Dimethylformamide

DMOAP Octadecyldimethyl(3-trimethoxysilylpropyl) ammonium chloride

DMPAP 2-Dimethoxy-2-phenyl acetophenone

DSC Differential scanning calorimetry

E1 Elastomer of **M1**

E2 Elastomer of **M2**

E3	Elastomer of **M3**
ee	Enantiomeric excess
FITC	Fluorescein isothiocyanate
F_S	Surface energy
F_V	Free energy per unit volume
g	Gram
G	Gauge
Hr	Hour
HTP	Helical twisting power
Hz	Hertz
I_c	Calculated intensity
ID	Inner diameter
I_o	Intensity of light given off light source
IPA	Isopropyl alcohol
IR	Infrared
ITO	Indium-tin oxide
K	Bulk elastic constant
K_{11}	Bend elastic constant
K_{22}	Twist elastic constant
K_{33}	Splay elastic constant
kHz	Kilohertz
kPa	Kilopascal
L	Length
λ	Wavelength
λ_{max}	Wavelength at maximum reflectance

LED	Light emitting diode
M	Molar
M1	4''-(Acryloyloxybutyl) 2,5-di(4'-butyloxybenzoyloxy)benzoate
M2	4''-(Acryloyloxybutyl 2,5-di(4'-heptyloxybenzoyloxy)benzoate
M3	11''-(Acryloyloxyundecyl) 2,5-di(4'-butyloxybenzoyloxy)benzoate
MF	Microfluidic
mg	Milligram
MilliQ	Ultrapure water
min	Minute
mL	Millilitre
mm	Millimetre
mol	Mole
mol%	Mole percent
n	Director
n	Refractive index
N/A	Not applicable
n_d	Number of droplets
NiM	Nanoparticle in microparticle
NIR	Near infrared
nm	Nanometre
NP	Nanoparticle
OD	Outer diameter
P	Pitch
p	Density
PDLC	Polymer dispersed liquid crystal

PEG 200 Polyethylene glycol 200

PI 1,4-Polyisoprene

POM Polarised light optical microscopy

PS Polystyrene

PTFE Polytetrafluoroethylene

PVA Polyvinyl alcohol

QD Quantum dot

r Droplet radius

R^2 Coefficient of determination

Re Reynolds number

Ref. Reference

RM257 4-(3-Acryloyloxypropyloxy) benzoic acid 2-methyl-1,4-phenylene ester

rpm Revolutions per minute

RSS Radial spherical structure

RT Room temperature

S Order parameter

SDS Sodium dodecyl sulfate

SEM Scanning electron microscopy

SM Suspension method

T_c Clearing temperature

T_g Glass transition temperature

THF Tetrahydrofuran

T_m Melting temperature

T_{NI} Nematic to isotropic phase transition temperature

ULH Uniform lying helix

UV	Ultraviolet
V	Fluid velocity
V_d	Volume of droplet
V_i	Volume of inner phase
Vis	Visible
V_{NP}	Volume of nanoparticle suspension
vol%	Volume percent
W	Width
w.r.t	With respect to
WE	Washed elastomer
W_E	Anchoring energy
wt%	Weight percent
γ	Interfacial tension
Δn	Birefringence
Δε	Dielectric anisotropy
Δχ	Diamagnetic anisotropy
ε	Dielectric permittivity
η	Viscosity
θ	Angle of incident light
μ	Average droplet diameter, length, width or particle aspect ratio
μL	Microlitre
μm	Micrometre
σ	Standard deviation
χ	Magnetic susceptibility

vii. List of Accompanying Material

Accompanying this thesis are Videos 1 – 13 discussed in Chapter 3. Video captions can be found below, as well as in the accompanying material.

Video 1: Video taken in brightfield transmission mode at 200x magnification of droplets of **M1-MF81**. Upon polymerisation into **E1-MF81** an instant geometry deformation occurred.

Video 2: Video taken in brightfield transmission mode at 200x magnification of nematic elastomer microparticles **E1-MF81** in the ten minutes after polymerisation, sped up 64x. Showing the microparticles move to pack more densely.

Video 3: Video taken in brightfield transmission mode at 200x magnification of droplets of **M2-MF80**. Upon polymerisation into **E2-MF80** an instant geometry deformation occurred.

Video 4: Video taken in brightfield transmission mode at 200x magnification, zoomed, cropped, and sped up 64x showing spindle shaped particles of **E1-MF81** undergoing a reversible shape change during a second heat/cool cycle from 25 – 140 – 40 °C, controlled at 10 °C/min.

Video 5: Video taken in brightfield transmission mode at 200x magnification, zoomed, cropped, and sped up 64x showing spindle shaped particles of **E2-MF80** undergoing a reversible shape change during a second heat/cool cycle from 25 – 140 – 40 °C, controlled at 10 °C/min.

Video 6: Video taken in brightfield transmission mode at 200x magnification of droplets of **M1-MF83** after being aligned on three stacked N42 bar magnets where the magnetic field was aligned vertical (↑) with respect to the video. Upon polymerisation into **E1-MF83** an instant geometry deformation occurred in the direction of the magnetic field.

Video 7: Video taken in brightfield transmission mode at 200x magnification of droplets of **M2-MF89** after being aligned on three stacked N42 bar magnets where the magnetic field was aligned vertically (↑) with respect to the video. Upon

polymerisation into **E2-MF89** an instant geometry deformation occurred in the direction of the magnetic field.

Video 8: Video taken in brightfield transmission mode at 200x magnification and sped up 64x showing spindle shaped particles of **E1-MF85** after being placed on a N42 ring magnet where the magnetic field was aligned horizontal (→) with respect to the video. Particles aligned with the magnetic field.

Video 9: Video taken in brightfield transmission mode at 200x magnification and sped up 64x showing spindle shaped particles of **E1-MF85** on top of a N42 ring magnet where the magnetic field was rotated 90 ° to be vertical (↑) with respect to the video. Particles rotated to align with the magnetic field.

Video 10: Video taken in brightfield transmission mode at 200x magnification and sped up 64x showing spindle shaped particles of **E1-MF97** on top of a N42 ring magnet where the magnetic field was rotated 180 ° to be vertical (↓) with respect to the video. Particles did not rotate 180° with the magnetic field.

Video 11: Video taken in brightfield transmission mode at 200x magnification and sped up 64x showing spindle shaped particles of **E2-MF88** after being placed on a N42 ring magnet where the magnetic field was aligned vertical (↑) with respect to the video. Particles aligned with the magnetic field.

Video 12: Video taken in brightfield transmission mode at 200x magnification and sped up 64x showing spindle shaped particles of **E2-MF88** on top of a N42 ring magnet where the magnetic field was rotated 90 ° to be horizontal (→) with respect to the video. Particles rotated to align with the magnetic field.

Video 13: Video taken in brightfield transmission mode at 200x magnification and sped up 64x showing spindle shaped particles of **E2-MF88** on top of a N42 ring magnet where the magnetic field was rotated 180 ° to be horizontal (←) with respect to the video. Spindle shaped particles did not rotate 180° with the magnetic field, however crescent shaped ones did rotate with the magnetic field.

viii. Acknowledgments

Firstly, thank you to my supervisor, Dr Verena Görtz for the opportunity to work on this project and explore this area of research under her supervision. I am hugely grateful for the incredible support, guidance and encouragement she has given me, particularly through the most uncertain of times of 2020. *Danke*.

I would also like to thank Dr Nick Evans and Dr Nathan Halcovitch for their advice and support as my panel members and Dr Sara Baldock for lending her SEM expertise to the project.

This project has spanned some tough times, however the support and friendship of a number of incredible people made getting to this point today so much easier. Thank you to my work family Gillian Laidlaw and Jack Lowe, I love you both and could not imagine doing this without you. *Merci* Marine Aublette and thank you Bette Beament and Bec Spicer for your friendship. Thank you to the rest of C21 for welcoming me in and letting me distract you all as the funniest person in the lab, good luck to my successor!

Thank you to my mum, dad, sisters and my whole family for literally everything – thank you for being so inspiring and for your love and support for everything I do. A special thanks goes to my niece Nellie, and Bunny too, for entertaining me and keeping my heart full. Finally to Scott, I love you so much, thank you for standing by my side throughout not only this PhD, but also through life. In the words of Little Mix, "*you put the sun up in my sky*".

This thesis is dedicated to John Chapman and Elsie Kaufman.

John was a talented chemist but more importantly a family man. His advice and wise words have guided me through life this far and will continue to do so. Elsie was the definition of gentleness and resilience. She was so proud of her family and her love was unwavering.

Thank you Grandad Jack and Grandma Elsie for inspiring me to be the best version of myself, I am so grateful and we miss you both every day.

ix. Author's Declaration

I declare this thesis is my own work and has not been submitted in support of an application for another degree at this, or any other, university.

Word Count: 64,732.

1 Introduction

1.1 Thesis Overview

This thesis centres around the investigation of various responsive liquid crystalline systems, from actuating nematic elastomer microparticles, to colour changing chiral nematic films.

Chapter 1 provides the fundamental background within the field, to give a basis for the discussions within this thesis. The nematic and chiral nematic phases are introduced in the context of phase structure and properties in bulk mixtures, elastomer films and systems within spherical confinement. The addition of nanoparticles to nematic systems is explored within the literature to provide a foundation for investigations later in this thesis. Chapter 2 introduces droplet production methods, particularly the microfluidic method and details how this method was used to produce monodisperse samples of droplets in the micrometre size range below 50 μm. In the following Chapter 3, production of bipolar nematic droplets and their response to external stimuli is discussed. Droplets were photopolymerised to produce bipolar nematic elastomer microparticles in different geometries, including spherical and spindle shaped. The morphology and responsiveness of the elastomer microparticles was then investigated. In chapter 4, the nanoparticle infiltration of bipolar nematic droplets is detailed. Several methods for the nanoparticle infiltration of droplets are discussed before photopolymerisation to produce nematic elastomer microparticles containing nanoparticles. In chapter 5 chiral nematic systems are discussed in the context of monomer mixtures doped with a chiral dopant, used to produce chiral nematic films, droplets and elastomer particles. Optical properties of the systems and the response of these to external stimuli were investigated. Penultimately, Chapter 6 provides the conclusions of this thesis. Finally, the experimental procedures are found in chapter 7, which details the experimental setup and parameters for producing all of the materials discussed within this thesis.

1.2 Liquid Crystal Phases

The liquid crystalline state exists between a solid crystalline state and an isotropic liquid state. Liquid crystals exhibit orientational order and hence have more order than an isotropic liquid, but less order than a crystalline solid, which exhibits both orientational and positional order. The degree of order present in liquid crystals allows for unique properties. Liquid crystal phases share some of the properties of a crystalline solid, whilst being fluid.[1]

In thermotropic liquid crystal phases, there are two main types of molecules, known as mesogens, which promote liquid crystalline order. They are characterised by their anisometric shapes, and known as calamitic (rod-like), and discotic (disc-like). For example, Figure 1a shows the general structure of a calamitic, rod-like, liquid crystal molecule. The two core groups, 1 and 2, are often benzene rings with a linker, 3, connecting the two. R and R' represent end groups. Changing the structure of the mesogen by altering 1, 2, 3 or R groups will vary the order and properties of the liquid crystal. Molecules interact by van der Waals' forces, which due to the anisometric shape of molecules, favours a common direction for the molecular axes to point in, known as the director (n), represented in Figure 1b.[1,2] Figure 1c shows an example of a calamitic mesogen, 5CB which displays a liquid crystal phase at room temperature, it can be seen that a rod-like shape is present due to the core of the molecule being composed of 2 bound benzene rings.

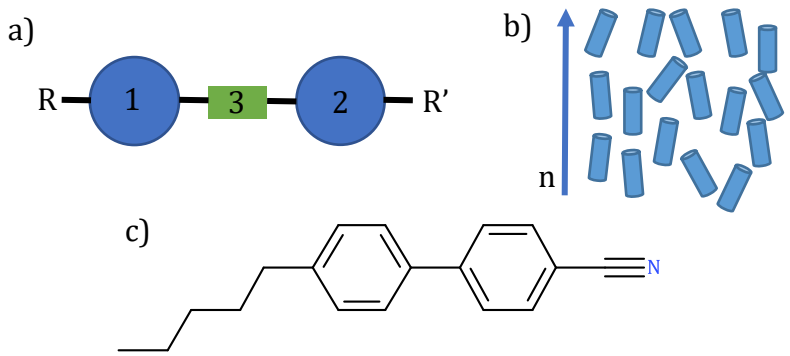

Figure 1: Cartoon representation of a general rod-like molecule (a) where 1 and 2 represent two core groups, often benzene rings, with a linker, 3, connecting the two. R and R' represent terminal chains which are usually hydrocarbon chains; cartoon representation of the nematic phase (b) where n represents the director. Redrawn from ref. 3. Molecular structure of 5CB (c).

There are several measures of orientational order, the order parameter (S) is commonly used to describe the degree of order in a uniaxial liquid crystal system and is calculated using Equation 1. Pointed brackets represent an average taken over many molecules in the system and θ denotes the angle between the director and the orientation of a single molecule. A perfectly aligned crystal is described by S = 1, whereas S = 0 describes an isotropic material with no order. A typical liquid crystal has more order than an isotropic material, but less than in a perfect crystal and hence in liquid crystalline materials the order parameter lies between 0.3 and 0.8.[3]

$$S = \langle \frac{3}{2} \cos\theta^2 - \frac{1}{2} \rangle$$

Equation 1: To calculate the order parameter.

Order of the liquid crystal is lost upon the transition from the liquid crystal state into an isotropic liquid, which is known as the clearing point (T_c, or T_{NI} in nematic systems).

1.2.1 The Nematic Phase

There are several types of liquid crystal phases, known as mesophases, which differ by the degree of order. The nematic phase is the least ordered of all the liquid crystal phases,[4] and will be investigated in this project. In the nematic phase, mesogens possess long-range orientational order, with the long molecular axes of mesogens, on average, pointing in the direction of the director, however no layered arrangement is present.

1.2.1.1 Anisotropic Properties

Anisotropy is the quality of a material having differing properties depending on the direction at which the property is measured in and arises in liquid crystal systems due to both the anisometric shape of molecules and the small degree of

order, described by S, compared to isotropic liquids. Anisotropy gives rise to useful properties which can be exploited for characterisation and alignment.

1.2.1.1.1 Birefringence

In isotropic materials the refractive index of the material is the same independent of the direction in which it is measured. This means that polarised light travels through an isotropic material at the same rate in any direction. However, in liquid crystalline materials, optical anisotropy, known as birefringence, is present due to the refractive index of the material being different depending on the direction of polarisation. Equation 2 shows that the birefringence (Δn) in a uniaxial nematic can be quantified as the difference between the refractive index of a material where light is polarised parallel to the director ($n_{\parallel}$) and the refractive index where light is polarised perpendicular to the director ($n_{\perp}$).[3,5] The refractive indices apply at optical wavelengths, hence at frequencies $\sim 10^{15}$ Hz, and are determined by anisotropic atomic and molecular polarisabilities.

$$\Delta n = n_{\parallel} - n_{\perp}$$

Equation 2: To calculate birefringence.

Birefringence can be exploited to characterise liquid crystal mesophases under polarised optical light microscopy (POM).

1.2.1.1.2 Dielectric and Diamagnetic Anisotropy

Dielectric materials are those which can be polarised in an electric field. The dielectric permittivity measures the polarisability of the dielectric material. Uniaxial liquid crystalline materials possess different dielectric permittivity values depending on directionality. Similar to in birefringence, the difference between the dielectric permittivity parallel to the director ($\varepsilon_{\parallel}$), and the dielectric permittivity which is perpendicular ($\varepsilon_{\perp}$) to the director describes the dielectric anisotropy ($\Delta\varepsilon$), as described in Equation 3. Dielectric constants are generally measured with

oscillating electric fields at low frequencies, typically 100 Hz to 100 kHz. At these frequencies thermally frustrated partial molecular reorientation contributes to the anisotropic permittivity values, as well as the atomic and molecular polarisabilities.

$$\Delta\varepsilon = \varepsilon_{\parallel} - \varepsilon_{\perp}$$

Equation 3: To calculate dielectric anisotropy.

Dielectric anisotropy gives rise to the ability of liquid crystals to align with electric fields. Where the dielectric anisotropy is positive the director will align parallel to the field, and if the dielectric anisotropy is negative the director will align perpendicular with the field above a certain value for the applied field.[3,6,7]

Furthermore, the majority of liquid crystalline materials are diamagnetic. Diamagnetic anisotropy ($\Delta\chi$) is present in uniaxial nematic liquid crystals due to the magnetic susceptibility parallel to the director ($\chi_{\parallel}$) being different to the magnetic susceptibility perpendicular to the director ($\chi_{\perp}$). The difference in these values describes the diamagnetic anisotropy, as shown in Equation 4. In calamitic nematic systems the magnetic susceptibilities are negative and $\chi_{\perp}$ is usually greater than $\chi_{\parallel}$, hence the diamagnetic anisotropy is usually positive. Molecular axes can be aligned in a magnetic field by exploiting this anisotropy, allowing for monodomain alignment of samples to be obtained. Magnetic alignment of mesogens is favourable as it reduces the free energy by aligning the director parallel to the magnetic field when $\Delta\chi$ is positive and perpendicular when it is negative.[8–10]

$$\Delta\chi = \chi_{\parallel} - \chi_{\perp}$$

Equation 4: To calculate diamagnetic anisotropy.

1.2.1.1.3 Elasticity

The lowest energy state of a liquid crystalline system is where there is uniform director present, however without the presence of external fields or alignment layers this is rarely observed. The director field is elastic, allowing for distortions of the director field to occur which can happen by bending, twisting or splaying. The bend deformation is a result of the director turning in its plane; the twist deformation is a result of the director turning around a perpendicular axis; and the splay deformation is a result of a tapered spreading of the director resulting in a wedge shaped director profile (Figure 2).[3] Each elastic distortion has an elastic constant associated with it, K_{11}, K_{22} and K_{33} for bend, twist and splay respectively. The elastic constants are used to calculate the overall contribution to the free energy per unit volume (F_V), using the Frank free energy density equation (Equation 5), where n is the director.[11]

$$F_V = \frac{1}{2}K_{11}[\nabla \cdot n]^2 + \frac{1}{2}K_{22}[\mathrm{n} \cdot (\nabla \times n)]^2 + \frac{1}{2}K_{33}[\mathrm{n} \times (\nabla \times n)]^2$$

Equation 5: Frank free energy density equation.[3]

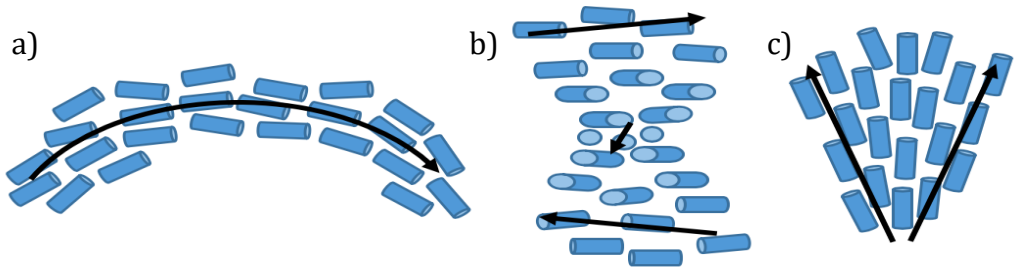

Figure 2: Cartoon representation of bend (a), twist (b) and splay (c) deformations of the director field where arrows denote the local director. Redrawn from ref. 3.

1.2.1.2 Texture and Alignment

Due to birefringence, liquid crystalline mesophases can be characterised under polarised light optical microscopy (POM). In POM, the sample is placed between two polarisers which are crossed 90° to each other. If the light was shone only through the crossed polarisers, or through an isotropic material, the light would be extinguished and blackness would be observed. However, in a birefringent material colours are observed. The colours observed when a birefringent layer is

placed between crossed polarisers are due to optical interference effects within the nematic layer because light polarised along the director travels at a different speed compared to light polarised perpendicular to the director. In unaligned samples, areas where the director changes in the sample result in a so called 'defect'. Defects are associated with abrupt spatial variations in the director alignment direction, hence they are areas where a single director cannot be determined. Defects are characterised by highly localised melting, on the nanometre scale, and a thus a loss of nematic order. Point and line defects occur where the director field aligns with either polariser and is observed as blackness within the sample, the pattern of these lines, give rise to characteristic textures for each mesophase.[3] For example, a uniaxial nematic phase gives rise to a *schlieren* texture, Figure 3 shows a cartoon representation of how the orientation of the mesogens with respect to the crossed polarisers gives rise to both 2 and 4-brushed *schlieren* brushes which make up the texture.

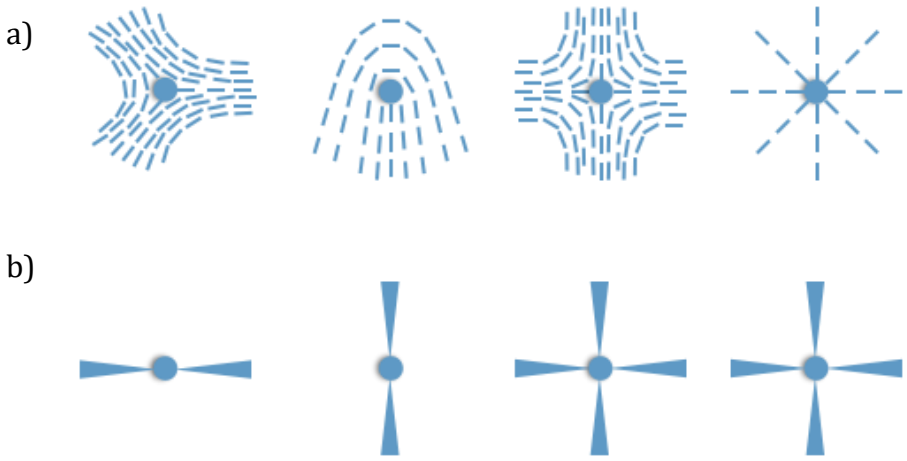

Figure 3: Cartoon representation of how mesogen orientation in a calamitic nematic produces defects (a) and with respect to crossed polarisers (vertical and horizontal with respect to page) produces to a *schlieren* texture with 2 and 4 brushes (b). Redrawn from ref. 3.

Figure 4 shows an example nematic schlieren texture where both 4-brushed (example highlighted in red) and 2-brushed (example highlighted in yellow) *schlieren* can be seen.

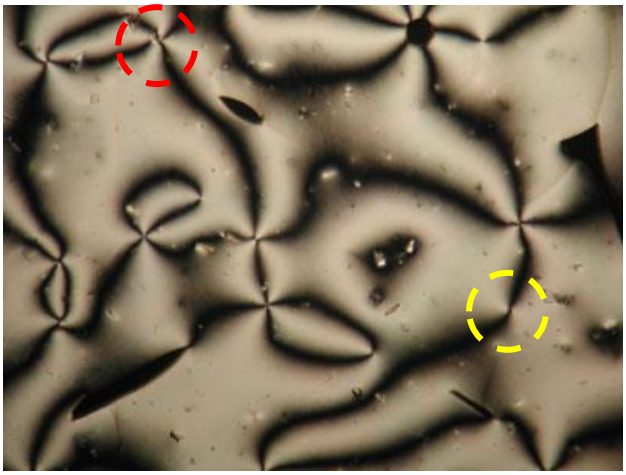

Figure 4: Polarised photomicrograph of a nematic phase liquid crystal displaying *schlieren* texture. Both 4-brushed (circled in red) and 2-brushed (circled in yellow) *schlieren* can be seen. Reproduced from ref. 12.

Defects are high energy areas and hence the lowest energy state for the director field is where it has a monodomain structure, with uniform director alignment over large distances. A monodomain structure can be promoted in thin films by treated alignment layers.[1,3] For example, rubbed polyimide can be utilised to successfully uniformly align mesogens between the two alignment layers. Rubbing the surface of the polymer orients the polymer chains parallel to the glass cell and introduces grooves. When the liquid crystalline material is introduced it flows into the cell along the grooves and the orientation of the polymer is transferred to the mesogens.[13,14] Hence, the rubbed polymer surface promotes mesogens to align parallel to the surface, this is known as homogeneous, or planar, alignment and is shown in Figure 5a.

The alignment cell surface can also be treated with a surfactant, for example octadecyltrichlorosilane or lecithin. The liquid crystalline material interacts with the surfactant on the surface *via* van der Waals' forces, to align the mesogens so that they are perpendicular to the surface, this is known as homeotropic alignment and is shown in Figure 5b.[15]

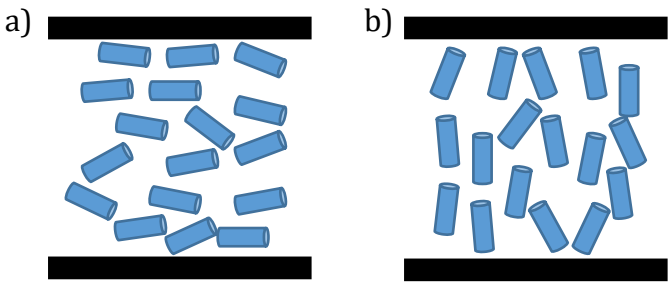

Figure 5: Cartoon representation of homogeneous (a) and homeotropic (b) alignment of nematic mesogens in an alignment cell where black bars represent the top and bottom of the alignment cell. Redrawn from ref. 3.

Alignment of mesogens can also be achieved by the use of external fields, such as electric or magnetic fields, due to their dielectric and diamagnetic anisotropy as discussed in the previous subsection.[3,6,7,9,10] In this thesis the responsiveness of nematic liquid crystals to magnetic fields will be investigated.

1.2.2 The Chiral Nematic Phase

1.2.2.1 Phase Structure

Introducing chirality into a nematic system, either by using a chiral nematogen or by introducing a chiral dopant that does not itself have to be liquid crystalline, for example CB15 (structure shown in Figure 6) is a common chiral dopant, may lead to a chiral nematic phase. In the chiral nematic phase, the asymmetry arising due to chirality promotes a periodic rotation in the director throughout the system.[3]

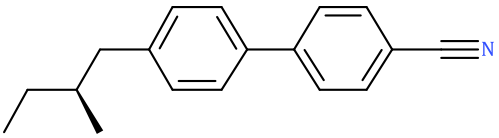

Figure 6: Molecular structure of chiral dopant CB15.

The rotation in the system makes up a helical superstructure (Figure 7) which has a handedness based upon the enantiomer of the chiral component. The pitch, P, describes one full rotation of the director and, therefore, the structure is repeated every half pitch. In doped systems the helical twisting power (HTP) can be described by Equation 6 which measures the degree to which the dopant

influences the twist of the helix. A positive HTP value indicates a right-handed helix and a negative value indicates a left-handed helix.[16,17] HTP shows that the pitch (P) can be tuned by altering the dopant concentration (c_d). Chiral dopants with relatively high HTP values are desirable so high dopant concentrations are not required to alter the helical pitch. The dopant acts as an impurity and therefore the higher the concentration of dopant, the lesser the phase stability.

$$HTP = \frac{1}{P \times c_d}$$

Equation 6: To calculate helical twisting power of chiral dopant.

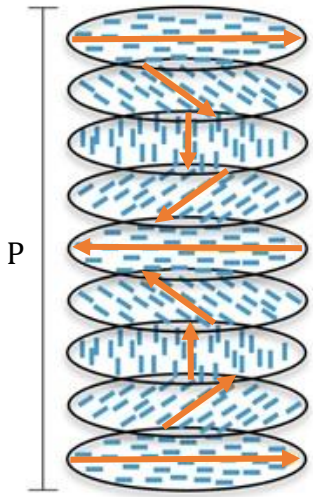

Figure 7: Cartoon representation of a helical macrostructure in the chiral nematic phase with pitch P, the rotation of the director denoted by arrows. Redrawn from ref. 3.

Temperature affects the pitch of the helix, this is due to an increase in temperature increasing the energy of the mesogens, which in turn increase the angle at which the director changes direction, and hence tightens the pitch.[18]

1.2.2.2 Texture and Alignment

As in the nematic phase, alignment cells can be utilised to align mesogens in the chiral nematic phase so that they exhibit either homogeneous or homeotropic

alignment, commonly known as uniform lying helix (ULH) alignment. This orients the chiral helices so that the helical axis is perpendicular to the mesogens' alignment, as represented in Figure 8.

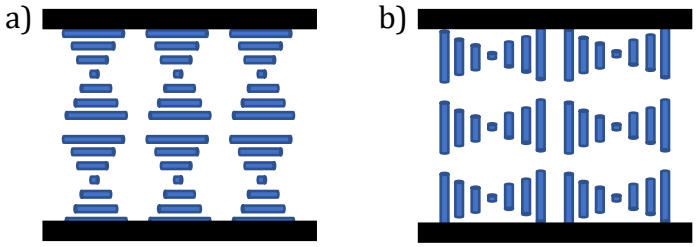

Figure 8: Cartoon representation of homogeneous (a) and ULH (b) alignment in the chiral nematic liquid crystal phase.

The chiral nematic phase can be characterised under POM due to the characteristic textures which are observed. The textures depend on the alignment in the sample, photomicrographs of chiral nematic textures are shown in Figure 9. A *Grandjean* texture (a) containing 'oily streaks' arises in chiral nematic systems with homogeneous alignment, whereas a fingerprint texture (b) occurs with ULH alignment. Where there is random orientation of helices within non-aligned systems, focal-conic (c) textures arise.[3,19]

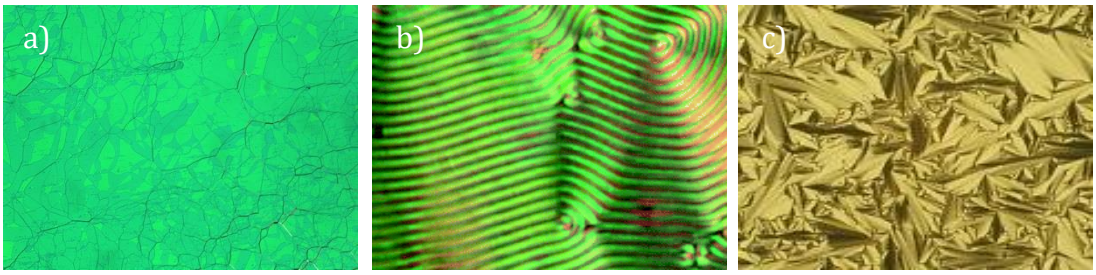

Figure 9: Polarised photomicrographs showing the *Grandjean* (a)[20], fingerprint (b)[21] and focal conic (c)[19] textures of the chiral nematic phase.

1.2.2.3 Selective Reflection

When incident light with wavelengths of the same order as the chiral pitch interacts with chiral nematic systems with homogenous alignment, an important optical property is observed, known as selective reflection. Circularly polarised light with the opposite handedness as the chiral helix is able to propagate along

the helix and is transmitted through the sample. However, polarised light of the same handedness as the chiral helix cannot propagate along the chiral helix and is reflected, hence the term selective reflection. The central reflection wavelength of the reflected light (λ) is proportional to the chiral pitch (P) and can be described using the Bragg reflection law (Equation 7), where $\bar{n}$ is the average refractive index.[3] If the wavelength of the reflected light is within the visible region then the sample is observed as being coloured. As the wavelength of selective reflection is dependent on the chiral pitch, altering the chiral pitch, for example as a result of temperature changes, varies the colour of the reflector.

$$\lambda = \bar{n}\, P \cos\theta$$

Equation 7: Bragg reflection law.[22]

Selective reflection depends upon the birefringence of the material, the wavelength of the reflected light must lie between $n_{\perp}$P and $n_{\parallel}$P. Hence, the larger the birefringence, Δn, the broader the reflection wavelength band.[3,23]

1.3 Liquid Crystal Polymers and Elastomers

1.3.1 Liquid Crystal Polymers

Polymers are high molecular weight molecules which are composed of repeating subunits, known as monomers, covalently bound together. Polymers in the solid-state may be semi-crystalline, and display a melting point, or be in an amphorous glassy state with low or no degree of crystallinity. The glass transition temperature (T_g) is the temperature at which the phase of the polymer changes from a viscoelastic state to a glass state. The properties of the polymer vary depending on the monomer, chain length and synthesis. Polymerisation of monomers, for example acrylate monomers, can be initiated by a radical initiator such as thermal initiator azobisisobutyronitrile; or photoinitiator diphenyl(2,4,6-trimethylbenzoyl)phosphine oxide. Thermal initiators decompose to produce radicals at elevated temperature which can initiate free-radical

polymerisation, whereas photoinitiators decompose upon irradiation with ultraviolet (UV) light to produce radicals.

If a mesogen contains a polymerisable unit, such as an acrylate group, and upon polymerisation displays a liquid crystal phase, then this is known as a liquid crystal polymer. To maintain mesogen alignment polymerisation is performed within the nematic phase, hence photoinitiation is generally preferred as the temperature of the system can be altered to maintain the liquid crystal phase. Upon polymerisation, the mesogen alignment is retained in the resulting polymer.

There are two types of liquid crystal polymer, main chain and side chain. Monomers which produce main chain liquid crystal polymers are bifunctional and upon polymerisation become incorporated into the polymer backbone with linker groups between mesogens, as depicted in Figure 10a. Side chain liquid crystal polymers are those where a mesogenic unit is bound to a spacer unit, which is then bound to a polymer backbone. The mesogen unit in side chain liquid crystal polymers can either be attached laterally (side-on to the polymer chain) or terminally (end-on to the polymer chain), as represented in Figure 10b & c.

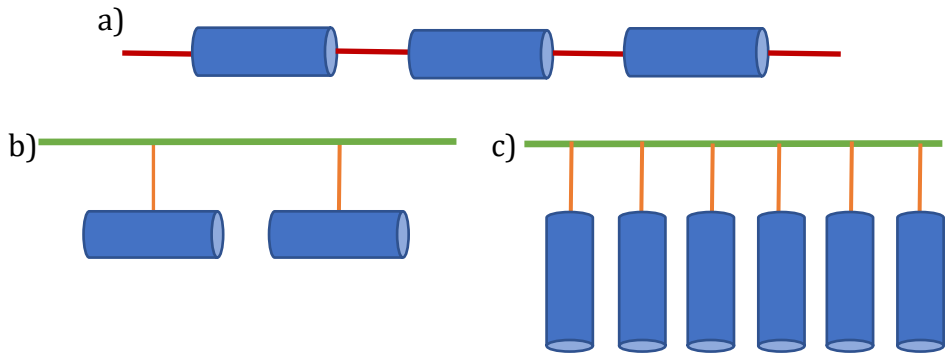

Figure 10: Cartoon representation of a main chain (a) and side chain (b & c) liquid crystal polymers with lateral (b) and terminal (c) mesogen (blue) attachment. Linker groups shown in red, spacer groups in orange and the polymer backbone in green.

A nematic phase is promoted by lateral attachment of mesogen in side chain liquid crystal polymers. The lateral attachment of mesogen allows for greater coupling between the mesogen and polymer backbone, giving rise to greater anisotropy within the polymer backbone. As the mesogens take up more space on the polymer backbone compared to when terminally attached, the polymer chain is drawn out

into an elongated coil conformation in the direction of the director.[13,24] Figure 11 shows the molecular structure of a monomer where the mesogen is attached laterally. The mesogenic unit is made up of a rigid core of three benzene rings with hydrocarbon terminal chains at each end. From the centre benzene ring, the spacer group is bound which attaches the mesogenic unit to the polymerisable acrylate group, bound to the other end.

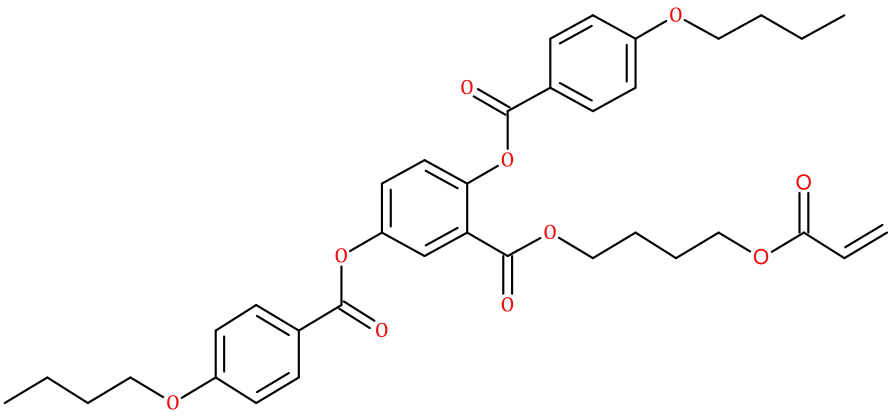

Figure 11: Molecular structure of a reactive mesogenic monomer where the mesogen is attached laterally to the polymerisable acrylate group *via* a spacer group.

As well as the mesogen itself, the spacer group and polymer backbone influence the thermal properties of the liquid crystal polymer. A shorter spacer group increases coupling of the mesogen and polymer backbone, which increases the anisotropy of the polymer, compared to liquid crystal polymers with longer spacer groups. Increasing the spacer length decreases the T_g due to greater decoupling of the mesogen and polymer backbone, resulting in a lower order parameter. The T_g of a system also decreases with increasing polymer backbone flexibility. The mechanical properties of the polymer backbone, and therefore flexibility, are altered with composition, for example polysiloxanes (Figure 12b) are more flexible so have a lower T_g, and therefore wider phase stability, than polyacrylates (Figure 12a). Despite this, polyacrylates are an example of a flexible polymer backbone and therefore their suitability for liquid crystal polymers to be investigated in this project is high due to relatively low T_g values, and facile synthesis by free-radical polymerisation.[3,25,26]

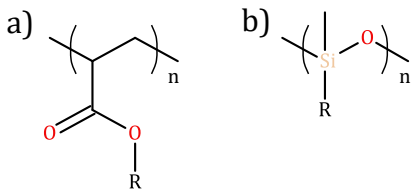

Figure 12: Molecular structures of repeat units of polyacrylate (a) and polysiloxane (b).

1.3.2 Liquid Crystal Elastomers

In liquid crystal polymers without crosslinking the mesogen alignment is retained, upon clearing into the isotropic phase and cooling back to the nematic phase, alignment is usually lost. Introducing a small amount (for example 10 mol% with respect to monomer) of crosslinking groups between liquid crystal polymer chains creates an elastic polymer network with a degree of shape memory. The shape memory allows for the liquid crystal elastomer to retain alignment through clearing to the isotropic phase and returning to the liquid crystal phase.[27]

1.3.3 Nematic Liquid Crystal Elastomers

A nematic liquid crystal elastomer is represented in Figure 13a which shows a diagram of a nematic liquid crystal elastomer where the blue rods represent mesogenic units and the black lines the polymer backbone with crosslinking.

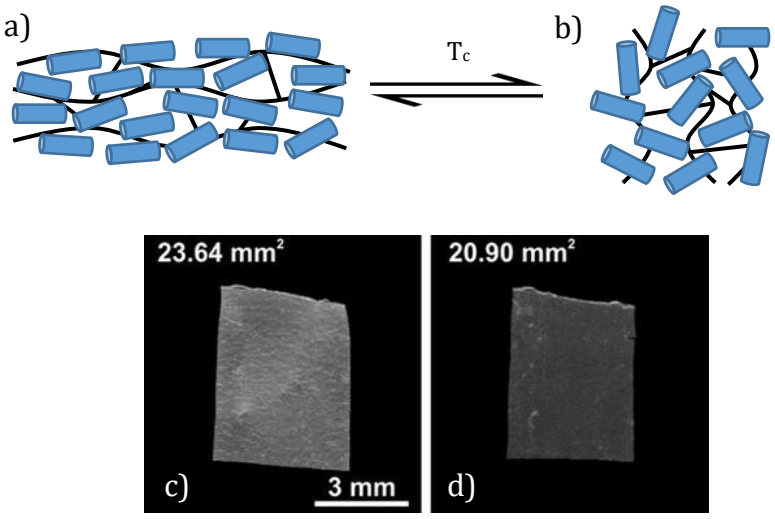

Figure 13: Cartoon representation of a lateral side chain liquid crystal elastomer (a) changing shape into a random coil (b) when passing through its phase transition temperature; photomicrographs showing a measured liquid crystal elastomer exhibiting a shape change, denoted by a decrease in area, when heated from 22.8 °C (c) to 74.4 °C (d). Photomicrographs reproduced from ref. 28.

Monodomain nematic elastomer films have been shown to display a change in shape when the temperature is increased above its T_{NI}. When the temperature is returned into the nematic phase, the film returns to its original elongated shape.[24] Figure 13a & b show a laterally attached side chain liquid crystal elastomer around the phase transition temperature. When the elastomer is heated above the T_{NI} and order is lost as the film becomes isotropic, the polymer chains adopt a random coil configuration and the elongation of the polymer network is lost. This is observed as a shape change. Once the temperature is returned, the mesogens reassemble and return the film to an elongated configuration from a random coil. Contrary to laterally attached systems, in elastomers where mesogen are attached terminally the mesogens are aligned perpendicular to the polymer backbone and therefore less anisotropy is transferred to the polymer chains and hence the degree of actuation response is lesser.[13,27]

An example of a shape change response to temperature can be seen in Figure 13c & d which shows the width of an aligned liquid crystal elastomer film decreasing when the sample is heated from 22.8 °C to 74.4 °C due to loss of alignment.[28] A reversible shape changing response to temperature allows for applications of liquid crystal elastomers as soft actuators which can be used for example as switches and valves in micromachinery.[29,30]

1.3.4 Chiral Nematic Liquid Crystal Elastomers

Chiral nematic elastomers can be produced by the polymerisation of a crosslinker with either a chiral liquid crystalline monomer or chiral nematic mixture of an achiral liquid crystalline monomer with a chiral dopant. Similar to the non-polymeric systems discussed previously, chiral nematic polymers and elastomers exhibit selective reflection which can be within the visible range, depending on the length of the helical pitch.[3]

Notably, the selective reflection in chiral nematic elastomers is responsive to mechanical stimuli. Mechanical deformation of chiral nematic elastomer films, for example by stretching or compressing, can cause a colour change of the films in monodomain parallel aligned samples. The chiral pitch is physically compressed upon stretching or manual compression, which reduces the wavelength of light

reflection, causing a blue-shift in selective reflection.[31–33] This allows for tuning of the selective reflection wavelength by not only CB15 concentration, but also by mechanical force. For example, Finkelmann *et al* produced dye-containing chiral nematic liquid crystal elastomer films which, when stretched, changed colour from orange to blue.[31] This colour change was due to the film thickness shortening upon stretching, compressing the chiral helices and hence causing a blue-shift in the selectively reflected light. This colour changing response to mechanical stimuli in chiral nematic elastomer films has also been reported for chiral imprinted films.[34–38] Responsiveness to compression gives rise to the application of pressure sensors for chiral nematic elastomer films which selectively reflect within the visible region of light.[31–33,39]

1.4 Liquid Crystal Droplets and Elastomer Microparticles

When a liquid crystal system is confined in a spherical geometry, as in a liquid crystal droplets, a number of unique properties arise. Droplets can be produced by several methods, including suspension of one immiscible phase within another or by microfluidics. These two main droplet production methods are discussed in chapter 2. Droplets of mesogenic monomer can be produced which contain photoinitiator and a crosslinker which can then go on to be polymerised to yield liquid crystalline elastomer particles.

1.4.1 Nematic Droplets

As in planar systems, nematic microdroplets exhibit two main surface anchoring conditions of the mesogens relative to the surface, either parallel or perpendicular. Figure 14 shows 2-dimensional cartoon representations of how the mesogens align with respect to the spherical droplet surface in parallel (a) and perpendicular (b) surface anchoring conditions. The composition of the droplets' dispersion medium is known to promote certain surface anchoring conditions. Sodium dodecyl sulfate (SDS) in water will promote perpendicular surface anchoring, for a radial configuration, by creating a pseudo-hydrophobic environment around the droplet.[40,41] On the other hand, polyvinyl alcohol in water will promote parallel surface anchoring, for a bipolar configuration.[42,43]

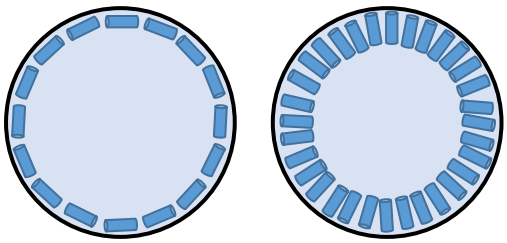

Figure 14: Cartoon representation of parallel (a) and perpendicular (b) surface anchoring in nematic liquid crystal microdroplets. Redrawn from ref. 44.

There are many possible director configurations in nematic systems such as monodomain, bipolar, twisted bipolar, concentric and radial, although many more can arise. Several configurations are represented in Figure 15. The director configuration which arises depends on the size of the droplet and the elastic energies of the systems. Hence, certain configurations are more likely to occur than others based on these parameters.

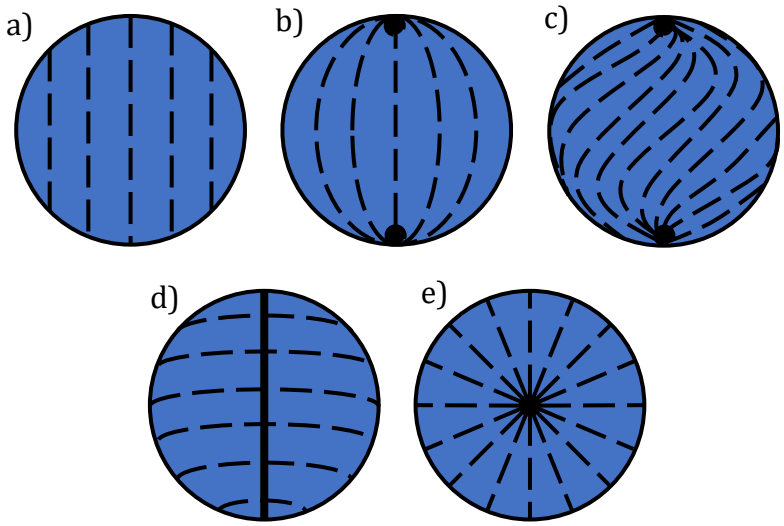

Figure 15: Cartoon representation of monodomain (a), bipolar (b), twisted bipolar (c), concentric (d) and radial (e) director configurations of spherically confined nematic systems. Redrawn from refs. 45, 46 & 47.

The size of the droplet has a strong influence on the director configuration in droplets as the elastic energy, F_V discussed previously (Equation 5), is proportional to the droplet radius and can be described as $F_V = rK$ where r is the droplet radius and K is the bulk elastic constant. The single constant, K, is used so as to combine the effects of K_{11}, K_{22} and K_{33}. Furthermore, the surface energy of the droplet is proportional to the squared radius and can be described as

$F_S = W_E r^2$ where W_E is the anchoring energy. Consequently, the director configuration of very small droplets (<1 μm) is governed by the bulk elastic energy to a greater degree than the surface energy and *vice versa*. Satisfying surface anchoring conditions in smaller droplets would require larger, and higher energy, bend and splay deformations to the director field compared to larger droplets. Hence, for droplets <1 μm, a monodomain nematic director configuration (Figure 15a) may be accessible to minimise the free energy by preventing the large, energetically costly, bend and splay deformations of the director field which are associated with the smaller droplet diameter.[45,47]

In larger micrometre sized droplets, the surface anchoring conditions have a greater influence on the director configuration. In parallel aligned droplets, the lowest energy director configuration is the bipolar configuration (Figure 15b). As the linear director cannot perfectly lie parallel to the curved surface of a 3-dimensional sphere, a pair of topological defects, known as boojums, arise at opposite poles of the droplet.[42,48] Splay deformations are present about the defects with energy determined by the magnitude of elastic constant K_{11}, and the bend deformation, with elastic constant K_{33}, dominates the remaining areas within the droplet due to the curvature of the defect field between boojums in a bipolar system. The balance between these elastic energies determines the lowest energy configuration of a system, with a high K_{33}/K_{11} value leading to a bipolar configuration. Whereas, if $K_{11}/K_{33} > 0.7$ a concentric configuration with mesogen aligned in concentric rings which become smaller inside the droplet and a defect line through the centre (represented in Figure 15d) is promoted instead, due to the lower free energy arising from increased splay energy contribution compared to bend energy. Furthermore, if the twist elastic energy (K_{22}) is small enough, a twisted bipolar configuration (Figure 15c) may be favoured to reduce the overall free energy of the system.[46]

In a spherical environment with perpendicular surface anchoring, a radial configuration (Figure 15e) is favoured which results in a topological defect inevitably forming in the centre of the sphere. The only elastic deformation present in a radial configuration is splay.[42]

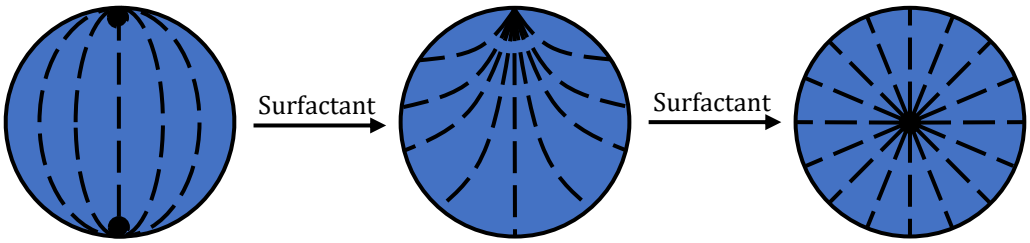

Figure 16: Cartoon representation of a bipolar director configuration (a) transitioning to a radial configuration (c) *via* an escaped radial configuration (b) in a nematic droplet with the addition of surfactant.

These are some of the common director configurations of a nematic in spherical confinement. Many more configurations are possible, including transition configurations as one director configuration transforms into another, for example, a so called 'escaped radial' configuration exists as a bipolar director configuration transitions to a radial director configuration (Figure 16). One method for transitioning the director field from bipolar to radial was performed by changing the surface anchoring conditions by introducing surfactant, such as SDS, into the aqueous dispersion medium. As it is polar, water will promote parallel surface anchoring however introducing surfactant, which creates a pseudo-hydrophobic environment around droplets, changes the surface anchoring conditions to promote perpendicular alignment. As the concentration of surfactant is increased the bipolar configuration transitions to a so called 'escaped radial' configuration, before transitioning to a radial configuration at higher concentrations.[48,49]

Spherically confined nematic systems give rise to characteristic textures when observed under POM. Radially aligned droplets give rise to a so called 'Maltese cross' texture, where a dark brush occurs when the director is parallel to either of the 90° crosse polarisers. Whereas bipolar droplets not only exhibit a Maltese cross texture, but also a so called 'baseball' texture (Figure 17) dependent upon the orientation of the droplet with respect to the crossed polarisers. For observation of a bipolar droplet's Maltese cross texture the polar axis of the droplet must be in a plane perpendicular to the plane of the crossed polarisers, any deviation from this orientation will give rise to the baseball texture. Hence, it is far more likely that a baseball texture, rather than a Maltese cross texture, is observed.[47,50]

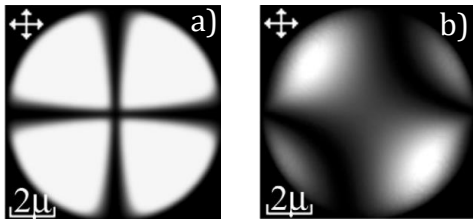

Figure 17: Theoretically calculated images of so called 'Maltese cross' texture (a) and 'baseball' texture (b), scale bar 2 µm. Reproduced from ref. 50.

1.4.2 Nematic Elastomer Microparticles

Polymerisation of nematic droplets containing monomer, crosslinker and polymerisation initiator (e.g. a photo or thermal initiator) can yield nematic elastomer particles. Similar to nematic elastomer films, these may be capable of an actuation response to temperature changes about the T_{NI}.

Taylor produced small micrometre sized bipolar elastomer particles, from bipolar nematic droplets produced by microfluidics (method discussed in the next chapters), which showed actuating properties.[51] The particles exhibit a reversible shape change, contracting in the direction of the director, as a response to temperature changes about their T_{NI}. Thus, the elastomer microparticles elongate in the direction perpendicular to the polar axis, which follows the director, and contract in the direction parallel to the polar axis.[51,52] Figure 18 shows this reversible shape change in a population of nematic elastomer microparticles. The highlighted microparticle flattens vertically and elongates horizontally with respect to the observer. This property gives rise to applications of bipolar nematic liquid crystal particles as soft microactuators in numerous applications including micromechanics, soft robotics, photonics and as artificial muscles.[29,30,53,54]

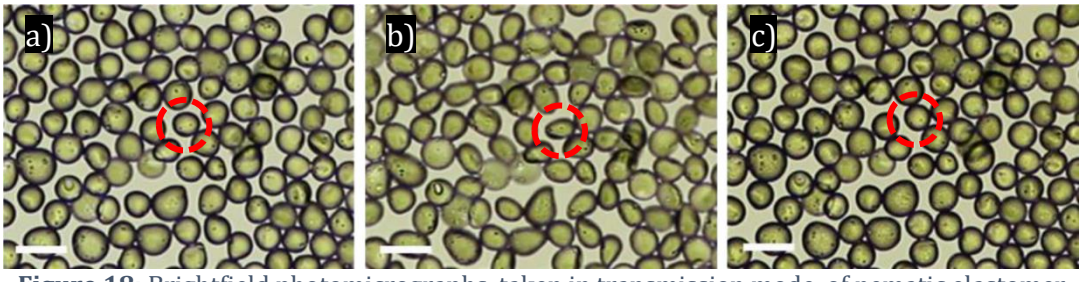

Figure 18: Brightfield photomicrographs, taken in transmission mode, of nematic elastomer particles of **M1** at 100x magnification: in the nematic phase at 100 °C (a); in the isotropic phase at 130 °C (b); and returned to the nematic phase at 100 °C (c). Scale bars 50 µm. Reproduced from ref. 51.

As well as spherical particles, examples of anisometric liquid crystal polymer particles have been reported. For example, droplets of a mesogenic monomer with non-polymerisable 5CB have been produced. Upon polymerisation, the mesogenic monomer formed a polymer network, however as 5CB is non-polymerisable it was not incorporated into the network. This meant that the 5CB could be removed after polymerisation, causing the particles to deform from spherical to spindle shaped due to the volume reduction. Due to a lack of crosslinking however, these particles did not actuate.[55–57]

Finally, 10 μm anisometric nematic elastomer particles have also produced by a two-step polymerisation method.[58–60] Liu *et al* produced partially polymerised 'droplets' of a mesogenic monomer, chain extender, crosslinker and photoinitiator mixture, by dispersion polymerisation. These partially polymerised droplets were then embedded into a PVA film which was stretched, and the stretched 'droplets' were polymerised a second time by photopolymerisation to yield nematic elastomer microparticles which maintained their anisometric shape. As these particles were crosslinked, they were able to undergo actuation upon heating and cooling about their phase transition temperature, shown in Figure 19.[58]

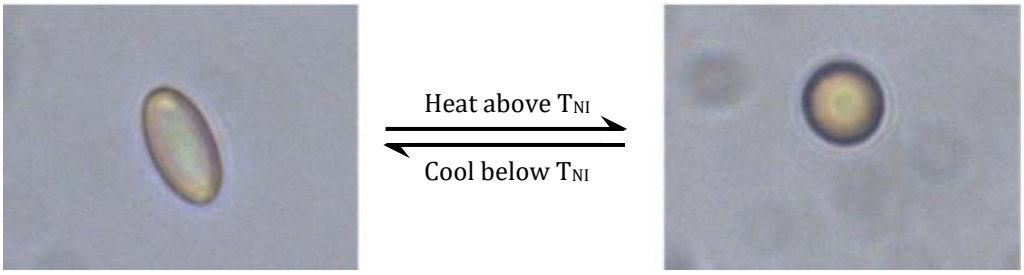

Figure 19: Brightfield photomicrographs showing the actuation of stretched nematic elastomer microparticles as a response to temperature change about the T_{NI}. Reproduced from Liu *et al*.[58]

1.4.3 Chiral Nematic Droplets and Elastomer Microparticles

Production of chiral nematic droplets allows for the spherical confinement of the characteristic helical superstructure of the phase. Much like chiral nematic mixtures and films, chiral nematic droplets can be produced from a chiral mesogen, or from an achiral mesogen doped with a chiral dopant.

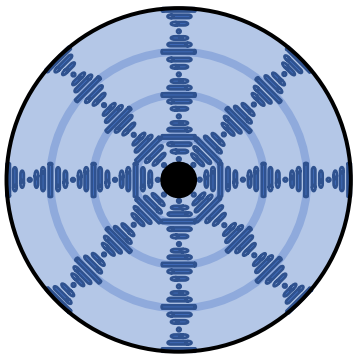

Figure 20: Cartoon representation of radial chiral nematic helical structure within a parallel aligned droplet. Redrawn from ref. 61.

Chiral nematic systems where the mesogens have parallel surface anchoring within spherical confinement may give rise to a radial helical structure (Figure 20). However, similarly to nematic droplets, the director configuration will depend on the fine balance of surface and elastic energies as well as droplet size. The radial chiral nematic configuration is characterised under POM by the observed texture. In systems with a longer pitch, in the micrometre range, a fingerprint texture is observed (Figure 21a). In systems with shorter helical pitch, on the same order as visible light, a Maltese cross texture is observed, arising due to the central topological defect (Figure 21b).[61]

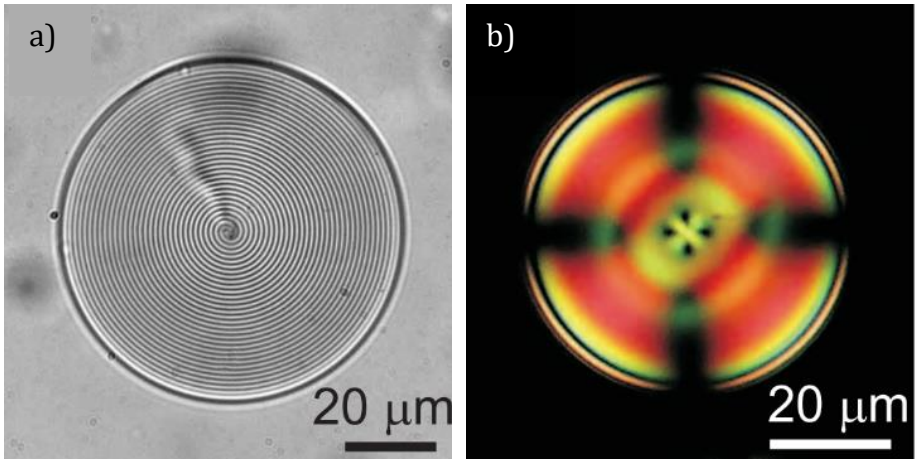

Figure 21: Polarised photomicrographs of chiral nematic droplets showing fingerprint (a) and Maltese cross textures (b). Reproduced from ref. 61.

Much like chiral nematic mixtures and films, chiral nematic droplets, where the helices are radially aligned and have a pitch within the visible region, are capable of selective reflection of visible light.[62,63] Under reflectance microscopy, selective

reflection is observed as a central coloured spot within the droplet. The selective reflection colour is seen in the centre as this is the point where the of incident light meets the chiral helices at 0°, and so the Bragg reflection law (Equation 7, section 1.2.2.3) shows that this must be the area reflecting the longest wavelength. As in films, the colour of the selective reflection is proportional to the helical pitch.

Further to the selective reflection colour, which is usually observed under reflectance microscopy as a central spot within the droplet or particles, photonic cross-communication can occur. Photonic cross-communication is characterised by bright coloured reflection lines which appear to radiate out from the centre of droplets, an example is shown in Figure 22 showing droplets produced by Fan *et al*.[64] The cross-communication occurs as a result of the spherical symmetry and optical Bragg reflection in a monodisperse hexagonally close-packed chiral nematic system. The interference reflects the packing symmetry of the hexagonal lattice, with cross coupling lines in Figure 22 originating from strong reflections and interferences involving both nearest and next nearest neighbours. Photonic cross-communication been reported in several chiral nematic systems, including those reported by Noh *et al* and Geng *et al,* who proposed the mechanism by which photonic cross-communication works. More recently examples were produced Peterson *et al*.[22,64–66]

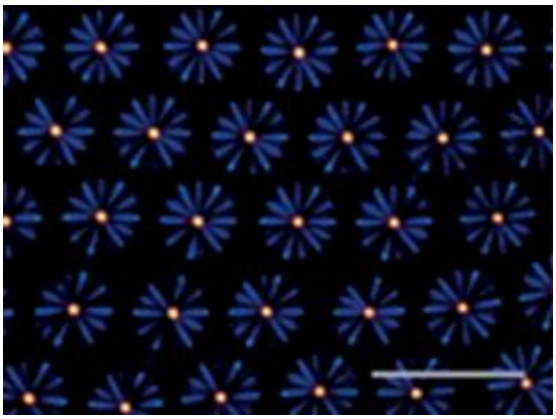

Figure 22: Photomicrograph, taken in reflection mode through crossed polarisers, of a monolayer of chiral nematic droplets displaying central selective reflection spots and photonic cross-communication lines. Reproduced from ref. 64. Scale bar 100 μm.

Figure 23 shows a cartoon representation of the angle between incident light and the helical pitch at θ = 0° as well as at θ = 45°. It can be seen that where θ = 0° the

longest wavelength possible for the reflector is given, $\lambda = n\mathrm{P}$. Due to the curvature of the sphere, any light not hitting the centre of the droplet enters at a non-zero angle of incidence compared to the radial helical axis. At any non-zero angle of incidence, the cosθ term of the Bragg reflection law results in shorter wavelengths of light being reflected. Where the reflection occurs between nearest neighbour droplets at θ = 45° the light is reflected into the nearest neighbour which then reflects the light back to the observer after a second reflection at the same angle, 45°. Hence, the shorter wavelength light is observed as cross-communication lines between the close-packed droplets. This can give rise to specific and controllable patterning which can be exploited in security applications like unique pattern detection tags.[66]

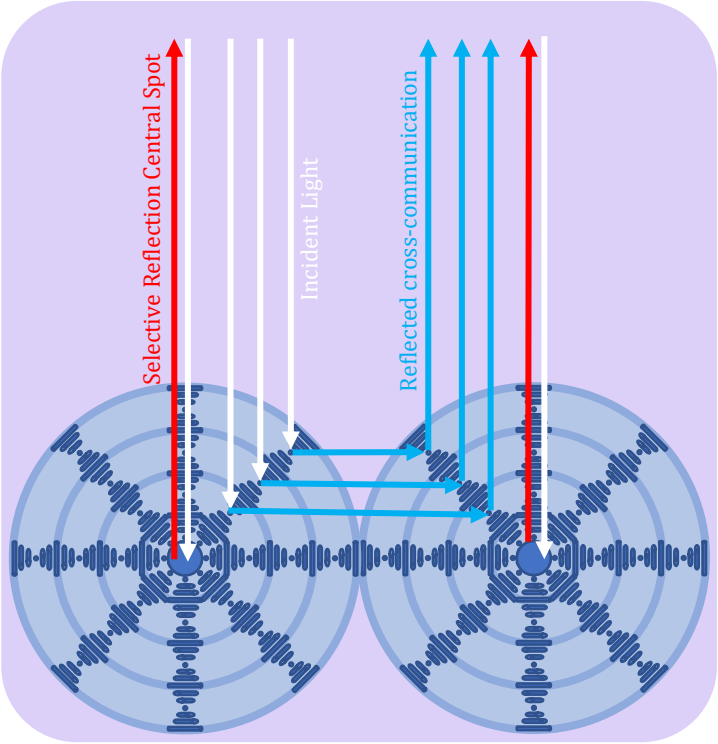

Figure 23: Cartoon representation of photonic cross-communication in chiral nematic droplets. White arrows represent incident light, red arrows the selective reflection spot where incident light enters at θ = 0° and the light blue vertical arrows reflected cross-communication where incident light enters at θ = 45°, transmitted between droplets along horizontal blue arrows. Redrawn from refs. 51 & 64.

Chiral nematic elastomer microparticles may be produced from chiral nematic droplets which contain mesogenic monomer, crosslinker, photoinitiator as well as

a chiral dopant (if the other components are achiral). Similar to films and achiral elastomer particles, upon polymerisation alignment is retained. Because of this retention of alignment, chiral helices persist and hence chiral nematic elastomer microparticles can be capable of selective reflection of wavelengths of light. As with droplets and films, if the helical pitch is within the visible region, then wavelengths of visible light are reflected which can be tuned by, for example, altering dopant concentration. Noh and Park exploited this by producing chiral nematic elastomer microparticles of CB15 doped mesogenic monomer mixture 'RMM727' which selectively reflected either red, yellow, green or blue light, depending on the CB15 concentration.[37] In addition to selective reflection, photonic cross-communication has also been observed to persist in monodisperse close-packed chiral nematic elastomer particles. However, the optical quality of the cross-communication is reported to become reduced post-polymerisation compared to the particles' droplet counterparts, where optical artifacts such as speckling becomes prevalent in the imaging.[37,67]

Mixtures of chiral nematic elastomer microparticles could be produced so that unique arrays of coloured and patterned microparticles could arise. This may lead to applications within security patterning, an application employed in the literature for other chiral nematic spherical systems, such as shells, by Geng *et al.*[22]

1.5 Nanoparticle Infiltration of Liquid Crystal Systems

In isotropic liquids interactions between free nanoparticles is governed by Brownian motion and electrostatic interactions between the nanoparticles and their dispersion medium. Due to their small size, the Brownian motion of nanoparticles is a significant driving force in producing randomly dispersed suspensions in isotropic liquids. In aqueous suspensions, electrostatic interactions between nanoparticles and the dispersion medium are able to overcome density differences, preventing nanoparticles aggregating, sinking or floating in the dispersion medium.[68] In contrast to isotropic liquids, nanoparticles in liquid crystals are influenced by the director of the system.

1.5.1 Nanoparticle Self-Assembly in Planar Monodomain Liquid Crystal Systems

There are several examples of successful infiltration of nanoparticles into anisotropic liquid crystal systems. For example, Škarabot *et al* homogenised silica nanoparticles with diameters in the micrometre range down to as small as 35 nm in 5CB, however stable dispersions did not form, as would be expected in an isotropic system. Instead, particles spontaneously formed self-assembled aggregates which the authors attributed to be due to the dominating interactions being elastic in origin.[69] These forces are able to extend over the micrometre scale.[70,71] When nanoparticles are introduced into a liquid crystal system, elastic deformation of the director field occurs as the alignment of mesogens is interrupted by the presence of the nanoparticle. As well as this, surface anchoring of mesogen to the nanoparticle surface itself further disrupts the director.[72] The director field experiences elastic deformations about the infiltrated particles to minimise disruption of the director field across the bulk system. As orientation of mesogens in the liquid crystal is interrupted, defects spontaneously form, due to the director not being defined in these regions.

Point defects and so called 'Saturn ring' defects are the two main types of defects which may arise as a result of perpendicular alignment of the mesogens to the nanoparticles surface. Perpendicular alignment of mesogen to the nanoparticle surface can be achieved by coating nanoparticles with surface coupling agents which induce mesogen orientation to the nanoparticle surface, by van der Waals' forces. An example of a surface coupling agent which promotes perpendicular alignment of the mesogens to the nanoparticle surface is DMOAP (structure shown in Figure 24).

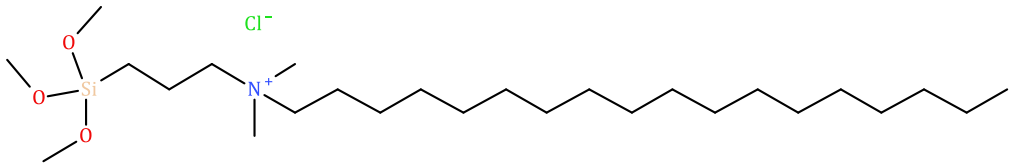

Figure 24: Molecular structure of DMOAP.

For point defects, a defect occurs positioned directly inside where the nanoparticle is located and another slightly above the nanoparticles surface (Figure 25a & c),

together these defects form a topological pair, hence they are known as a topological dipole.[72–75] For Saturn ring defects, a circular defect in the plane and around the circumference of the nanoparticle occurs (Figure 25b & d). The symmetry of a Saturn ring defect can be described as quadrupolar, hence the defect is known as a topological quadrupole.[72] It has been found that point defects transform into Saturn ring defects when the cell thickness is decreased below a critical value. In a 5CB system infiltrated with 2.32 μm silica microparticles this critical value was established as ~3.5 μm.[76]

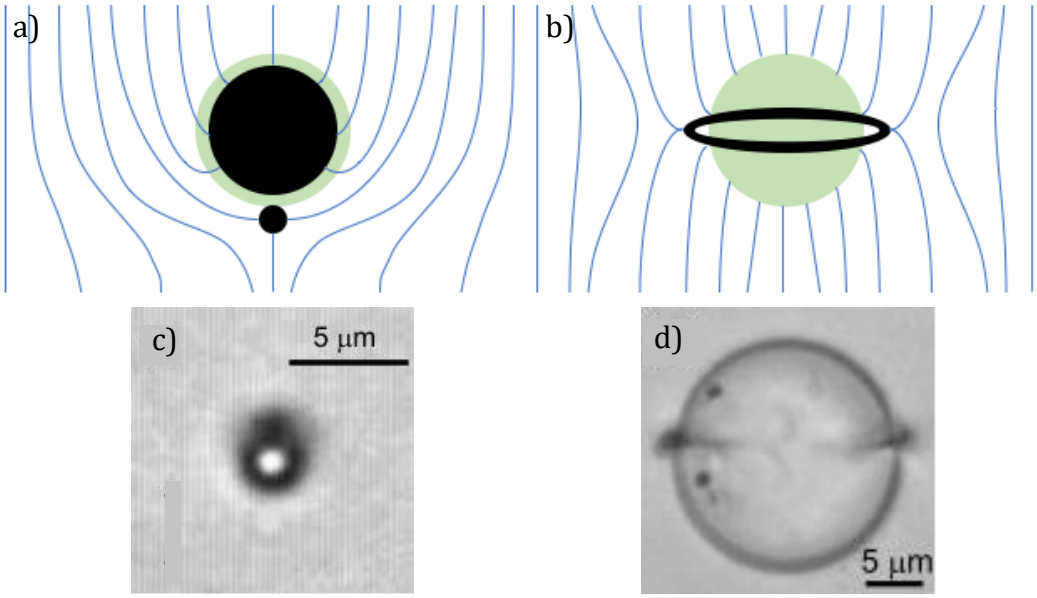

Figure 25: Cartoon representation of the distortion of the director field, represented by blue lines, caused by infiltration of a nematic system with a nanoparticle (transparent green) showing point defects (a) and a Saturn ring defect (b). Redrawn from ref. 74. Photomicrographs through crossed polarisers of silica microparticle in nematogen 5CB showing point defects (c) and a Saturn ring defect (d) reproduced from refs. 72 & 77.

As discussed previously, disrupting the alignment of the mesogens causes deformation of the director field which has an elastic energy cost. In order to reduce the elastic energy cost and minimise the overall free energy of the system, nanoparticles have been found to self-assemble into chains along defects. This is essentially an overlapping of defects induced by each particle, replacing areas of director field deformation to minimise the overall extent and number of induced defects formed.[69] Nanoparticles are held in chains by structural forces imposed by the elastic energy of the liquid crystal system.[78] Decreased separation between

nanoparticles therefore decreases the total energy of the system due to less disruption being present, and thus is represented by a smaller overall defect.[72]

Nanoparticles which exhibit both point defects and Saturn ring defects can form one-dimensional chains of nanoparticles. Point defects allow for straight nanoparticle chains to form along the rubbing direction of the cell's polyimide layers as a nanoparticle will localise with its own dipolar defects aligned with its neighbour. This is repeated to form long one-dimensional chains (Figure 26a) of nanoparticles self-assembled within the nematic liquid crystal. Two-dimensional assemblies of hexagonally packed nanoparticles have also been observed.[70,74,77] Nanoparticles which exhibit a Saturn ring defect induce assembly of kinked nanoparticle chains (Figure 26b) which are perpendicular to the rubbing direction of polyimide layers as the direction of the Saturn ring defect is itself perpendicular to the polyimide layer's rubbing direction. Two-dimensional lattice-like assemblies of nanoparticles tend to form from nanoparticles which induce Saturn ring defects (Figure 26c).[76]

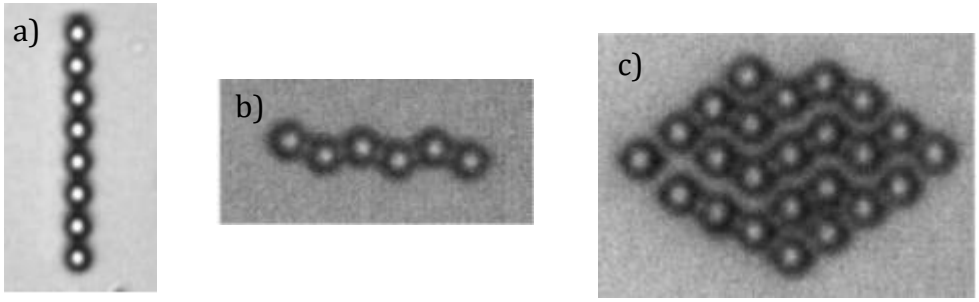

Figure 26: Photomicrographs of silica nanoparticle chains (a & b) and a lattice-like assembly (c) in a nematic 5CB system. Polyimide rubbing direction vertical with respect to page. Reproduced from refs. 77 & 76.

Aggregation of particles in a liquid crystal system about induced defects has been observed using a range of nanoparticle sizes, from micrometre sized down to particles with diameters of 35 nm. However, when using silica particles with a diameter as small as 22 nm, in a liquid crystal system of 5CB, aggregation is not observed. As the extent of elastic distortion is proportional to the size of the infiltrate, particles of smaller size have a much smaller distortional effect on the liquid crystal alignment.[69] It is thought that the elastic distortion for these particles is so small that electrostatic interactions and thermal energy effects outweigh the

effect of the elastic energies in producing strong enough forces to hold nanoparticles in aggregated chains, so Brownian motion of free particles is observed.[69]

1.5.2 Nanoparticles in Planar Defect Stabilised Liquid Crystals

The so called 'blue phases' (BPs) are an example of frustrated chiral liquid crystal phases. Blue phases occur in highly chiral liquid crystals, typically over a very narrow temperature range as the system approaches its clearing point. Unlike the single-twisted helices of the chiral nematic phase, blue phases have a double twist helical structure. As these double twist helices cannot effectively pack to fill space, a cubic structure of double twist helices is adopted (Figure 27) which induces a periodic and ordered patterns of defect lines.[3] The frustration in these systems arises when the increased twist deformation of the director field outweighs the energetic expense of forming defect lines. Hence, the regular array of defects becomes the ground stable structure. There are three classifications of the blue phase, BPI, BPII and BPIII. BPI and BPII form a cubic lattice of defect lines, whereas BPIII gives rise to an amphorous network of defect lines.[79]

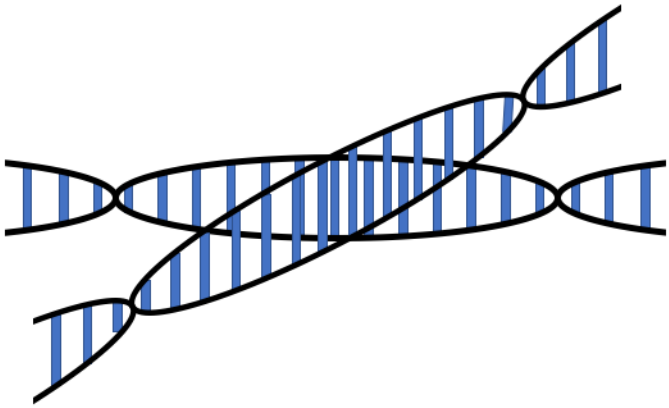

Figure 27: Cartoon representation of double twist helices where blue rods represent mesogens. Redrawn from ref. 3.

The lattice of defect lines formed by blue phases can act as a template for introduced nanoparticles to localise into.[80] This may occur when the nanoparticles introduced are small and exhibit weak surface anchoring, i.e. the composition of the nanoparticle at the surface is such that there are relatively few van der Waals'

interactions between the nanoparticle surface and mesogens for alignment, compared to nanoparticles which induce stronger surface anchoring. Similar to monodomain liquid crystal systems, the introduction of additional defects into the system is unfavourable as the self-assembled mesogenic system becomes distorted. Hence, nanoparticles migrate to already present defect lines so as to not introduce any more defects into the defect-dominated system.[79] When nanoparticles localise into already existing defects elastic deformation is eliminated as aligned areas of mesogens are not deformed. The total free energy change of the system is minimised by defect localisation of nanoparticles, as the nanoparticles essentially remove some of the volume of the defect by inhabiting them.[81] The reduction in energy associated with nanoparticle localisation into defects has resulted in blue phase stabilisation, where the temperature range at which the blue phase exists is increased.[79,82–84]

Self-assembly of nanoparticles along the 3D defect lattice lines could give rise to the building of complex 3D nanostructures of nanoparticles within a blue phase template. Experimental work has been completed using a liquid crystalline mixture of 4′-hexyloxy-4-cyanobiphenyl (6OCB) and CB15, which exhibits a blue phase. Gold nanoparticles with diameters of 4.7 nm were introduced into the blue phase lattice. Characterisation by small angle x-ray scattering suggested that the gold nanoparticles localise into tetrahedral structures within the blue phase defects, as seen in Figure 28. It is anticipated that polymerisation could preserve the 3D cubic nanostructures.[80]

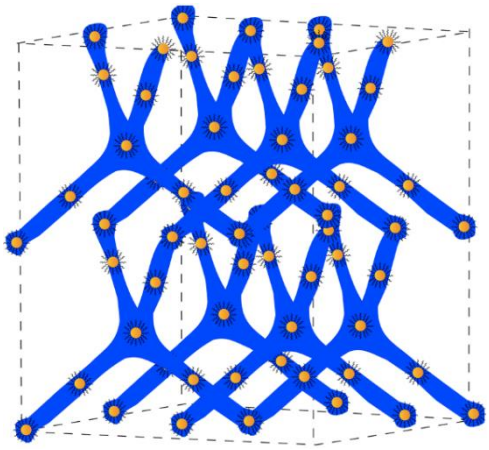

Figure 28: Cartoon model showing possible 3D arrangement of gold nanoparticles (orange) in tetrahedral defect lines (blue) of BPII. Reproduced from ref. 80.

1.5.3 Nanoparticles in Liquid Crystal Droplets and Microparticles

1.5.3.1 Nanoparticles in Liquid Crystal Droplets

Nanoparticle infiltration of spherically confined liquid crystals is a relatively new field of research. Currently, there are few examples of nanoparticle infiltration of liquid crystal microdroplets. The current examples mainly use variations of a suspension method to introduce the nanoparticles into liquid crystal droplets.

Mondiot *et al* introduced nanoparticles into bipolar nematic liquid crystal microdroplets with the nanoparticles localised in two defects. Droplets of 5CB were produced in a dispersion medium of water and glycerol (90 %v/v), to promote a bipolar configuration, which also contained 0.01 %w/v fluorescent polystyrene or silica nanoparticles with diameters of 1 μm. As the nanoparticles used were fluorescent, combined fluorescence and brightfield microscopy allowed for the observation that exactly two nanoparticles were present in some of the 5CB droplets, located one in each polar defect (Figure 29).[85]

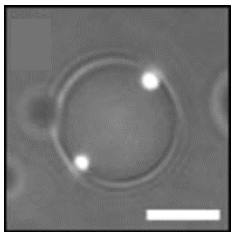

Figure 29: Combined brightfield and fluorescence photomicrograph to show localisation of two fluorescent 1.0 μm polystyrene nanoparticles in a 7.8 μm 5CB droplet, scale bar 5 μm. Reproduced from ref. 85.

As the bipolar droplets have two topological defects present, migration of nanoparticles into these defects is the product of energetics within the droplets. The anchoring of a nanoparticle at the surface of the droplet increases the overall surface energy, however positioning these at the already present defects minimises elastic distortion of the director field and effectively removes defect volume. Additional defects are not introduced elsewhere within the droplet, which would interrupt orientational ordering of the mesogens and increase elastic energy. The decrease in elastic energy outweighs the increase in surface energy, where the nanoparticles protrude from the surface,[85] and therefore minimises the overall free energy of the system when introducing nanoparticles. It is therefore

energetically favourable for the nanoparticles to migrate to defects, rather than elsewhere in the droplet, much like how nanoparticles localise into the topological defects present in blue phase systems discussed in the previous subsection.[79–81,86]

Melton *et al* infiltrated radial nematic microdroplets of 5CB with 6 nm semiconductor nanoparticles by utilising the suspension method with a solution of SDS in water (1 wt%). Fluorescent 6 nm diameter quantum dots (QD) composed of a ZnO shell surrounding a CdSe core were suspended in the mesogenic phase and consequently the QDs were incorporated into droplets, which were held in the isotropic phase. Cooling into the nematic phase produced a radial configuration of droplets, due to the pseudo-hydrophobic environment created by SDS around the droplet.[40,41] It was found that QD clusters with diameters of ~0.5 – 2 μm migrated into the middle of the droplet to localise in the central defect of the radial droplets, as observed under fluorescence microscopy, shown in Figure 30.[43] Again, nanoparticle localisation is due to elastic forces imparted on nanoparticles by disrupting the mesogen alignment in system.

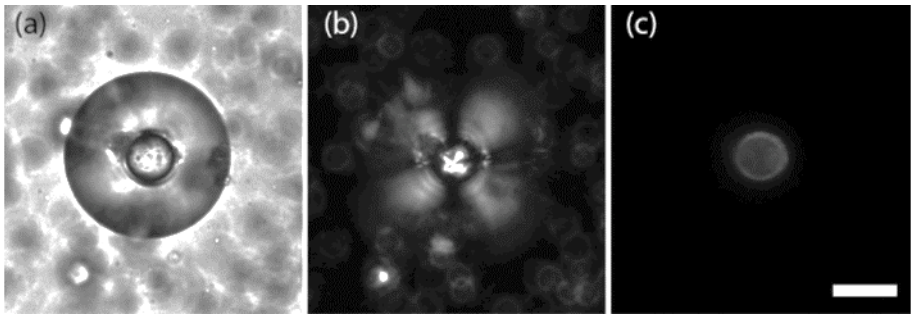

Figure 30: Brightfield (a), polarised (b) and fluorescence (c) photomicrographs to show localisation of clustered semiconductor nanoparticles into the central defect of a radial nematic 5CB droplet. Reproduced from ref. 43.

Chiral nematic microdroplets of 5 – 50 μm diameter have been produced which exhibit more complicated so called 'radial spherical' defect structures (RSS). These defect structures are characterised by two surface defects which are close in proximity, with a twisted disclination line connecting them *via* the centre of the droplet, shown in Figure 31a & b. When infiltrating these with two 1 μm diameter polystyrene nanoparticles it was found that they localise where the defects meet the surface of the microdroplet (Figure 31c). Again, this is due to elastic forces imparted by mesogen alignment in the droplet. However, when 200 nm

polystyrene nanoparticles were introduced they did not localise in the surface defects, suggesting that they are too small to impart a large enough strain to the aligned system to introduce significant elastic deformation, hence localisation does not take place.[87] This shows that there is a degree of size-dependence which governs localisation into defects, similar to the size-dependence discussed in monodomain nematic systems.

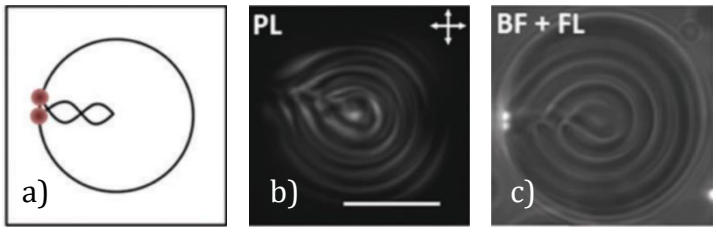

Figure 31: Cartoon representation of RSS defects (a); polarised photomicrograph of chiral nematic droplet showing RSS defects (b); combined brightfield and fluorescence photomicrograph (c) to show surface defect localisation of two 1 μm polystyrene nanoparticles in a chiral nematic droplet. Reproduced from ref. 87.

1.5.3.2 Nanoparticles in Liquid Crystal Microparticles

It is worth noting that there are several methods for producing non-liquid crystalline polymer microparticles with nanoparticles held inside the polymer matrix (NiMs). NiMs come in several forms, usually hollow shells (microcapsules) containing drug-loaded nanoparticles for drug delivery in biomedicine. The shells are produced by a modified suspension polymerisation method which produces aqueous droplets within organic droplets within the aqueous bulk. The aqueous droplet in the centre of the microcapsule diffuses out of the capsule, into the bulk, leaving a hollow core. Depending on which phase the nanoparticles are dispersed in, they can be located in the hollow core or within the polymer matrix of the microcapsule wall. Production of NiMs has been successfully accomplished using both nanoparticles and microparticles in the micrometre range.[88]

On the other hand, in liquid crystal microparticles, nanoparticle location is governed by the elastic forces in the system. Low quantities (one or two) of nanoparticles within liquid crystal polymer microparticles have been produced by Mondiot *et al*.[85] This is the only example of a nematic polymer microparticle containing up to two nanoparticles, one nanoparticle in each topological defect of a bipolar microparticle.

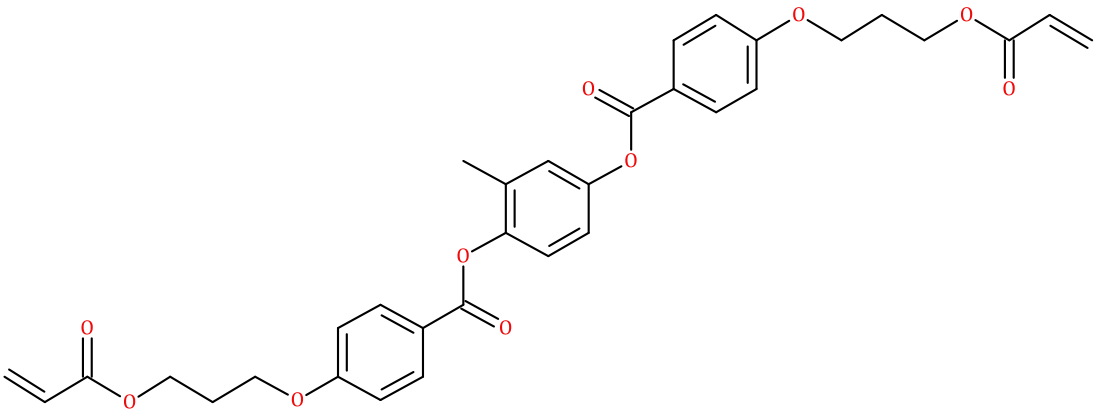

Figure 32: Molecular structure of RM257.

Mondiot *et al* prepared the nanoparticle containing nematic polymer microparticles as follows. Nanoparticle infiltrated liquid crystal microdroplets of a mesogenic monomer containing crosslinker and photoinitiator were produced using the suspension method as described in the previous subsection (the suspension method is described in more detail in section 2.2). These microdroplets were then photopolymerised under UV light to yield liquid crystal polymer microparticles. Droplets of the monomer phase, which was made up of 20 wt% mesogenic monomer, RM257 (Figure 32) in 5CB and photoinitiator DMPAP, were suspended in the water and glycerol (90 %v/v) dispersion medium which also contained 0.01 %w/v fluorescent polystyrene or silica nanoparticles with diameters of 1 μm. As the dispersion medium was water and glycerol (90 %v/v) a bipolar configuration was promoted. Photopolymerisation of droplets took place under UV light to yield nematic microparticles with nanoparticles held at poles within the polymer matrix, as shown in Figure 33. This was proven using imaging by fluorescence microscopy. Both nanoparticle infiltrated non-polymerised droplets and polymerised particles were heated above their T_{NI}. The droplets were observed and showed nanoparticles dissociated away from the poles and met in the middle of the droplet, whereas nanoparticles in polymerised particles stayed at the poles, hence showing they were held in place by the polymer matrix, proving their localisation was preserved by polymerisation.[85] As the microparticles were liquid crystal polymers, and not elastomers there was no actuation response about the phase transition.

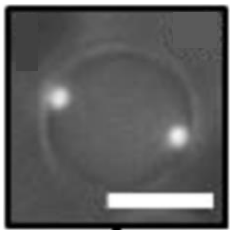

Figure 33: Combined brightfield and fluorescence photomicrograph showing preservation of two fluorescent 1.0 μm polystyrene nanoparticles in a 6.7 μm 5CB polymer microparticle, scale bar 5 μm. Reproduced from ref. 85.

In the literature, as far as we are aware, there are no examples of controlled nanoparticle infiltration of liquid crystal elastomer microparticles to produce elastomer microparticles with single nanoparticles localised into topological defects. Therefore, this will be an aim of this thesis so that the properties of nanoparticle infiltrated nematic elastomer microparticles can be investigated.

1.6 Project Aims

- To produce monodisperse nematic droplets by microfluidic methods in the small micrometre range with defined confinement structures, characterised by polarised light optical microscopy.
- To infiltrate nematic microdroplets with fluorescent nanoparticles by a modified microfluidic method; the location of nanoparticles within droplets to be characterised by fluorescence microscopy.
- To polymerise nematic droplets, both with and without nanoparticles, to produce nematic elastomer microparticles of various geometries and characterise their thermal and optical properties by polarised light optical microscopy and their morphology by scanning electron microscopy.
- To investigate responsive properties of synthesised nematic droplets and elastomer microparticles to external stimuli such as temperature and magnetic fields.
- To produce chiral nematic mixtures and films, as well as monodisperse droplets and elastomer microparticles by microfluidics and characterise thermal and optical properties by polarised light optical microscopy,

reflectance microscopy, UV-Vis-NIR spectroscopy and differential scanning calorimetry.

- To investigate the responsive properties of chiral nematic systems produced to external stimuli, such as temperature and pressure, as well as chiral dopant removal from elastomer systems.

2 Droplet Production Methods

2.1 Overview

Many of the aims of this thesis rely on the production of microparticles of liquid crystalline material. In order to make these, several methods could be employed including emulsion polymerisation, seed polymerisation, suspension polymerisation and microfluidics.[59,85,89–94] In order to produce microparticles, droplets of polymerisable material are produced first. The two main methods reported for droplet production are either a variation of a suspension method, or more recently microfluidic methods.[85,90,95,96] In this thesis, the focus is on the microfluidic method, however the suspension method was utilised also.

In this chapter a short overview of both methods is presented as well as investigations which were performed to optimise the microfluidic method with the aim of producing droplets with as small diameters as possible, whilst being able to maintain control of the confinement textures. As discussed in the previous chapter, the size of droplets influences the nematic confinement texture, with small <1 μm droplets being dominated by only the elasticity of the nematic, which produces monodomain droplets.[45,47] On the contrary, where diameters are too large (for example >300 μm) systems have been reported to act like non-aligned bulk systems, despite being confined within a spherical geometry.[97] Hence, the production of droplets of controllable size will be important for this thesis, as the main aims rely on quality and controlled confinement of bipolar droplets.

2.2 Suspension Method

Microdroplets can be produced by emulsion of a droplet phase within an immiscible dispersion medium to create so called oil-in-water or water-in-oil emulsions depending on the system. To produce liquid crystal droplets a liquid crystalline phase is used. Upon combining, the system forms two layers: the dispersion medium, commonly water with a stabiliser to prevent droplet coalescence, and a liquid crystalline layer. The layered system is then agitated by rapid stirring, homogenising or shaking, and due to the incompatibility of phases,

suspended droplets of the liquid crystal in the dispersion medium are observed, as seen in Figure 34.[44,85,90,98,99]

The size of droplets is determined by the agitation speed, the viscosities of the liquid crystal and dispersion medium as well as the concentration and type of stabiliser. Stabilisers work by forming an interfacial layer around droplets which reduces the affinity for the droplets to coalesce.[85,99]

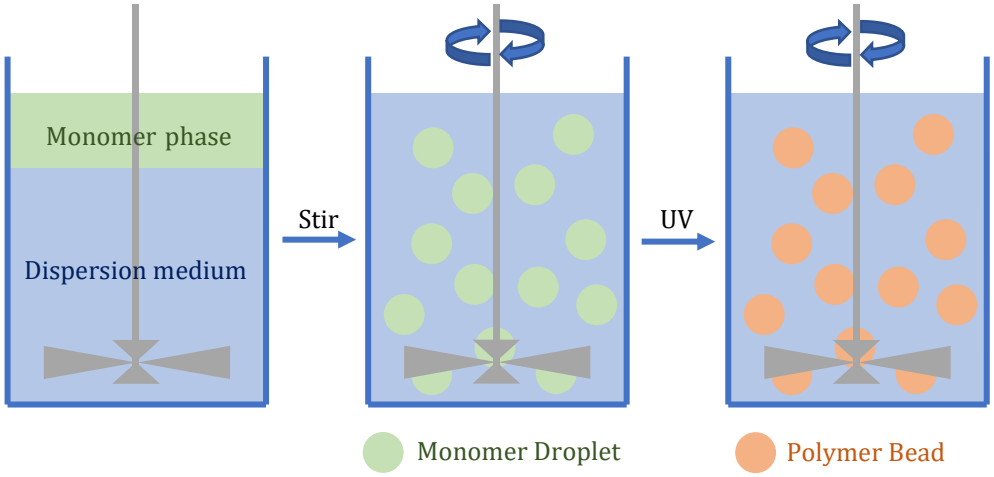

Figure 34: Cartoon diagram of the suspension polymerisation process. Redrawn from ref. 51.

Suspension polymerisation is a common method for producing polymer microparticles. After droplets have been produced by agitating immiscible layers of monomer and dispersion medium as described above, the dispersion is then irradiated with UV light to polymerise the droplets into polymer microparticles, as shown in Figure 34. To produce liquid crystal microparticles the monomer phase is made up of a mesogenic monomer and photoinitiator. Photopolymerisation of the liquid crystal monomer droplets with UV light produces liquid crystal microparticles.

There are several advantages to using the suspension method for droplet and microparticle production, such as the fact that suspensions are quick and easy to set up and can be performed on fairly large scale. However, a major drawback of the suspension method is that the droplets produced are polydisperse, with a large size distribution.[44,98,100] For example, Omi *et al* produced polystyrene

microparticles by suspension polymerisation with diameters up to 10 μm but with a size distribution of 10%, which is considered polydisperse.[89,101,102]

2.3 Microfluidic Method

On the other hand, microfluidics uses a microfluidic chip device with micrometre sized channels to manipulate the flow of microlitre volumes of fluid. In droplet microfluidics, the flow conditions of two immiscible phases are exploited to produce droplets of controllable size, from the nanometre to millimetre scale. Furthermore, the dispersity of droplets produced is highly controlled, allowing for monodisperse populations of droplets to be fabricated.[100,103] One of the aims of this thesis is to produce monodisperse droplets, hence the microfluidic method was selected for droplet production over the suspension method, despite the disadvantage of the microfluidic method being slower and more technically challenging to set up and run.

2.3.1 Microfluidic Setup and Chip Design

There are several different chip designs which can be utilised to create various microfluidic systems, such as the T-junction, flow-focussing, co-flowing and membrane setups.[96,104–106] All of these microfluidic systems manipulate the flow of two immiscible liquids to produce droplets of one within the other. The hydrodynamic flow of the system is described by the Reynolds number (*Re*), which refers to the turbulence of the flow, and capillary number (*Ca*) which describes the viscous drag forces between the immiscible outer and inner phases (also known as outer and inner fluids). The Reynolds number is calculated as described in Equation 8, where p is the density, V is the velocity, D is the diameter of the tube in which the fluid flows, and η is the viscosity of the fluid.[101] In microfluidics the flow needs to be laminar, with as little turbulence as possible, and hence a low Reynolds number (<1000) is required, although in the micrometre sized channels this tends to be much smaller, generally <1.[107,108]

$$Re = \frac{pVD}{\eta}$$

Equation 8: To calculate Reynolds number.[101]

The capillary number is calculated as described in Equation 9, where η is the viscosity, V the velocity and γ is the interfacial tension between immiscible fluids.

$$Ca = \frac{\eta V}{\gamma}$$

Equation 9: To calculate capillary number.[101]

In a co-axially aligned flow-focussing microfluidic device (a cartoon representation is shown in Figure 35) the capillary numbers of both the outer and inner fluids are important. The shearing force exerted by the outer fluid to the inner fluid at the droplet tip (where the droplet of inner fluid is produced) pinches the stream to create a droplet, which is carried away through a collection tip by the flow of the outer fluid for collection. An increase in the ratio of the capillary number of the outer fluid and inner fluid, Ca_o/Ca_i, results in decreasing droplet diameter due to an increase in shearing force between the immiscible phases. As the flow rates are proportional to Ca values, changing the ratio of the flow rates of the outer and inner fluids also results in the altering of droplet size. An increase in the outer fluid flow rate decreases droplet size, as does a decrease in inner fluid flow rate.[101,109] As the ratio of viscosities of the fluids are also proportional to Ca, the same rationale as above shows droplet size is also governed by fluid viscosities.[110–112] It is worth noting that a balance needs to be found between the inner and outer phase flow rates so as to prevent collection of the inner phase at the droplet tip or jetting. Jetting occurs when the inner phase flow rate is proportionally too high compared to the outer phase, resulting in a jet which breaks into droplets downstream of the collection tip which introduces instability and therefore produces droplets with greater polydispersity.[89,113–115]

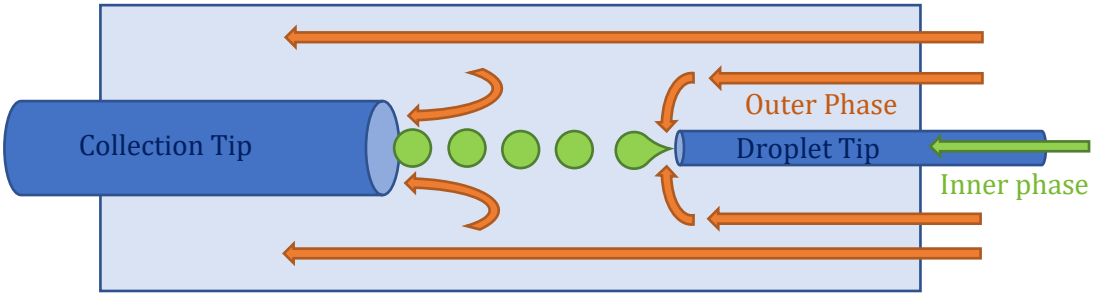

Figure 35: Cartoon diagram of microfluidic droplet preparation process using a coaxially aligned flow-focusing device. Redrawn from ref. 51.

In addition, Serra *et al* investigated the relationship between tip size and droplet size. They found that smaller droplet tips resulted in smaller droplets and that the ratio between the average droplet diameter (D_d) and droplet tip diameter (D_t), D_d/D_t, was related to the polydispersity of the sample. The smaller D_d/D_t, the more monodisperse the sample.[101,116] Furthermore, previously in the group, Taylor found that the smoothness of the droplet tip effected droplet dispersity and so implemented a sonication step in the making of droplet tips (discussed below) to ensure a smooth tip was produced.[51] It is thought that smooth droplet tips minimise turbulence in the hydrodynamic flow and *vice versa*.

Overall, droplet diameter and sample dispersity can be controlled by altering any of the parameters discussed in the previous paragraphs, which allows for smaller and less polydisperse droplets to be produced, compared to the alternative suspension method.[42,101,116]

With the aforementioned parameters in mind, a microfluidic chip design was previously developed in the group and utilised in this project to build microfluidic chips for microfluidic droplet production.[51] An example chip, and the tips within imaged under brightfield microscopy, as well as a cartoon representation of the chip design is shown in Figure 36. The full chip building procedure can be found in the experimental chapter (section 7.2). The droplet and collection tips were fabricated from round glass capillaries which were pulled on a glass pipette puller and placed in an ultrasonic bath to cleanly break and reduce the tip diameter to ~15 – 30 μm for droplet tips and ~180 – 240 μm for collection tips. The tips were cut to size and aligned in 3-dimensions within a square glass capillary, which had been glued to a glass microscope slide, to be ~45 – 140 μm apart. The glass

capillaries were then glued down so that they remained in place. Connectors made from cut-to-size syringe needles and glued over each capillary opening which were to be used as inlets and outlets. The inlet connectors were connected to syringes which were mounted upon syringe pumps to control the flow rates of the inner and outer fluid contained in syringes.

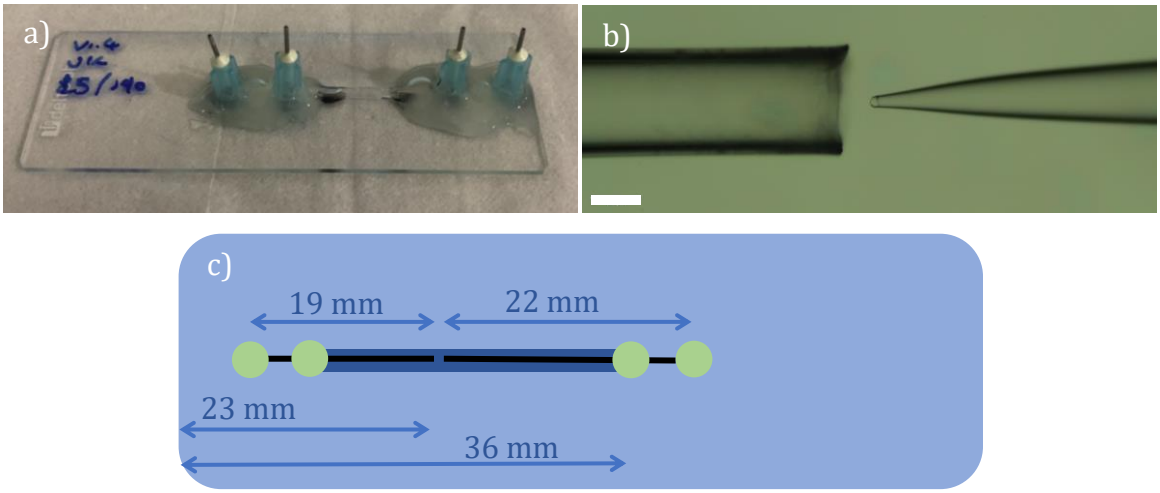

Figure 36: Photograph of microfluidic chip (a); brightfield photomicrograph in transmission mode of droplet and collection tips at 100x magnification, scale bar 100 µm (b). Cartoon representation of a microfluidic chip design showing connectors (green), droplet and collection tips (black), and outer fluid capillary (dark blue), all mounted upon a microscope slide (c). Cartoon redrawn from ref. 51.

As the nematic monomers investigated in this thesis (discussed in more detail in the next chapter) are solid at room temperature, in order to load them into a microfluidic device they would either require heating above their melting point or dissolution into solvent. Heating the microfluidic setup would involve submerging the whole chip in an oil bath, so that the inner phase remains fluid, introducing further complication to the setup. Furthermore, nematic droplets have been known to become aligned by the shearing force of the flowing outer phase,[117,118] outweighing surface anchoring conditions. For example escaped concentric or bipolar configurations have been accessed in elastomer particles and shells produced from nematic droplets due to flow alignment. Flow alignment occurs when the director alignment is defined by the shear forces between the nematic inner phase and the outer phase under flow. Where controllable and specific configurations, such as bipolar, are required, flow alignment is undesirable.[119,120]

In this thesis careful control over the alignment is required to produce high quality bipolar textures, so to avoid flow alignment and allow for room temperature droplet production, the inner phase was dissolved in chloroform.

In the general method, the 97.5 vol% chloroform solution of monomer, photoinitiator and crosslinker (collectively the inner phase), was flowed through the droplet tip (generally at 140 μL/hr) into the co-flowing high viscosity outer phase, 3 wt% PVA in water (generally at a flow rate of 15 mL/hr previously in the group), which is immiscible with the inner phase, producing an oil-in-water emulsion of isotropic droplets in the outer fluid. The PVA acts to stabilise the droplets and prevent coalescence. The droplets were then collected in a collection dish, through the collection tip.[42,52,111,114,120,121] Upon solvent evaporation, the chloroform leaves the droplets, by dissolution into the outer phase before evaporating, reducing their volume, and therefore diameter, by a controlled degree, yielding much smaller anisotropic droplets.[42,51,122] A full description of materials and experimental parameters can be found in the next chapter, section 2.3, and the experimental chapter (section 7.3).

The coefficient of variation (CV) was used to determine the dispersity of the samples of droplets produced, calculated using Equation 10 where σ is the standard deviation and μ is the average droplet diameter (or later in this thesis length, width or aspect ratio) measured as described in section 3.2. The lower the CV value, the less size dispersity across the sample. Monodispersity can generally be described as a sample with a 'good' CV value of <5%, values greater than this define a polydisperse sample. Typically a dispersity of less than 5% is achieved by microfluidics.[101] Having a low dispersity sample of droplets allows for the generation of hexagonally packed monolayers of droplets.[64,121]

$$\%CV = \frac{\sigma}{\mu} \times 100$$

Equation 10: To calculate coefficient of variation (CV).[114]

2.3.2 Method Optimisation

The basis for this microfluidic setup was previously developed in the group.[51] However, significant optimisation focused on variables such as tip position and alteration of flow rate to improve upon the previously achieved smallest droplet sizes, and quality of confinement textures. Previously in the group the main flow rate utilised for the outer fluid was 15 mL/hr, however to reduce droplet sizes, this was increased to 16 mL/hr. All microfluidic parameters can be found in the experimental chapter (section 7.3.1.2, Table 12).

To investigate the effect of altering the outer fluid flow rate on the diameters of droplets, this variable was isolated from all experiments, by comparing systems where only the outer fluid flow rate was changed. The tip diameters (20 and 200 μm for droplet and collection tips respectively), fluid compositions and inner flow rate (140 μL/hr) were common across all the experiments in this investigated. At an outer fluid flow rate of 15 mL/hr the average isotropic droplets diameter produced was 60 μm with a CV of 2.1%, whilst those produced using an outer fluid flow rate of 16 mL/hr were on average 58 μm in diameter with a CV of 1.5%. These results show that increasing the outer fluid flow rate by only 1 mL/hr not only improved the monodispersity of samples, but also reduced droplet diameters. Increasing the outer fluid flow rate alters the hydrodynamic flow of the system by increasing the outer fluid capillary number which in turn increases Ca_o/Ca_i, as discussed previously. Increasing this ratio describes an increase in the shearing force between the inner and outer fluids and hence the droplet is pinched off from the droplet tip sooner, and more reliably, at higher outer fluid flow rates. Therefore, the droplet diameter and variance are reduced. Increasing the outer fluid flow rate is preferable to decreasing tip sizes for producing smaller droplets, as smaller droplet tips tend to get blocked much easier. The degree of variation in droplet size is very small compared to the initially investigated setup which was previously employed in the group, Taylor reported a CV of 3.3% for 54 μm of droplets of the composition prepared with a 15 mL/hr outer flow rate. There are few reported CV values for droplets of similar composition (high chloroform content), however in the literature microfluidic methods yielded for example isotropic aqueous droplets in oil,[114] and nematic droplets in a PVA water outer fluid[42,121] which generally report CVs as '<3%'.[42,114,121]

The initial setup was based on a previously reported coaxially aligned device developed by Utada *et al*,[123] which was modified in previous work in the group by Taylor,[51] for optimisation of the tip sizes and fluid compositions. In order to further develop the chip design, another study within this thesis was to optimise the positioning of the droplet and collection tips with respect to each other, again with the aim of altering the hydrodynamic flow within the microfluidic chip to reduce droplet diameters. Whilst a distance between the droplet and collection tips of ~80 μm was previously employed in the group, the effect of altering this was not investigated. A selection of experiments were performed where tip sizes (20 and 200 μm for droplet and collection tips respectively), flow rates (140 μL/hr and 15 mL/hr for the inner and outer fluids respectively), as well as the fluid compositions were kept constant to isolate the tip distance variable. Droplets were made according to the general procedure above (and discussed in more detail in the experimental chapter). The distance between the droplet and collection tips measured using ImageJ software. The resulting isotropic droplet diameters were plotted against the distance between the droplet and collection tips, shown in Figure 37. There was a trend observed, increasing the distance between tips, increased the droplet diameter. The plot showed a coefficient of determination (R^2) of 0.82, showing good correlation between the tip distance and droplet diameters. This relationship can be attributed to the change in hydrodynamic flow of the system with altering tip distance. At smaller tip distances, the local flow rate of the outer fluid entering the collection tip increases as the overall outer fluid flow rate is maintained. Increasing the outer fluid flow rate, increases the capillary number which describes increased shear forces being exerted from the outer fluid, to the inner fluid about the tips, and hence the inner fluid stream is pinched off sooner, resulting in smaller droplet diameters.

This was an ongoing study of the relationship between tip distance and droplet diameter throughout this project. Hence, in order to produce small droplets of controllable size, the droplet-collection tip distance should become a focus in future microfluidic chip building, in combination with smaller tip sizes and faster outer fluid flow rates than previously utilised in the group.

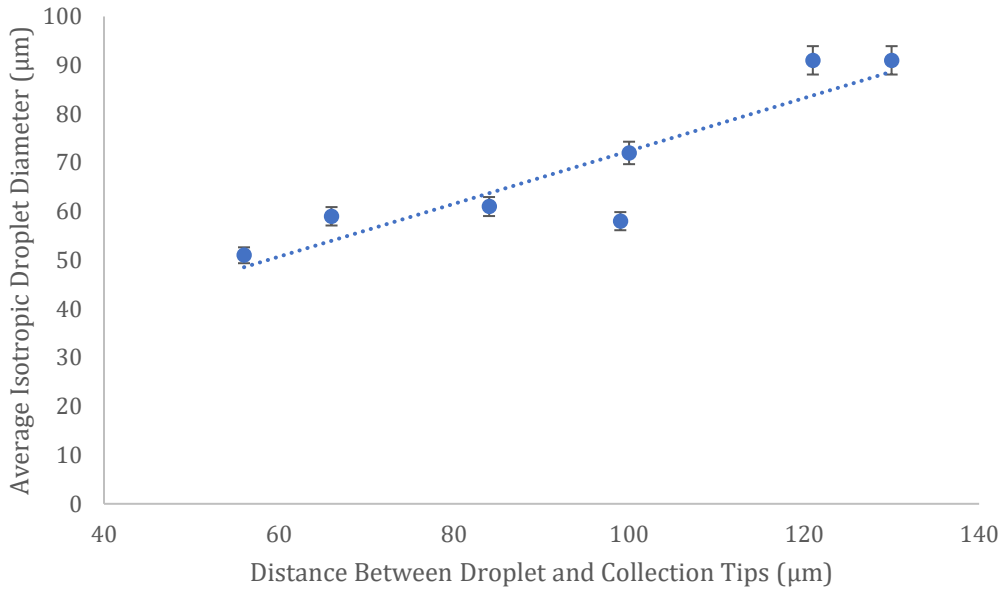

Figure 37: Graph showing the relationship between the droplet-collection tip distance and the resulting isotropic droplet diameters. Dashed line is a guide to the eye.

The two main optimisations performed here, of increasing the outer fluid flow rate and decreasing the distance between the droplet and collection tips, allowed for the production of smaller droplets than previously possible, with diameters as small as 18 µm post-solvent evaporation, whilst also displaying a significant improvement on CV compared to both the literature ('<3%')[42,114,121] and values reported previously in the group (average ~2.5%).[51] The lowest variance obtained here was 0.7%, and the overall average was 1.8% (excluding polydispersity caused by blockage or jetting).

2.4 Conclusion

Whilst several methods could be employed to produce liquid crystalline droplets for the production of elastomer microparticles to fulfil some of the main aims of this project, microfluidics was selected as the most appropriate due to the fine control over droplet diameter through a number of variables, as well as the low rates of polydispersity seen in microfluidics.

Two main parameters were investigated for changing the hydrodynamic flow within microfluidic chips with the aim of producing smaller droplets in lower size dispersity compared to those produced previously in the group and in the

literature. These parameters were the outer fluid flow rate and the distance between droplet and collection tips. It was seen that when the outer fluid flow rate was increased by only 1 mL/hr, not only was the droplet diameter reduced, but the CV was also improved showing more monodisperse samples could be produced. Finally, a study of the relationship between the microfluidic tip distances and resulting droplet size showed that reducing the distance between droplet and collection tips provided another facile route to reducing droplet diameters and hence should be implemented into future microfluidic chip building. Both of these optimisations, in combination with the method development previously performed in the group, has allowed for the production of smaller droplets with lower size dispersity that were previously accessible.[42,51,101,114,121]

3 Responsive Bipolar Systems

3.1 Overview

This chapter outlines the microfluidic production of nematic droplets and nematic elastomer microparticles of various geometries, with characterisation of the resulting sizes, size distributions and confinement textures. The nematic droplets and microparticles were investigated for their response to external stimuli such as temperature and magnetic fields.

Three liquid crystalline monomers were selected for investigation. The molecular structures of the chosen monomers for producing bipolar nematic droplets and elastomer particles are shown in Figure 38, and their thermal properties are listed in Table 1. The monomers differ by their terminal chain length or length of their spacer group. Monomer **M1** has been fairly widely researched by several groups, including ours, for preparation of actuating elastomer particles.[41,42,51,60,111,124–127] The thermal properties of the resulting elastomers, **E1**, **E2** and **E3** upon polymerisation of **M1**, **M2** and **M3** are also listed in Table 1. Elastomer microparticles of **M1**, **E1**, exhibit a large actuation, displaying a 36% change in aspect ratio, about its T_{NI} of ~116 °C. On the other hand, the elastomer of **M2**, **E2**, has been previously investigated within the group and was found to have a comparable degree of actuation to **E1**, displaying a 38% change in aspect ratio, but at a lower T_{NI} of ~76 °C, due to the longer terminal chains present in the monomer which introduce greater conformation freedom, compared to that which is present in systems with shorter terminal chains, resulting in decreased packing ability and thus a lower the phase transition.[3] A lower actuation temperature is beneficial for real world applications. The elastomer of **M3**, **E3**, also has a lower T_{NI} of ~86 °C. **M3**'s longer spacer group, compared to **M1** and **M2,** increases decoupling of the mesogens to the polymer backbone in its elastomer counterpart, **E3**, therefore the loss of alignment about its T_{NI} has a negligible shape change effect on the nematic elastomer microparticles upon clearing into the isotropic phase.[51]

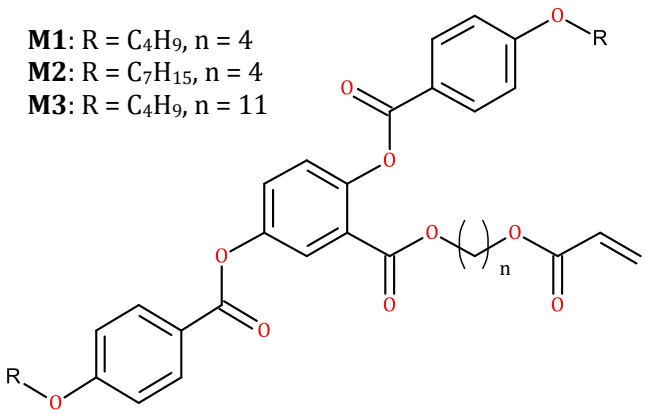

Figure 38: Molecular structure of nematic liquid crystal monomers **M1, M2** and **M3**.

Table 1: Thermal properties of nematic monomers **M1**, **M2** and **M3** as well as their elastomer counterparts **E1**, **E3** and **E3**. Data obtained previously in the group by DSC at a 10 °C/min heat/cool rate. Phase transition temperature taken from peak onset on heating; glass transition temperature taken from the midpoint on cooling.[51]

Monomer	T_m	T_{NI}	Elastomer	T_g	T_{NI}
M1	72.9	85.4	**E1**	42.8	116.1
M2	54.6	70.8	**E2**	17.3	76.0
M3	53.2	69.5	**E3**	15.6	86.3

3.2 Bipolar Nematic Droplets

To investigate confinement of the systems mentioned above, droplets of **M1**, **M2** and **M3** have been prepared using the microfluidic method. The droplets produced were collected in 40 mm petri dishes and contained the mesogenic monomer, crosslinker 1,6-hexanediol diacrylate (10 mol% w.r.t monomer) and photoinitiator diphenyl(2,4,6-trimethylbenzoyl) phosphine oxide (2 mol% w.r.t monomer), all dissolved in chloroform (97.5 vol% w.r.t monomer), with an outer fluid of PVA in water (3 wt%). Full details of the microfluidic parameters used to produce droplets in each experiment can be found in the experimental chapter (section 7.3.1, Table 12), alongside mean droplet diameters and observations under POM. For measuring droplet diameters, they were imaged by brightfield microscopy in transmission mode, where the sample is illuminated by white light from below the sample and observed from above. Measurements of droplet diameters for calculating average droplet diameters, generally from 20 droplets per photomicrograph but sometimes up to 100, were then taken using ImageJ

software. The CV was calculated as described in the previous chapter (section 2.3.1).

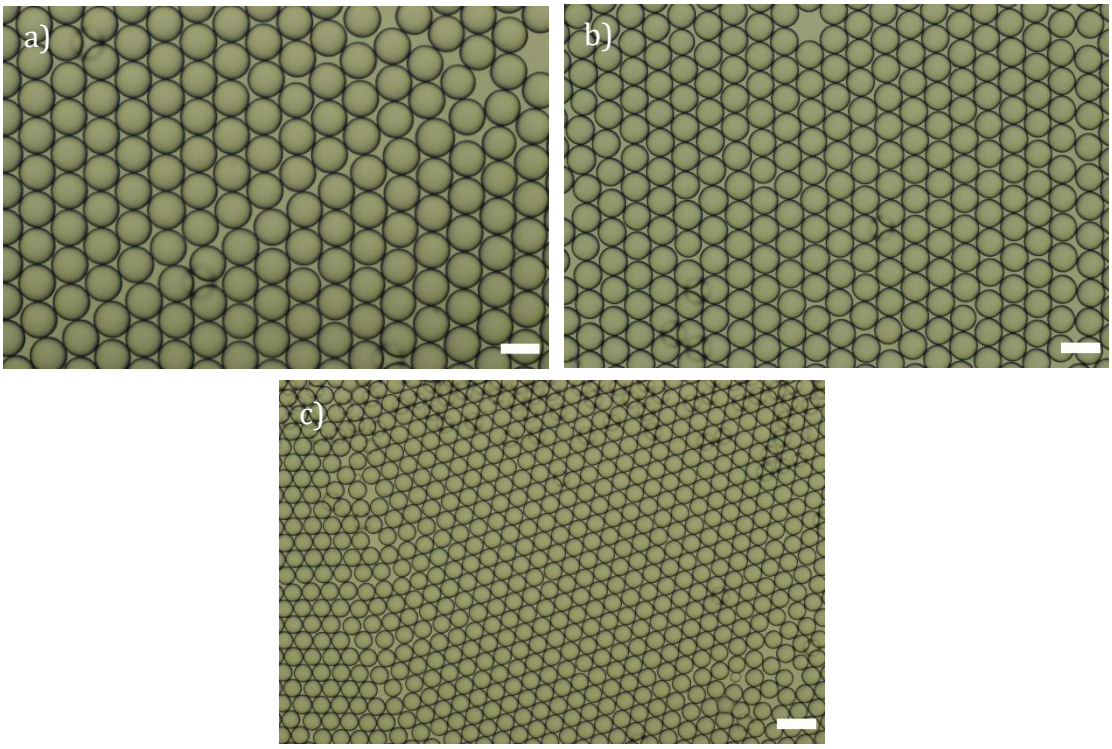

Figure 39: Brightfield photomicrographs, taken in transmission mode, of isotropic droplets of the **M1** chloroform solution from **M1-MF2** (a), **M2** chloroform solution from **M2-MF80** (b) and **M3** chloroform droplets from **M3-MF87** (c). Taken at 100x magnification, scale bars 100 μm. Average diameters: 91 μm (a), 72 μm (b) and 47 μm (c).

Figure 39 shows isotropic chloroform-containing droplets of **M1**, **M2** and **M3** collected in glass petri dishes with the PVA in water outer fluid taken from example experiments. The volume of droplets collected was small enough that they did not cover the whole area of the bottom of the dish, and hence generally remained in a layer one droplet thick, although some layering did occur close to the chip outlet. It can be seen in the imaging that hexagonal close-packed monolayers self-arranged in the collection dishes as a result of the narrow size distributions due to droplet production *via* the microfluidic method. The resulting droplets were in the isotropic phase due to their high chloroform content. Measurements showed that the droplets produced had a narrow size distribution, for example Figure 40a shows a droplet size distribution graph from experiment **M1-MF2** in which isotropic droplet diameters only differed by ±5 μm (CV = 3.8%) from the average diameter of 92 μm. As previously discussed (section 2.3.2), the droplet size could

be minimised by increasing the outer fluid flow rate or reducing the distance between droplet and collection tips. However, there was variation seen between experiments, due to these parameters being investigated, as well as different tip sizes being utilised. Overall, the isotropic droplets containing chloroform had mean diameters of between 41 and 117 µm depending on the individual experiment with average CV values of 1.8%, where there was no chip blocking or jetting, and as low as 0.7% in experiments **M1-MF41**.

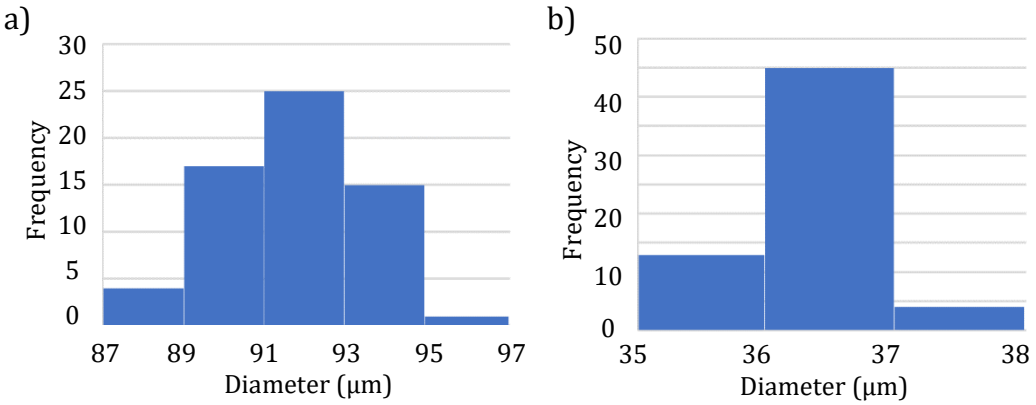

Figure 40: Droplet size distribution of droplets containing **M1**, from experiment **M1-MF2**, before (a) and after (b) solvent evaporation.

The chloroform containing droplets were allowed to evaporate overnight in a solvent evaporation step, whilst remaining within the PVA in water outer fluid, to yield droplets of monomer, photoinitiator and crosslinker which had reduced in diameter by on average 41% to between 18 and 45 µm depending on the individual experiment. The average CV for nematic droplets remained approximately the same as isotropic droplets before solvent evaporation; in nematic droplets being on average 1.8%, (where there was no chip blocking or jetting), and as low as 0.8% in experiments **M1-MF72** and **M2-MF88**. However, in some experiments, such as the example from **M1-MF2** in Figure 40b an improved, narrower size distribution was found after solvent evaporation as a diameter variance of only ±1 µm (CV = 1.4%) was observed compared to ±5 µm (CV = 3.8%) in isotropic droplets.

During solvent evaporation droplets were imaged under POM in transmission mode, where transmitted light is passed through the sample which is located

between two 90° crossed polarisers (vertical and horizontal with respect to the observer), to characterise the nematic texture. Photomicrographs taken under POM in this thesis will be known as 'polarised photomicrographs'.

Monitoring the solvent evaporation closely allowed for the texture development of the droplets to be observed. Figure 41 shows screenshots from a video taken through crossed polarisers of **M1** droplets from experiment **M1-MF67** in the final minutes of solvent evaporation. The screenshots were taken 30 seconds apart and show how the nematic texture arose. Initially the texture appeared in many domains to give a polydomain texture seen in screenshots (a – g). After approximately two minutes the polydomain texture became one domain, the baseball texture, shown in screenshots (h – p). To the best of our knowledge, in the literature there is no discussion of texture development in nematic droplets upon solvent evaporation. However, in 50 – 300 μm 5CB droplets, Chen *et al* experimentally described the development of a nematic texture on cooling from the isotropic phase as occurring over several 'regimes' (following modelling by Bradac *et al*). They describe that, as the texture begins to develop, it gives rise to the so called 'domain regime', characterised as a polydomain structure. In the domain regime, many small domains arise as the order parameter in the system increases exponentially. As the rate of increase in the order parameter increases over time, the smaller domains are dominated by the growth of larger domains. Following this, the so called 'confinement regime' takes place as elasticity and surface anchoring dominate the confined system. Finally, the so called 'late stage regime' occurs where individual defects dominate the system.[128,129]

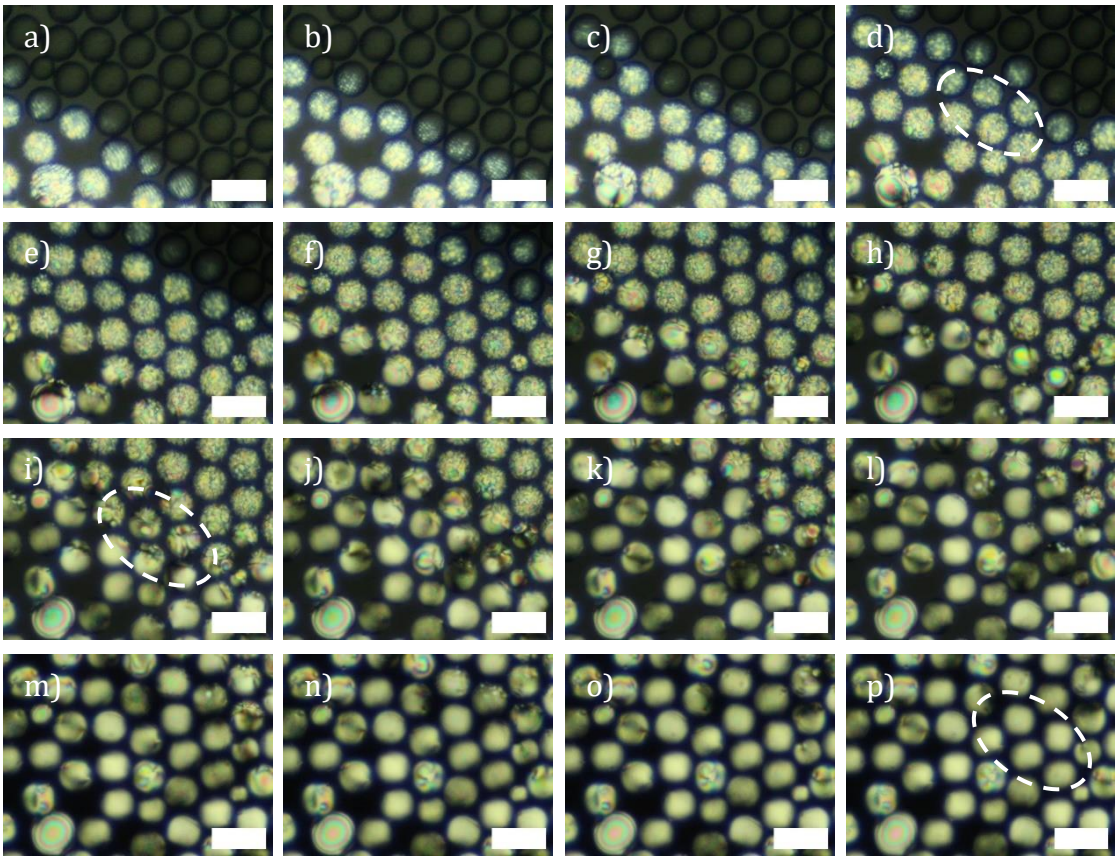

Figure 41: Screenshots from a video taken through crossed polarisers in transmission mode of droplets of **M1** from experiment **M1-MF67** during solvent evaporation after ~4 hours. Screenshots taken 30 seconds apart showing nematic texture development. Taken at 500x magnification, scale bars 50 μm. Average diameters: 33 μm.

Although the analysis by Chen *et al* is based upon cooling from the isotropic to nematic phases, rather than solvent evaporation, similarities to the development of the nematic texture can be drawn with the textures seen in Figure 41. The initial polydomain texture seen, for example in the highlighted droplets in (d), show the small domains of the domain regime which occur as the order parameter slowly increases at a critical chloroform concentration. As the chloroform concentration decreases further, the order parameter increases at a greater rate and the elastic and surface anchoring energies dominate the system in the confinement regime, promoting the growth of larger domains, for example in the highlighted droplets in (i). Finally, in the late stage regime the topological defects define the confinement, as the homogeneous surface anchoring, promoted by the PVA in water outer fluid, dominates the director configuration, resulting in a defined confinement texture, for example in the highlighted droplets in (p).

The nematic texture which developed here will be investigated in the discussion which follows, however, for **M1** and **M2**, this was not the final texture which developed. Figure 42a & b shows photomicrographs of droplets of **M1** from experiment **M1-MF12** after solvent evaporation. A defined nematic texture cannot be seen, instead an undefined and grainy texture was observed. Further to this, brightfield imaging showed the droplets shape had deformed slightly from spherical. The same undefined and grainy texture could be seen for droplets of **M2** (Figure 42c & d; experiment **M2-MF20**) after solvent evaporation, although some displayed a Maltese cross texture perhaps due to crystallisation symmetry. **M2** droplets had much greater geometry deformation away from spherical to give jagged, irregular shapes. It was concluded from these observations that the droplets had crystallised. The solvent evaporation step is carried out at room temperature and **M1** and **M2** have melting points of 76 °C and 55 °C respectively,[51] and so crystallisation occurred, despite the addition of photoinitiator and crosslinker introducing impurity. Monomer **M3** on the other hand has a melting point of 37 °C,[51] however crystallisation of droplets did not occur due to the introduction of impurity in the form of the photoinitiator and crosslinker which decreased the melting point to below room temperature.

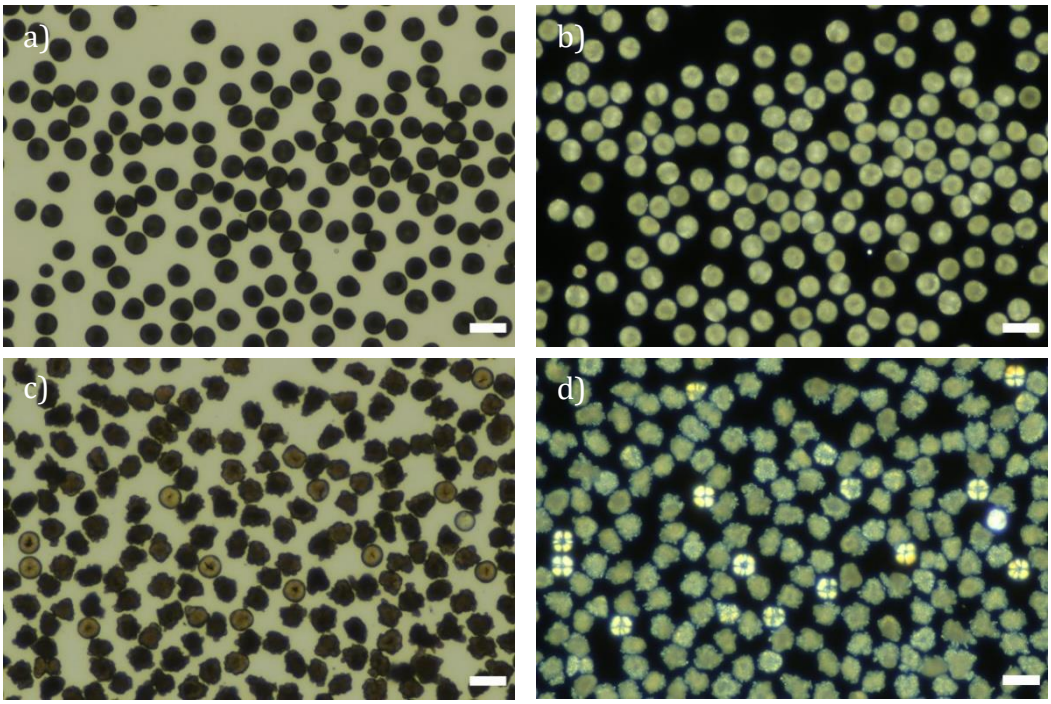

Figure 42: Brightfield (a & c) and polarised (b & d) photomicrographs of crystallised **M1** droplets from **M1-MF12** (a & b) and crystallised droplets of **M2** from **M2-MF20** (c & d). Taken in transmission mode at 200x magnification, scale bars 50 µm.

Time lapse imaging overnight using photos taken every 10 minutes was performed of droplets in 40 mm collection petri dishes (used as part of the general procedure) containing outer fluid, to reveal when crystallisation occurred during solvent evaporation when using the general microfluidic method as described previously. As the droplets reduced in size the texture became out of focus, so imaging is fairly poor. Despite this, it could be seen that, that the nematic texture did develop after ~12 hours and was sustained for ~1 – 3 hours before crystallisation occurred. Example photomicrographs from a time lapse of **M1** droplets during solvent evaporation are shown in Figure 43, in (a) no birefringence was present at 11 hours, however, after 12 hours, shown in (b), the imaging shows birefringent droplets, with a nematic texture. Next, the photomicrograph in (c) shows that approximately half of the droplets had crystallised after an additional hour. Finally (d) shows that ~ 3 hours after the texture developed, the majority of droplets had crystallised.

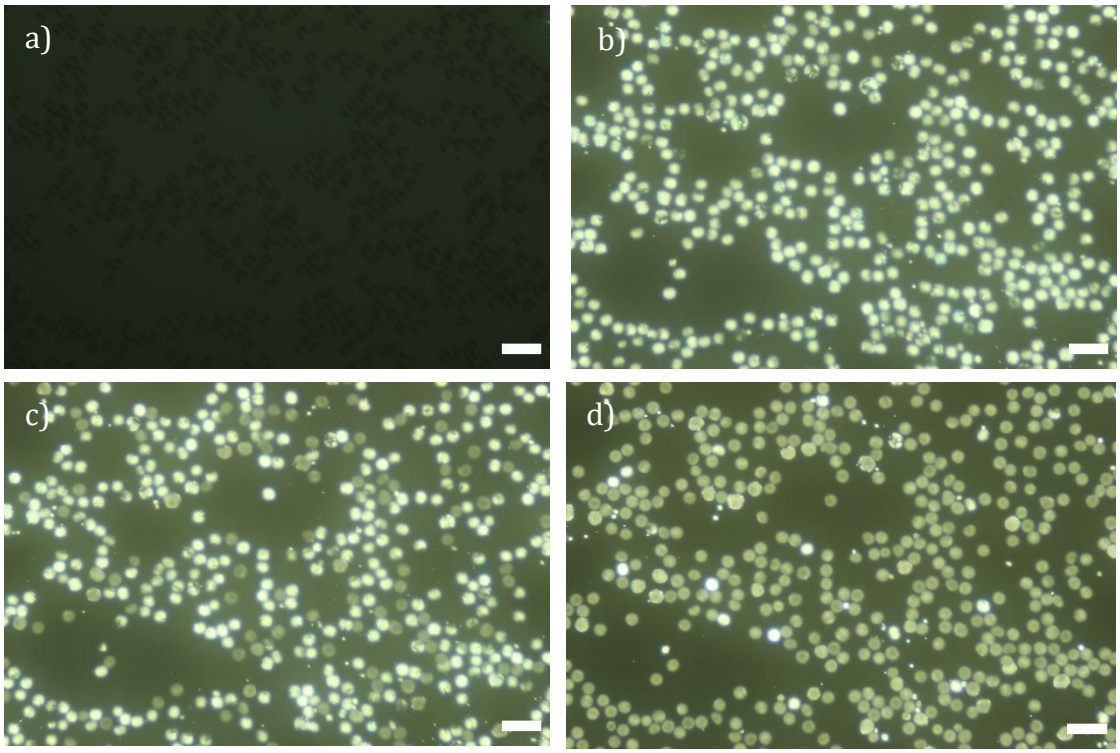

Figure 43: Polarised photomicrographs of **M1** droplets from **M1-MF58** after 11 (a), 12 (b), 13 (c) and 15 (d) hours of solvent evaporation. Taken at 200x magnification, scale bars 50 µm. Average diameters: 25 µm.

A shorter solvent evaporation length was investigated to control the length of solvent evaporation and optimise the texture development stage of droplet production. A smaller volume of droplets was collected in 40 mm collection dishes and diluted 2.5 – 4x with outer fluid, compared to the initial method where droplets were produced in a ratio to the outer fluid governed by the flow rate (i.e. in the general method at inner and outer fluid flow rates of 140 μL/hr and 16 mL/hr respectively, the ratio of total volume of droplets to outer fluid volume in a given dish was 140 : 16000). For example, in experiment **M1-MF67** 1.0, 1.5 or 2.0 mL was collected from the microfluidic experiment in a 40 mm dish and 3.0 mL additional outer fluid was added, reducing the total volume of droplets to outer fluid volume ratios to 140 : 64000, 140 : 48000 and 140 : 40000 respectively (or, for simplicity, 4x, 3x and 2.5x dilution from the general method). This dilution, resulted in shorter solvent evaporation, and nematic textures developed over ~3 – 5 hours, instead of ~10 – 12 hours. The evaporation of chloroform from droplets occurs due to the slight solubility of chloroform in water. Therefore, chloroform migrates from the droplets into the water solution, before evaporating into the air.[42] Hence, diluting the collection dishes with outer fluid, reduces the concentration of chloroform in the outer fluid, increasing the rate of solvent evaporation from the droplets.

Shortening solvent evaporation allowed for the nematic texture of **M1** and **M2** droplets to be studied in an accessible timescale to enable time dependant imaging before crystallisation, hence collection dish dilution was implemented when using these monomers. As **M3** droplets did not crystallise upon solvent evaporation, dilution of the outer fluid was not required, and solvent evaporation was allowed to occur overnight.

The late stage regime of solvent evaporation gave rise to an aligned confinement texture within the droplets, promoted by the parallel surface anchoring imparted by the PVA in water solution. As discussed in the introduction chapter, parallel surface anchoring in micrometre sized droplets may give rise to a bipolar texture. In order to elucidate the nematic texture of the droplets, they were imaged under POM and the texture analysed.

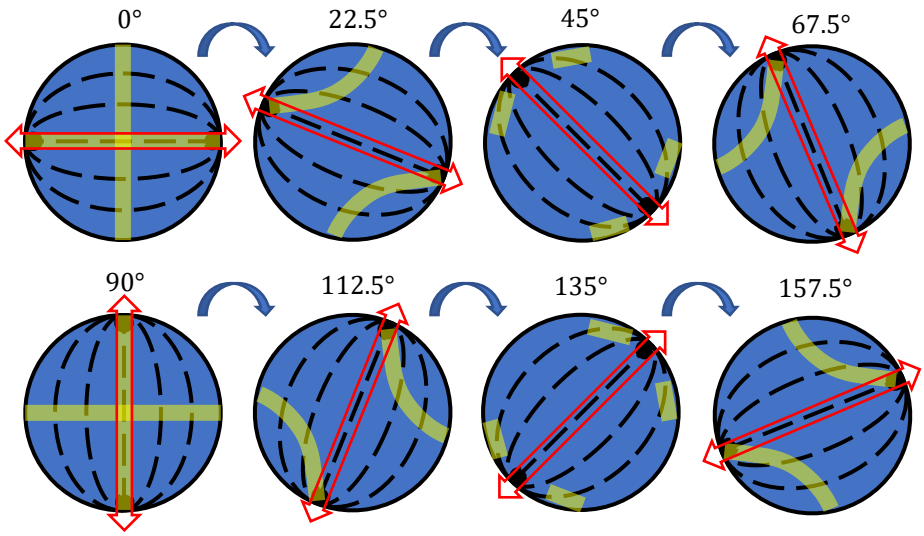

Figure 44: Cartoon representation showing the bipolar texture evolution through rotation of a bipolar droplet. Where the polarisers are crossed vertically and horizontally with respect to the droplet, highlighted yellow areas show where mesogens line up with the polarisers, resulting in black isogyres under POM. Red arrows show the overall director and bipolar axis or droplets. Redrawn from ref. 130.

Figure 44 shows a cartoon representation of the texture evolution of bipolar droplets under POM upon rotation, redrawn from Haseloh *et al.*[130] Imaging under POM allows for, not only the identification of the confinement texture, but also the location of the polar defects due to the pattern of the shifting isogyres. The areas in the cartoon highlighted in yellow show where mesogens in a bipolar configuration line up with crossed polarisers (where they lie vertical and horizontal with respect to the image). Where the mesogens align with the polarisers, light is extinguished and so under POM the pattern represented by the yellow highlighted areas is observed as black isogyres. The shape and location of these isogyres upon shifting through rotation, allow for the defect location, and therefore overall director orientation, to be found.

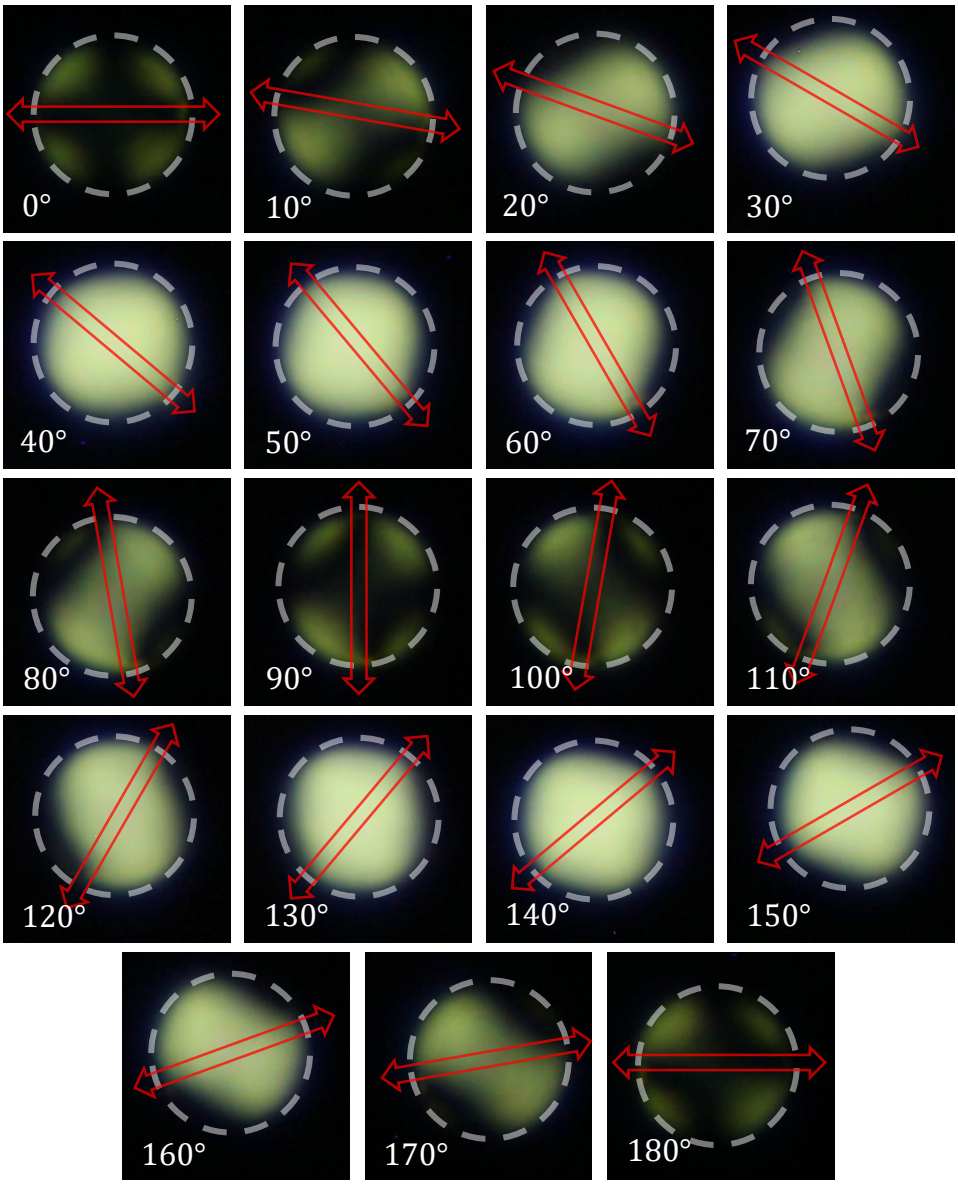

Figure 45: Polarised photomicrograph of an **M3** nematic droplet from **M3-MF49** showing the texture evolution as the droplets were rotated through 180° between the crossed polarisers, which were vertical and horizontal with respect to the plane of observation. Taken in transmission mode at 200x magnification, cropped and zoomed by 2.5x. Red arrows represent the polar axis. Droplet diameter: 32 μm.

Figure 45 shows a nematic droplet of **M3**, post-solvent evaporation. It can be seen that there was a clear baseball texture present under POM imaging which can be seen through rotation of the droplet, giving evidence for the presence of a bipolar texture, as expected due to the parallel surface anchoring. Furthermore, the polar axis could be determined for the location of the bipolar defects within the droplet, using the shifting isogyres as represented in Figure 44. In the first image of Figure 45 a cross-like texture is observed through the crossed polarisers, indicating that the polar axis could be vertical or horizontal with respect to the plane of

observation. It is not until the droplet was rotated that a horizontal or vertical orientation could be determined. Upon rotation by 10° clockwise, the isogyres shifted so that one was present in the top left and one in the bottom right, which is characteristic of a clockwise rotation from a horizontal orientation, as per Figure 44. Hence, the polar axes and overall director could be defined as horizontal in the first image, which then rotated with the droplet by 10° per photomicrograph. Throughout the full 180° rotation the texture remained clear and symmetrical as expected, showing a defined bipolar configuration.

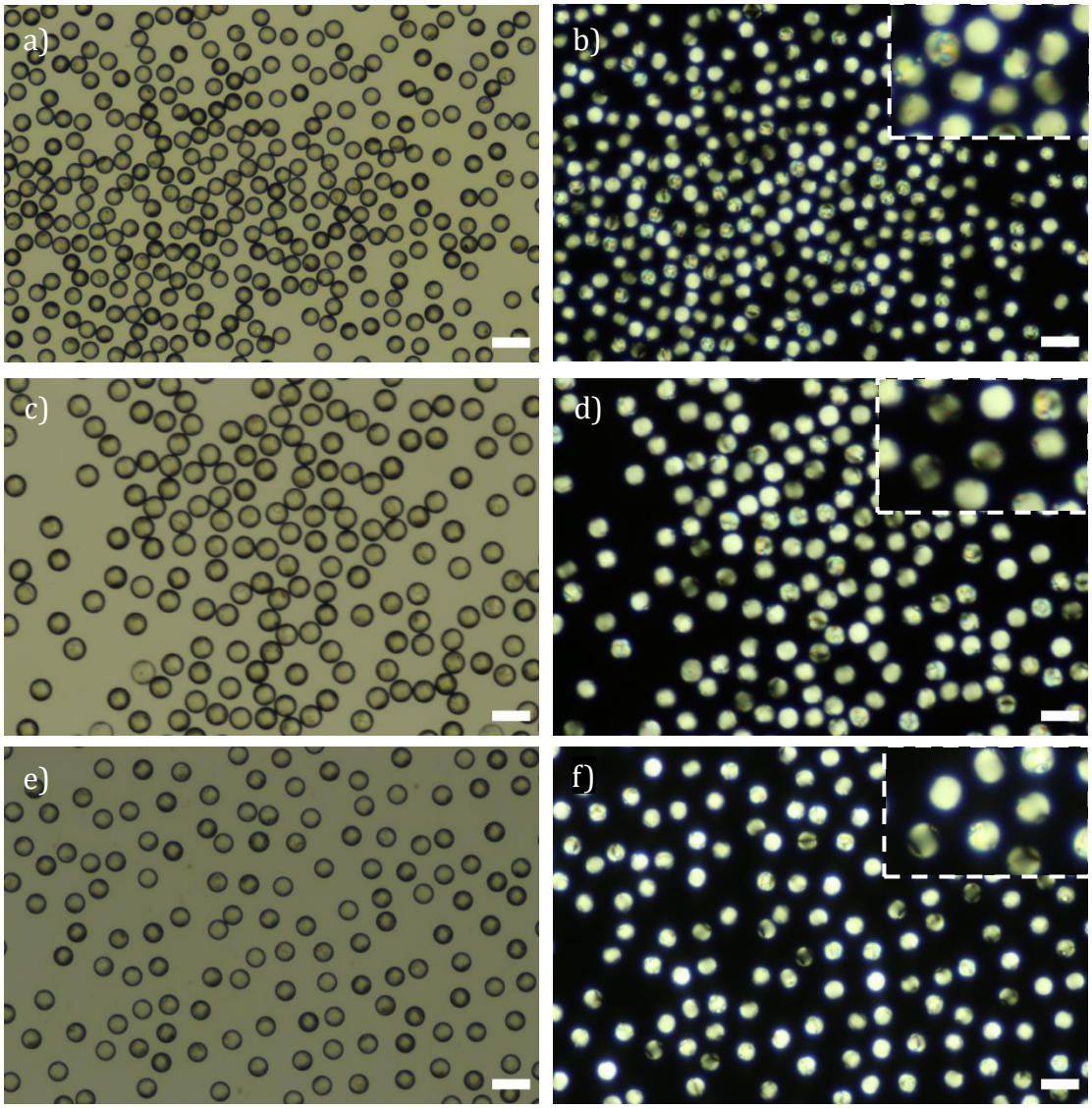

Figure 46: Brightfield (a, c & e) and polarised (b, d & f) photomicrographs of bipolar nematic droplets of **M1** from **M1-MF97** (a & b), **M2** from **M2-MF80** (c & d) and **M3** from **M3-MF19** (e & f) with average diameters of 23, 26 and 29 µm respectively. Taken at 200x magnification in transmission mode, scale bars 50 µm. Polarised photomicrographs show a 2x zoomed area in the top right corner. Average diameters: 23 µm (a), 29 µm (c) and 26 µm (e).

Figure 46 shows examples of photomicrographs of droplets of **M1**, **M2** and **M3** under POM after solvent evaporation, and Figure 47 shows example droplets from the photomicrographs above, zoomed in by 6x to look more closely at the baseball texture of the bipolar configuration, showing polar axes in cartoon representations. Figure 47 shows a selection of droplets with defined bipolar textures, conducive of high quality internal alignment of mesogens within the droplets, which is also reflected in the majority of other droplets from these samples, seen by the baseball textures present in Figure 46. However, not all droplets displayed such a defined texture. Slight disruption to the baseball texture can be seen in several droplets from each of these examples, particularly for **M1** and **M2** droplets. This deviation from a perfect bipolar texture suggests a small degree of disruption to the internal alignment within some droplets, despite maintaining parallel alignment. The same observations were found for droplets across the whole size range produced within this thesis, as well as for **M1**, **M2** and **M3** droplets previously produced in the group within a similar size range as those in Figure 46. There are several possible explanations for this phenomenon. In a large population of droplets it is not uncommon to find some droplets with non-equilibrium textures due to mesogen orientation becoming 'trapped' in configurations at local energy minima during texture alignment, rather than the overall energy minimum of the bipolar configuration. Similarly, non-ideal configurations can exist where the defects simply become displaced so that they are no longer exactly on opposite sides of droplets. Furthermore, there could be other factors at play, such as droplet interaction with the bottom surface of the petri dishes used or even disruption caused by the presence of trapped nanometre-sized dust particles within droplets.

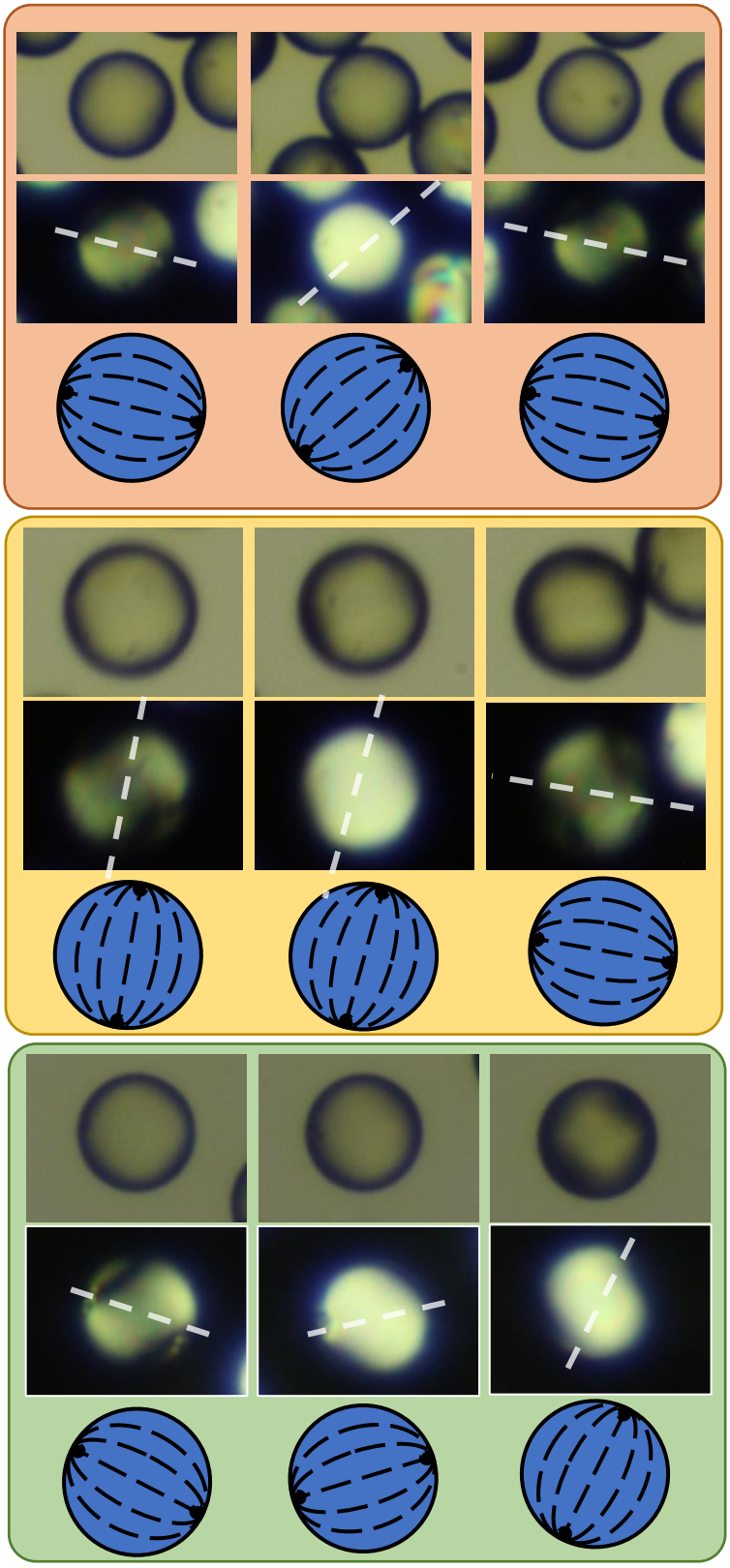

Figure 47: Orange, yellow and green boxes containing 6x zoomed and cropped photomicrographs of individual droplets of **M1** from **M1-MF97**, **M2** from **M2-MF80** and **M3** from **M3-MF19** respectively. The top row of each box shows the brightfield imaging, the middle is polarised imaging and the bottom a cartoon representation of the suggested polar axis orientation based upon the baseball texture pattern. Original photomicrographs correspond to those in Figure 46. Average diameters: 23 µm (orange box), 29 µm (yellow box) and 26 µm (green box).

The presence of monodomains and isogyres which are consistent with a bipolar configuration in the droplets shows that they were produced in a size range that was large enough that the bulk elastic energy of the system did not dominate surface anchoring conditions to produce monodomain droplets. This allowed for the PVA in water outer fluid to promote parallel surface anchoring within droplets. Furthermore, droplets were small enough that the elastic forces were sufficiently relatively strong from the surface anchoring direction to influence the elastic distortion in the droplet, resulting in a monodomain. The bipolar configuration here shows that the splay to bend elastic energy ratio (K_{33}/K_{11}) in the system must be balanced in a relatively high value, such that a bipolar configuration is favoured over others, such as a concentric configuration which requires the inverse ratio (K_{33}/K_{11}) to be >0.7.[45–47] As discussed previously, the droplets produced had small micrometre sized average diameters of as small as 18 μm, with an overall average CV of 1.8. Compared to other literature examples with larger droplet sizes the dispersity of the droplets produced reliably in this thesis showed monodispersity values in line with, and improved on, reported values. For example Fernández-Nieves *et al* produced anisotropic 30 μm droplets, and Cramer *et al* produced non-liquid crystalline droplets, *via* a microfluidic method, of 60 μm and in both examples the dispersity was reported as '<3%' as discussed in section 2.3.[42,114,121] The smaller sizes reported in this thesis are significant to the quality of the internal alignment of droplets, due to the size dependence of the elastic constants and therefore lowest energy configuration.

3.3 Bipolar Nematic Elastomer Microparticles

Photopolymerisation of nematic droplets of **M1**, **M2** and **M3** was performed for investigation of their response to altering polymerisation conditions, and the resulting particles' response to external stimuli such as temperature and magnetic fields (discussed in a later subsection).

Bipolar nematic droplets of **M1**, **M2** and **M3** containing crosslinker and photoinitiator were produced by microfluidics as described in the previous section. The collection dishes containing droplets were irradiated using a 365 nm UV LED light source for 10 – 60 minutes at various temperatures (from room

temperature to 107 °C) and various intensities to investigate the effect of polymerisation conditions. Polymerisation conditions for each experiment are detailed in section 7.3.3 of the experimental chapter. The resulting **E1**, **E2** and **E3** microparticles were investigated by POM; **E1** microparticles were also imaged under scanning electron microscopy, which was not possible for **E2** and **E3** microparticles.

The particles were washed either at elevated temperature (80 °C) or room temperature by removing ~2 mL of the ~4 mL outer fluid and replacing it with ~2 mL MilliQ water. Details of the procedure can be found in the experimental chapter (section 7.3.3). Once the particles were in pure water and all the PVA removed, this was successively replaced with 25, 50, 75 % polyethylene glycol 200 (PEG 200) in water before replacing with 100% PEG 200 several times. Having PEG 200 as the outer fluid allowed for imaging of the particles at elevated temperatures where water would begin to boil and fog up the microscope objective.

To prepare samples for SEM, the nematic microparticles of **E1** were washed at room temperature by removing 2 mL of ~4 mL of outer fluid and replacing it with 2 mL MilliQ water, the dish was then left for 30 minutes to allow for the PVA to dissolve in the water before repeating the washing 20 times to ensure all the PVA was removed. The water was then removed using a syringe and the dish dried in a vacuum oven at 35 °C for 3 days. Samples were mounted on aluminium stubs with carbon discs and sputter coated with a gold coating for imaging. Unfortunately, due to their lower glass transition temperatures of 17.3 and 15.6 °C respectively, the washing and drying of **E2** and **E3** particles did not result in samples of high enough quality for imaging by SEM. Holes in particles seen in SEM are explained by small volumes of residual chloroform evaporating from elastomer particles in the vacuum oven. Circular discs present on particle surfaces where particles were stuck to the bottom of petri dishes in the oven.

The aspect ratios of the resulting elastomer particles were calculated using Equation 11, and are reported in the experimental chapter (section 7.3.3, Table 15), alongside polymerisation parameters, particle dimensions and POM observations. It is worth noting that there is a degree of error to the calculated

aspect ratios arising from the measurements of true aspect ratios of the non-spherical microparticles relying on particles being positioned with their long axis in the same plane as the imaging stage. This horizontal orientation of non-spherical particles could not be verified for any particles whilst manual measurement was performed, and hence the particles' major axes could have been underestimated.

$$Aspect\ Ratio = \frac{length\ of\ particle's\ major\ axis}{length\ of\ particle's\ minor\ axis}$$

Equation 11: To calculate the aspect ratio of particles.

3.3.1 Spherical Nematic Elastomer Microparticles

3.3.1.1 Polymerisation in the Isotropic Phase

Droplets of **M1**, **M2** and **M3** containing photoinitiator and crosslinker were polymerised according to the general procedure in the previous section, however this was performed above their respective pure T_{NI} values of ~85, ~70 and ~69 °C (the addition of photoinitiator and crosslinker will have slightly depressed the phase transition temperatures). Thus, **M1** droplets were polymerised at 107 °C 40 cm away from a 50% intensity light source, whilst both **M2** and **M3** droplets were polymerised at 70 °C 30 cm away from a 50% intensity light source.

Figure 48 shows the resulting elastomer particles **E1**, **E2** and **E3** after polymerisation in the isotropic phase, upon cooling into the nematic phase to room temperature. It was observed in the polarised imaging that the nematic elastomer microparticles had a polydomain texture, due to a lack of imposed confinement texture alignment in the isotropic phase. As the droplets were polymerised in the isotropic phase, the elastomer network formed with no anisotropy. Upon cooling into the nematic phase, the mesogens could not reorient to align into the previous bipolar configuration due to the reduced degrees of freedom whilst bound to the elastomer network which templated a more random regime of orientation of the mesogens.

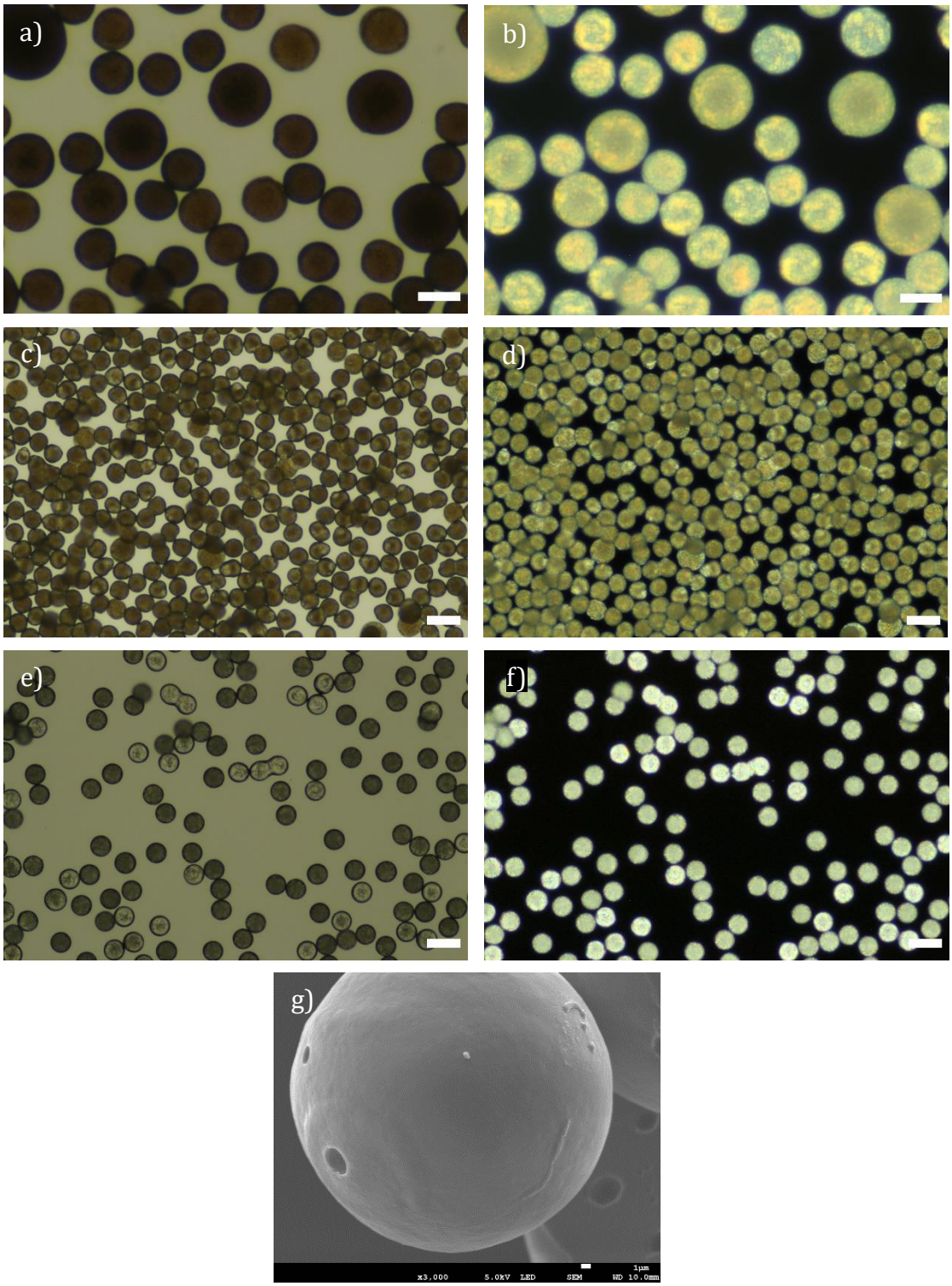

Figure 48: Brightfield (a, c & e), polarised (b, f & f) and SEM (g) photomicrographs of **E1** (a, b & g), **E2** (c & d) and **E3** (e & f) elastomer microparticles polymerised in the isotropic phase, at 107 °C (a, b & g), 70 °C (c – f). Taken from **E1-MF63** (a, b & g), **E2-MF78** (c & d) and **E3-MF49** (e & f). Taken at 200x magnification, scale bar 50 µm (c – f); 500x magnification, scale bars 25 µm (a & b); 3000x magnification, scale bar 1 µm (g).

It can also be seen in Figure 48 that the resulting elastomer microparticles remained spherical, particularly in the SEM image of an **E1** microparticle. The lack

of alignment meant that the elastomer microparticles remained within a spherical geometry throughout polymerisation.

In heat/cool cycles particles of **E1** and **E2** shown in Figure 49 showed a negligible change in dimensions upon clearing, into the isotropic phase and cooling back to the nematic phase. The **E1** microparticles (a – c) at 26 x 26 µm throughout the experiment and the particle in (d – f) changed minimally from 30 x 28 µm to 28 x 28 µm and back when heated into isotropy and cooled back into the nematic phase. As the elastomer backbone was polymerised in the isotropic phase, a random coil configuration was adopted by the elastomer matrix, rather than the stretched out structure of a monodomain nematic required for actuation, as discussed in the introduction (section 1.3.3).

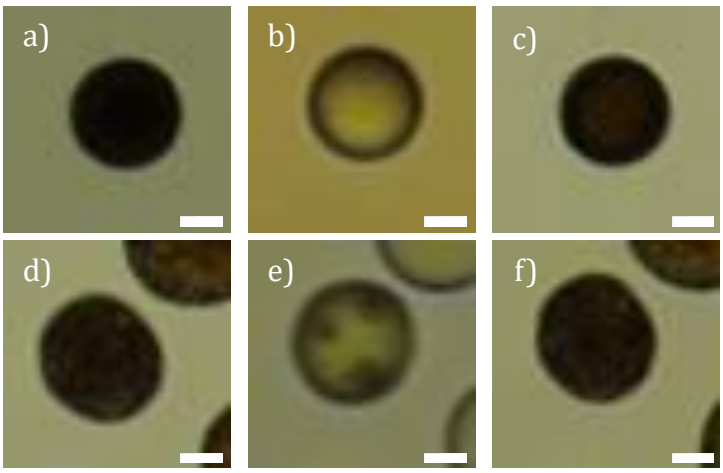

Figure 49: Brightfield photomicrographs, in transmission mode, of **E1** and **E2** elastomer microparticles which were polymerised in the isotropic phase, from **E1-MF66** (a – c) and **E2-MF78** (d – f) when heated from the nematic phase, 25 °C (a & d), to the isotropic phase at 140 °C (b) or 100 °C (e) and then cooled back to the nematic phase, 25 °C (c) or 30 °C (f). Originally taken at 200x magnification, cropped and zoomed in by 5.5x. Scale bars 10 µm.

3.3.1.2 Polymerisation in the Nematic Phase

Figure 50 shows elastomer microparticles of **E3**, which were produced from **M3**, crosslinker and photoinitiator containing droplets, photopolymerised in the nematic phase, at 45 °C, either at 50% intensity 30 cm away (a & b) or 100% intensity 6 cm away from the UV light source. The polarised imaging shows that whilst bipolar alignment was retained, the was some deviation away from the more defined textures found in the **M3** droplets pre-polymerisation. A loss in texture uniformity in particles, compared to droplets, is common

post-polymerisation. Although clear baseball textures can no longer be seen in all cases, possibly due slight alignment disruption due to small shrinkage upon polymerisation, isogyres which shifted through rotation were observed under POM, an example is shown in Figure 50e alongside representations of a suggested microparticle orientation based upon the shifting isogyres.

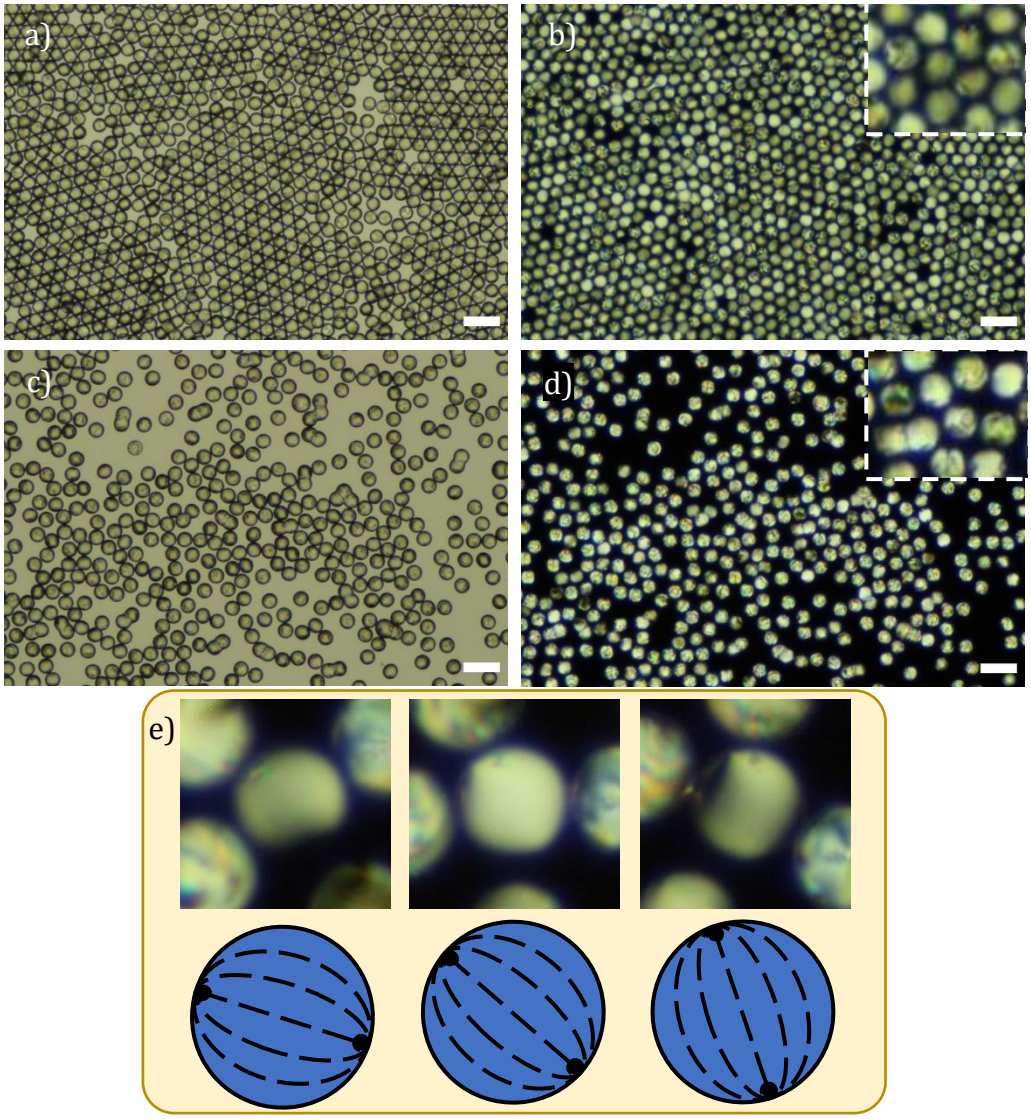

Figure 50: Brightfield (a & c) and polarised (b & d) photomicrographs of **E3** nematic elastomer microparticles polymerised at RT at 50% intensity from 30 cm away in **E3-MF87** (a & b) and 100% intensity from 6 cm away in **E3-MF73** (c & d). Zoomed in areas zoomed by 2.9x. Taken at 200x magnification, scale bars 50 µm. (e) shows an elastomer microparticle cropped and zoomed in 5x which is rotated by 30° and 60° left to right; cartoon representations of the suggested microparticle orientation are shown underneath.

In addition, **E3** elastomer particles showed negligible deformation away from a spherical shape under lower intensity polymerisation conditions of 50% at 30 cm away from the UV source as well as at higher intensity of 100% from 6 cm away. This can be seen in Figure 50 where the particles observed were mostly spherical, with an average aspect ratio of 1.03 – 1.04, aside from those which had fused together. In addition, **E3** elastomer microparticles do not actuate as a response to temperature change about their T_{NI}, as reported previously in the group,[51] as well as seen in the photomicrographs of Figure 55. Figure 55 shows nematic **E3** elastomer microparticles heated from the nematic phase, through to the isotropic phase and underwent very small shape change. The long 11-carbon spacer group in monomer **M3** decouples the mesogen unit and the polymer backbone. This decoupling means that the anisotropy of the mesogens is only very weakly imparted onto the polymer backbone, if at all, and hence the matrix remains isotropic which is not conducive to actuation. The dimensions of the particle highlighted changed from 26 x 26 μm to 27 x 27 μm. Upon cooling and returning to the nematic phase the dimensions also returned to 26 x 26 μm. The small increase in dimensions observed in the highlighted particles could have been possibly due to thermal expansion or some minimal coupling of the mesogens to the polymer backbone through the long spacer group.

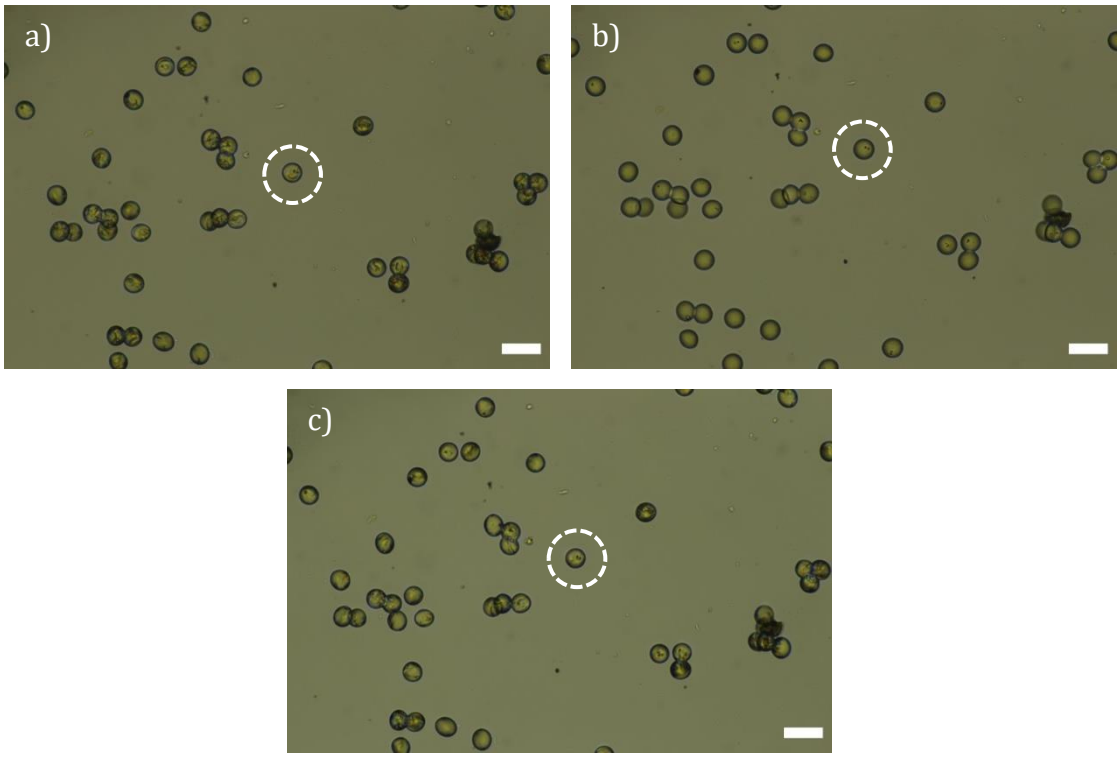

Figure 51: Brightfield photomicrographs, in transmission mode, of **E3** nematic elastomer microparticles, from **E3-MF19** when heated from the nematic phase, 55 °C (a), to the isotropic phase at 105 °C (b) and then cooled back to the nematic phase, 60 °C (c). Taken at 200x magnification, scale bars 50 μm. Highlighted particles referenced in text.

On the other hand, it was difficult to obtain spherical nematic elastomer microparticles of **E1** and **E2**. Droplets of either **M1** or **M2** containing crosslinker and photoinitiator were polymerised in the nematic phase, examples shown in Figure 52 show **E1** particles which were polymerised at 7% intensity 30 cm from the UV light source at room temperature; and **E3** particles polymerised at 50% intensity 30 cm away from the light source at 55 °C.

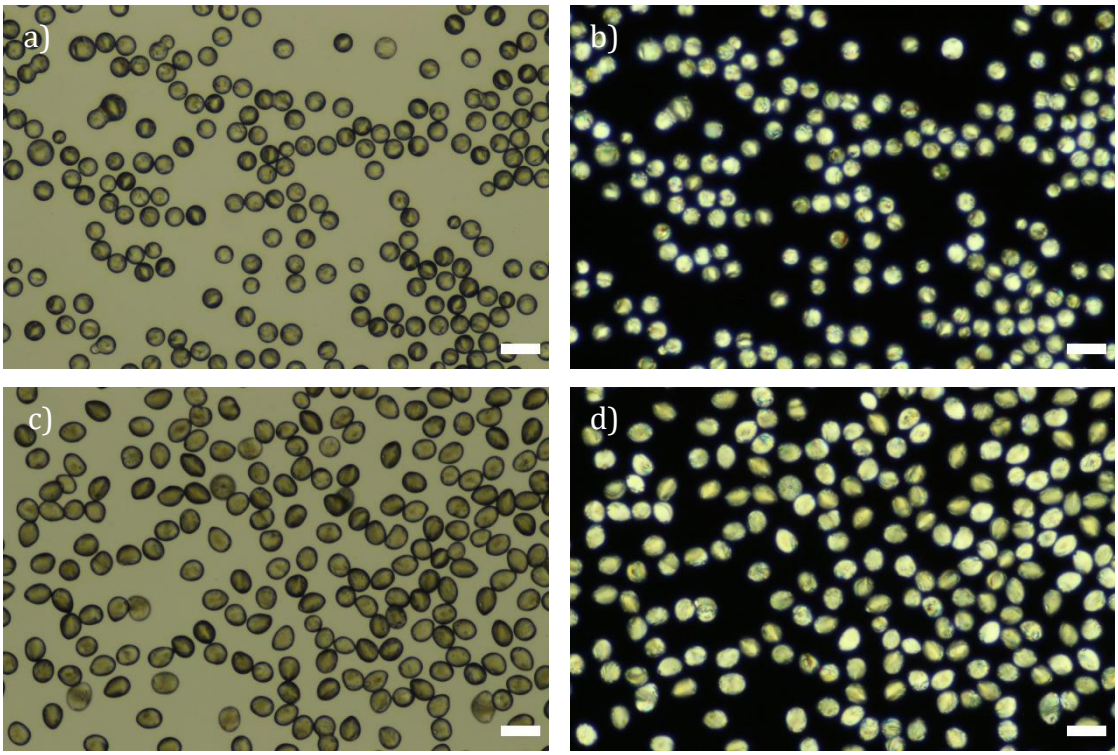

Figure 52: Brightfield (a & c) and polarised (b & d) photomicrographs of nematic elastomer microparticles of **E1** from **E1-MF69** polymerised at 7% intensity (a & b) and **E2** from **E2-MF78** polymerised at 55 °C (c & d). Taken at 200x magnification, scale bars 50 μm.

It is clear that photopolymerisation allowed for retention of the nematic alignment. However, the textures, again, were slightly distorted, possibly due to some slight shrinkage upon polymerisation, although the geometry deformation away from spherical is likely a larger contributor to the alignment disruption. Despite this, a nematic confinement texture was indicated in the imaging, resembling a bipolar texture, shown in Figure 53, which shows the particle predominantly appears to exhibit a monodomain alignment, in which there is some isogyre rotation as the orientation angle is changed between cross polarisers. Monodomain alignment is further backed up by the actuation response of the particles.

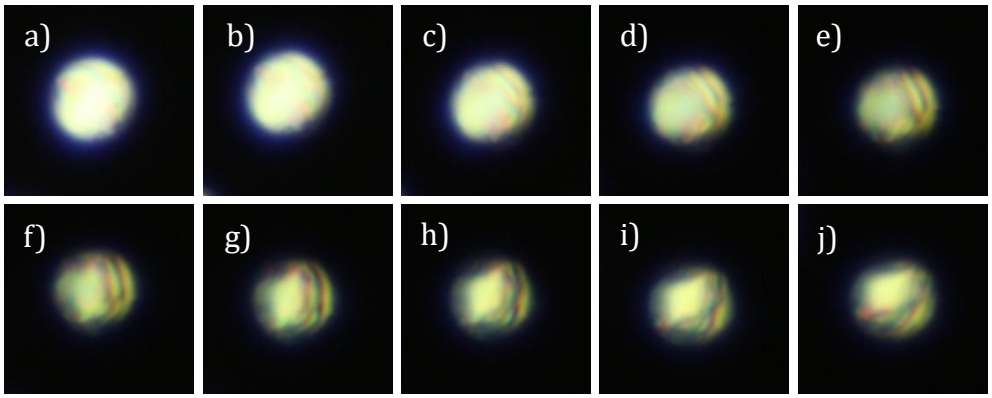

Figure 53: Polarised photomicrograph showing a **E1** elastomer microparticle from **E1- MF69** upon a 90° rotation with respect to the crossed polarisers in 10° increments from (a) – (j). Originally taken at 200x magnification, cropped, and zoomed in by 1.7x. Corresponds to **E1** particles in Figure 52.

Figure 54 shows **E1** and **E2** elastomer microparticles undergoing a heat/cool cycle after washing and replacing the dispersion medium with PEG 200. It was observed that the **E1** particle underwent a 40% change in aspect ratio upon clearing, and the **E2** particle a 49% change in aspect ratio. These results are in line with those previously reported in the group, of ~36% for **E1**, as well as in the literature for much larger (~500 μm) **E1** microparticles and 62 μm **E1** elastomer micropillars which saw a ~40% aspect ratio change and 30% length contraction respectively.[51,52,124,131] The results show that there is a strong degree of coupling between the mesogenic units and the polymer backbone in both **E1** and **E2**, and terminal chain lengths have little effect on this degree of coupling.

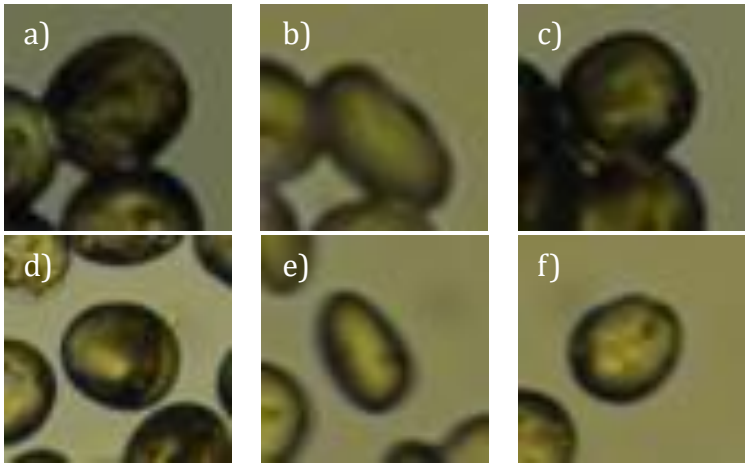

Figure 54: Brightfield photomicrographs, in transmission mode, of **E1** (a – c) and **E2** (d – f) nematic elastomer microparticles from **E1-MF22** and **E2-MF78** undergoing a reversible shape change when heated from the nematic phase, 80 °C (a) or 25 °C (d), to the isotropic phase at 140 °C (b) or 100 °C (e) and then cooled back to the nematic phase, 80 °C (c) or 25 °C (f). Originally taken at 200x magnification, cropped, and zoomed by 6.2x (a – c) or 5.0x (e – f).

Overall, it is clear that it was facile to produce spherical nematic elastomer microparticles of any of the monomers when polymerising in the isotropic phase, however these microparticles were polydomain. When polymerising **M3** droplets in the nematic phase spherical **E3** bipolar nematic elastomer particles were produced, albeit with some small disruption to the internal alignment. Finally, upon polymerisation of **M1** and **M2** droplets in the nematic phase, whilst aligned nematic elastomer microparticles were produced, it was difficult to maintain a spherical geometry, hence a further investigation into this geometry deformation was carried out for the production of anisometric elastomer microparticles.

3.3.2 Anisometric Nematic Elastomer Microparticles

A clear deformation in geometry, i.e. a deviation away from a spherical shape, was observed in **E1** and **E2** microparticles upon polymerisation. This deformation is distinct from the actuation shape-changes in response to temperature observed for these systems and occurs at the point of polymerisation of **M1** and **M2** containing droplets almost instantly. For context, Video 1 (videos are found in the accompanying electronic folder to this thesis titled "Supplementary Videos", video figure captions are found within the folder and in section vii) shows **E1** droplets which remarkably underwent a very fast shape deformation, from a spherical geometry to an elongated spindle shaped geometry, at the point of UV light exposure during polymerisation. These droplets were polymerised at a high intensity, showing a greater degree of deformation than those discussed in the previous subsection.

To investigate this phenomenon further, a systematic study of the effect of altering the polymerisation conditions was performed. Controlling the geometry of particles could allow for tuning of the aspect ratio to produce particles with specific geometries for their application.

3.3.2.1 Effect of Polymerisation Conditions on Particle Geometry

The effect of altering the photopolymerisation conditions of the monomer containing droplets into elastomer microparticles, specifically the intensity of the

UV light was investigated. The intensity was changed by two means, firstly the Omnicure system itself has an intensity percentage setting from 5% up to 100%. Secondly, the LED was positioned at different distances from the sample to be irradiated, the closer the sample the more intense the beam as it is spread over a smaller surface area. To calculate an intensity value from these parameters Equation 12 was used; where I_c was the calculated intensity, I_o was the Omnicure intensity displayed on the light source and d was the distance of the LED from the irradiated sample. The resulting calculated intensities used in polymerisations can be found in Table 2. As a radiometer wasn't used to measure the intensity output of the UV LED, the true relationship between the percent intensity and the actual intensity is unknown. Hence, the values given by the following equation should be treated as arbitrary values. The equation was used so that the intensity and distance variables could be combined for analysis and the different polymerisation conditions compared.

$$I_c = I_o \frac{1}{d^2}$$

Equation 12: To calculate the intensity from the Omnicure distance and percent intensity parameters.

Table 2: Calculated intensities for the various polymerisation conditions used.

Omnicure Intensity (%)	Distance (cm)	Calculated Intensity (% cm^{-2})
7	30	0.01
50	40	0.03
50	30	0.06
100	30	0.11
100	6	2.78

Figure 55 shows a plot of the calculated intensity of the UV light used to polymerise droplets of **M1** and **M2** to produce particles of **E1** and **E2** against the resulting particle aspect ratios. Although there is no clear trend, especially at lower intensities, at the highest intensities, the aspect ratios of the particles were much

higher than at the lower intensities for the majority of experiments, and always for **E2**. For the average aspect ratio of particles polymerised at room temperature at each intensity, in **E1** the aspect ratio increased with intensity and dramatically increased at the highest intensity. For **E2**, the average aspect ratio remained almost constant for the three lowest intensities, at ~1.24 – 1.26 and then dramatically increased to 1.59 with the highest UV intensity. Whilst there is no defined trend, the results here show that by controlling the intensity, we are more likely to get particles of certain aspect ratios.

In these experiments and the data in the experimental chapter (section 7.3.3, Table 15), it can be seen that the polydispersity of microparticles remained low in most cases with slightly higher CV compared to droplets, likely due to differences in geometry deformation, average CV for particle length and width was 4.3%, and the average CV for aspect ratios across **E1** and **E2** experiments was ~5% (where experiments where droplets were polydisperse due to blockage and jetting were not included in calculations). These aspect ratios show that, despite the variance of aspect ratios for different samples polymerised under the same intensity, the resulting microparticles in each individual sample were monodisperse and uniform, particularly seen in droplets of larger aspect ratios where greater shape uniformity was observed.

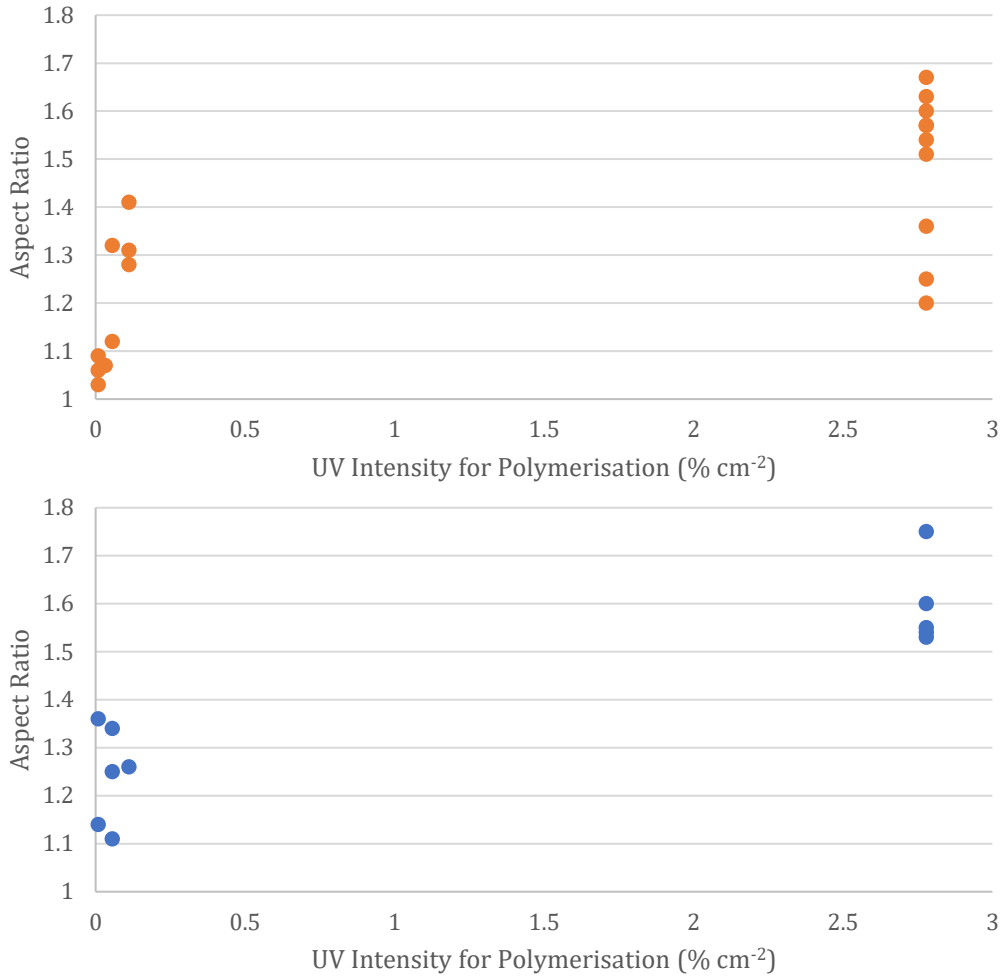

Figure 55: Plots of the effect of polymerisation UV intensity on the aspect ratio of bipolar nematic elastomer microparticles of **E1** (top) and **E2** (bottom) polymerised at room temperature.

Figure 56 and Figure 57 show photomicrographs of some of the samples analysed to produce the graphs in Figure 55. It can be seen that the particles produced at lower intensities are less elongated than those of higher intensities and the imaging shows that there was more of a variation of particle shape at lower polymerisation intensities than higher. Additionally, it was observed that at higher intensities the particles anisometric shape was much more regular, where particles were mainly spindle shaped (Figure 56g and particularly in Figure 57c). To produce a uniform sample of spindle shaped nematic elastomer particles, the most successful polymerisation conditions at the highest intensity investigated of 100% at 6 cm away at room temperature. In SEM photomicrographs, some surface wrinkling was observed, this will be more closely investigated in section 3.3.2.4.

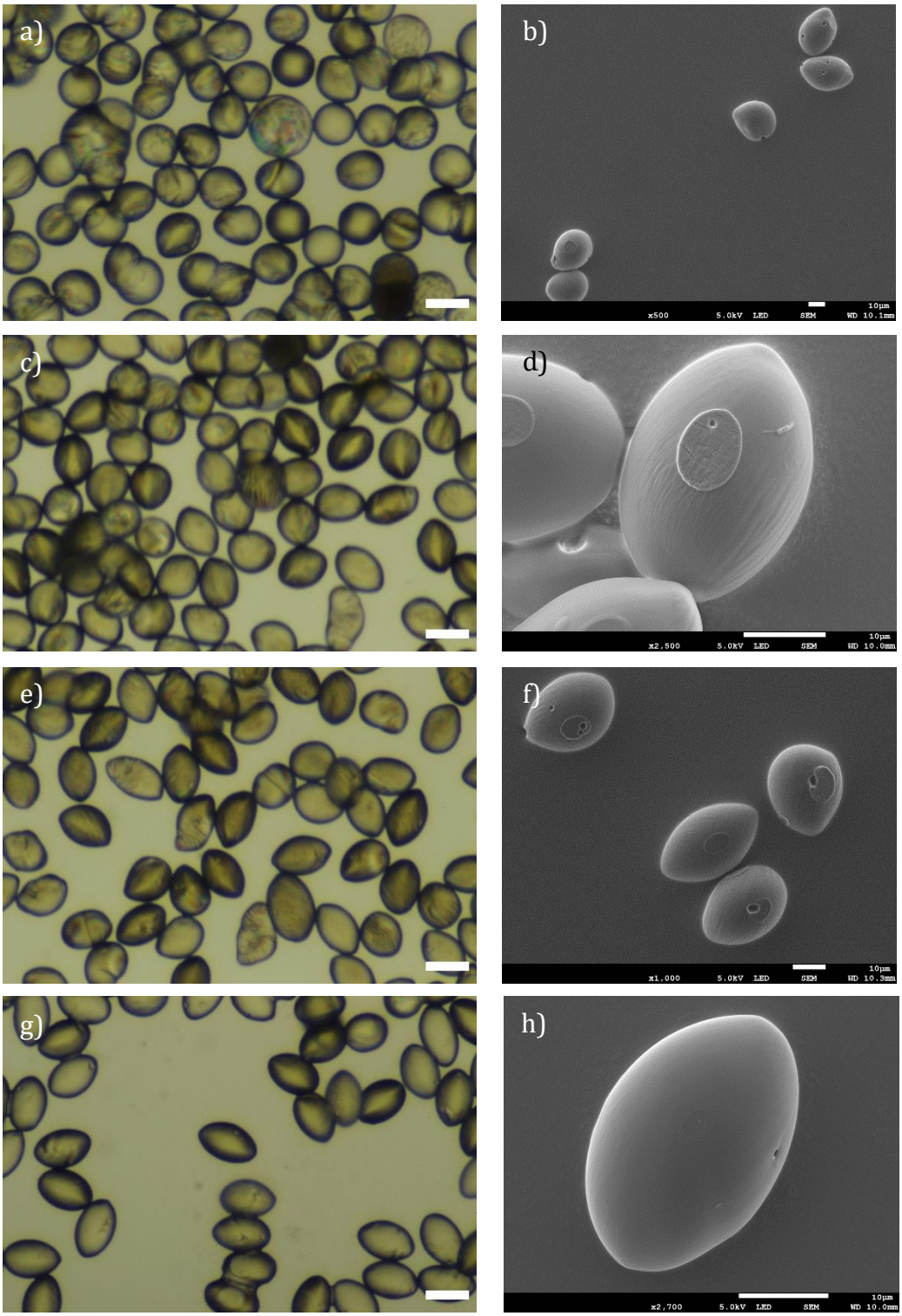

Figure 56: Brightfield photomicrographs (a, c, e & g) and SEM photomicrographs (b, d, f & h) of **E1** nematic elastomer microparticles from **E1-MF64** (a – f) and **E1-MF66** (g & h) polymerised 30 cm (a – f) or 6 cm (g & h) away from a UV source at 7% (a & b), 50% (c & d) and 100% (e – h) intensity at 55 °C. Brightfield photomicrographs taken at 500x magnification, scale bars 25 μm. SEM images taken at 500x (b), 2500x (d), 1000x (f) and 2700x (h) magnification, scale bars 10 μm.

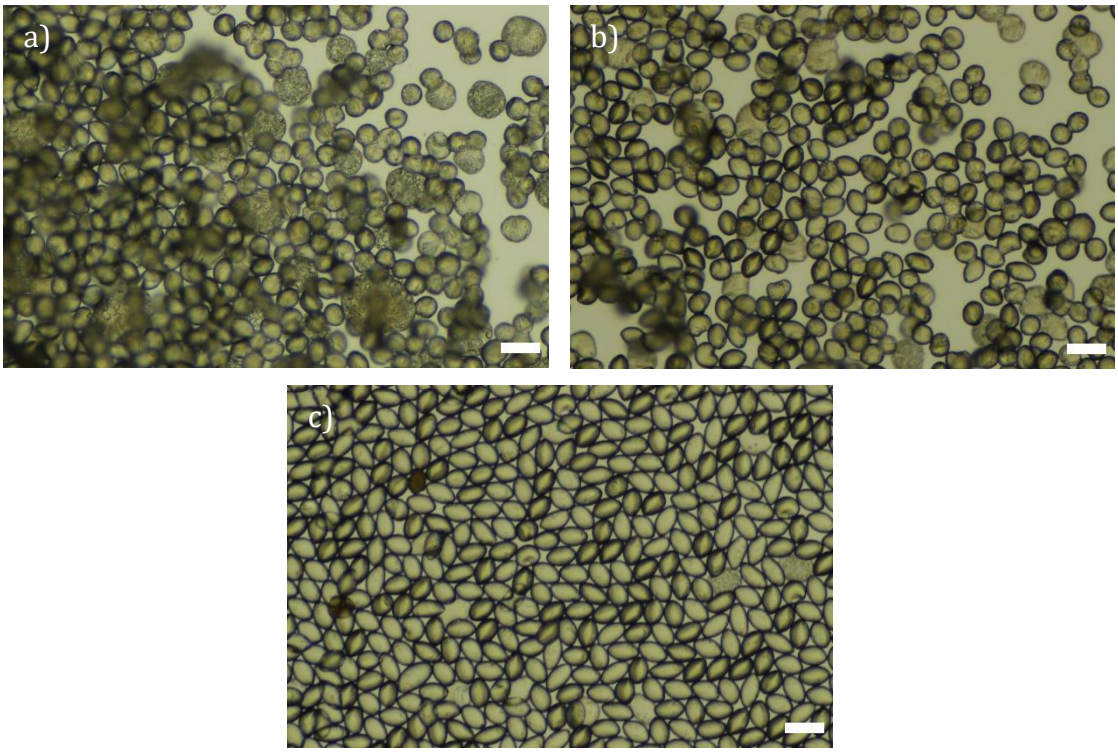

Figure 57: Brightfield photomicrographs of **E2** nematic elastomer microparticles from **E2-MF75** (a & b) and **E2-MF80** (c) polymerised 30 cm (a & b) and 6 cm (c) away from a UV source at 7% (a), 50% (b) and 100% (c) intensity at RT. Taken at 200x magnification, scale bars 50 μm.

Previously in the literature, anisometric nematic particles have been produced by polymerising droplets containing mixtures of polymerisable mesogens in combination with non-polymerisable mesogens, for example, RM257 and 5CB. When the spherical elastomer particles were produced, the non-polymerisable mesogen was washed out causing a volume reduction resulting in an anisotropic contraction which was observed as a deformation of the particle geometry to give spindle shaped particles.[55–57,85] Wang *et al* and Mondiot *et al* explain this as an anisometric volume contraction due to anisotropic templating of the polymer matrix in the initial bipolar configuration. This means that the polymer chains were stretched and aligned parallel to the director, from one boojum to the other, and so the volume reduction occurs in the perpendicular direction to this which creates a spindle shaped geometry.[57,85] Another method for producing anisometric elastomer microparticles involved deforming droplet geometry by stretching a matrix the droplets were embedded in, then polymerisation was performed to preserved the elongated geometry.[59] However, this work, building on previous work within the group, confirmed that both anisometric, spindle shaped, nematic

elastomer microparticles of **E1** as well as **E2** could be produced instantaneously upon polymerisation without the need for additional synthesis steps such as washing out unreacted materials or manual stretching.

There are few theories as to why this spontaneous deformation occurs upon polymerisation. One of which includes anisotropy in the polymerisation itself, where the UV light interacts with the photoinitiator, or the produced radicals interact with monomers, at a preferential orientation with respect to the director within the droplets, polymerising them along one axis at a faster rate than another axis. Anisotropic polymerisation has been used in nematic and chiral nematic films to tune the properties of the film, such as controlling surface wrinkling, polarisability and patterning;[132–135] albeit these examples use an anisotropic photoinitiator which is contrary to our use of an isotropic photoinitiator, hence this explanation would rely on the nematic system imparting some anisotropy onto the photoinitiator.[51] This rationalisation could explain why polymerisation temperature has little effect on the particle geometry, as increasing temperature would increase the rate of polymerisation but would not mitigate the polymerisation rate differential between the parallel and perpendicular director-irradiation axes. However, as the photoinitiator is not anisotropic itself this theory seems unlikely. In order to provide our own reasoning, a deeper texture analysis of the droplets and microparticles is required, whilst focusing in on the moment of geometry deformation in the next subsection.

3.3.2.2 Elongation and Texture of Anisometric Nematic Elastomer Microparticles

To further investigate the geometry deformation upon photopolymerisation of droplets to produce the most elongated, spindle shaped, particles the polymerisation was performed on a microscope to allow for observation during the polymerisation.

Video 1 shows bipolar nematic droplets of **M1** containing photoinitiator and crosslinker with areas in a monolayer after gentle agitation of collection dishes. Upon irradiation with UV light an instant geometry deformation occurred from spherical to spindle shaped. Video 2 shows a 64x sped up ten minute period

post-polymerisation where the spindle shaped particles move to pack more efficiently to fill gaps. It is impossible in POM photomicrographs to compare a droplet before polymerisation with an anisometric microparticle post-polymerisation due to the particle movement which occurred during the 10 minute polymerisation. However, POM imaging before polymerisation can be compared with a video screenshots taken from Video 1, shown in Figure 58. It can be seen in this figure that the droplets deformed in random directions with respect to each other, this is because the droplets were in random orientations with respect to each other. The zoomed in examples show droplets where the polar axis can be found, as represented in the cartoon diagrams. Upon irradiation, there appeared to be a correlation between the elongation direction and the polar axis direction, albeit given the latter was not always clearly defined. The same result was found for **E2**, and a video of the geometry deformation upon polymerisation can be seen in Video 3.

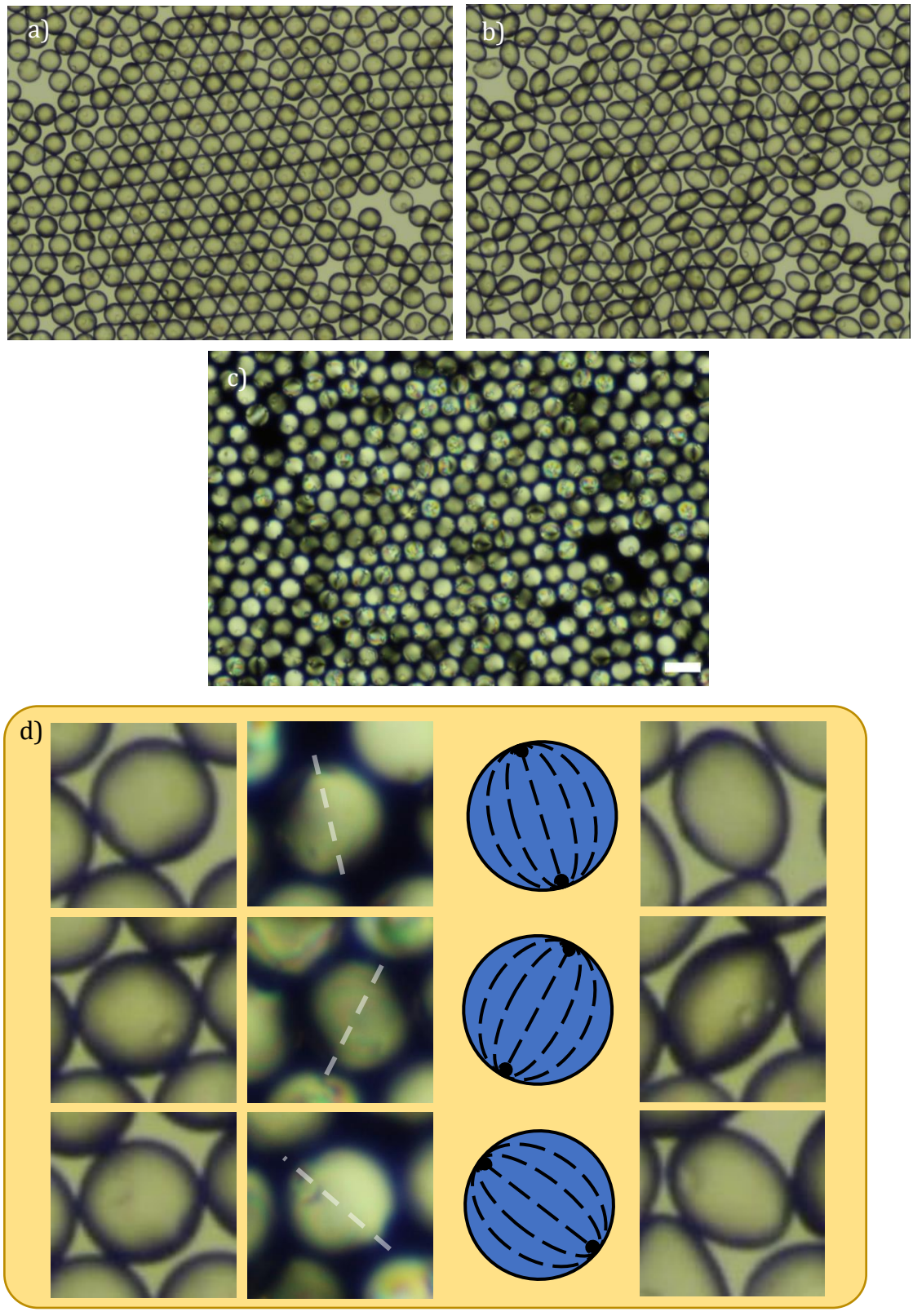

Figure 58: Brightfield Video 1 screenshots (a & b) and polarised photomicrograph (c) of **M1** droplets from **M1-MF81** (a & c) before polymerisation into spindle shaped **E1** microparticles from **E1-MF81** (b). Taken at 200x magnification, scale bars 50 µm. (d) shows 3 droplets from (a & c) and particles from (b), which have been cropped and zoomed by 3x, the polarised images were used to indicate the direction of the polar axis, represented by the cartoons in the 3rd column.

The elongation deformation occurs so as to push the polar defects of the bipolar system out from the droplet to the tips of the spindle within the forming elastomer microparticle, which could be inferred from the observations in Figure 58d where the elongation occurred along the polar axis, likely pushing the defects to the spindle tips (a deeper texture analysis is found in the paragraphs which follow). This would have the effect of reducing the splay at the poles as the local geometry at a spindle tip is pointed; and reducing the bend deformation of the director field as the curvature of the spindle shape is less bent than that of a sphere. The strong coupling of the anisotropy of the mesogen to the emerging polymer matrix means that the affinity for the mesogens to push the defects out, is transmitted to the elastomer backbone resulting in deformation of the elastomer matrix into the spindle shape (which explains the lack of particle geometry deformation seen for **E3**, section 3.3.1.2, Figure 50, due to the decoupling effect of the long 11-carbon spacer group between the mesogen and the polymer backbone resulting in an isotropic polymer backbone). As the elasticity jump is a large and fast jump from the relatively small nematic elasticity within the droplet to the large degree of elasticity associated with the elastomer matrix, the polymer chains do not have the time to reorient to preserve a spherical geometry and hence the spindle shape is captured. The jump in elasticity outweighs the minimisation of the surface energy, which usually keeps the droplet spherical, allowing the geometry deformation to occur to reduce elastic energy, by reducing splay and bend of the director field.[51,136–139] In this explanation, other contributions may come from anisotropic shrinkage during polymerisation as new bonds form, similar to that reported by Wang *et al* and Mondiot *et al* upon volume reduction by removal of non-polymerisable material, mentioned in the previous subsection.[57,85] However, at lower polymerisation intensities, the slower rate of polymerisation allows for some polymer chain reorientation to occur, hence the degree of deformation is less.

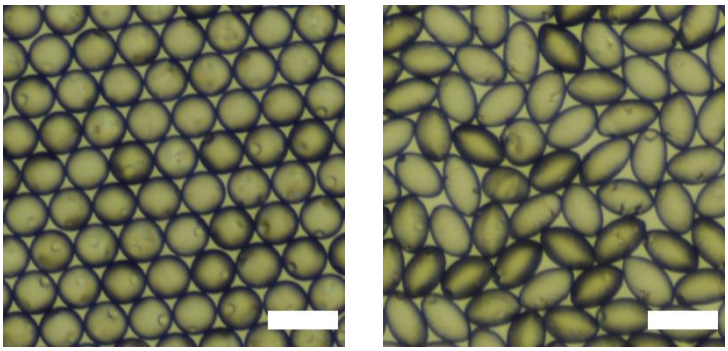

Figure 59: Brightfield photomicrographs of nematic droplets (a) and elastomer microparticles of **E1** from **E1-MF81**. Taken at 200x magnification, cropped to 242.16 x 242.7 μm, scale bars 50 μm.

It was noted in Video 2 that the elongated particles moved and rearranged to fill gaps and pack more efficiently. The packing efficiency of spindle shaped microparticles of **E1** was calculated using ImageJ by processing the cropped photomicrographs found in Figure 59 of a set area of droplets and particles in a monolayer. The images were processed to find the area of the gaps between droplets and particles which was used to calculate the percentage area of the 242.16 x 242.70 μm samples which was occupied by either a droplet or a particle. The maximum packing density of 2D circles is 90.6%.[140] It was found that the packing efficiencies of spherical droplets and elongated particles were comparable, calculated from the 2D image, being 90.1% and 90.6% respectively.

Once polymerised, the texture of the elongated spindle shaped particles was examined under crossed polarisers. When elongated particles were rotated through 180° (Figure 60), the texture changed, but more interestingly it is not symmetrical as you would expect a bipolar particle to be. When the particle is angled vertical with respect to the plane of observation (Figure 60a) it is slightly dim, when rotated to 45° (e & f) it becomes brightest, as it continues through to 90° in the same direction it is dim again (j) and then through to 135° it is bright in the middle with dark edges (n & o), at 170° it returns to dim (r) as it approaches 180°. When comparing the particle at 45° and 135°, in a bipolar configuration it would be expected that the texture be the same and isogyres would shift to cross if the director field was symmetrical in that direction, but in this case, it is not.[141] However, the imaging suggests that there is 180° symmetry, which is consistent with what would be seen in a twisted bipolar configuration. A cartoon representation of the twisted bipolar configuration can be seen in Figure 61. The

two notable features are that there are still two boojums present, one at each pole of the spindle; and that between the polar defects the mesogen alignment twists. When the particle is rotated from 0° to 180°, as represented across a row in the figure, at 45° and 135° the internal mesogen arrangement is not aligned in the same direction, however at a 180° rotation, it is.[142–144] This gives rise to the non-symmetrical striations causing the dimming of a 135° particle, if the 45° particle is bright and *vice versa*, which was observed experimentally and shown in Figure 60.

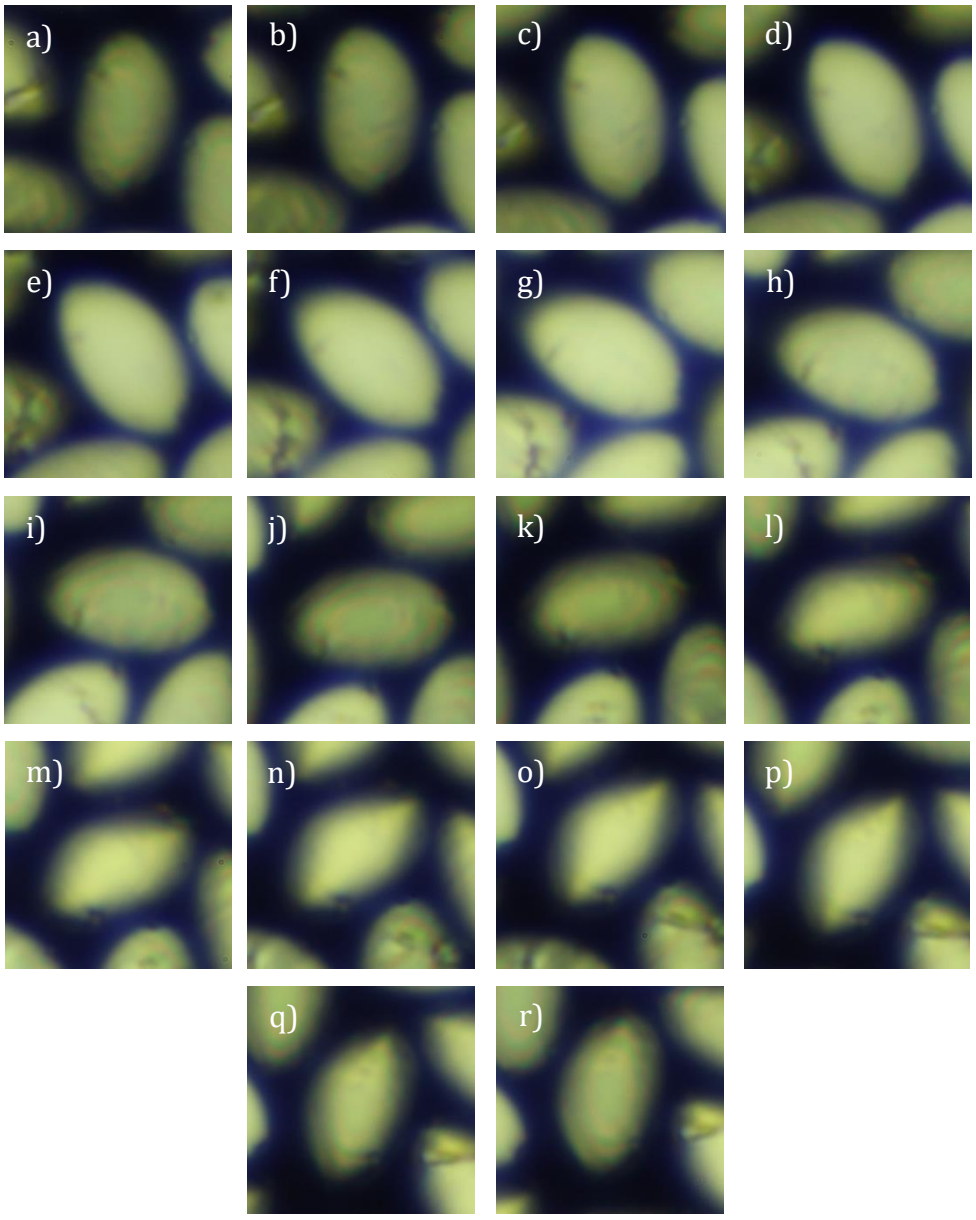

Figure 60: Polarised photomicrograph of an **E1** nematic elastomer microparticle from **E1-MF70** zoomed in by 3.2x showing the particle rotating through 170° in 10° increments from (a – r). Original photomicrograph taken at 500x magnification.

The second row in Figure 61 is a mirror image, showing that the twist can occur in two directions, clockwise and anticlockwise. Notably, the two configurations of twisted bipolar alignment were observed in populations of particles of **E1** and **E2**.

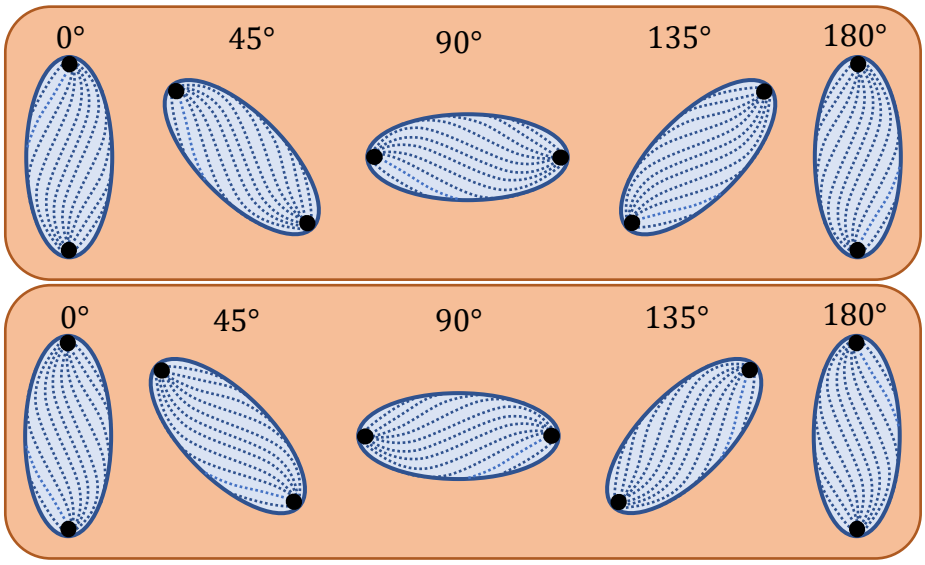

Figure 61: Cartoon representation of twisted bipolar particles with opposite twist (top and bottom rows) showing the internal particle alignment through 45° turns.

In Figure 63 several particles are highlighted which point in a 45° direction away from vertical. It was observed that not all particles in the 45° orientation were brightest without dark edges; and at 135° not all particles were bright in the middle with dark edges. Some particles had the opposite observation, suggesting that the two opposite twist directions of the twisted bipolar configuration were present in the population of particles.

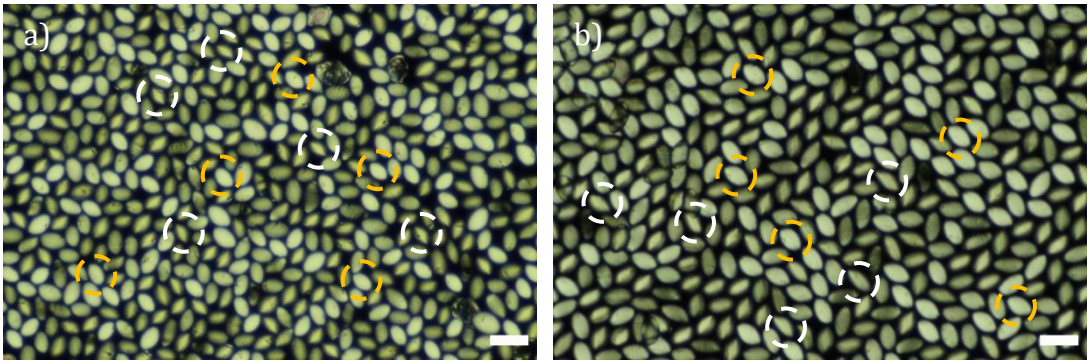

Figure 62: Polarised photomicrographs of nematic elastomer microparticles of **E1** from **E1-MF70** (a) and **E2** from **E2-MF80** (b). Taken at 200x magnification, scale bars 50 µm. Circles indicate particles oriented at an anticlockwise 45° angle (↖) where orange circles show five random particles with the brightest birefringence and white circles show five random particles with the dark edged birefringence.

This is an example of how the initially achiral material, being the spherical bipolar droplets, underwent a configuration change to produce a structurally chiral particle. Similar findings have been published by Ansell *et al* and Wang *et al*, who produced anisometric particles of RM257 by washing out non-polymerisable 5CB, which was present in the droplets, post-polymerisation as mentioned previously. The reduction in volume from polymer particles caused an anisotropic contraction, resulting in a twisted spindle shaped structure where a reorientation of the internal alignment of the anisometric particles occurred to introduce twist into the system to minimise splay and bend director field deformations. Furthermore, Ansell *et al* described particles with opposite twist directions.[55,57] Thus, the small shrinkage upon polymerisation in **E1** and **E2**, may also be anisotropic and contribute to the induced twist of the system. Additionally, it is thought that the sudden change in aspect ratio of the microparticle caused a shift in the balance of elastic energies within the system, causing a twist elastic deformation to arise to alleviate high splay in the elastic system.[142]

Overall, it is demonstrated here that conditions were found which allowed for the reliable preparation of nematic elastomer microparticles with defined director configurations and high shape anisotropy, showing a high degree of uniformity across particle populations. Large monolayer assemblies of anisometric particles were produced by polymerising **E1** and **E2** particles at a high intensity, using the UV light source from 6 cm away at 100% intensity. In addition, the geometry deformation required no additional steps, unlike the methods reported in the literature which required removal of non-polymerisable components, or mechanical stretching. The geometry control and reliable production of these uniform anisometric nematic elastomer microparticles may allow for the particle shape to be tailored to their specific application, whether that be in micromechanics, microfluidics, sensing, or soft robotics for example.[29,55,57,145,146]

3.3.2.3 Response of Anisometric Nematic Elastomer Microparticles to Temperature Change

The actuation response of these anisometric **E1** elastomer microparticles was previously proven in the group. In order to reproduce this response in **E1** and **E2**

spindle shaped microparticles, they were first washed and then the outer fluid replaced with PEG 200 as described in section 7.3.3. After washing, the quality of the samples was reduced due to particles sticking together, optimisation of the washing process is required to prevent this in future investigations. The response of the elastomer microparticles to temperature changes across their T_{NI} was investigated. Microparticles of **E1** and **E2** were heated from the nematic phase at room temperature into the isotropic phase at 140 and 100 °C respectively, before cooling back into the nematic phase and repeating the heat/cool cycle a second time. The elastomer microparticles were observed under brightfield microscopy so that the microparticles' outlines could be seen clearly, and dimensions measured.

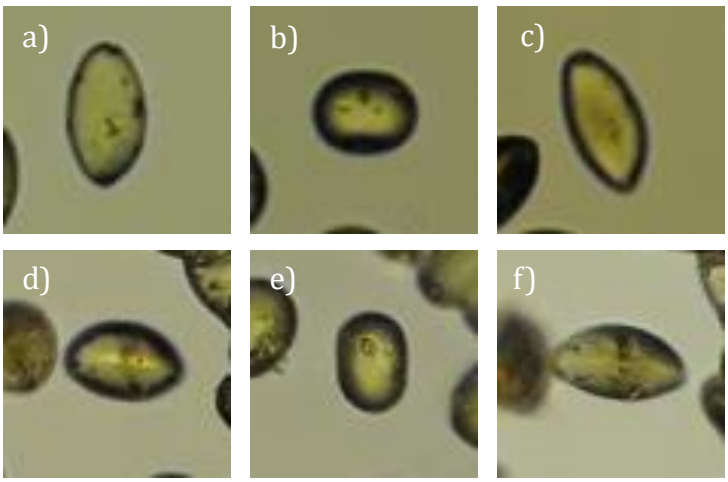

Figure 63: Brightfield photomicrographs, in transmission mode, of **E1** (a – c) and **E2** (d – f) nematic elastomer microparticles from **E1-MF81** and **E2-MF80** undergoing a reversible shape change when heated from the nematic phase, 80 °C (a) or 25 °C (d), to the isotropic phase at 140 °C (b) or 100 °C (e) and then cooled back to the nematic phase, 80 °C (c) or 25 °C (f). Originally taken at 200x magnification, cropped, and zoomed in by 4x.

The anisometric, spindle shaped particles shown in Figure 63, underwent a reversible shape change response to temperature when heated into the isotropic phase and cooled back to the nematic phase. Video 4 shows a video of the second heat/cool cycle of the anisometric **E1** microparticle captured at 200x magnification, zoomed, cropped and sped up by 64x. The dimensions of the particle shown in Figure 63a – c changed from 47 x 25 µm to 27 x 33 µm upon clearing, a contraction of the major axis by an impressive 43% and an elongation of the minor axis by 32% which was an overall 56% change in aspect ratio as it

changed from 1.88 to 0.82. As the already anisometric particles underwent such a dramatic shape change, the major and minor axis switched. Upon cooling back to the nematic phase, the particles returned to 48 x 24 μm showing excellent reversibility. Throughout the heat/cool cycles, particles stuck together as they came into contact with each other. Similarly, Video 5 shows a video of the second heat/cool cycle of the anisometric **E2** particle shown in Figure 63d – f. The dimensions of the anisometric spindle shaped **E2** particle changed from 43 x 23 μm to 22 x 32 μm upon clearing, a 39% elongation in the minor axis and a 49% contraction in the major axis, showing an aspect ratio change of 64%, from 1.87 to 0.68. Once returned to the nematic phase upon cooling, the dimensions of the particle returned to 26 x 30 μm. Both of the aspect ratio changes, for **E1** and **E2**, are similar to the value previously reported in the group of 65% aspect ratio change.[51] In both cases highlighted in Figure 63, an elongation in the direction perpendicular to the polar axis occurred as alignment was lost, whilst a contraction in the direction of the polar axis simultaneously occurred to preserve the volume of the elastomer microparticles. When particles were cooled back into the nematic phase reversibility was demonstrated as the microparticles original dimensions were restored, showing that the degree of crosslinking was at a great enough extent to revert to the polymer chain's original alignment.

There are very limited results in the literature for the actuation investigations of elongated, spindle shaped particle. Martinez *et al* produced anisometric particles of a main chain liquid crystal elastomer, rather than side chain as reported in this thesis. The main chain elastomer particles had diameters of 7 μm and aspect ratios of 1.90, upon clearing to the isotropic phase the aspect ratio changed by 42% to 1.11.[147] It is impressive that the anisometric particles produced of **E1** and **E2** have comparable and even larger, in the case of **E2**, actuation responses than their main chain counterparts; showing the coupling between the mesogen and polymer backbone is particularly strong.

3.3.2.4 Surface Wrinkling in Nematic Elastomer Microparticles

As briefly mentioned in the previous sections, when samples of **E1** elastomer microparticles were imaged under SEM, wrinkling was observed on the surface of

many of the particles. Wrinkling occurs as a result of compressive strain when a critical stress threshold is exceeded and is characterised as a form of surface buckling.[148,149] This was also observed under POM imaging for **E1** and **E2** microparticles. In order to assess the conditions under which the wrinkling occurred, the SEM images taken from **E1** particles, and the POM imaging of **E2** particles, produced under different polymerisation conditions were analysed.

Figure 64 shows **E1** particles polymerised at different temperatures but under the same UV intensity, 50% from 30 – 40 cm. In the brightfield POM image (e) it can be seen that there are striation lines (i.e. the darker and lighter lines), on the surface of the elastomer microparticles. These striation lines appear to correspond to the clearly visible wrinkles in the SEM imaging, particularly see in (c) and more faintly in (a) and (b). From the SEM imaging it can be deduced that when polymerised at room temperature the particle only showed faint surface wrinkling (a), and when the polymerisation temperature was increased to 55 °C the wrinkles became more distinct (b). When polymerised at 70 °C the wrinkles were much more pronounced (c). This shows that surface wrinkling was temperature dependant; as the polymerisation temperature was increased the wrinkles became more prevalent in the elastomer microparticles. However, it can be seen that when the temperature was increased above the phase transition and the particles were polymerised in the isotropic phase, the spherical particles no longer exhibited surface wrinkling (d).

Although imaging of **E2** particles was not possible under SEM as the particles did not survive drying in the vacuum oven, wrinkling could be observed for **E2** particles under brightfield and polarised imaging. The imaging revealed that particles of **E2** followed the same trend as particles of **E1**. Figure 65 shows that light striation, caused by surface wrinkling, was present across all polymerisation intensities investigated, 7, 50 and 100%, at RT; and when the polymerisation temperature was increased to 55 °C, striation, and therefore wrinkling, was much more defined under brightfield imaging, suggesting that the higher polymerisation temperature again caused more defined wrinkling on the surface of **E2** particles.

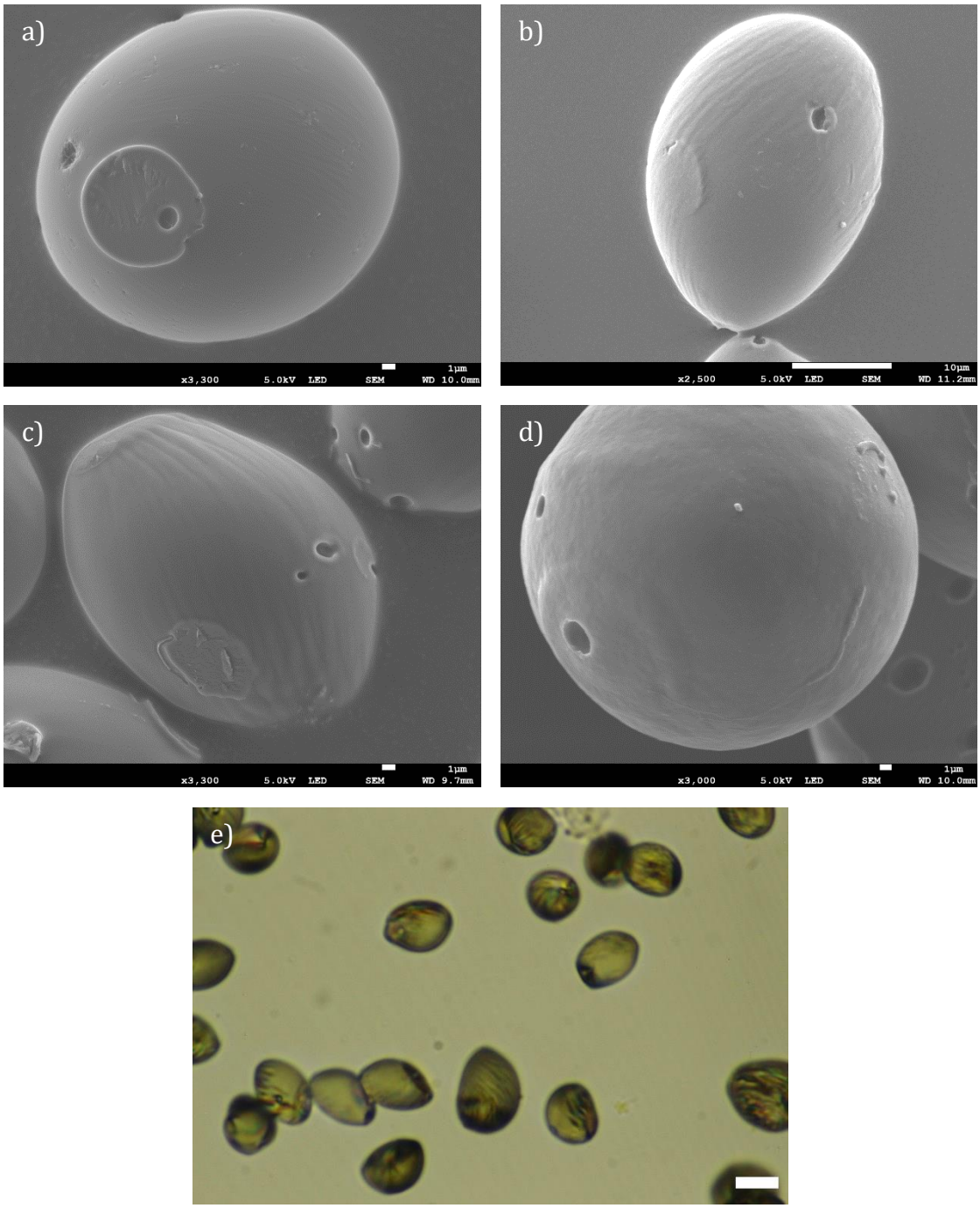

Figure 64: SEM photomicrographs (a – d) of **E1** particles from **E1-MF63** (a, b & d) and **E1-MF72** (c). Polymerised for 20 minutes at 30 – 40 cm away from a 50% intensity 365 nm UV light source at RT (a), 55 °C (b), 70 °C (c) and 107 °C (d). Brightfield photomicrograph taken in transmission mode at 55 °C of **E1** particles from **E1-MF63** polymerised at 55 °C after cooling to room temperature and returning to 55 °C. Taken at 3300x (a & c), 2500x (b), 3000x (d) and 200x (e) magnification, scale bars 1 µm (a, c & d), 10 µm (b) and 50 µm (e).

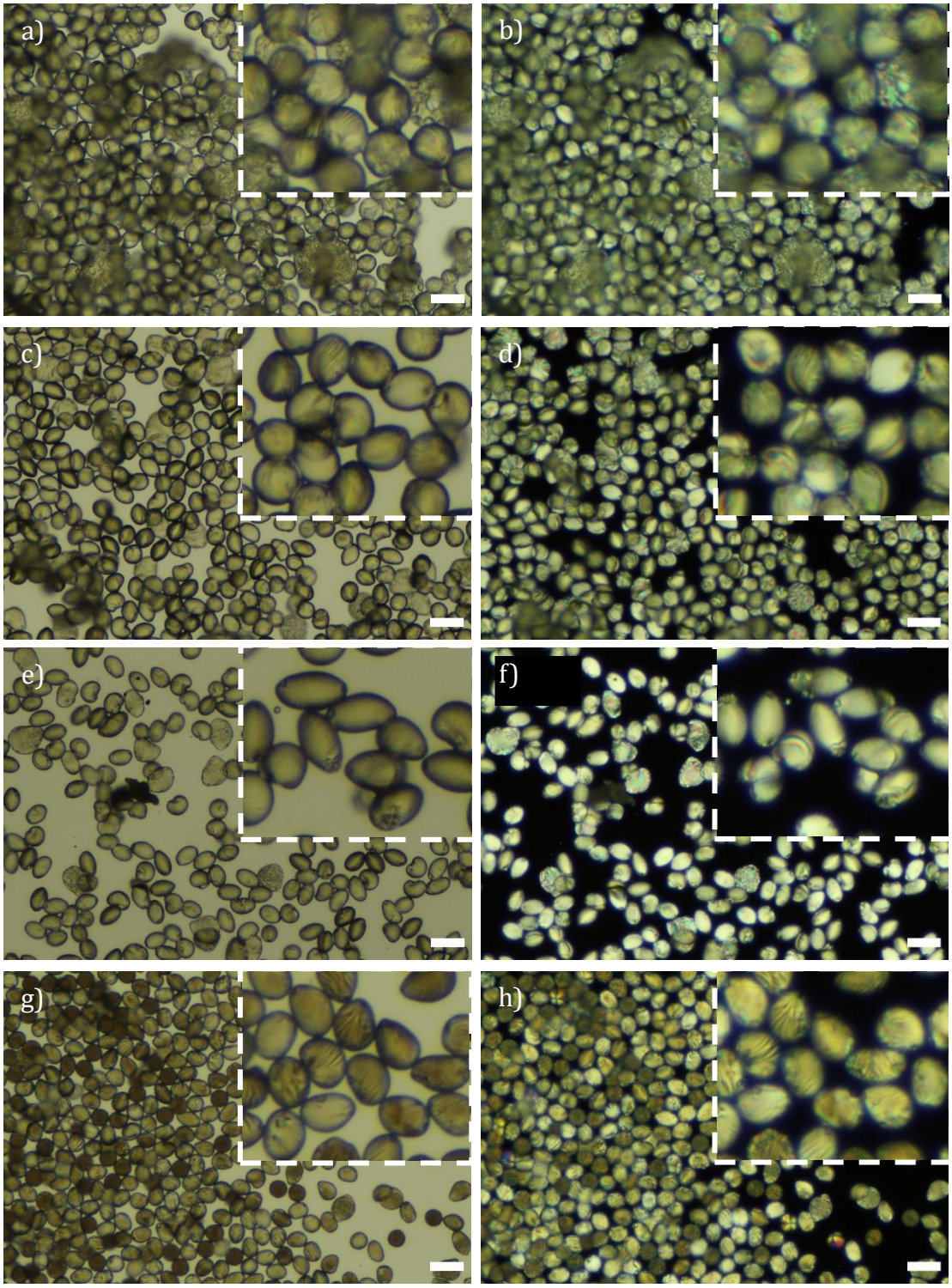

Figure 65: Brightfield (a, c, e & g) and polarised (b, d, f & h) photomicrographs taken in transmission mode of **E2** nematic elastomer microparticles from **E2-MF75** (a – f) and **E2-MF77** (g & h) with 2.5x zoomed in areas shown in the top right of each photo. Particles polymerised at RT (a – f) or 55°C (g & h) for 20 – 40 minutes at 7% (a & b), 50% (c & d) and 100% (e – h) intensity 30 cm away from a 365 nm UV light source. Taken at 200x magnification, scale bars 50 μm.

In contrast, Figure 66 shows particles which were polymerised at the same temperature, room temperature, but at different intensities of 7, 50 and 100% from 30 cm away and 100% from 6 cm away from the UV source. Between all the SEM photomicrographs, there was visually little difference between the wrinkle intensity for particles polymerised at any of the intensities, even at the very high intensity of 6 cm away at 100%, which suggests that the intensity of the polymerisation does not play a dominating part in particle wrinkling.

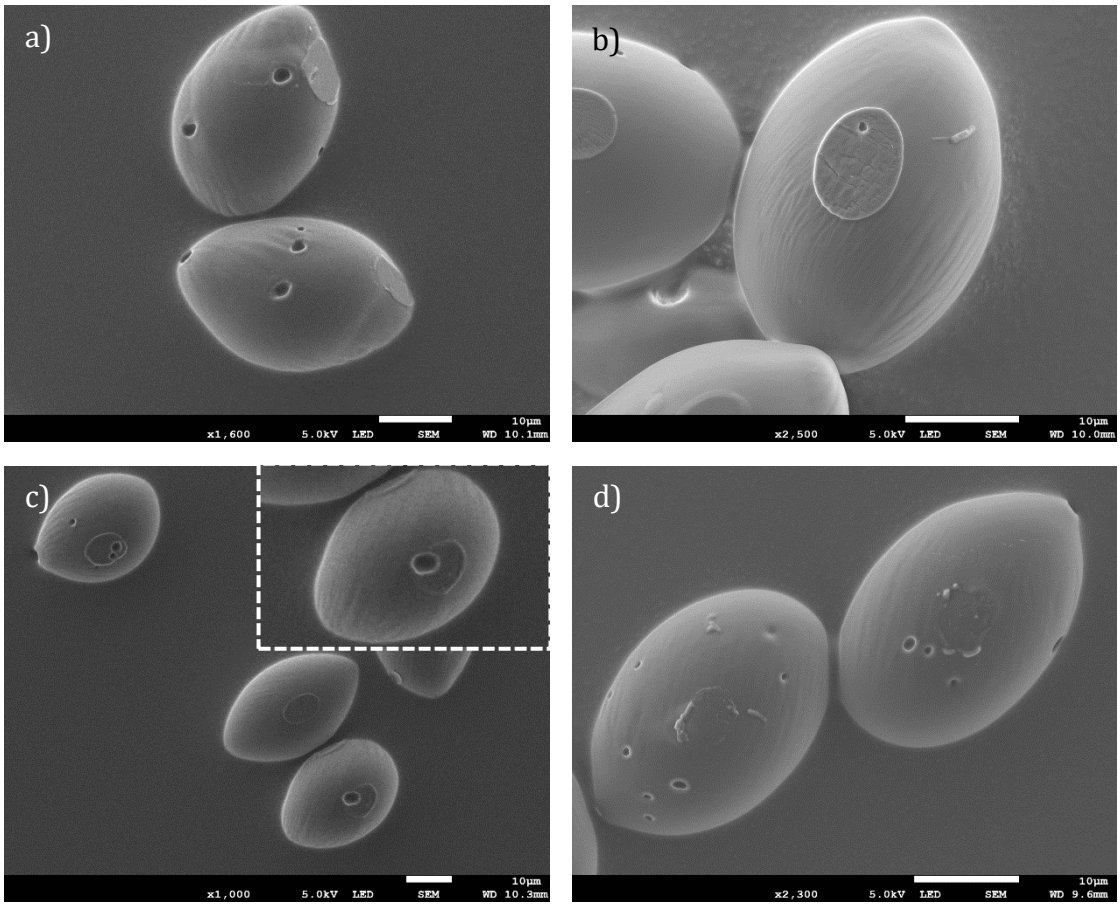

Figure 66: SEM photomicrographs of **E1** particles from **E1-MF64** (a – c) and **E1-MF72** (d). Polymerised at RT at 30 cm (a – c) or 6 cm (d) away 365 nm UV light source at 7% (a), 50% (b), 100% (c & d) intensity for 20 – 30 minutes. Taken at 1600x (a), 2500x (b), 1000x (c) and 2300x (d) magnification, scale bars 10 µm. A 1.6x zoomed in section of (c) allows for better visualisation of wrinkling on a microparticle.

In addition to these observations, the wrinkling seen in the SEM images of Figure 64 and Figure 66 show the wrinkling is anisotropic in it's periodic directionality. This, and the loss of wrinkling upon isotropic polymerisation, suggests that the wrinkling is as a result of the nematic alignment within the

particle. It appears that the wrinkles follow the twisted bipolar pattern with the wrinkles twisting between poles, clearly visible in Figure 64b & c as well as all of the particles shown in Figure 66, running in parallel to mesogen alignment. Figure 67 shows a zoomed in section of Figure 66c to look at the wrinkling on the two particles highlighted. Interestingly, it can be seen that the particles wrinkle pattern had the opposite twist to one another, represented by the cartoon drawings in the figure. This is further evidence of not only wrinkling following the nematic configuration, but also that both twist directions of the twisted bipolar nematic configuration in anisometric particles was present upon polymerisation induced geometry deformation, as discussed in section 3.3.2.2, Controllable and directional wrinkling is uncommon in isotropic polymer microparticles, and difficult to achieve where desired. Usually, the wrinkles of isotropic polymer microparticles follow no particular pattern and occur in any direction.[150–152] Because of this, it is significant that the nematic elastomer microparticles reported here did exhibit anisotropic wrinkling on anisometric particles, whilst the fabrication of them is relatively facile.

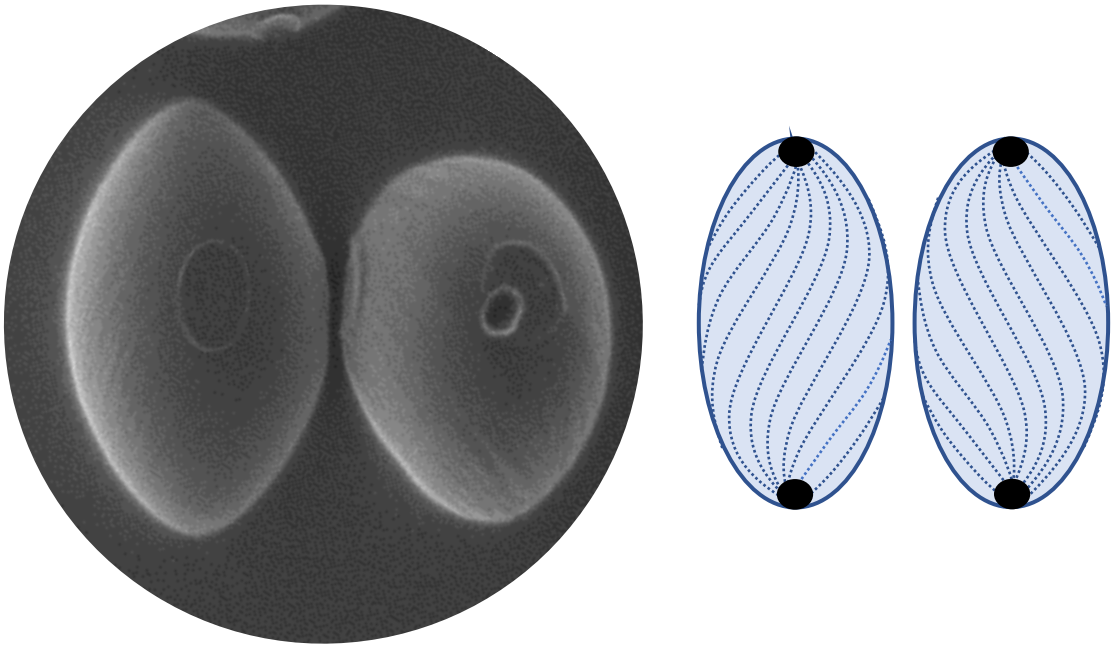

Figure 67: Portion of SEM photomicrograph found in Figure 66c zoomed in by 2.8x to show two particles with wrinkling of opposite twists and cartoon representations of the two twists observed in the particles.

Similar twisted wrinkling was reported by Ansell *et al* in their spindle shaped twisted bipolar particles, where they were explained as due to the shrinkage of the particle upon washing away non-polymerisable 5CB, which also caused the twist, further suggesting the small volume contraction due to polymerisation may be occurring anisotropically in **E1** and **E2** microparticles.[55]

It is thought that the anisotropic wrinkling seen in the **E1** and **E2** systems may be akin to wrinkling of nematic films in literature. In such systems, a bilayer is produced where the anisotropic film is atop of an elastic or fluid substrate in a bilayer. During polymerisation of **E1** and **E2** droplets, it is thought that the surface polymerises first upon irradiation with the UV light. When the surface of the particles polymerises first, this becomes like an elastomer film over the top of the unpolymerised centre with different thermal expansion coefficients, as well as elastic properties, and so upon heating the system, the difference in the degree of expansion between layers induces stress. If the stress is above a critical value then the surface buckles causing wrinkling. Whilst this partially explains why wrinkling is more prevalent at higher polymerisation temperatures, as observed in **E1** and **E2** microparticles, it does not explain the directional anisotropy of the wrinkling.[153–158]

Kang *et al* produced an aligned nematic elastomer film, which was crosslinked at high temperature (120 – 150 °C) using a plasma treatment, resulting in anisotropic, directional and periodic wrinkling of the film surface in the direction of the director.[159] The authors explained the presence of wrinkles as, again being due to stress induced by the presence of a bilayer-like structure upon heating, due to the plasma treatment of the surface. The directionality of the wrinkling was attributed to arise due to the direction of the thermal strain, where thermal strain occurred due to the thermal expansion coefficients of the system. As the thermal expansion coefficients,[160] as well as elasticity, in nematic systems are anisotropic, the bilayer-like system shrunk, on cooling, in a preferred direction, which was perpendicular to the director. Hence, the anisotropic expansion and shrinking in the system produced anisotropic, directional wrinkling parallel to the direction of the director. It is postulated that the same reasoning applied to the planar films produced by Kang *et al*, may contribute to our observations for nematic **E1** and **E2**

elastomer microparticles, which exhibited anisotropic wrinkling parallel to the director. It is thought that wrinkling in **E1** and **E2** was observed to a greater extent at higher polymerisation temperatures than at lower temperatures because at higher temperatures the nematic system has a lower order parameter, therefore upon cooling there is a greater differential in the elasticity of the system, arising due to anisotropic elastic constants. The larger differential, would result in a larger bucking response at the surface, leading to more pronounced wrinkling, as observed in this investigation.

Finally, on the contrary, there was no sign of striation in any **E3** particles under brightfield and polarised imaging, suggesting that the decoupling of the mesogen and polymer backbone caused by the longer spacer unit reduces, or completely prevents, anisotropic surface wrinkling. It is expected that in order to have the directional wrinkling response, polymer chains must have anisotropy imparted upon them by the mesogen alignment, so as to be aligned along the surface of the microparticle in a common direction. In an **E3** system, the longer 11-carbon spacer group compared to the 4-carbon spacer in **E1** and **E2**, decouples the anisotropy of the mesogen from the polymer backbone and therefore the polymer is expected to be in a random coil configuration which is not conducive to directional expansion and shrinkage.

Overall, there is strong evidence that the wrinkles of **E1** and **E2** elastomer particles are a product of the nematic internal alignment, due to the fact that the wrinkling followed the twist of the bipolar alignment of the elongated particles, with the two opposite twist directions being observed. The anisotropic wrinkling is thought to be a product of anisotropic thermal expansion coefficients. There is a clear temperature dependence to the wrinkling but no strong correlation to polymerisation intensity. Controlled anisometric surface wrinkling of elastomer particles is another morphological phenomenon which has seldom been reported in the literature. It is particularly difficult to produce controlled directional wrinkling in isotropic polymer particles, thus the directional wrinkling seen here is particularly significant. It is expected that particles with surface wrinkling could have improved gripping capabilities in applications like soft robotics, micromechanics, or microfluidics with increased surface area. Wrinkling may also

be useful in templating or could possibly direct and control the flow of a gas or liquid over the surface of the particle.[154,161]

3.4 Response of Nematic Droplets and Elastomer Microparticles to Magnetic Fields

As discussed in the introduction chapter (section 1.2.1.1.2), most uniaxial nematic materials are diamagnetic, and as the magnetic susceptibility in these systems in anisotropic, they possess diamagnetic anisotropy. In calamitic the diamagnetic anisotropy is usually positive which favours alignment of the director parallel to the magnetic field.[8–10,162] Magnetic alignment of nematics in planar systems is a known property, for example in the literature, Wei *et al* have reported that when using a 1 Tesla neodymium magnet the mesogens of a bulk nematic mixture of **M1** aligned so that a uniform director across the sample was achieved. The aligned mixture was then utilised to produce monodomain elastomer rods.[124]

In this chapter the magnetic response of confined nematic systems will be investigated with the aim of exploiting the magnetic field to aid in the alignment samples of **M1**, **M2** and **M3** droplets before exploring photopolymerisation of these systems in the presence of the magnetic field, and thereafter the response of anisotropic elastomer microparticles in the magnetic field. Due to the success Wei *et al* had using 1 Tesla strength neodymium magnets for nematic alignment, N41 neodymium magnets will be utilised which have a strength of 1.32 Tesla.

3.4.1 Magnetic Alignment of Bipolar Nematic Droplets

Dishes of either isotropic droplets during solvent evaporation, or nematic droplets after solvent evaporation were placed atop of either an N42 diametrically magnetised neodymium ring magnet or three stacked N42 neodymium bar magnets. The bar magnets were stacked so that there was a flat surface for the dish to be placed upon. Nematic droplets were swirled for ~30 – 60 seconds and isotropic droplets left for solvent evaporation under exposure to the magnetic field. The strength of an N42 magnet is 1.32 Tesla, upon stacking three of these, the strength is not increased 3-fold, in fact the increase in magnet strength upon stacking is small. As the dishes were swirled on top of the magnets in the same

plane as the bottom of the dish, the magnetic field lines, represented in Figure 68, also passed through the dish parallel to the bottom of the dish.

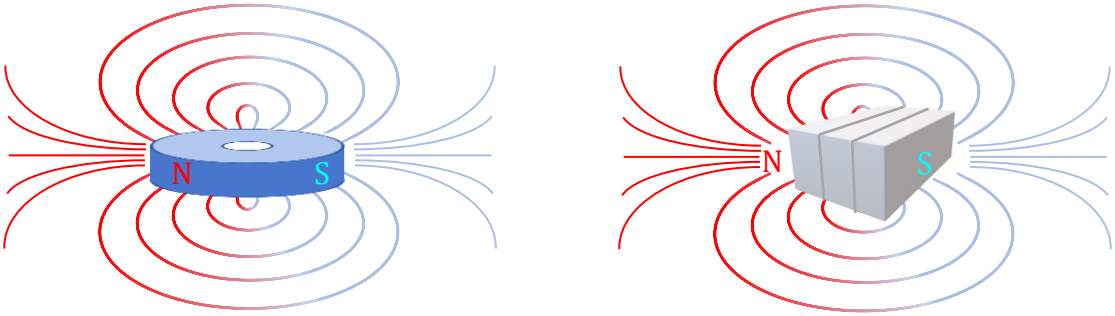

Figure 68: Cartoon representation of the magnetic field lines produced from the N42 diametrically magnetised neodymium ring magnet (left) and three stacked N42 neodymium bar magnets (right) used to align polar axes of nematic droplets where petri dishes are swirled on top of the magnets.

After solvent evaporation or swirling of nematic droplets on top of the magnets, the dishes were imaged under POM. Figure 69 shows photomicrographs from magnetic alignment experiments of **M1**, **M2** and **M3**. It is clear through crossed polarisers, that most of the droplets appeared as bright circles with few isogyres. This shows the droplets were in a very specific orientation with respect to the crossed polarisers, and for the majority of droplets to have this specific orientation, rather than a population of randomly oriented droplets, as in section 3.2, Figure 46 and Figure 47, which were not subjected to a magnetic field, shows that the majority of droplets in each population had become aligned with their polar axes pointing in a common direction. The alignment was not perfect as seen by some droplets exhibiting different textures however this could be due to agitation upon moving from the stacked magnets to the microscope stage for imaging.

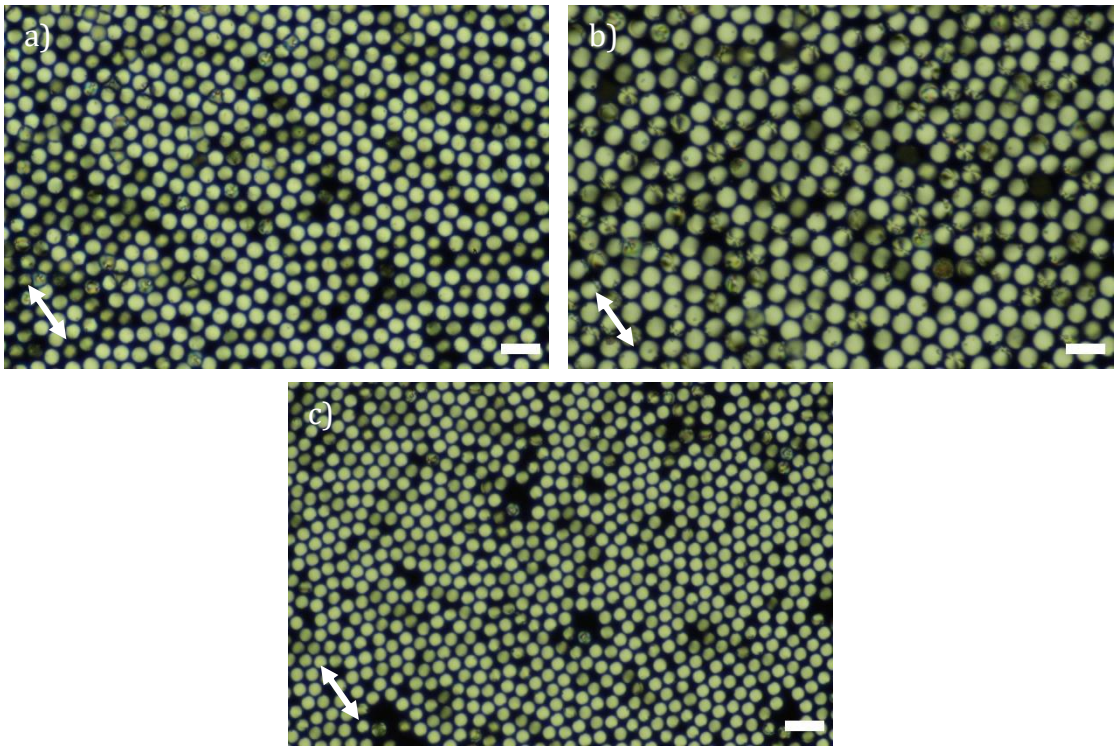

Figure 69: Polarised photomicrographs of bipolar nematic droplets of **M1** from experiment **M1-MF97** (a), **M2** from **M2-MF89** (b) and **M3** from **M3-MF87** (c). Droplets had been aligned by swirling on top of three stacked N42 bar magnets. Taken in transmission mode at 200x magnification, scale bars 50 μm. Arrows denote magnetic field direction.
Average diameters: 23 μm (a), 30 μm (b) and 19 μm (c).

Isotropic **M1** droplets containing chloroform were also placed upon the top of three stacked N42 bar magnets during solvent evaporation. As the solvent evaporated the dishes were swirled to agitate the sample into forming a monolayer. During the final stages of solvent evaporation, a nematic texture developed in the presence of the magnetic field. Figure 70 shows a POM photomicrograph of the resulting droplets. The nematic texture which developed looked mostly uniform across the sample, similar to the nematic droplets agitated in the presence of a magnetic field. Again, indicating a common orientation of droplets within the population of **M1** nematic droplets, suggesting the presence of the magnetic field led to polar axes alignment.

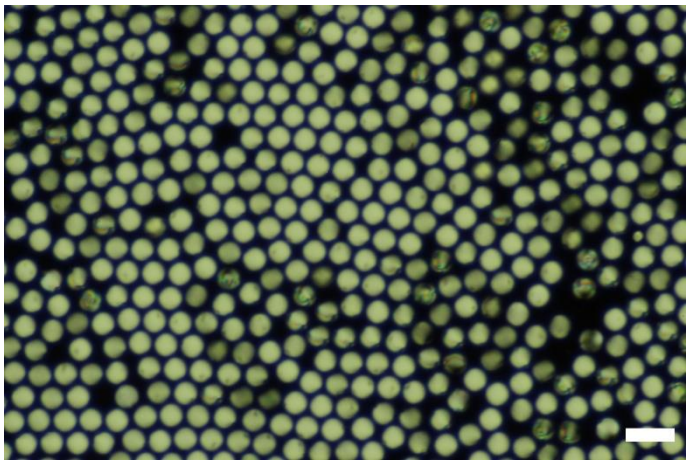

Figure 70: Polarised photomicrograph of bipolar nematic droplets of **M1** from experiment **M1-MF83**. Solvent evaporation of chloroform from isotropic droplets had been carried out on top of three stacked N42 bar magnets as the texture developed. Taken in transmission mode at 200x magnification, scale bars 50 μm. Magnetic field direction not noted. Average diameters: 27 μm.

In the previous two figures, the droplets had been imaged with the magnetic field direction, which the dish had been aligned to, slightly rotated which gave rise to the presence of very minimal texture features aside from the bright birefringence of the droplet. In order to promote more prominent texture features, rotation of the samples with respect to the crossed polarisers was employed. Figure 71 shows droplets of **M3** which had been aligned with the magnetic field in the same direction in photomicrographs in Figure 69. The microscope stage was then rotated 10° in each of the photomicrographs which followed (b – s) through 180° in total. As the crossed polarisers were fixed vertically and horizontally with respect to the plane of observation it could be seen that the nematic texture changed through the rotation. Notably, the majority of the droplets changed together further reinforcing the idea that the polar axes are aligned in the sample. The droplets went from their brightest birefringence at 0° through to their dimmest at around 90° as mesogens align with the polarisers, back to their brightest again at 180° due to the symmetry of the bipolar texture.

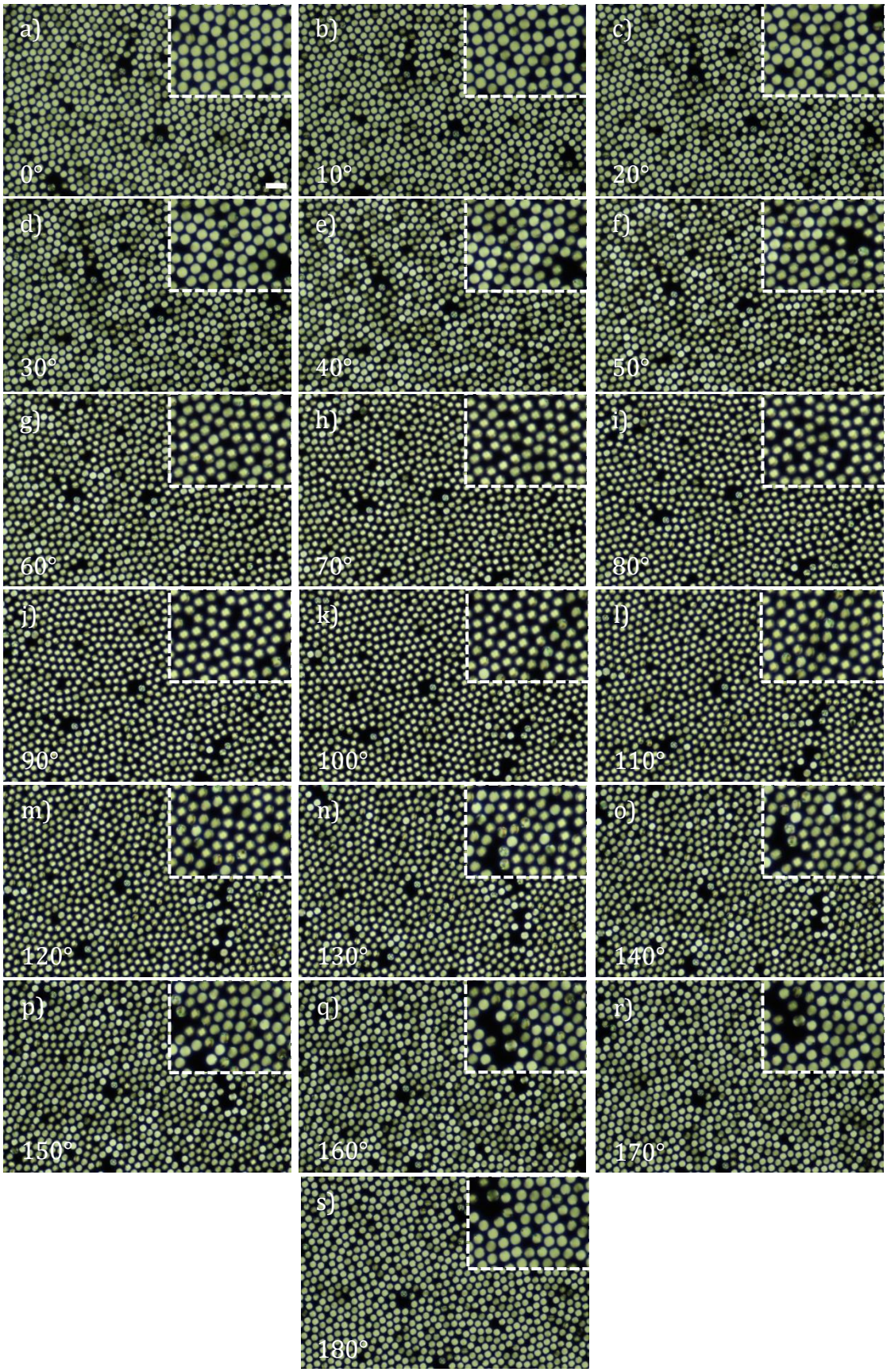

Figure 71: Polarised photomicrographs taken in transmission mode of bipolar nematic droplets of **M3** from experiment **M3-MF87** at 200x magnification, highlighted area zoomed in by 1.5x, scale bar 50 μm. The sample was rotated anticlockwise by 10° between photomicrographs. Average diameters: 19 μm.

In addition, droplets which were subjected to a magnetic field post-solvent evaporation by agitation atop of the stacked magnets, were zoomed in upon and rotated with respect to crossed polarisers to confirm the droplet orientation with respect to the magnetic field. Figure 72 shows photomicrographs and cartoon representations beneath each photo indicating the polar direction, elucidated by the position of isogyres and in some cases visible defects through imaging under crossed polarisers. In these samples of droplets and across all magnetically aligned samples, it was observed that the majority of droplets within the population displayed a common texture evolution upon rotation. The orientation of the droplets clearly corresponded with the magnetic field line orientation through samples (as denoted in the polarised images by the yellow arrows). This shows that the magnetic field aligned the droplets so that the polar axes pointed in the same direction as the magnetic poles.

As mesogens are diamagnetic and have diamagnetic anisotropy, they have a preferential axis to align with the magnetic field.[3,8,162] When the diamagnetic anisotropy is positive, which is usual for calamitic nematic systems like **M1**, **M2** and **M3**, the free energy of the system within a magnetic field is reduced by aligning the director parallel to the magnetic field.[8–10] When confined within a bipolar droplet the overall director follows the polar axis, so to retain the energetically favourable bipolar configuration, the polar axis aligns with the field, minimising the free energy contribution of both the elasticity within the bipolar droplets, as well as the contribution of the magnetic field effects on the system. It is unclear whether the bipolar droplets are undergoing an internal director rearrangement or whether the whole droplets are rotating, however it is suggested that both scenarios may be happening in tandem to a certain degree, due to the reliance on the swirling agitation as well as some loss of bipolar alignment, as seen in Figure 71 where rotation through 180° does not result in crossing isogyres. The same results here were seen for all three of the monomers investigated, **M1**, **M2** and **M3**. If the nematic droplets were not agitated, atop of the magnet then randomly oriented polar axes were present, as in non-magnetically aligned systems like those reported in section 3.2, and shown in Figure 46 and Figure 47.

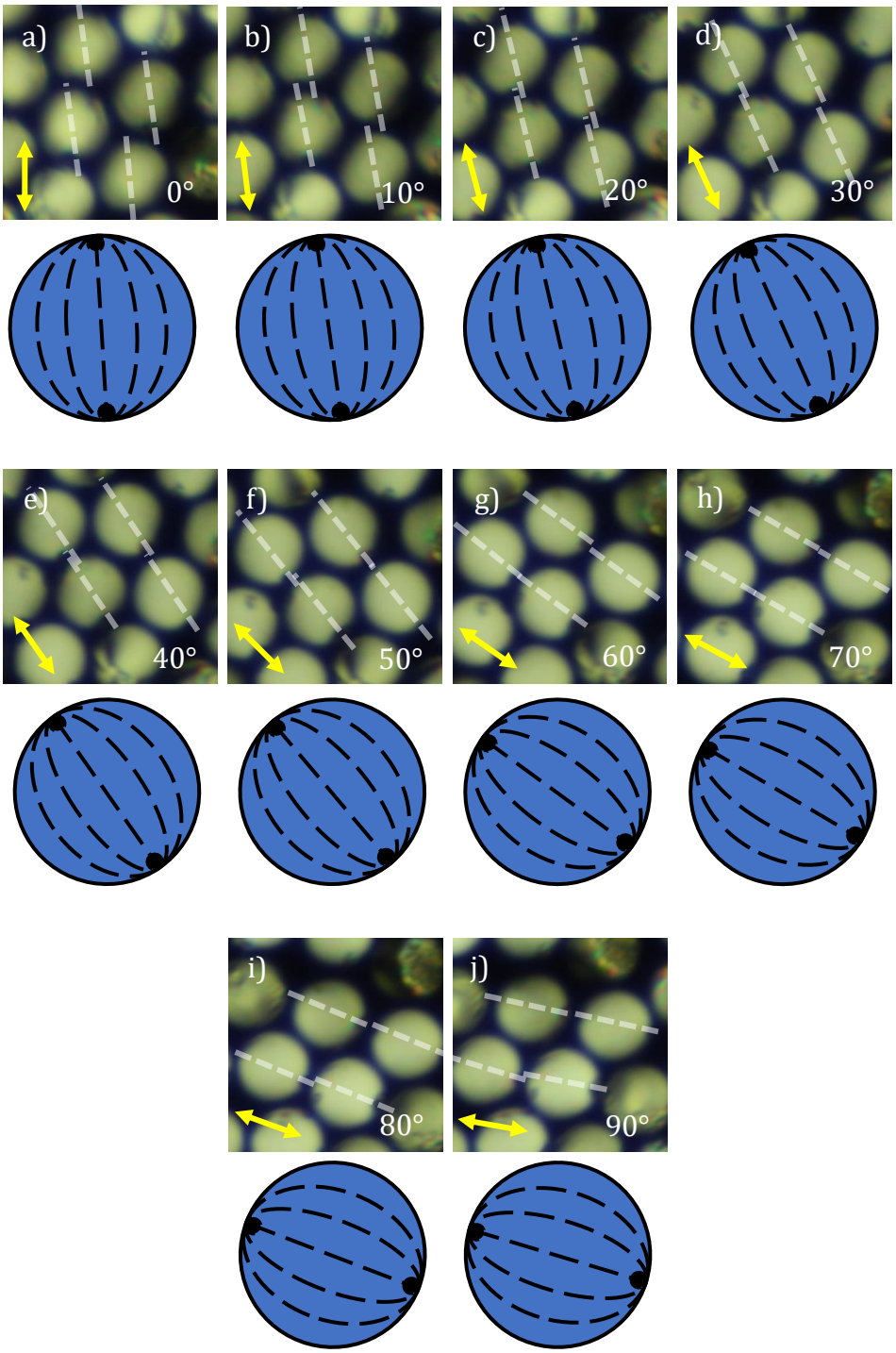

Figure 72: Polarised photomicrograph of an **M2** nematic droplet from **M2-MF89** showing the texture evolution as the droplets were rotated through 180° between the crossed polarisers, which were vertical and horizontal with respect to the plane of observation. Taken in transmission mode at 200x magnification, cropped and zoomed by 1.6x. White dashed lines represent the suggested polar axis and yellow arrows represent the magnetic field direction which the droplets were subjected to. Cartoon representations underneath each photomicrograph display the inferred droplet orientation. Average diameters: 30 μm.

As discussed in the introductory chapter, section 1.2.1.1.2, magnetic anisotropy in mesogens can allow for director alignment with magnetic or electric fields.

Ahmad *et al* report magnetic alignment of monodomain nematic droplets using a weak magnetic field (0.1 Tesla), however this relied on the dispersion of ferromagnetic nanoparticles in the nematic mixture, rather than relying on the magnetic anisotropy of the nematic mesogen itself.[9] Although, magnetic alignment of bulk nematic mixtures, used to produce nematic elastomer pillars was reported by Wei *et al*, using a neodymium magnet of similar strength (1 Tesla).[124] Magnetic alignment of bipolar nematic droplets has seldom been reported in the literature, Candau *et al* predicted and reported the polar axis alignment of bipolar nematic droplets within an emulsion using a 0.1 Tesla magnet on ~<40 μm droplets.[10] Similarly, Krakhaleva *et al* have reported that polar axis alignment occurred in polymer dispersed liquid crystal (PDLC) films of 7 – 20 μm bipolar non-polymerisable droplets with parallel surface anchoring akin to that in this thesis, as well as other surface anchoring conditions, when an electric field of 90 – 250 V was passed through the film.[6,7] This is analogous to our findings for magnetically aligned droplets, albeit the **M1**, **M2** and **M3** droplet have the advantage of not being confined within a PDLC film and have the ability to be polymerised into self-supporting elastomer particles. It is expected that alignment of **M1**, **M2** and **M3** droplets will also be possible under electric fields, unfortunately the equipment required to investigate this was not available to the group during our investigation.

3.4.2 Photopolymerisation of Magnetically Aligned Nematic Droplets

The magnetically aligned droplets, containing **M1** or **M2** with photoinitiator and crosslinker were employed to produce anisometric elastomer microparticles by polymerising the droplets at high intensity, 6 cm away from the UV light source at 100% intensity, at room temperature. Full polymerisation conditions can be found in the experimental chapter (section 7.3.3, Table 15). In order to observe the geometry deformation at the point of polymerisation, the polymerisation was carried out on the microscope and captured in video.

Figure 73 show screenshots from Video 6 (a & b) and Video 7 (c & d) of before and straight after UV irradiation of droplets of **M1** (a & b) and **M2** (c & d). As soon as the UV lamp was turned on, a rapid elongation deformation parallel to the director was observed to produce anisometric spindle shaped particles of either **E1** or **E2**,

as described in section 3.3.2. As the precursor droplets were aligned with a magnetic field (direction indicated by the white arrow), the particles elongated in a common direction to each other within the population. These results confirm that the elongation occurs along the polar axis, providing further evidence for our theory that the elongation occurs to push out the defects from the centre of the forming microparticles as discussed in section 3.3.2.2. As the droplet polar axes can be manipulated using a magnetic field, it is possible that the direction of elongation could occur in any chosen direction. Control of this elongation in an individual microparticle, or as a population of microparticles in this way has not been previously reported and gives rise to promising applications in areas such as micromechanics and soft robotics for example where anisometric particles could act as microactuators or micro stirrers. Polymerisation, and therefore elongation, could be performed in situ to, for example, trap the particles in place or block off channels in microfluidics.

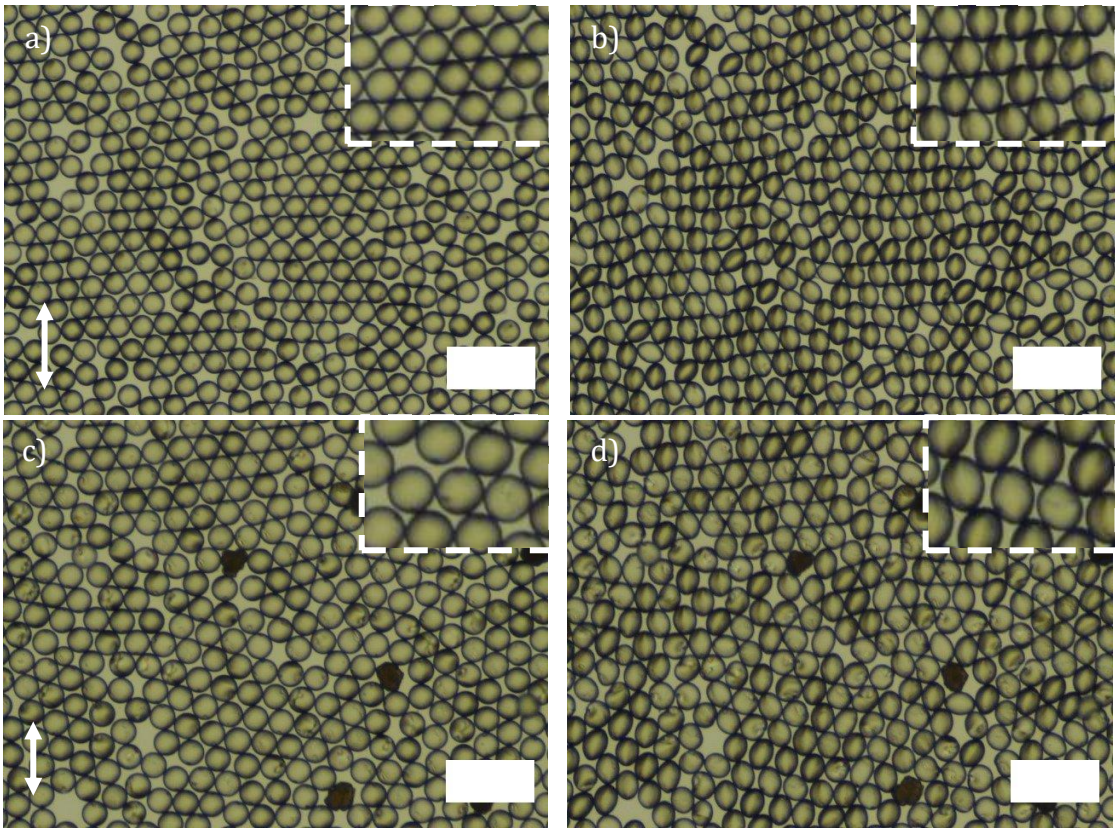

Figure 73: Screenshots from Video 6 (a & b) and Video 7 (c & d) taken in brightfield transmission mode of **E1** (a & b) and **E2** (c & d) elastomer microparticles before (a & c) and 1 second after (b & d) irradiation with UV light from dishes of **E1-MF83** and **E2-MF89** aligned in the magnetic field direction indicated by white arrows. Taken at 200x magnification, scale bars 100 μm, area shown in top right zoomed in by 1.6x. Average diameters: 27 μm (a) and 30 μm (c).

It is worth noting that some crescent shaped **E2** particles can be seen in Figure 73d, it is expected that these were produced due to polymerisation and geometry elongation about a small area of crystallisation.

When looking at the nematic texture of the anisometric microparticles produced from magnetically aligned droplets, shown in the polarised imaging shown in Figure 74, it was not the case that the handedness of bipolar twist was always totally random, as reported in the microparticles described in section 3.3.2.2, Figure 62, which had not been magnetically aligned. When the spindle shaped particles were produced from droplets aligned in a magnetic field it was observed that, particularly in the **E1** sample, one bipolar twist was selected for over the other. This can be seen in the figure as all of the particles in (a) which oriented at a 45° angle were at their brightest, there were no particles pointing in that direction with the opposite handedness as shown by the lack of dark edges of particles oriented at 45°. In **E2** this was also observed to an extent, the particles highlighted in (b) were the only particles of the sample which pointed at 45° and appeared with dark isogyres around the edge, as opposed to in section 3.3.2.2, Figure 62. where only a small selection were highlighted. There is clearly a preference in both samples produced from magnetically aligned droplets for one handedness of bipolar twist over the other handedness, this likely arises from unsymmetrical alignment of the magnetically aligned droplets, as discussed in the previous subsection.

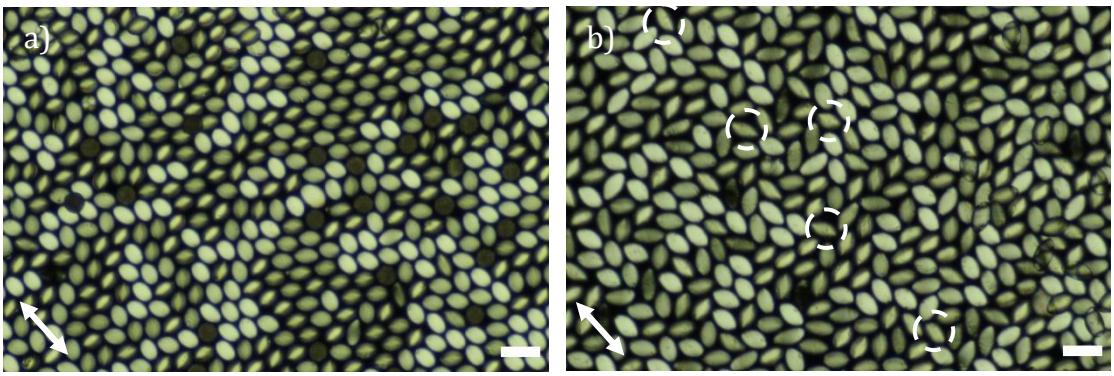

Figure 74: Polarised photomicrographs of nematic elastomer microparticles of **E1** from **E1-MF83** (a) and **E2** from **E2-MF80** (b). Taken at 200x magnification, scale bars 50 μm. Circles indicate particles oriented at a 45° angle (↖) where white circles show particles with the dark edged birefringence. Droplets were aligned prior to polymerisation with a magnetic field, white arrows indicate the field direction.

It is expected that if the bipolar twist handedness had been selected for using magnetic alignment, then a common wrinkle twist direction would also be promoted, suggesting deeper control of the surface morphology in nematic elastomer particles could be possible.

3.4.3 Response of Nematic Elastomer Microparticles to a Magnetic Field

Due to the successes of aligning nematic droplets with a magnetic field, the effects of a magnetic field on bipolar nematic elastomer microparticles was investigated. Dishes containing nematic elastomer microparticles of **E1** and **E2** in the outer fluid of PVA in water were placed on top of a N42 diametrically magnetised neodymium ring magnet so that the magnetic field would pass through dishes parallel to their base. It was possible to image the microparticles whilst they were within the magnetic field as a ring magnet was utilised which was placed on the microscope with the sample on top of it.

Video 8 shows **E1** particles placed on top of the magnet, which had its magnetic polar axis aligned horizontally with respect to the plane of observation, at 64x speed, over 30 minutes real time. Over the 30 minutes, the majority of the randomly oriented spindle shaped particles rotated to align horizontally with the magnetic field. Figure 75a & b shows screenshots taken straight after placing on the magnet and 30 minutes later, where the common particle direction can be seen. The magnet was then rotated by 90° to be vertical with respect to the plane of observation. Photos were taken every minute and a video time lapse produced, seen in Video 9. Figure 75c & d show the first and last photomicrographs taken over 30 minutes after rotating the magnet. The microparticles rotated to align with the rotated magnetic field in ~15 – 30 minutes. The particles in the samples in brightfield microscopy appeared to be either light coloured or with dark edges, this corresponds to the internal alignment, as seen under polarised imaging in Figure 74 of this section, and polarised imaging in section 3.3.2. This is a product of the anisotropic refractive indices which produce birefringence under polarised imaging. In a separate experiment, the magnet was rotated ~180° (time lapse Video 10) showing this time the particles did not rotate 180°, as the nematic polar axes were already aligned with the magnetic field (some very slight rotation was

observed as the magnet was not turned a perfect 180°; due to movement in the dispersion medium the particles appear to go out of focus). Figure 75e & f shows the initial and final orientations of particles where the magnetic field was rotated 180°. It is clear that it is the nematic polar axis of the particles which aligns with the magnetic field due to the orientation of the particles being observed as parallel with the magnetic field. The magnetic field is thus strong enough to move the particles through the outer fluid (PVA in water).

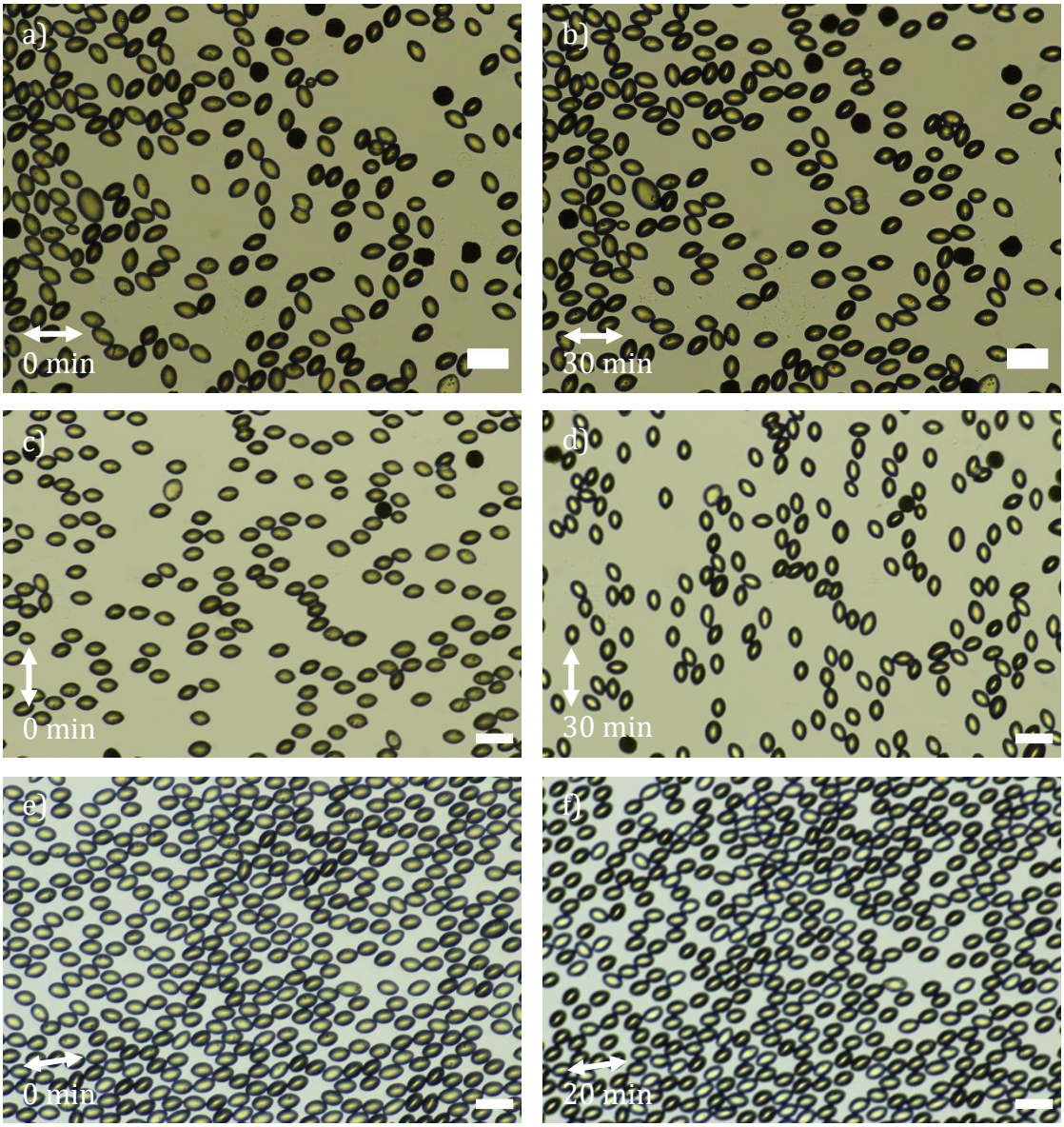

Figure 75: Video screenshots from Video 8 (a & b) and photomicrographs (c – f) taken in brightfield transmission mode of **E1** particles from **E1-MF85** (a – d) and **E1-MF97** (e – f). Particles aligned with magnetic field direction, indicated by white arrows, between (a & b) where a magnet was introduced and (c & d) where a magnet was rotated 90°, but there was little change between (e & f) after magnetic field was rotated 180°. Taken at 200x magnification, scale bars 50 μm.

Elongated spindle shaped nematic elastomer microparticles of **E2** exhibited comparable behaviour to their **E1** counterparts. Video 11 shows **E2** particles, again, aligned with the magnetic field which was oriented vertically in ~15 minutes, also shown in screenshots Figure 76a & b. The magnetic field was then rotated 90° but this time an area of the dish was imaged which had a domain of dense-packing as well as more spread out particles. Video 12, and Figure 76c & d, show the result of rotating the magnetic field 90° to be horizontal with respect to the plane of observation. It was observed that the particles within the densely packed area failed to align with the field, likely due to the force exerted by the magnetic field not being strong enough to overcome the friction of particles pushing past one another. However, particles which were more spread out did align with the field after ~15 minutes. Lastly, a time lapse was taken of particles placed in the magnetic field which had been rotated 180° which can be seen in Video 13 with the initial and final photomicrographs shown in Figure 76e & f. It was observed that whilst the majority of spindle shaped particles did not rotate with the magnetic field due to their polar symmetry, the crescent shaped particles which resulted from initial crystallisation of droplets during polymerisation, did rotate 180° due to the loss of symmetry about the bend of the microparticle.

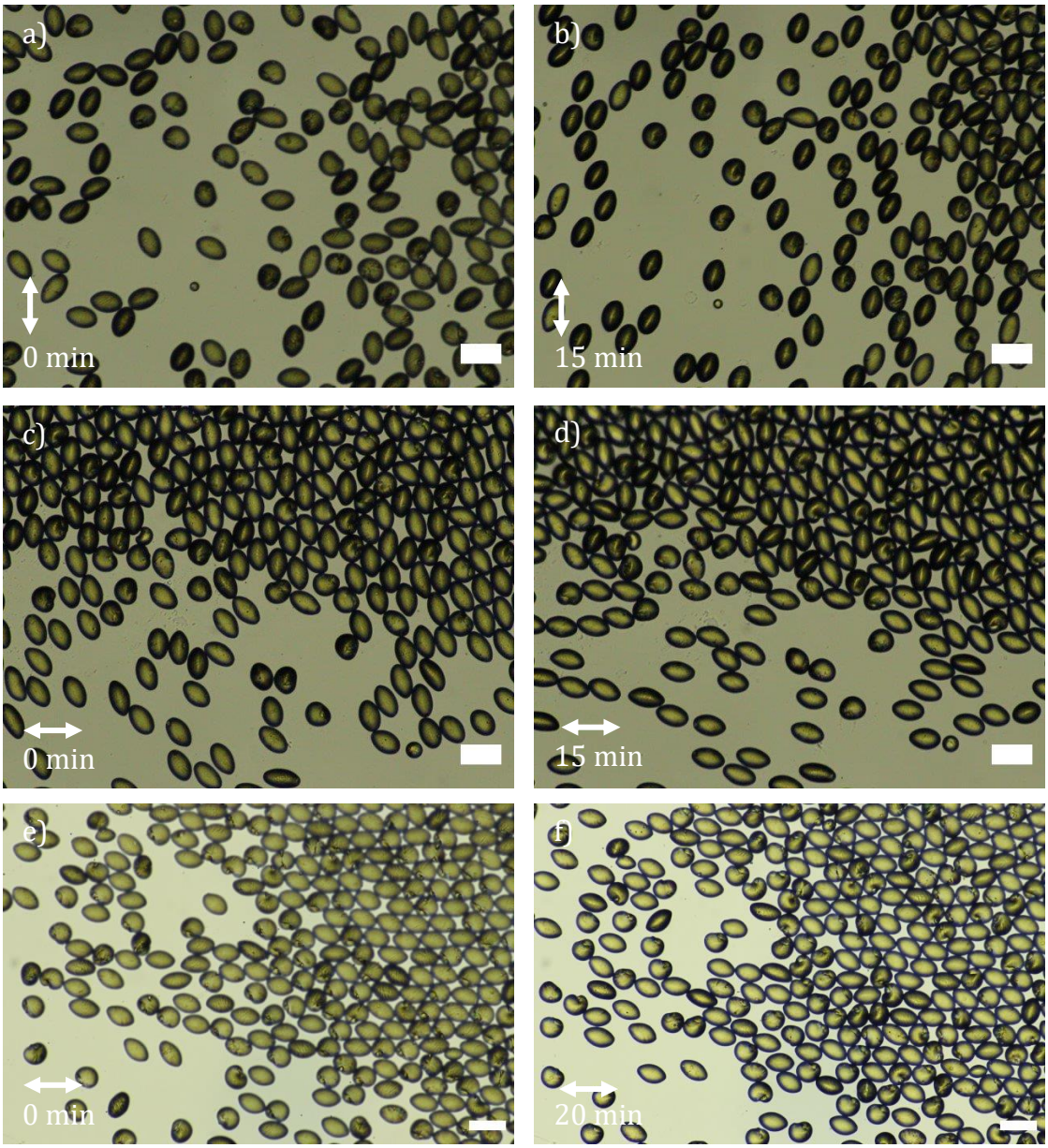

Figure 76: Video screenshots from Video 11 (a & b) and Video 12 (c & c) and photomicrographs (e & f) taken in brightfield transmission mode of **E2** particles from **E2-MF88**. Particles aligned with magnetic field direction, indicated by white arrows, between (a & b) where a magnet was introduced and (c & d) where a magnet was rotated 90°, but there was little change between elongated particles in (e & f) after magnetic field was rotated 180° although crescent shaped particles did rotate. Taken at 200x magnification, scale bars 50 µm.

Several magneto active elastomers have been reported in the literature, however the majority are nanocomposites to introduce magnetic nanoparticles into the nematic elastomer.[163–166] In the literature, the magnetic anisotropy of materials has been exploited to align non-liquid crystalline polymer fibres such as 30 µm diameter polyethylene fibres and 10 µm diameter carbon fibres within magnetic fields.[167] Furthermore, fragments of nematic elastomer film have also been

reportedly aligned within a magnetic field to allow for common director orientation within the population of fragments.[168] It is thought that the same driving force for droplet polar axis alignment is at play in the microparticle rotations described here. As the anisometric elastomer microparticles are diamagnetic, the magnetic field promotes alignment of the molecular axes, and therefore overall director, to be parallel with the field as this represents the lowest free energy configuration of the particles within the field. As the mesogen cannot reorient within the elastomer, which likely would not occur anyway so as to not disrupt the twisted bipolar configuration, the whole particle must rotate to align the polar axes parallel with the field. This ability to rotate anisometric particles using an external field further gives rise to their use within applications as micro stirrers within microfluidics or micromechanics. To the best of our knowledge there are no reports in the literature of the magnetic response of anisometric nematic liquid crystal elastomer microparticles, and so the results here are likely a first within the field.

Overall, the alignment of anisotropic **M1**, **M2** and **M3** droplet polar axes in a population was found to be controllable with a magnetic field to produce samples of droplets in densely packed monolayers oriented in one common direction. Hexagonal magnetically aligned arrangements of bipolar droplets could be transformed instantaneously into arrays of spindle shaped liquid crystal elastomer microparticles where all long axes pointed in a common direction. When magnetically aligned droplets were polymerised, it was found that a bipolar twist direction was selected for, likely due to some loss of bipolar alignment pre-polymerisation, making the configuration unsymmetrical.

Remarkably, the orientation of the spindle shaped particles of **E1** and **E2** was found to also be responsive to an external magnetic field. The orientation of particles could be manipulated by introducing and rotating a magnetic field, producing populations of elongated particles pointing in, and rotating to align with, a common direction which could give rise to their use as micro stirrers in micromechanics. To the best of our knowledge there are no reports in the literature of anisometric particles with ordered axes allowing for this

unprecedented manipulation of ordered arrays *via* the exploitation of defect alignment.

3.5 Conclusion

To conclude, several bipolar nematic systems have been investigated here for their characterisation and responsivity to external fields. Bipolar nematic droplets were produced of **M1**, **M2** and **M3** in particularly small and monodisperse populations with CVs as low as 0.8% compared to literature values for similar sized droplets reported as '<3%'.[42,114,121] During production of droplets, the solvent evaporation stage was carefully controlled to produce nematic droplets with excellent bipolar alignment.

The bipolar nematic droplets were polymerised, preserving the texture to an extent, although disruption to the texture was observed, likely caused by shrinkage and geometry deformation. Despite the texture disruption, parallel alignment appeared to remain present. Bipolar and twisted bipolar nematic elastomer microparticles of various geometries were produced. It was found that for **E1** and **E2**, the intensity of polymerisation had a significant effect on the aspect ratios of the particles produced, whereas the effect of polymerisation temperature was unclear. At very high polymerisation intensities, highly anisometric spindle shaped nematic elastomer particles could be produced reliably in monodisperse populations. The particles had a twisted bipolar nematic configuration with both twist directions being present. The actuation response of **E1** and **E2** nematic elastomer microparticles was investigated and it was found that the responses were comparable with those previously reported in the group.[51] The actuation response seen in anisometric particles of **E1** and **E2** gives rise to possible applications within micromechanics as microactuators, sensors or in soft robotics.[29,145,146]

Anisometric particles exhibited surface wrinkling, possibly due to polymerisation of the droplet surface more rapidly than the inside of the droplet. Wrinkling could be intensified by polymerisation at higher temperatures. Notably, the surface wrinkling on the microparticles was anisotropic in that it was directional, which was controllable by the internal alignment of the microparticles. Hence, twisted

bipolar anisometric elastomer microparticles exhibited periodic, twisted wrinkling around the microparticle, something that would be extremely difficult to achieve in an isotropic system. This anisotropic wrinkling could lend to applications in templating, micromechanics or microfluidics, perhaps increasing grip or directing flows.[154,161]

Finally, the response of nematic droplets and elastomer microparticles to a magnetic field was reported. It was found that bipolar droplets with aligned polar axes could be produced by the introduction of a magnetic field. Upon polymerisation ordered arrays of anisometric microparticles were exhibited, which in turn could be manipulated to rotate the particles in a contactless way, using the magnetic field. To the best of our knowledge, this is a novel response in the field and could broaden the nematic elastomer microparticles' applications in micromechanics as not only microactuators, but also particles capable of moving in alternative arrangements, for example as micro stirrers.

4 Nanoparticle Infiltrated Bipolar Systems

4.1 Overview

The heavily investigated field of nanomaterials has recently been combined with liquid crystal research in the development of nanoparticle infiltrated liquid crystal systems.[43,44,85,87,125] In this chapter, an investigation into the incorporation of nanoparticles into the topological defects of micrometre sized elastomer particles in a controlled way is discussed, alongside the resulting properties of the nanoparticle infiltrated elastomers.

Two of the monomers investigated in the previous chapters, **M1** and **M3**, were utilised in the investigation for their thermal properties which allow for droplets and particles to exhibit a bipolar configuration at room temperature (discussed in chapter 3), and, in the case of **E1**, proven actuation response to temperature change. As well as these monomers, 5CB was utilised to produce non-polymerisable bipolar nematic droplets whilst developing methods for nanoparticle infiltration.

In the remainder of this thesis the term nanoparticles will be used to describe any spherical particle with a diameter of 1 μm or less. Fluorescent nanoparticles were selected for observation of nanoparticle localisation within nematic droplets using fluorescence microscopy.[43,85,87] Amine and sulfate modified fluorescent polystyrene nanoparticles, with diameters of 1.0 μm and 0.5 μm respectively, were initially selected due to their commercial availability and a previously reported successful infiltration of nematic bipolar droplets, composed of either 5CB and mixtures of 5CB with RM257, by Mondiot *et al*.[85] In addition, in the literature, smaller particles of 200 nm did not localise into topological defects,[87] thus larger particles were selected. Polystyrene nanoparticles were chosen over silica nanoparticles as the polystyrene surface promotes homogeneous alignment and are compatible with the polymer elastomer particles in the literature, whereas for these properties in silica particles, further surface treatment steps are required. Later in this chapter, surface modification of nanoparticles is discussed to introduce a chemically bound fluorescent moiety.

In this chapter the term 'fluorescence photomicrograph' refers to photomicrographs obtained by during fluorescence microscopy. In fluorescence microscopy the sample is irradiated with specific wavelengths of light using filters in reflectance mode to excite fluorophores. The reflected light then passes through another filter so that only the wavelengths of light that the fluorophore emits are observed. The images were either produced in greyscale and edited to be coloured green or they were produced in colour. Hence, as the fluorophores used in this chapter emit green light, green areas on these photomicrographs occur due to fluorescence.

4.2 Nanoparticle Containing Bipolar Nematic Droplets

4.2.1 Nanoparticle Infiltration of Bipolar Nematic Droplets by Post-production Methods

Nanoparticle infiltration of droplets was first attempted by the introduction of nanoparticles after isotropic or nematic droplets had been produced, in post-production steps. With the aim of producing droplets containing up to two nanoparticles, a series of experiments were performed where the nanoparticle concentration was varied from high to very low, the minimum, two nanoparticles per nematic droplet, being determined as follows.

The volume of an individual droplet (V_d / μm^3) was found using Equation 13 where r is the droplet radius (μm). The number of droplets collected (n_d) was then found using Equation 14, where V_i is the volume of inner phase collected (μL). The volume of the nanoparticle suspension required (V_{NP} / μL) for a x : 1 nanoparticle to microdroplet ratio was then found using Equation 15, where [NP] is the nanoparticle suspension concentration as supplied (particles/μL).

$$V_d = \frac{4}{3}\pi r^3$$

Equation 13: To calculate the volume of individual droplets.

$$n_d = \frac{V_i}{V_d \times 10^{-9}}$$

Equation 14: To calculate the number of droplets collected.

$$V_{NP} = \frac{x \times n_d}{[NP] \times 10^{-3}}$$

Equation 15: To calculate the volume of nanoparticle suspension required to produce a nanoparticle to microdroplet ratio of x : 1.

The corresponding ratio of nanoparticles to nematic droplets was found from the supplier's nanoparticle suspension concentration and the estimated number of droplets produced. This ratio has been reported for each infiltration attempt in Table 3.

Table 3 shows that several methods were investigated for nanoparticle infiltration of bipolar nematic droplets. All investigated non-microfluidic post-production methods were based upon the method presented in the only literature example of successful infiltration of a 5CB bipolar nematic droplet and a polymerised particle composed of a mixture of RM257 and 5CB, where two nanoparticles localised, one in each pole, as performed by Mondiot *et al*.[85]

Table 3: Details of the type, ratio and post-production method of addition of crosslinked polystyrene nanoparticles to nematic microdroplets. Addition methods A – D are defined in the body text which follows.

Identifier	Nanoparticle Diameter (μm)	Nanoparticle Surface Groups	Nanoparticle : Droplet Ratio	Addition Method
M1-MF2a	0.5	Sulfate	Excess (0.01 wt%)	A
M1-MF2b	0.5	Sulfate	Excess (0.01 wt%)	A
M1-MF3a	0.5	Sulfate	Excess (0.01 wt%)	A
M1-MF3b	1.0	Amine	Excess (0.01 wt%)	A
M1-MF5a	1.0	Amine	Excess (0.01 wt%)	A
M1-MF5b	1.0	Amine	Excess (0.01 wt%)	A
M1-MF5c	1.0	Amine	Excess (0.01 wt%)	A
M1-MF5d	1.0	Amine	Excess (0.01 wt%)	A
M1-MF5e	1.0	Amine	Excess (0.01 wt%)	A
5CB-SM1a	1.0	Amine	Excess (0.01 wt%)	B
5CB-SM1b	0.5	Sulfate	Excess (0.01 wt%)	B
5CB-SM2a	1.0	Amine	2 : 1	B
5CB-SM2b	0.5	Sulfate	2 : 1	B
5CB-MF11a	1.0	Amine	2 : 1	C
5CB-MF11b	0.5	Sulfate	2 : 1	C
5CB-MF11c	0.5	Sulfate	4 : 1	C
5CB-MF11d	1.0	Amine	4 : 1	C
5CB-MF14a	1.0	Amine	2 : 1	C
5CB-MF14b	1.0	Amine	4 : 1	C
5CB-MF14c	1.0	Amine	8 : 1	C
M3-MF21a	1.0	Amine	4 : 1	D
M3-MF21b	0.5	Sulfate	4 : 1	D
M3-MF25a	1.0	Amine	4 : 1	D
M3-MF25b	1.0	Amine	4 : 1	D

For method A, droplets of **M1** were produced by microfluidics and the nanoparticles were added to collection dishes before the solvent evaporation stage. It was thought that adding nanoparticles before solvent evaporation would allow for them to enter droplets as the nematic texture developed, driven by the

diffusion of the polystyrene nanoparticles from the polar aqueous outer fluid to the less polar chloroform droplets. As the nanoparticles would be added whilst the chloroform evaporated from droplets, no liquid crystalline order, and thus no elastic deformation, would be present, therefore being an energetically favourable method for infiltration into droplets. Figure 77 shows photomicrographs from fluorescence imaging, taken from experiment **M1-MF3a**. It can be seen that samples of nematic droplets which contained no nanoparticles were not fluorescently active under the fluorescence filter set utilised. However, nematic droplets in samples which had nanoparticles added before solvent evaporation were fluorescently active. It was concluded that, due to the long contact time between nanoparticles and droplets during solvent evaporation, the fluorescent dye had leached from the polymer matrix of the nanoparticles into the nematic droplets[85] and hence the whole nematic droplets exhibited fluorescence. This made determining the number of nanoparticles and their location within bipolar nematic droplets impossible.

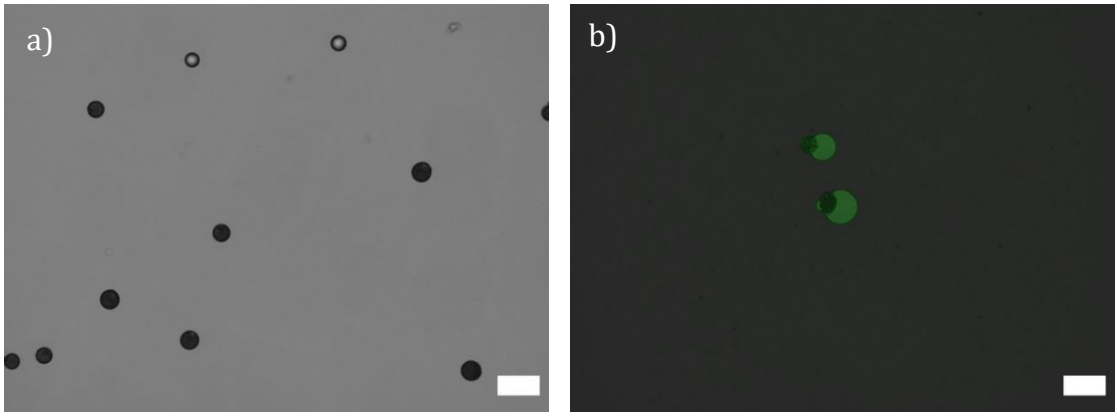

Figure 77: Fluorescence photomicrographs (coloured green) overlaid with greyscale brightfield photomicrographs of nematic **M1** droplets infiltrated no nanoparticles from **M1-MF3** (a) and infiltrated with 0.5 μm sulfate modified polystyrene nanoparticles from **M1-MF3a** (b). Taken at 200x magnification, scale bars 50 μm. Dark spots on droplets are contamination of the sample. Average diameters: 22 μm.

Although the manufacturer would not divulge which dye was present in these nanoparticles, the excitation and emission properties suggest it may be a common fluorescent dye known as DiO, the molecular structure is shown in Figure 78. The leaching occurred as the dye was not bound to the polystyrene particles, and so in chloroform the polystyrene particles swell, releasing the dye into the chloroform

droplets in which the dye is soluble. Leaching is not an issue in aqueous suspension, as water does not swell the polymer particles.

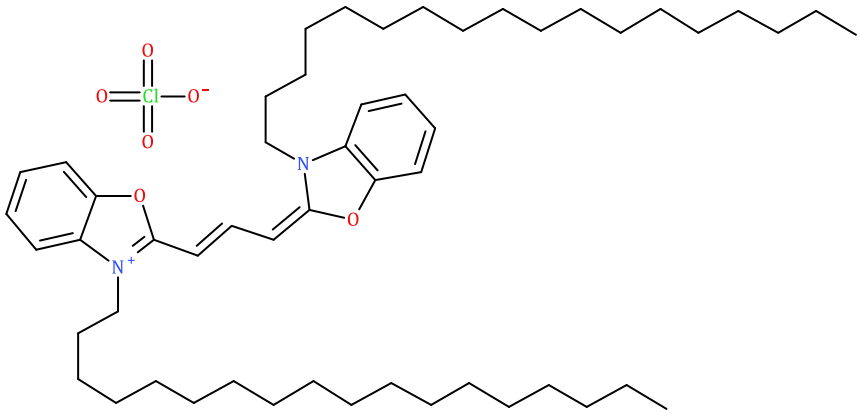

Figure 78: Molecular structure of fluorescent dye DiO.

In an attempt to avoid the dye leaching issues, method B was investigated. In method B, droplets of 5CB were produced by the suspension method, full details can be found in the experimental chapter (section 7.3.2.1, Table 13). Nanoparticles were added to a water/glycerol solution in high excess, at 0.01 wt%. The nanoparticle suspension was then used as a dispersion medium for nematic droplet production by the suspension method with the water/glycerol solution promoting a bipolar configuration. To the dispersion medium, 5CB was added and the resulting mixture was agitated by rapid shaking for 1 minute. A bipolar nematic configuration was confirmed as the baseball texture was observed by imaging droplets under POM, as seen in Figure 79. Whilst the average diameters were within a reasonable range, for **5CB-SM1** and **5CB-SM2** 27 µm and 25 µm respectively, a very large droplet size distribution was present as expected when employing the suspension droplet production method. For example, experiment **5CB-SM1** saw droplets in the range of 3 to 104 µm with a CV of 73.9%.

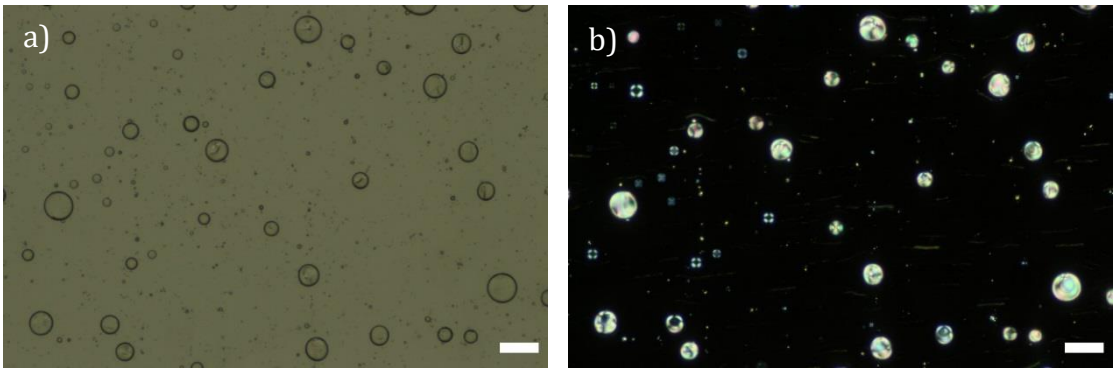

Figure 79: Brightfield (a) and polarised (b) photomicrographs, taken in transmission mode, of nematic droplets from **5CB-SM1** at 100x magnification, scale bars 100 µm.

The resulting droplets were also imaged under fluorescence microscopy at timed intervals from between 1 and 6 hours after nanoparticle addition. A large number of nanoparticles had infiltrated droplets by 1 hour, and leaching had not occurred to an extent where nanoparticles' location could not be seen, shown in Figure 80a. After 6 hours, individual nanoparticles could no longer be seen and the whole nematic droplet became fluorescently active, as seen in Figure 80b. It was found that in 5CB droplets, nanoparticles could be visualised for approximately 5 hours before the extent of leaching became too much to distinguish individual nanoparticles by fluorescence microscopy. Leaching was slower here than in the previous method as, whilst the dye is still compatible with the 5CB droplet, 5CB does not swell the polymer matrix of the polystyrene nanoparticles as much as in chloroform, hence leaching occurs at a slower rate. Dye leaching was also reported by Mondiot *et al* from fluorescent polystyrene nanoparticles into 5CB droplets.[85]

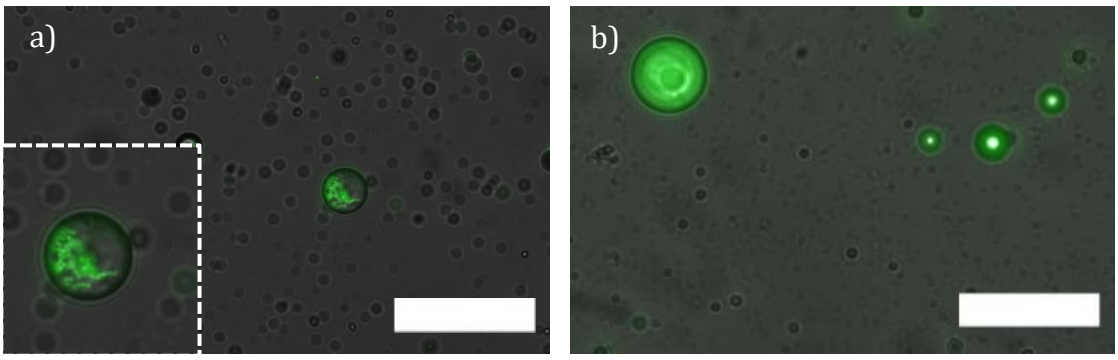

Figure 80: Fluorescence photomicrographs (coloured green) overlaid with greyscale brightfield photomicrographs of nematic 5CB droplets infiltrated with and 1 µm amine modified polystyrene nanoparticles from experiment **5CB-SM1b**, imaged after 1 hour (a) and 6 hours (b) at 400x magnification, zoomed in by 1.7x, highlighted area in (a) zoomed by a further 2x, scale bar 50 µm.

Nanoparticles were also added in the minimum concentration required to infiltrate each droplet with two nanoparticles, a 2 : 1 ratio, as determined by Equation 13 and Equation 14, although accurate calculations were not possible due to the high variance in droplet diameters. A 2 : 1 ratio is the minimum concentration required to infiltrate droplets with one nanoparticle in each pole. However, upon fluorescence imaging, there was no evidence of any nanoparticles infiltrating droplets.

This method proved successful in infiltrating bipolar nematic droplets with nanoparticles at high nanoparticle to droplet ratios, but the same result could not be seen at lower nanoparticle concentrations within the time limitation imposed by dye leaching. It is expected that reducing the polydispersity of droplets and optimisation of the nanoparticle concentration would yield more controllable nanoparticle infiltration rates.

In a further series of experiments (method C) microfluidic nematic droplets of 5CB were produced *via* solvent evaporation as described in the experimental chapter (section 7.3.1.1, Table 11) which exhibit a bipolar texture, as shown in Figure 81c, and a much narrower droplet size distribution, demonstrated in Figure 81d, compared to those produced by the suspension method. For example, droplets produced in experiment **5CB-MF14** had an average diameter of 26 μm with a range from 25 to 27 μm, yielding a more reasonable CV of 1.9%.

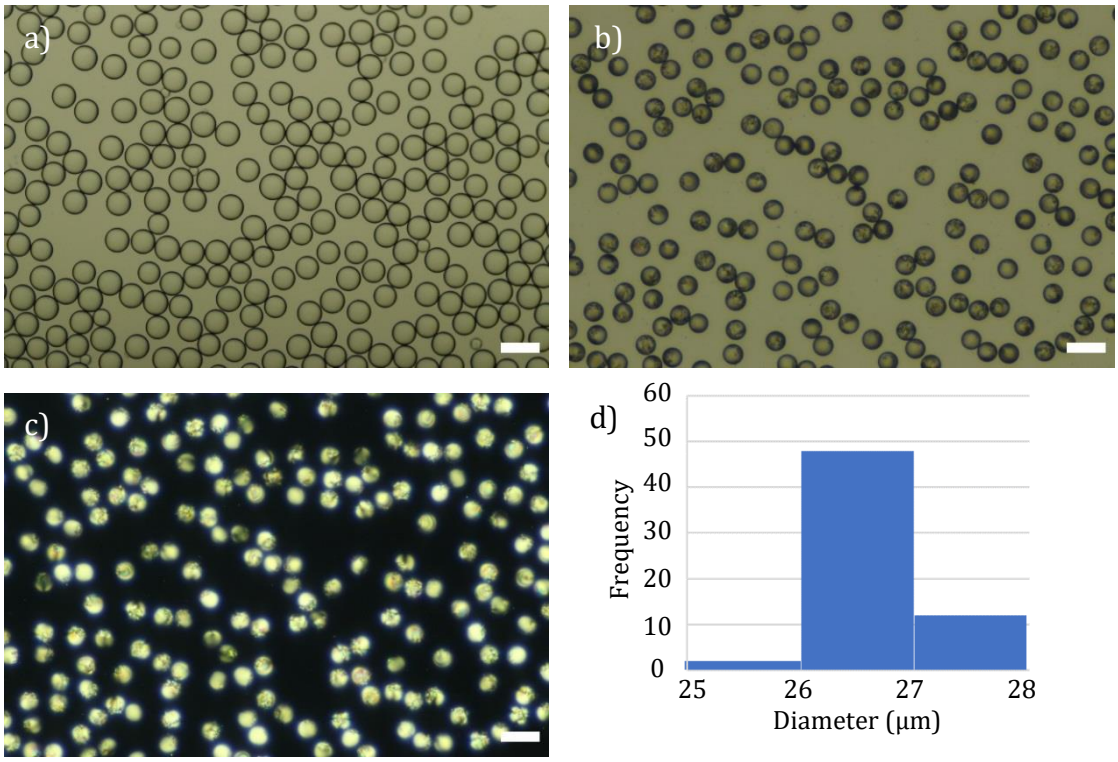

Figure 81: Brightfield photomicrograph, taken in transmission mode, of isotropic droplets at 100x magnification, scale bar 100 µm (a); brightfield (b) and polarised (c) photomicrographs, taken in transmission mode, of bipolar nematic 5CB droplets at 200x magnification, scale bars 50 µm; nematic droplet size distribution graph (d). From experiment **5CB-MF14**. Average diameters: 26 µm.

In a series of experiments, nanoparticles were added to the collection dishes containing nematic droplets, after solvent evaporation. The effect of increasing the nanoparticle to droplet ratio was investigated by utilising ratios of 2 : 1, 4 : 1 and 8 : 1 whilst imaging samples by fluorescence microscopy.

Figure 82a shows that at a ratio of 2 : 1 no infiltration of nematic droplets by nanoparticles occurred over the 3-hour timeframe the droplets were observed for. The nanoparticles remained in the dispersion medium. When observed one hour after addition into the samples, collection dishes containing ratios of 4 : 1 and 8 : 1 nanoparticles to nematic droplets showed similar results, no nematic droplets were observed containing any nanoparticles. However, 3 hours after addition, collection dishes containing ratios of 4 : 1 and 8 : 1 showed some nematic droplets contained singular nanoparticles at the droplet surface. Unfortunately, the fluorescence microscope used in these initial experiments was not equipped to image through crossed polarisers, so the nanoparticles location with respect to the defects could not be determined. These observations showed that ratios of 4 : 1

and 8 : 1 were high enough to infiltrate droplets with singular nanoparticles, but not so high that several nanoparticles infiltrated droplets. Hence, a ratio of 4 : 1 nanoparticles to nematic droplets was deemed the most appropriate for future infiltrations. However, at all of the nanoparticle ratios investigated here, it could be seen that nanoparticles remained in the dispersion medium as slow diffusion had not yet allowed them to reach the droplets. It is expected that if the samples were left for longer, more nanoparticles would infiltrate the droplets. However, as method C relied upon the very slow process of diffusion, increasing the time for nanoparticle infiltration would lead to leaching of dye, making observation under fluorescence microscopy ineffective.

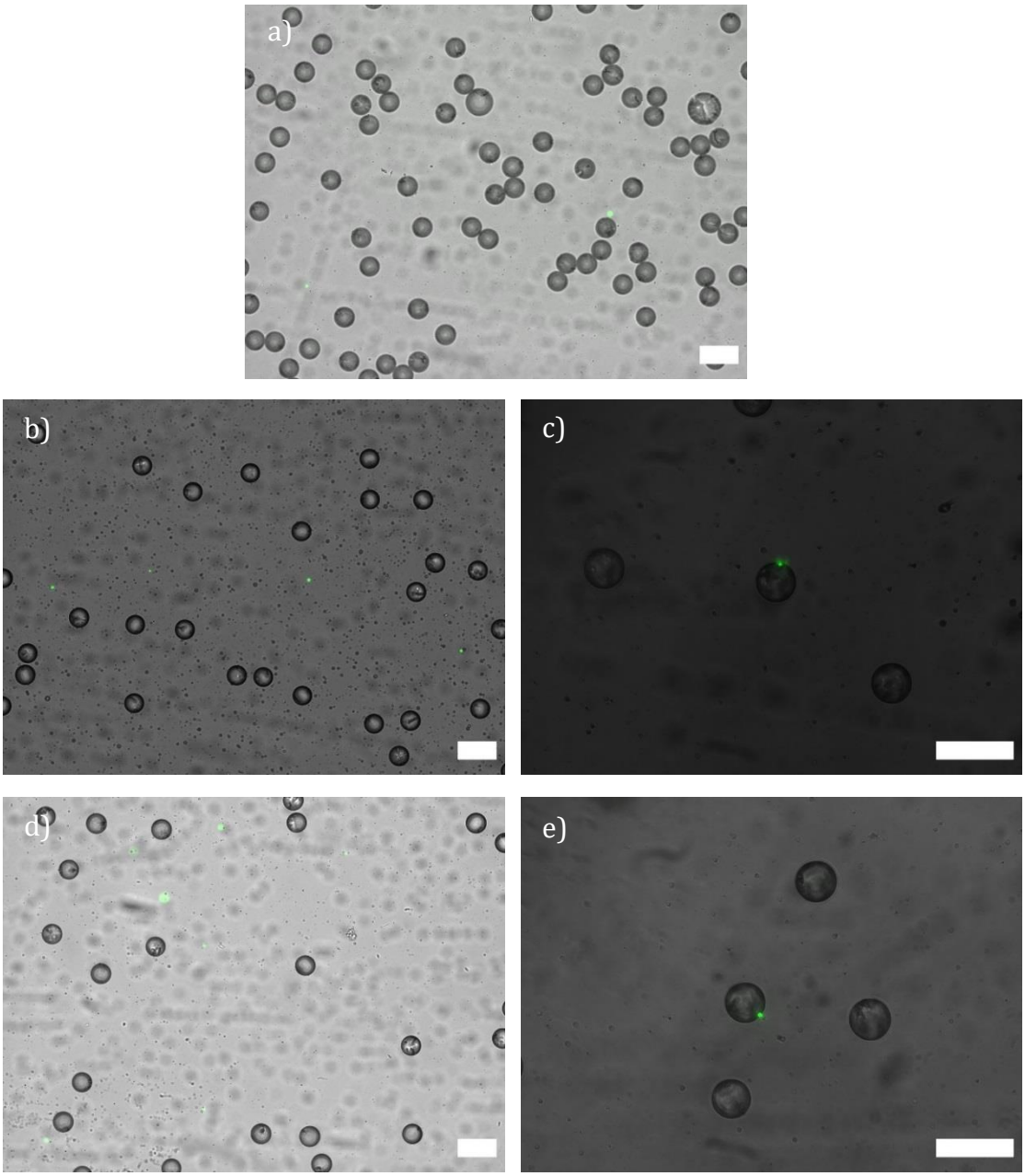

Figure 82: Fluorescence photomicrographs (coloured green) overlaid with greyscale brightfield photomicrographs of nematic 5CB droplets infiltrated nanoparticles in ratios of 2 : 1 (a), 4 : 1 (b & c) and 8 : 1 (d & e) from experiments **5CB-MF14a**, **5CB-MF14b** and **5CB-MF14c**. Imaged after 1 hour (b & d) and 3 hours (a, c & e). 200x magnification (a, b & d), 400x magnification (c & e), all scale bars 50 μm. Average diameters: 26 μm.

Agitation of the sample should increase the probability of a nanoparticle meeting the surface of a droplet by aiding the diffusion of nanoparticles in the sample. Method D followed a similar process to method C, however this time the nematogen was monomer **M3** and agitation was introduced. Bipolar nematic droplets of **M3**, were produced by the microfluidic method as described in chapters 2 and 3. Collection dishes were combined into high-walled vials to which

nanoparticles were added, in 4 : 1 ratio to droplets as this ratio saw success in infiltrating a singular nanoparticle into droplets when employing method C. The vials were subjected to agitation by an orbital shaker plate for one hour at 300 rpm. Vials were used over dishes to prevent spillage and allow for clamping onto the shaker plate which would not have been possible with the glass dishes droplets were produced in.

Upon imaging under fluorescence microscopy, it was clear that the agitation had increased the likelihood of finding nanoparticles within the nematic droplets. Several nematic droplets were observed which had one nanoparticle at the droplet surface. Furthermore, one nematic droplet was observed which contained two nanoparticles on opposite sides of the droplet at its surface, as shown in Figure 83. However, it is important to note that a significant proportion of nematic droplets remained without any nanoparticles infiltrated.

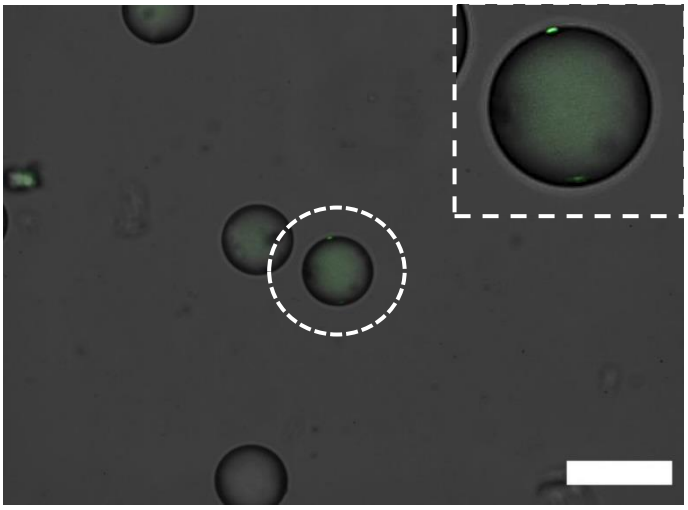

Figure 83: Fluorescence photomicrograph (coloured green) overlaid with greyscale brightfield photomicrograph of a bipolar nematic droplet of **M3** infiltrated with two nanoparticles from experiment **M3-MF21a** at 400x magnification, scale bar 50 μm. Highlighted droplet zoomed in by 2.3x, shown in the top right corner. Average diameters: 34 μm.

In an attempt to identify the optimal agitation time and speed for nanoparticle infiltration of nematic droplets, droplets were shaken with nanoparticles in vials at 200 rpm and 300 rpm. Samples from vials were taken using a pipette and loaded onto slides for imagining under fluorescence microscopy every 30 minutes. The experimental conditions and observations are detailed in Table 4.

Table 4: Details of agitation time and speed of sample agitation with corresponding observations made during fluorescence microscopy from **M3-MF25**. *out of ~hundreds of nematic droplets.

Time (min)	Agitation Speed (rpm)	Droplets Observed Containing 1 Nanoparticle*	Droplets Observed Containing 2 Nanoparticles*	Notes
0.5	200	4	0	Slight dye leaching
	300	1	0	No dye leaching
1	200	3	1	Major dye leaching
	300	6	1	Slight dye leaching
1.5	200	4	0	Major dye leaching
	300	4	3	Major dye leaching
2	200	2	0	Droplets deformed
	300	3	0	Major dye leaching

Due to leaching of dye from nanoparticles, which occurred relatively early compared to experiments without agitation, the number of droplets actually containing one or two nanoparticles was likely higher than the observations detailed in Table 4. However, some information could be inferred from the leaching. The dye leached from nanoparticles within the first half hour of agitation at 200 rpm, whereas this took place between 30 minutes and 1 hour in the samples shaken at 300 rpm. This, and the fact that more droplets could be seen containing one nanoparticle at 200 rpm compared to 300 rpm, suggests that nanoparticles entered droplets sooner when shaken at 200 rpm than they did at 300 rpm. Figure 84 shows nematic droplets of **M3** infiltrated by one nanoparticle after agitation at both 200 and 300 rpm.

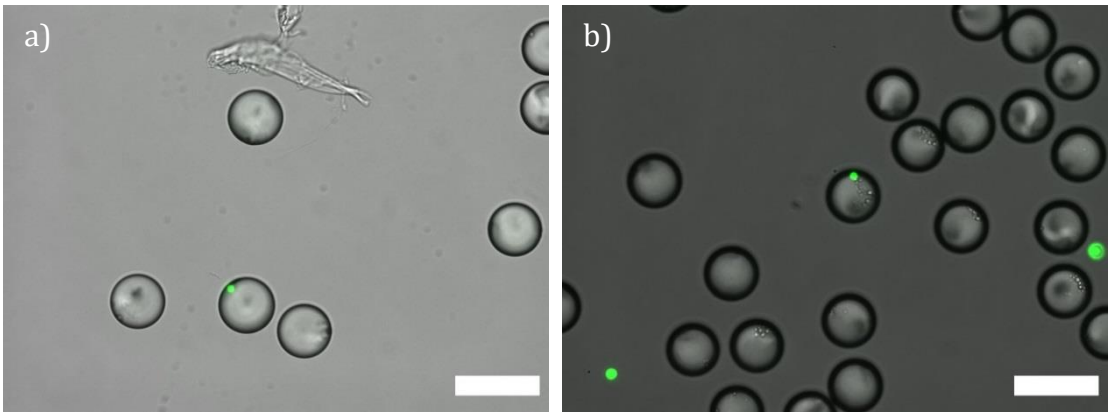

Figure 84: Fluorescence photomicrographs (coloured green) overlaid with greyscale brightfield photomicrographs of bipolar nematic droplets of **M3** infiltrated with up to one 1 nanoparticle after 1.5 hr agitation at 200 rpm (a) and 1 hr agitation at 300 rpm (b). Taken from experiments **M3-MF25a** & **M3-MF25b** at 400x magnification, scale bars 50 µm. Average diameters: 32 µm.

The largest number of nematic droplets containing two nanoparticles was observed after agitation at 300 rpm for 1.5 hours (Figure 85), suggesting that the optimum conditions were agitation at 300 rpm for 1 – 1.5 hours. However as major leaching had occurred in both samples by then, it is unclear whether there were more droplets containing 2 nanoparticles which could not be seen.

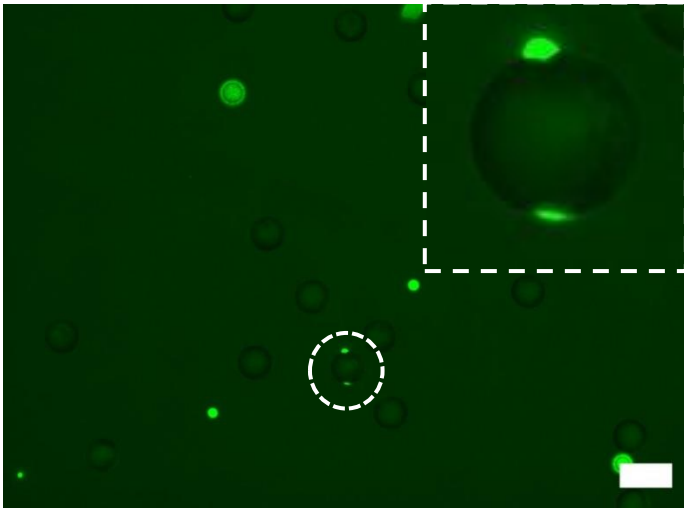

Figure 85: Fluorescence photomicrograph of bipolar nematic **M3** droplets in **M3-MF25a** after 1.5 hr agitation at 300 rpm. Photomicrograph coloured green and the colour saturated to see droplet boundaries. Taken at 200x magnification, scale bar 50 µm. Highlighted droplets zoomed in by 5x, shown in top right corner. Average diameters: 32 µm.

After 2 hours of agitation at 200 rpm, it was observed that droplets had deformed, as seen in Figure 86, this was likely due to a degree of photopolymerisation of the droplets, caused by exposure to ambient light.

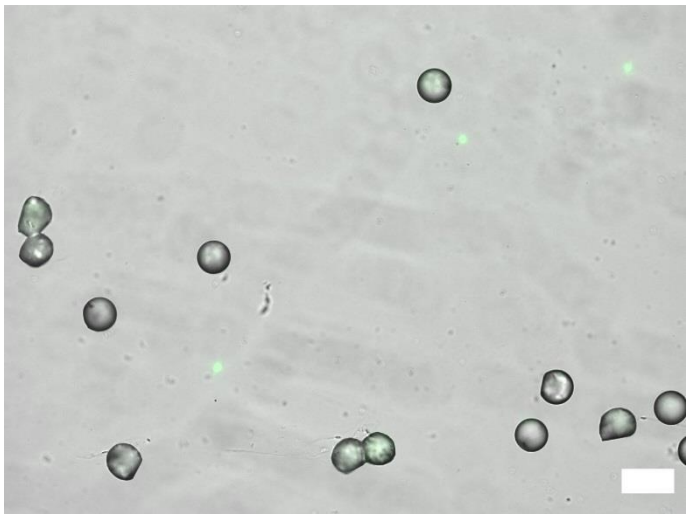

Figure 86: Fluorescence photomicrograph (coloured green) overlaid with greyscale brightfield photomicrograph showing the deformation of bipolar nematic droplets of **M3** infiltrated after 2 hr agitation at 200 rpm in experiment **M3-MF25b** taken at 200x magnification, scale bar 50 μm. Average diameters: 32 μm.

It is clear this last method variation was the most successful investigated for nanoparticle infiltration of nematic droplets as droplets containing two nanoparticles, at opposite sides of the droplet, were observed. Furthermore, this result was repeated for a number of samples. Although, results show that only a small proportion of droplets were infiltrated by nanoparticles, i.e. the majority of droplets did not contain any nanoparticles, it has been proven that two nanoparticles can be incorporated at opposite sides of bipolar nematic droplets using this method.

Whilst the methods presented in this section for the infiltration of nematic droplets with nanoparticles did show some success, there were two main limitations. Firstly, low nanoparticle infiltration rates of nematic droplets which will always remain low despite agitation, as this leads to greater droplet polydispersity, and also despite high nanoparticle excess as diffusion of the particles would remain slow. Secondly, the leaching of fluorescent dye is time limiting, so the diffusion time of particles cannot be increased without losing the

ability to observe the location of nanoparticles. For all post-production methods investigated it was not possible to determine the average number of nanoparticles which had infiltrated droplets for various reasons, including the dye leaching, as well as too few droplets becoming infiltrated, and too many nanoparticles infiltrating droplets. Therefore, all of the limitations discussed show that the post-production nanoparticle infiltration methods investigated were not a viable way forward for infiltrating droplets in a reliable and controlled way. In order to remove the limitations imposed by post-production nanoparticle addition methods, an alternative method for nanoparticle infiltration using different nanoparticles was investigated.

4.2.2 Nanoparticle Infiltration of Bipolar Nematic Droplets by a Microfluidic Method

4.2.2.1 Preparation of Polymer Nanoparticles for Microfluidics

To avoid the limitations associated with a diffusion-controlled infiltration of nanoparticles, incorporation of nanoparticles into the inner phase of microfluidic experiments was investigated. This required the suspension of nanoparticles in organic solvent rather than the readily available buffer suspension. As previously discussed, when using nanoparticles where the dye was not covalently bound, the dye leached from nanoparticles into isotropic droplets, and to a lesser extent the nematic droplets, meaning that the nanoparticles location within droplets could not be determined by fluorescence microscopy. Hence, to incorporate fluorescent nanoparticles into the organic microfluidic inner phase without dye leaching, the fluorescent dye required covalent binding to the surface of the nanoparticles so that upon nanoparticle swelling, the dye would be unable leave the nanoparticle and dissolve into the chloroform or nematic mixture.

For the preparation of the surface modified nanoparticles, a ‘click’ reaction between fluorescent dye fluorescein isothiocyanate (FITC) and amine groups on the surface of 1.0 μm amine modified crosslinked polystyrene nanoparticles was performed to create covalent linkages between the nanoparticles and the fluorescent moiety, as shown in Scheme 1. Here, the amine group on the

nanoparticle surface and the isothiocyanate group on FITC react together to form a thiourea group between the nanoparticle and fluorescent dye molecule.[169–172]

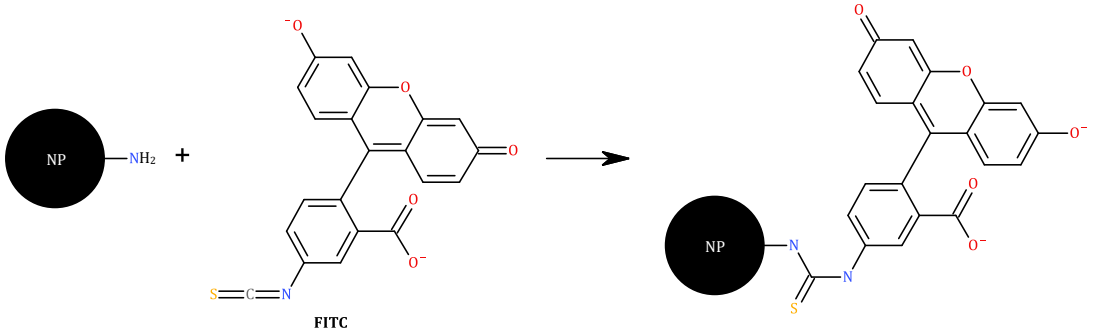

Scheme 1: Covalent binding of fluorescein isothiocyanate to amine modified nanoparticles.

Amine modified polystyrene nanoparticles were suspended in a 0.1M sodium hydrogen carbonate buffer solution to which FITC in dimethylformamide (DMF) was added and the suspension was mixed in the dark overnight at room temperature. The suspension was then centrifuged, and the supernatant containing any unbound FITC was replaced with MilliQ water before resuspension of the nanoparticles. Full experimental details can be found in the experimental chapter (section 7.5). The resulting nanoparticles had a concentration of 0.5 %w/v. Upon imaging by fluorescence microscopy, shown in Figure 87, it could be seen that the resulting nanoparticles were fluorescently active and had not irreversibly aggregated.

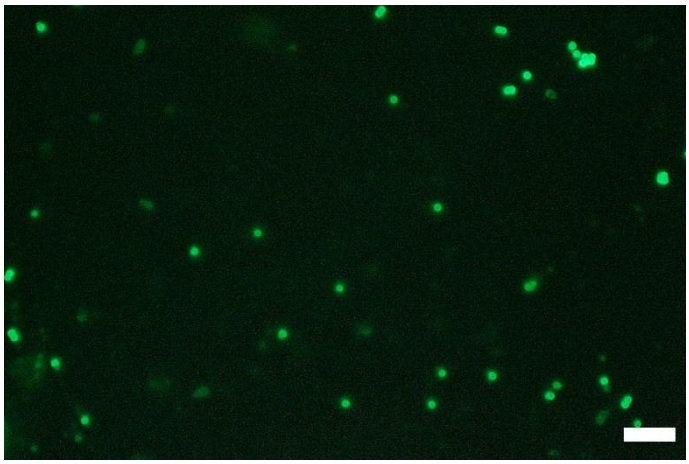

Figure 87: Fluorescence photomicrograph of FITC modified 1.0 µm polystyrene nanoparticles suspended in MilliQ water. Taken at 1000x magnification, scale bar 10 µm.

Due to the immiscibility of water (the suspension was supplied in, and surface modification performed in, an aqueous suspension) and chloroform (necessary for compatibility with the microfluidic inner phase) an intermediate suspension medium was required for the suspension medium exchange from water to chloroform. Washing of the particles with solvent could have been attempted using various methods including dialysis or spin filters, however the centrifuge and resuspension method was deemed the most appropriate for larger 1 μm nanoparticles.[173] When changing the composition of the suspension medium, aggregation commonly occurs, therefore the exchange was carried out carefully over increasing solvent concentrations in water. FITC dyed nanoparticles were suspended in isopropyl alcohol (IPA) by centrifuge and resuspension in increasing concentrations of IPA in water several times up to 100% IPA. Upon imaging the nanoparticles by fluorescence microscopy, it could be seen that they were still fluorescently active and there was little to no aggregation, hence the suspension of the nanoparticles in IPA was stable, shown in Figure 88a. A suspension medium exchange into acetone was also attempted instead of IPA, however the suspension was not stable as nanoparticles irreversibly aggregated upon attempted resuspension in 75% acetone in water. To allow for incorporation into the microfluidic inner phase, a small volume, 50 or 100 μL, of the nanoparticles in IPA suspension was made up to 1 mL with chloroform and vortexed. The resulting suspension was a stable suspension of FITC tagged nanoparticles in 90 – 95% chloroform/IPA solution. The nanoparticles were bright under fluorescence microscopy, shown in Figure 88b, and there was no evidence of dye leaching from the nanoparticles. The small fraction of IPA present in the nanoparticle suspension became negligible in microfluidic experiments due to further dilution with chloroform, so it was expected that the solvent evaporation stage would proceed as normal even with a small volume of IPA still present.

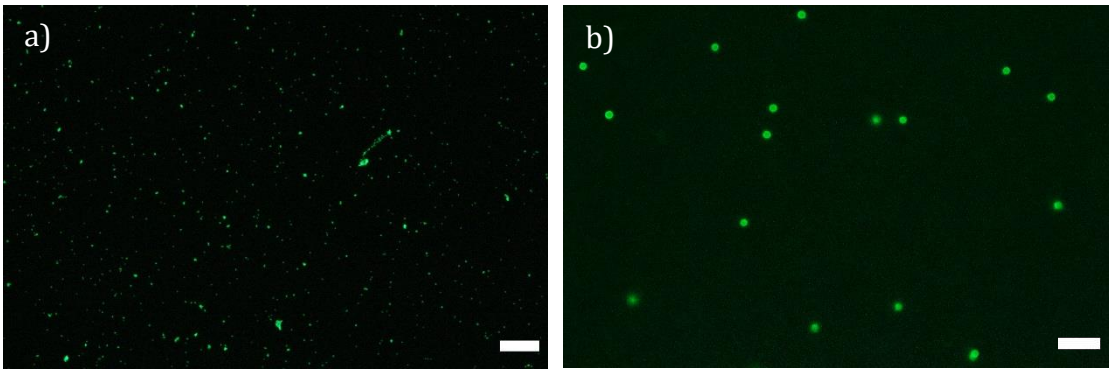

Figure 88: Fluorescence photomicrographs of FITC modified 1.0 µm polystyrene nanoparticles suspended in IPA (a) and chloroform (b). Taken at 200x and 1000x magnification respectively, scale bars 50 µm (a) and 10 µm (b).

The nanoparticle suspensions were diluted throughout the dying and dispersion medium exchange methods. If 50 µL of the IPA suspension was made up to 1 mL with chloroform the resulting suspension had a concentration of 2.5 x 10^{-3} %w/v which was to be used where a nanoparticle to droplet ratio of 2 : 1 and 4 : 1 was required. Whereas, if 100 µL of the IPA solution was made up to 1 mL with chloroform, the concentration of nanoparticles in the suspension was 5 x 10^{-3} %w/v, this concentration was used where ratios of 7 : 1 or 8 : 1 were required. It was found that exposure to light caused photobleaching over time, meaning that the fluorescence of the nanoparticles became dimmer. Photobleaching occurs when the structure of the fluorophore changes by degradation or by covalent interaction of the fluorophores whilst in their excited state. These structural modifications prevent fluorescence and hence appear to fade under fluorescence imaging.[174,175] This introduces a small limitation to imaging the nanoparticles as fluorescence imaging quality decreased the more they were exposed to light. To avoid photobleaching nanoparticles were kept in the dark for as long as possible throughout the binding of the dye, as well as during microfluidic experiments.

4.2.2.2 Microfluidic Infiltration of Nematic Droplets with Nanoparticles

In a series of microfluidic experiments, the concentration of nanoparticles was varied. Several nanoparticle to droplet ratios were investigated, from 2 : 1 to 8 : 1. Nanoparticle ratios were calculated using Equation 13 – Equation 15, however

they were based on estimated droplet diameters as nanoparticles were added pre-production. Full experimental parameters, infiltration ratios and experimental observations are found in the experimental chapter (section 7.3.2.2, Table 14).

During microfluidic setup the calculated volume of the 1 μm FITC tagged nanoparticles in chloroform was added to the chloroform solution containing the monomer, crosslinker and photoinitiator to make up the inner phase. Vortexing was utilised to agitate the suspension, aiding uniform dispersion nanoparticles in the inner phase before loading into a glass syringe. Whilst the nanoparticle suspension was stable enough in chloroform that aggregation was avoided, it was not perfectly stable hence settling within the syringe occurred over time, so as soon as the suspension was loaded into the syringe, the syringe pumps were turned on to start the experiment. Figure 89 shows a cartoon representation of the setup for the microfluidic nanoparticle infiltration method. Ditter *et al* utilised a microfluidic method to produce elastomer microparticles composed from an **M1**, crosslinker and photoinitiator mixture, however no solvent was introduced into the inner phase so magnetic nanoparticles were added directly to the monomer mixture which was heated to 90 °C to melt the inner phase and reduce the viscosity, allow for it to flow through their microfluidic device. The nanoparticles were added in large quantity (up to 6 wt%) and so were introduced into the resulting elastomer microparticles in large, uncontrolled, numbers with no indication of localisation.[125]

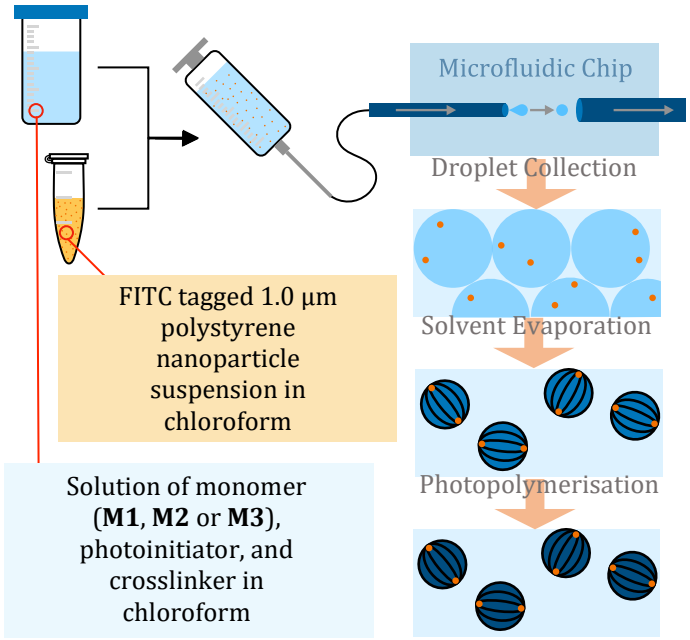

Figure 89: Cartoon representation of the microfluidic setup used to produce nematic elastomer microparticles containing nanoparticles.

Apart from the experiment being performed in the dark, and the introduction of nanoparticles into chloroform solution containing the monomer, crosslinker and photoinitiator, experimental conditions remained as previously described in chapters 2 and 3. As previously, the isotropic droplets were produced and collected in the outer fluid of PVA in water. Figure 90 shows an example photomicrograph from fluorescence imaging of a sample of chloroform droplets containing monomer **M3** as well as FITC tagged nanoparticles, which were introduced in nanoparticle to droplet ratios of 4 : 1. It can be seen that the majority of droplets contained at least one nanoparticle, and several of the droplets contained two nanoparticles. Additionally, no nanoparticles were observed outside of the droplets, confirming compatibility with the chloroform. The fluorescence imaging of isotropic droplets was used to calculate the approximate droplet incorporation rate and average number of nanoparticles within droplets, detailed in the experimental chapter (section 7.3.2.2, Table 14) as well as the averages in Table 5, so that photobleaching would be minimised and to improve the accuracy of counting nanoparticles. Nanoparticles were randomly located within the droplets; this is to be expected in the isotropic droplets as there is no nematic order to produce elastic forces within droplets to direct nanoparticles to localise. As the droplets were produced by microfluidics,[44,51] a narrow dispersity

was produced, for example **M3-MF96** has a CV of 1.1%, compared to the 5CB droplets produced by a suspension method in **5CB-SM1** which had a CV of 73.9%. The similarity in droplet diameters allowed for the formation of monolayers of hexagonally packed droplets. The method developed here for incorporating nanoparticles into droplets produced by microfluidics was successful in producing droplets in the same small micrometre size range which were just as monodisperse as those without nanoparticles described in chapters 2 and 3. The number of nanoparticles entering each droplet was fairly predictable and heavily relied on no aggregation of the nanoparticles within the chloroform microfluidic inner phase solution.

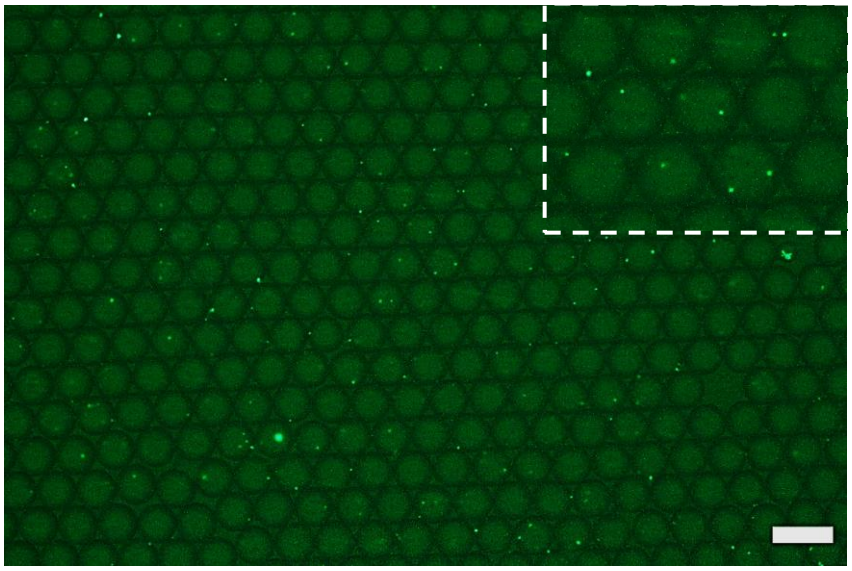

Figure 90: Fluorescence photomicrograph of isotropic **M3** in chloroform droplets containing nanoparticles introduced in a 4 : 1 ratio, from **M3-MF96**. Taken at 100x magnification, scale bar 100 µm. Section with 1.9x zoom shown in top right corner. Average diameters: 65 µm.

Table 5: Average nanoparticle infiltration rates of isotropic droplets containing monomers **M1** and **M3**, as well as the average number of nanoparticles per droplets; *calculated from nanoparticle containing droplets only.

Identifier	Nanoparticle : Droplet Ratio	Average % of Droplets Infiltrated with Nanoparticles	Average Number of Nanoparticles per Droplet*
M1	4 : 1	58%	1.69
	6 : 1	40%	1.75
	7 : 1	73%	2.88
M3	2 : 1	35%	1.17
	4 : 1	66%	1.68
	7 : 1	78%	2.48

As previously described, in the solvent evaporation step the chloroform was allowed to evaporate slowly from the droplets, reducing droplet diameter by an average of 42%. After solvent evaporation, droplets displayed a nematic phase at room temperature, generally with a bipolar configuration as characterised by baseball textures observed under POM although the imaging quality was not always high enough to confirm this is true for all droplets, examples of which can be seen in the figures which follow. The effects of varying the ratio of nanoparticles to droplets was investigated to optimise the droplet infiltration rate.

Figure 91 shows droplets of **M3** with nanoparticles introduced at a 2 : 1 nanoparticle to droplet ratio. Fluorescence imaging revealed that many of the nematic droplets contained one nanoparticle localised at the surface, however no nematic droplets were found to contain two nanoparticles. The average number of nanoparticles which infiltrated droplets at this ratio was 1.17, for 35% of droplets, the remaining droplets did not contain any nanoparticles. The irregular shaped and dark coloured droplets in Figure 91a show dust contaminated droplets. The polarised photomicrograph in Figure 91b suggests the bipolar configuration was retained as the characteristic isogyres of the nematic baseball textures can be seen, particularly in the zoomed in area of the figure.

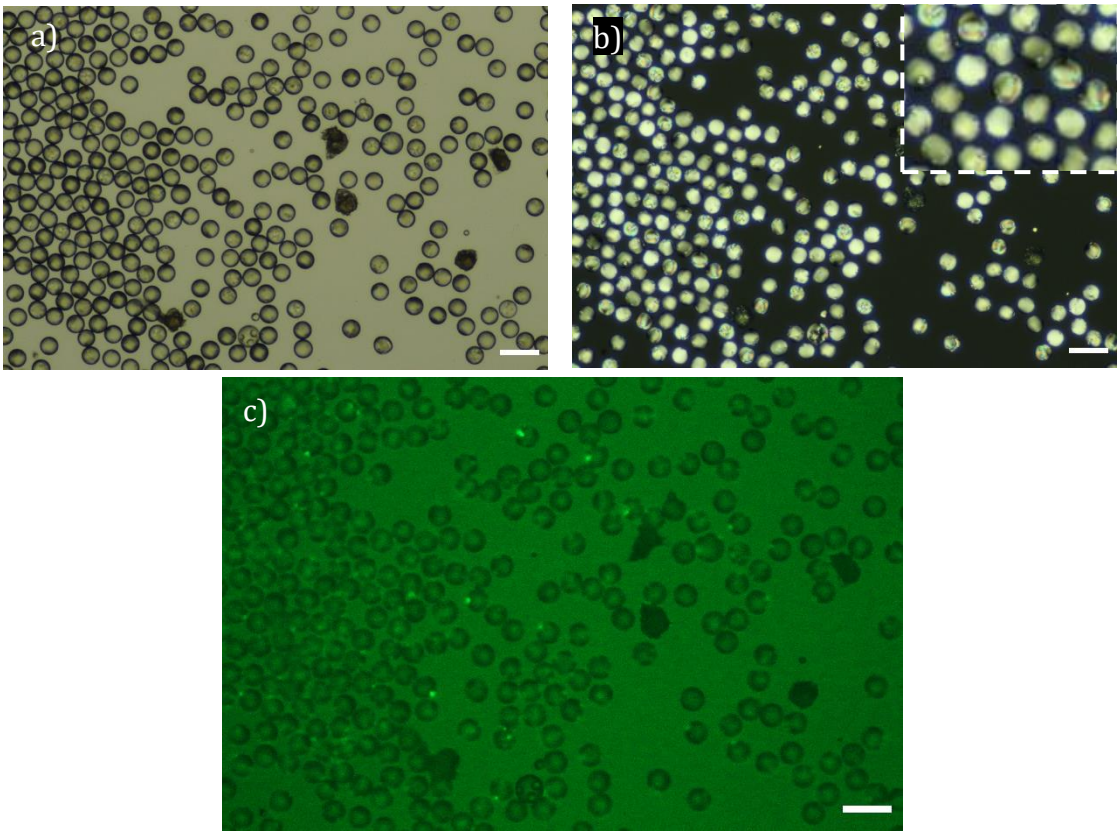

Figure 91: Brightfield (a) and polarised (b) photomicrographs taken in transmission mode, and fluorescence photomicrograph (c) of bipolar nematic **M3** droplets from **M3-MF32** containing nanoparticles which were introduced in ratios of 2 : 1. Taken at 200x magnification, scale bars 50 µm. Zoomed section of (b) was cropped and zoomed in by 2x. Average diameters: 23 µm.

In an attempt to increase the nanoparticle introduction rate for droplets with the aim of producing **M1** and **M3** droplets containing two nanoparticles, a ratio of 4 : 1 was utilised. Figure 92 and Figure 93 show **M3** and **M1** droplets infiltrated at a 4 : 1 ratio under brightfield, polarised and fluorescence imaging. The polarised photomicrographs show a fairly defined bipolar nematic texture in the majority of droplets, which will be discussed in the coming paragraphs. Under fluorescence imaging it was observed that when using a larger nanoparticle to droplet ratio of 4 : 1 compared to 2 : 1, a greater proportion of the bipolar nematic droplets contained at least one nanoparticle, and some contained two. The average number of nanoparticles which infiltrated droplets using a 4 : 1 ratio was 1.68, for 66% of droplets in **M3** and similarly 1.69, for 58% of droplets in **M1**. When comparing the droplets before (Figure 93d) and after (Figure 93c) solvent evaporation, it can be seen that there was a comparable spread of nanoparticles within droplets across both samples, showing that there was no loss of nanoparticles and indicating nanoparticle compatibility with both the isotropic and the nematic droplets. The

highlighted droplet in Figure 92c shows two nanoparticles within the droplet, in the majority of cases observed, it could be seen that where two nanoparticles were within a droplet, as in this case, they were located on ~180° opposite sides of the droplet at the surface, as observed by Mondiot *et al* in 5CB droplets with one nanoparticle localised into each bipolar defect. However, a more detailed look at the POM imaging is required to determine if this is in fact the case.

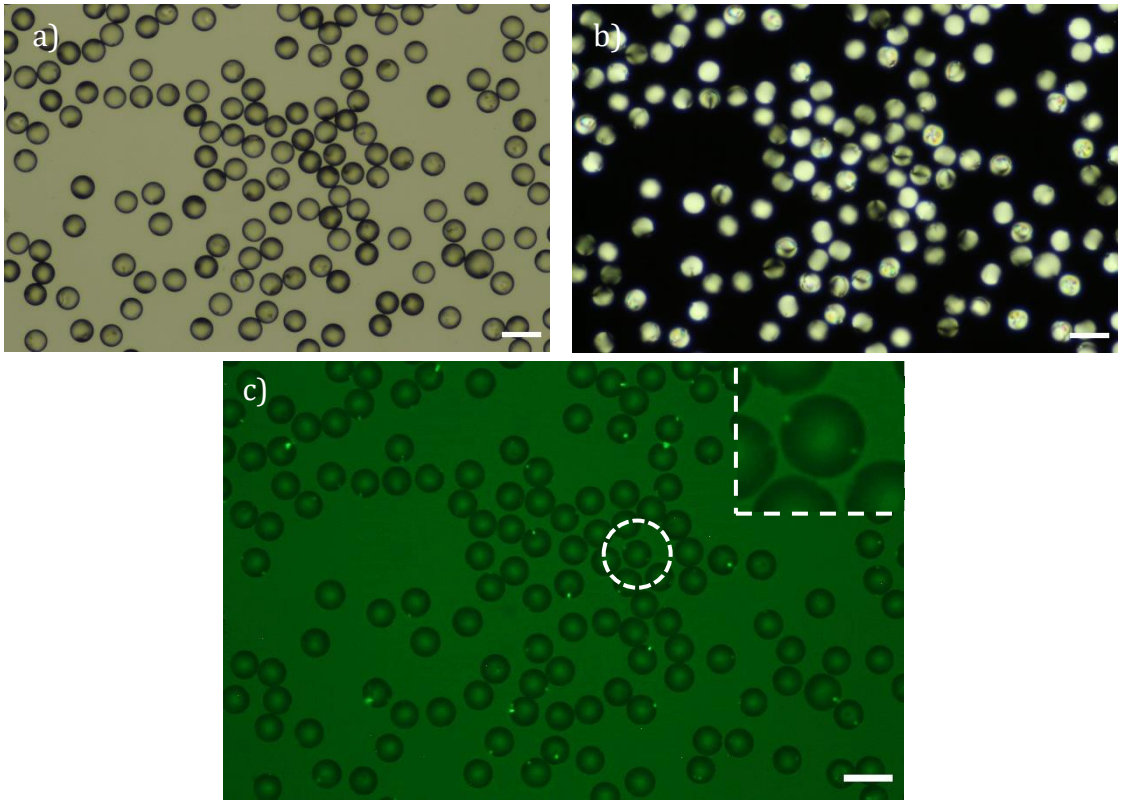

Figure 92: Brightfield (a) and polarised (b) photomicrographs taken in transmission mode, and fluorescence photomicrograph (c) of bipolar nematic **M3** droplets from **M3-MF33** containing nanoparticles which were introduced in ratios of 4 : 1. Taken at 200x magnification, scale bars 50 µm. Droplet circled in white is zoomed in by 3x, shown in the top right corner of the photomicrograph, showing two nanoparticles within the droplet. Average diameters: 30 µm.

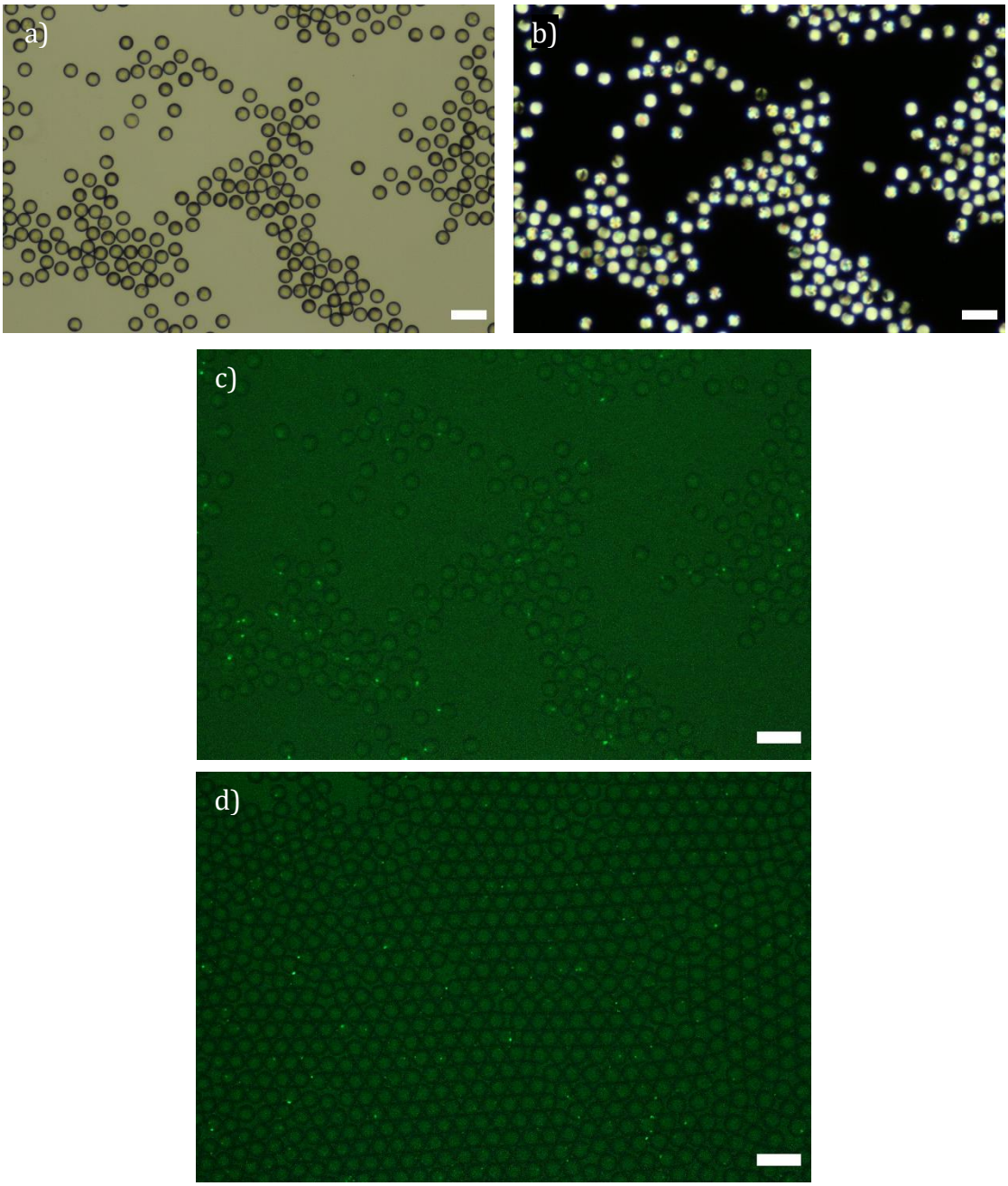

Figure 93: Brightfield (a) and polarised (b) photomicrographs taken in transmission mode, and fluorescence photomicrograph taken in reflection mode, overlaid with the brightfield image (c & d) of bipolar nematic (a – c) and isotropic (d) **M1** droplets from **M1-MF61** containing nanoparticles which were introduced in ratios of 4 : 1. Taken at 200x magnification, scale bars 50 µm (a – c), 100x magnification, scale bar 100 µm (d). Average diameters: 20 µm (a – c) and 50 µm (d).

The fluorescence imaging provided some indication of defect localisation, however further analysis of the location of the nanoparticles with respect to the defects was required to confirm this. Hence, the nematic texture in the POM imaging through crossed polarisers was studied in conjunction with the fluorescence imaging. Figure 94 and Figure 95 show a selection of droplets (**M3** and **M1** respectively)

from the previous two figures where the image has been zoomed in to the individual droplets so as to see the features clearer.

The first two rows in Figure 94 show particles with their polar axes diagonal with respect to the observer, as shown in their cartoon representations. This can be inferred due to the dark isogyres seen in the polarised photomicrographs in the top right and bottom left areas of the droplets.[130] The fluorescence imaging revealed that one nanoparticle is localised into one of these defects in both droplets. Furthermore, in both droplets there was evidence of some small disruption to the director field in these areas, observed as dark spots, despite an overall bipolar texture persisting. This can be seen in both the polarised and brightfield images, labelled with white arrows. The photomicrographs in the third and fourth rows also indicated some small disruption to the bipolar configuration, the polarised photomicrograph in the third row shows the polar axis lay close to horizontal as the isogyres shifted towards the centre of the droplet,[130] however the texture is not symmetrical as would be expected of a bipolar configuration. In the fourth row a similar texture would be expected as the droplet was close to horizontal, however an isogyre was observed going from one pole to the other, indicating even greater disruption to the bipolar configuration of the droplet, perhaps as two nanoparticles were localised within the polar defects, rather than one in the other droplets.

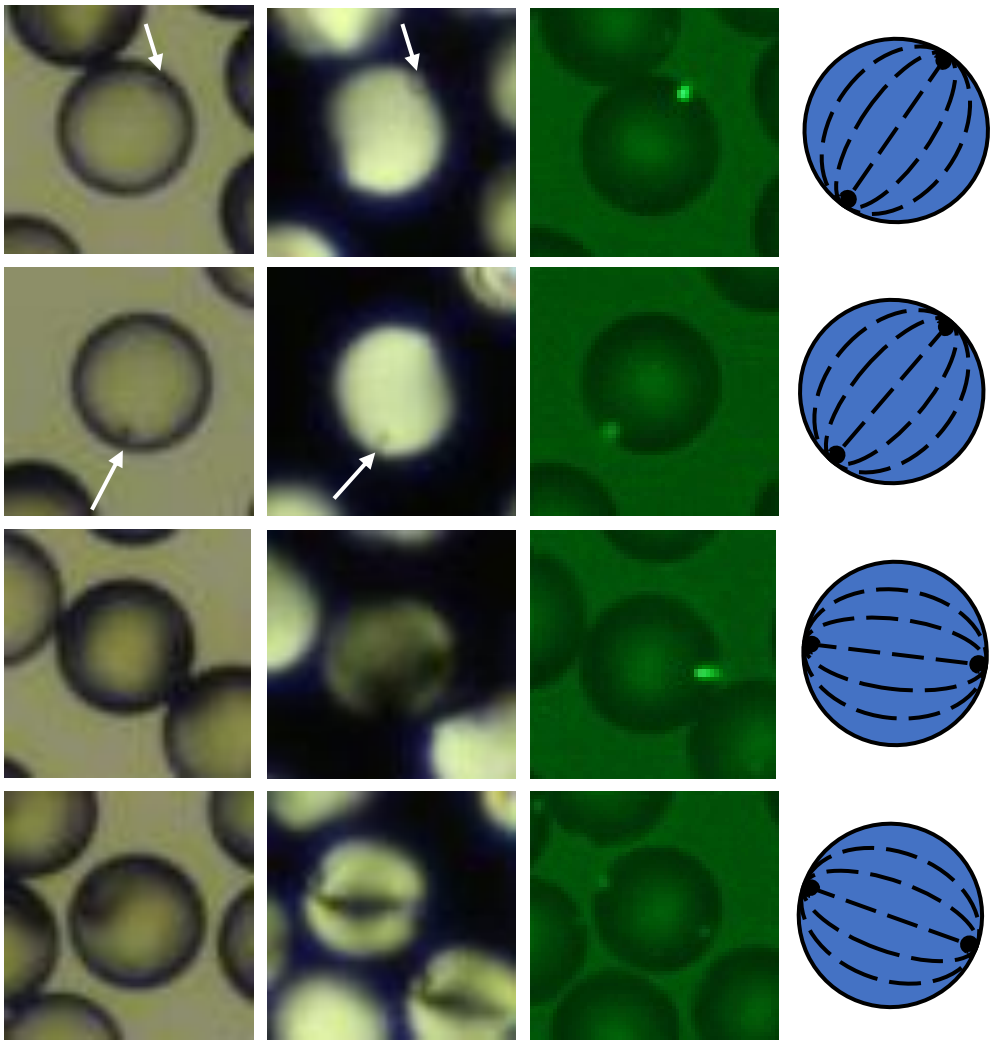

Figure 94: Brightfield (first column), polarised (second column) and fluorescence (third column) photomicrographs of **M3** droplets containing nanoparticles from **M3-MF33**. Cartoon representation of the suggested bipolar droplet orientation (last column). Each row is imaging from a different droplet of the sample in Figure 92, taken at 200x magnification, cropped and zoomed in by 6x. Arrows indicate areas mentioned in text. Average diameters: 30 µm.

The droplets in the first three rows of Figure 95 show similar results, albeit more difficult to see due to the imaging quality when zooming in on the photomicrographs of these smaller, 20 µm, droplets. In the first row, isogyres in the polarised photomicrograph were symmetrical and arched across two opposite sides of the droplet, which is characteristic of a droplet in a close to vertical orientation (~22.5° from vertical).[130] With this in mind, the nanoparticle seen in the fluorescence image appears to be located within where the defect was expected to be. The droplets in the second and third row however display textures which again indicate some disruption to the director in the bipolar configuration by lack of symmetry of the isogyres. The imaging presented by Mondiot *et al*

indicates similar slight disruption of the bipolar configuration about localised nanoparticles was present in some of their small micrometre sized 5CB droplets infiltrated with 1 μm polystyrene nanoparticles, shown in Figure 96.[85] In the polarised image (Figure 96a) the baseball texture is slightly distorted, as seen by the dark spot where the nanoparticle is located, indicated with an orange arrow, as well as some loss of symmetry within the texture. Furthermore, a spot can also be seen in the same position of the brightfield image, indicated by a blue arrow in Figure 96b. It can be seen that where nanoparticles were not present, shown in section 3.2, Figure 46 and Figure 47, this type of local director distortion was not observed, further indicating that it is the nanoparticles which are disrupting the field. This slight distortion of the bipolar configuration is in line with what was observed in infiltrated **M1** and **M3** systems, showing the bipolar configuration does persist in droplets containing small numbers of nanoparticles, at least up to two, albeit with some slight distortion of the director field about the nanoparticles.

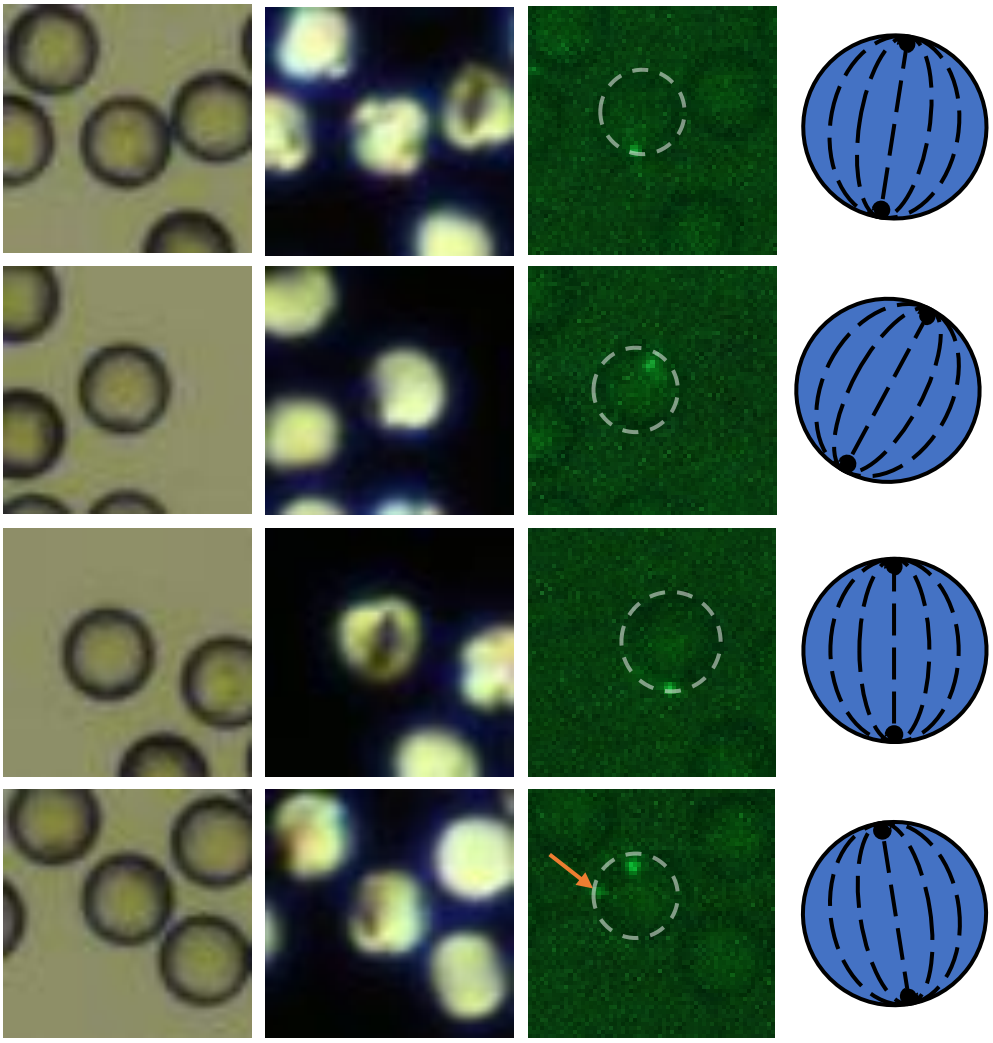

Figure 95: Brightfield (first column), polarised (second column) and fluorescence (third column) photomicrographs of **M1** droplets containing nanoparticles from **M1-MF61**. Cartoon representation of the suggested bipolar droplet orientation (last column). Each row is imaging from a different droplet of the sample in Figure 93, taken at 200x magnification, cropped, and zoomed in by 6x. Orange arrow indicates second nanoparticle discussed in text. Average diameters: 20 µm.

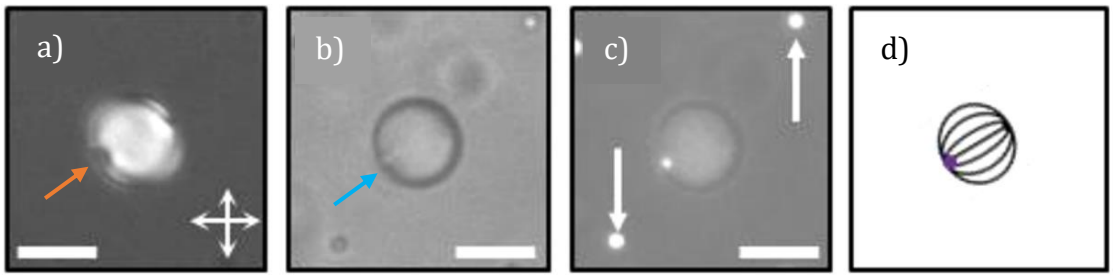

Figure 96: Polarised (a), brightfield (b) and fluorescence overlaid with brightfield (c) photomicrograph of a bipolar nematic 5CB droplet infiltrated with one 1 µm fluorescent polystyrene nanoparticle localised into a polar defect, shown in cartoon representation (d). Scale bars 5 µm, reproduced from Mondiot *et al*.[85] Orange and blue arrows discussed in text, white arrows indicate free nanoparticles.

In all of these cases so far, the localisation of the nanoparticles observed suggests that the elastic forces imposed by nanoparticles interrupting the director field directed them to localise into the topological defects, to prevent new defects forming which would be energetically unfavourable areas of high elastic energy. When localised at the surface within the already present bipolar defects, the high splay elastic energy was reduced, outweighing an increase in surface energy caused by nanoparticle addition. Overall the free energy of the system was minimised and therefore polar localisation of nanoparticles was favoured.[69–71,78,86] Despite this, some local disruption of the bipolar texture was observed and is to be expected upon the incorporation of nanoparticles into the nematic droplets despite defect localisation, likely due to the surface anchoring of the nanoparticle itself, which for polystyrene particles is homogeneous.[85,86] These results are in line with those reported by Mondiot *et al* discussed previously, however they present few droplets out of the population, suggesting low infiltration rates. Whereas the results here show the majority of droplets contained at least one defect localised nanoparticle.

Furthermore, in the final row of Figure 95, it can be seen that there were two nanoparticles, however only one of these appeared to be localised within a polar defect. The other nanoparticle, indicated by the orange arrow, does not appear to be located within one of the topological defects. Whilst having nanoparticles localise into the 180° apart topological defects represents the energy minima, simulation work by Rahimi *et al* and Londoño-Hurtado *et al*, coupled with experimental observations, show that in the central region of a bipolar droplet a local energy minimum is present. As elastic energy is relatively small at ~40 – 140° from one of the poles, it plateaus and falls to a local minimum at 90° from the boojums (the droplet equator).[86,176] This is not exclusively seen in droplets of a bipolar configuration, the same equatorial local minimum is found in twisted bipolar droplets.[87] In the bottom row of Figure 95, this is where the second nanoparticle appears to have localised. Where a nanoparticle is migrating through a bipolar droplet toward free energy minima they can become trapped in the local minimum found at the equator before reaching the overall minima located at the poles. Furthermore, it takes time for nanoparticles to find these energy minima whilst migrating through the droplet, the shorter solvent evaporation of **M1**

(implemented to prevent crystallisation) compared to **M3** may have led to the trapping of particles prior to the optimum location being found.

Figure 97 shows nematic **M3** and **M1** droplets which were infiltrated by two nanoparticles, seen in the fluorescence microscopy photomicrograph. The POM photomicrographs were again used to elucidate the position of the polar axes and therefore where the poles of the bipolar droplets were, the isogyres, similar to those seen in the droplets in the top two rows of Figure 94 show that the polar axis must lay in the diagonal directions indicated by the cartoon representations,[130] which in turn shows that the nanoparticles seen in the fluorescence imaging were located one in each pole of the bipolar droplets.

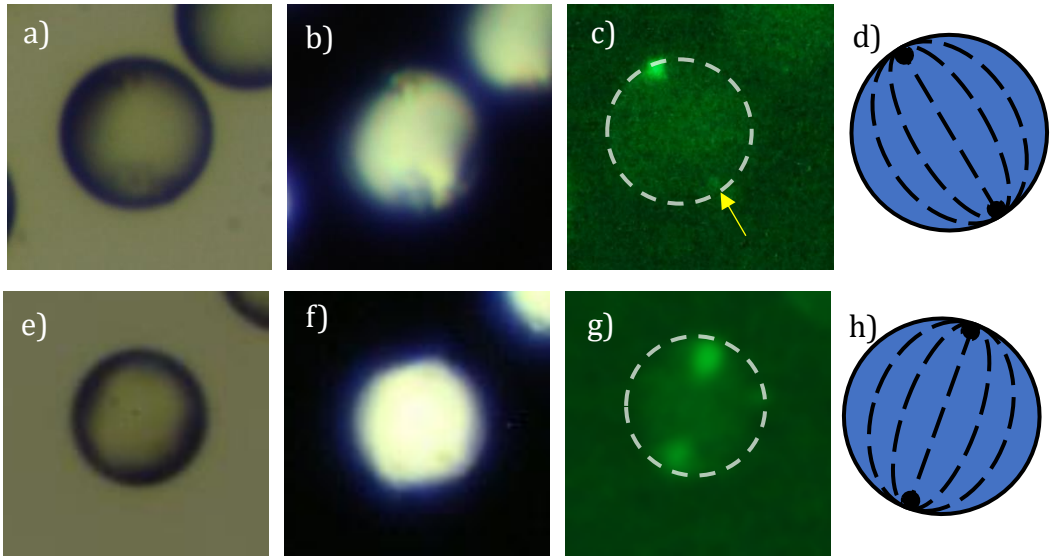

Figure 97: Brightfield (a & e), polarised (b & f), fluorescence (c & g) photomicrographs of **M3** from **M3-MF96** (a – c) and **M1** from **M1-MF58** (e – g) bipolar nematic droplets and cartoon representation of suggested droplet orientation (h). Yellow arrow indicates position of a dim nanoparticle. Taken from **M3-MF96** at 200x magnification, cropped and zoomed by 15x (top row) and 12x (bottom row).

Droplets with higher nanoparticle concentrations were also investigated. Nematic **M3** and **M1** droplets were produced using nanoparticle to droplet ratios of 7 : 1 and are shown in Figure 98 and Figure 99. The fluorescence imaging shows that the majority of droplets contained more than two nanoparticles which seemed to be randomly orientated at the surfaces of the droplets, examples are shown in Figure 98c & d. The average number of nanoparticles which infiltrated droplets using a 7 : 1 ratio was 2.48, for 78% of droplets in **M3** and 2.88 for 73% of droplets

of **M1**. Furthermore, in both cases the brightfield imaging shows that the droplets were very slightly deformed, and some had merged together in **M3**, perhaps indicating premature polymerisation, however this is speculative as is unclear why high nanoparticle loadings could cause this. The polarised photomicrographs show that the droplets did not have a defined texture, instead an ill-defined grainy texture was observed which is indicative of a polydomain configuration. It is thought that a higher number of nanoparticles infiltrating droplets interrupted the formation of a bipolar configuration, resulting in the polydomain grainy, ill-defined textures. Previously in Figure 94 and Figure 95, it was seen that one or two nanoparticles were able to slightly disrupt the director field locally, hence having a greater number of nanoparticles within the nematic droplets allows for greater disruption of the director field, resulting in no bipolar texture being formed.

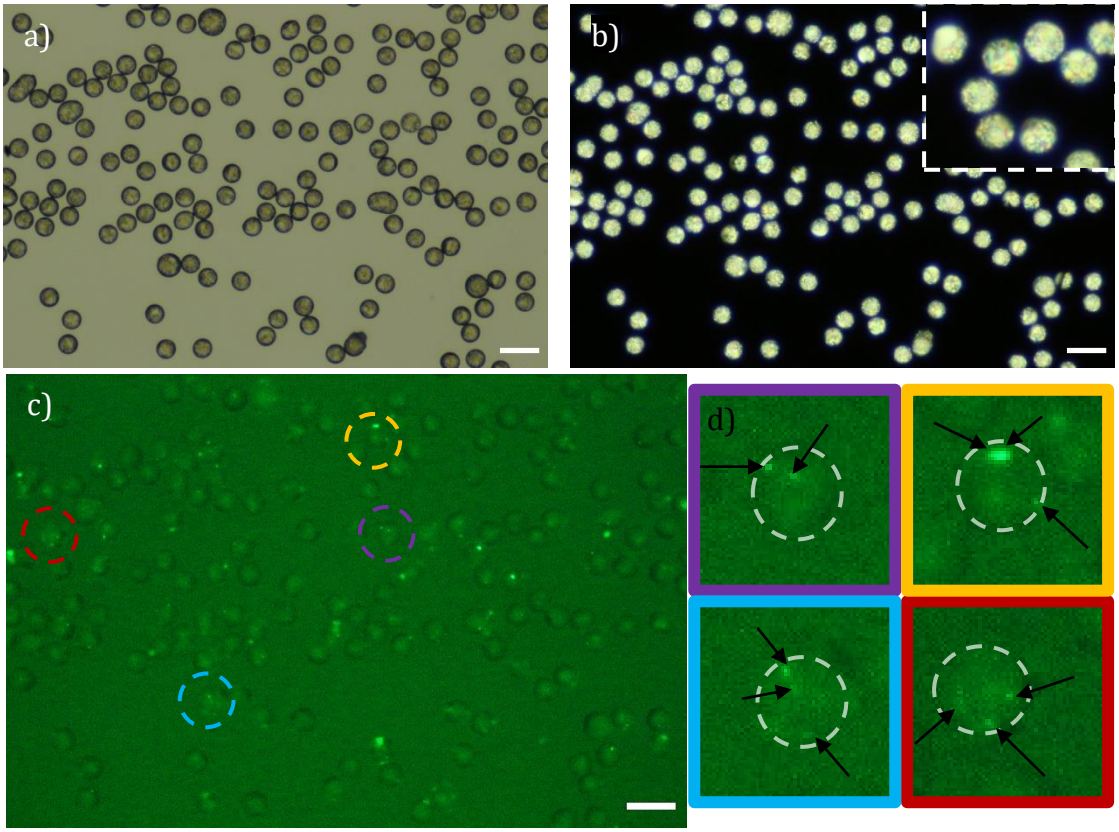

Figure 98: Brightfield (a) and polarised, with zoomed section in top right (b) photomicrographs taken in transmission mode, and fluorescence photomicrograph (c) of bipolar nematic **M3** droplets from **M3-MF48** containing nanoparticles which were introduced in ratios of 7 : 1. Taken at 200x magnification, scale bars 50 µm. Section highlighted in (b) zoomed in by 1.7x and droplet highlighted in (c) zoomed by 3.4x, shown (d) in corresponding colours, nanoparticles indicated by black arrows. Average diameters: 25 µm.

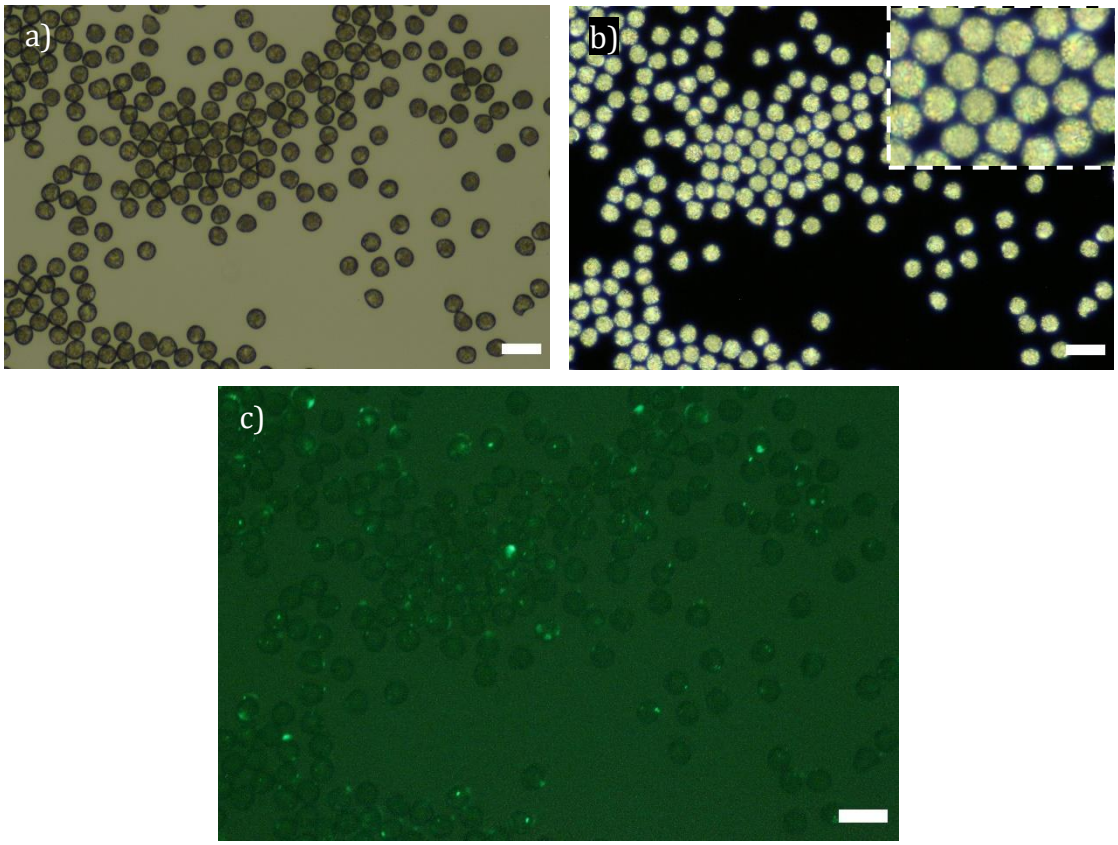

Figure 99: Brightfield (a) and polarised (b) photomicrographs taken in transmission mode, and fluorescence photomicrograph overlaid with the brightfield image (d) of nematic **M1** droplets infiltrated with 7 : 1 nanoparticle to droplets in **M1-MF47**. 200x magnification, scale bars 50 µm. Highlighted section zoomed in by 2.1x shown in top right corner of each photomicrograph. Average diameters: 25 µm.

Whilst nanoparticle to droplet ratios were calculated for use in the microfluidic infiltration method, it can be seen that the calculated number of nanoparticles were not located in each droplet in the experimental results. There are several reasons for this observation. Firstly, the calculated volume of nanoparticle suspension added for the ratio was dependent on the final droplet diameters, which were not known until after the microfluidic experiment was run. Therefore, the calculated volume of nanoparticles for the ratio was only an estimate based upon an expected droplet diameter. Secondly, the nanoparticle suspension in chloroform was not a perfectly stable suspension. Throughout the microfluidic experiment, lasting approximately two hours, some nanoparticles settled in the syringe and were not suspended in the inner phase for incorporation into droplets due to the inability to resuspend nanoparticles once they were within the syringe. Finally, it is expected that many nanoparticles were lost whilst binding FITC to the nanoparticles' surface and during dispersion medium exchange after several

centrifuge, supernatant replacement and resuspension cycles, therefore the suspension concentrations have to be considered as estimations.

Overall, when looking at the proportion of droplets which contained nanoparticles, higher incorporation rates were achieved with the microfluidic method, where nanoparticles were incorporated into the inner phase, than in previously reported methods relying on diffusion, or agitation-assisted diffusion, of nanoparticles from an outer phase into the isotropic or nematic droplets. Furthermore, varying the concentration of nanoparticles showed that there was an upper limit of how many nanoparticles could be incorporated into the nematic monomer droplets before the bipolar texture and, to an extent, the spherical geometry of the droplets was lost, this was approximately at nanoparticle to droplet ratios of 7 : 1. As a nanoparticle to droplet ratio of 4 : 1 showed high infiltration rates of nanoparticles across the population of droplets containing 1 – 2 nanoparticles without disrupting the nematic alignment, ratios of approximately 4 : 1 were therefore selected as appropriate for production of droplets containing up to two nanoparticles using the reported microfluidic method. The microfluidic method developed here resulted in greater control of the infiltration of droplets than previously reported methods,[43,85,87,125] allowing for reliable incorporation of fluorescently tagged polystyrene nanoparticles into nematic monomer droplets, whilst maintaining a small droplet size and dispersity. In the future, further fine-tuning of the concentration optimisation should be performed to increase the proportion of droplets produced containing two nanoparticles.

4.3 Nanoparticles in Bipolar Nematic Elastomer Microparticles

The nematic droplets of **M1** and **M3** containing nanoparticles, crosslinker and photoinitiator, produced by the microfluidic infiltration method were irradiated in the nematic phase with a 365 nm UV lamp, full polymerisation conditions can be found in the experimental chapter (section 7.3.3, Table 16). Photopolymerisation by irradiation with UV light yielded crosslinked nematic microparticles containing nanoparticles. Figure 100 and Figure 101 show examples of nematic elastomer particles, containing nanoparticles, composed of **E1** and **E3** under brightfield, polarised and fluorescence imaging. It was a

challenge to image the nanoparticles by fluorescence microscopy due to photobleaching of the dye during the previous steps of synthesis and imaging at these stages.

The photomicrographs in Figure 100 and Figure 101 show elastomer microparticles of **E3** and **E1** respectively. It can be seen in the brightfield image that minimal deformation from the spherical droplet shape occurred for **E3**, whereas there is some elongation of the particles produced of **E1**. As discussed in section 3.3.1, monomer **M3** has a long 11-carbon spacer group which decouples the mesogen and polymer backbone, and hence no geometry deformation occurs upon polymerisation; whereas the shorter 4-carbon spacer group in **M1** allows for coupling of the mesogen to the polymer backbone allowing for a shape deformation to occur. Compared to the POM imaging seen for nematic **E3** and **E1** elastomer microparticles which were not infiltrated with nanoparticles in chapter 3 (section 3.3.1, Figure 52), the bipolar texture was much less defined, particularly in **E3**. As in nanoparticle infiltrated droplets, some distortion of the bipolar configuration is to be expected, and even more so post-polymerisation, as polymerisation itself results in some texture distortion, also seen in microparticles which did not contain nanoparticles in section 3.3.1. Fluorescence imaging of the nanoparticles within the elastomer microparticles of **E3** and **E1** revealed that nanoparticles remained localised within the microparticles throughout and after polymerisation, including throughout the photopolymerisation induced droplet geometry deformation in **E1**. However, imaging was challenging at this stage due to photobleaching over the entire production process. The fluorescence imaging challenges, combined with the distortion of the bipolar texture through crossed polarisers made determining the nanoparticle location within most of the nematic elastomer particles impossible.

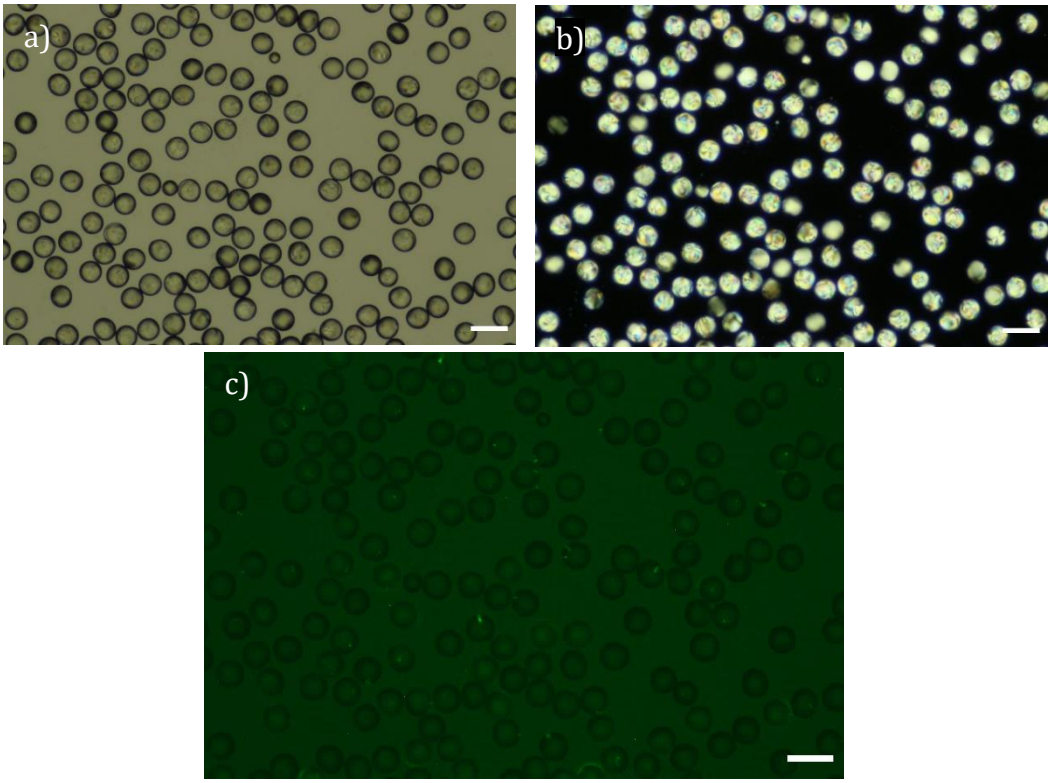

Figure 100: Brightfield (a) and polarised (b) photomicrographs, and fluorescence photomicrograph (c) of bipolar nematic **E3** elastomer microparticles from **E3-MF33** containing nanoparticles introduced in ratios of 4 : 1. Taken at 200x magnification, scale bars 50 µm.

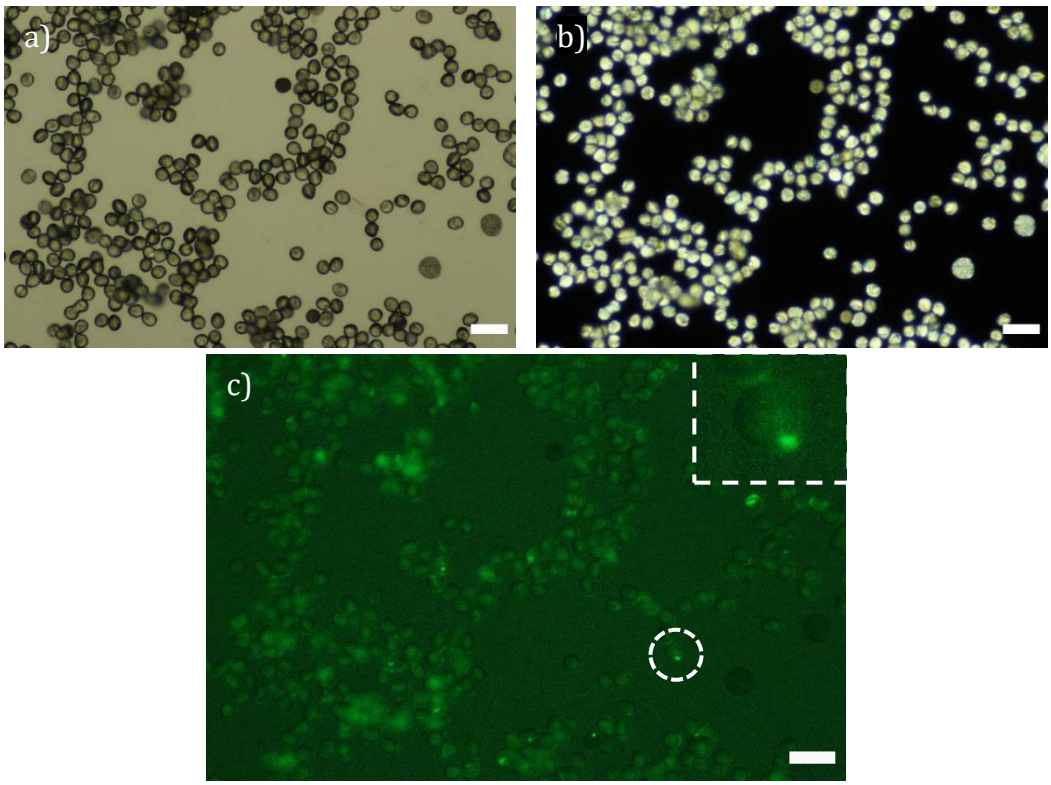

Figure 101: Brightfield (a) and polarised (b) photomicrographs and fluorescence photomicrograph overlaid with brightfield photomicrograph (c) of bipolar nematic **E1** elastomer microparticles from **E1-MF61** containing nanoparticles introduced in ratios of 4 : 1. Taken at 200x magnification, scale bars 50 µm. Highlighted particle zoomed in 4x, shown in top corner.

Nevertheless, a less-distorted bipolar texture can be seen in some **E3** particles from Figure 100, which are shown in zoomed in versions in Figure 102. In these elastomer microparticles, the clearer baseball textures allowed the polar axis to be determined, indicated by the cartoons.[130,177] It was observed that the nanoparticles seen in the fluorescence imaging appeared to be where one of the polar defects was expected to be located in each of the three microparticles, suggesting polar defect localisation, albeit only confirmed in a small selection of particles out of the sample, which was preserved during the polymerisation. Preservation of the location of nanoparticles in droplets through polymerisation into polymer microparticles was reported by Mondiot *et al* and Şengül *et al* for bipolar nematic polymer particles consisting of a mixture of non-polymerisable 5CB with reactive mesogen RM257 and 5CB.[44,85,178] In both cases droplets were produced in broad size ranges from ~4 μm to ~10 μm. Mondiot *et al* showed the location of one or two 1 μm polystyrene nanoparticles at the polar defects was preserved throughout polymerisation to produce polymer particles containing nanoparticles, although only a small proportion of droplets were infiltrated in the first place. Whereas Şengül *et al* showed that polymerisation preserved the location of much smaller ~97 nm silica nanoparticles which coated the surface of a whole population of nematic microparticles rather than just a small sample, although there was no control of the number of nanoparticles within microparticles.

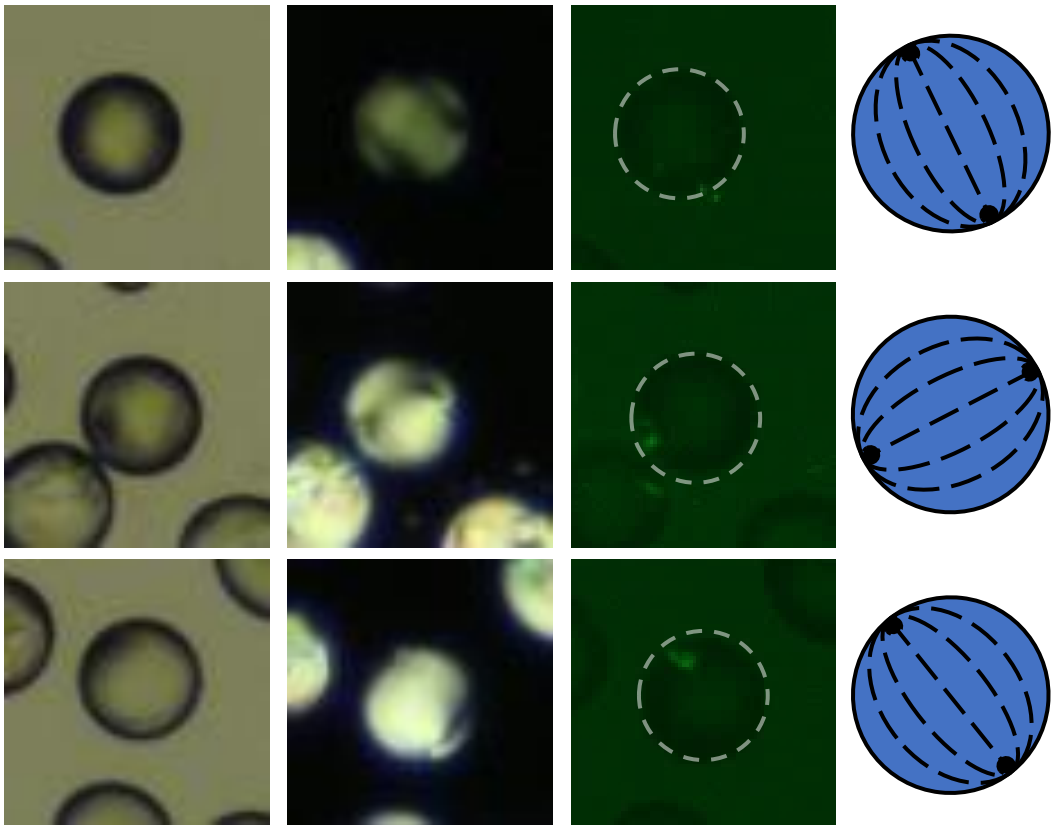

Figure 102: Brightfield (first column), polarised (second column) and fluorescence (third column) photomicrographs of **E3** elastomer microparticles containing nanoparticles from **E3-MF33**. Cartoon representation of the suggested bipolar axis orientation (last column). Each row is imaging from a different elastomer microparticles of the sample in Figure 100, taken at 200x magnification, cropped, and zoomed in by 5.1x. Average diameters: 30 μm.

Finally, SEM imaging was performed in an attempt to see the nanoparticles within the elastomer microparticles. Surface 'patches' have been described in the literature,[44,85,179] where nanoparticle patches are present at the poles of the polymer particles with some surface area of the embedded nanoparticle emergent through the surface of the microparticle. Hence, it was expected that these may be visible under SEM. Figure 103 shows the SEM photomicrographs of a sample of **E1** particles containing nanoparticles, however they do not reveal any obvious signs of the nanoparticles at the surface of any particles. As discussed previously, the holes which can be seen at the surface of particles are thought to be due to the removal of any remaining chloroform from the particles upon drying in the vacuum oven. This suggests that the nanoparticles within the **E1** particles may be fully embedded in the polymer particle at the poles, rather than being slightly emergent through the particle surface. According to simulation by Sumer *et al*, emergent behaviour of nanoparticles in droplets is dependent on shape,

composition and size of nanoparticles.[179] Hence, varying these parameters couple possibly result in a change in the emergent behaviour of nanoparticles in **E1** and **E3**.

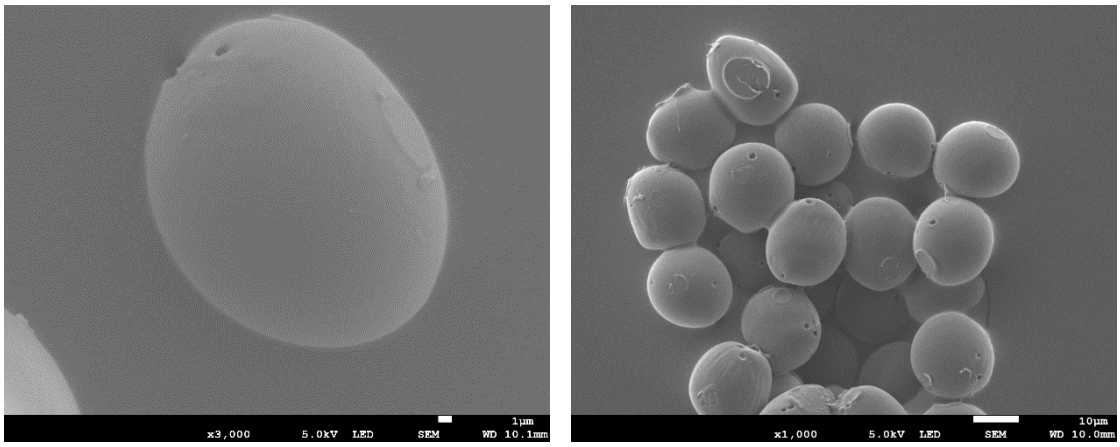

Figure 103: SEM photomicrographs of **E1** particles from **E1-MF58** (a) and **E1-MF61** (b) of nematic elastomer microparticles containing nanoparticles, introduced at ratios of 4 : 1. Taken at 3000x magnification, scale bar 1 µm (a) and 1000x magnification, scale bar 10 µm (b).

4.3.1 Response of Nanoparticle Containing Nematic Elastomer Microparticles to Temperature Change

The nematic elastomer microparticles were washed with MilliQ water to remove the PVA, before replacing the water with PEG 200 for high temperature imaging to allow for the investigation of the microparticles' response to temperature change, as described in the experimental chapter (section 7.3.3).

Bipolar nematic elastomer particles of **E3** infiltrated with nanoparticles were heated from 25 °C (Figure 104a & b), in the nematic phase, to 110 °C (Figure 104c & d), above the T_{NI} of the elastomer, at 86 °C, into the isotropic phase. After the elastomer particles cleared into the isotropic phase, the temperature was returned to the starting temperature of 25 °C (Figure 104e & f), bringing the elastomer microparticles back into the nematic phase. During the temperature experiment the heating/cooling rate was controlled at 10 °C/min. As expected, the microparticles had a negligible shape change about the T_{NI}, due to decoupling between the mesogen and polymer backbone because of the long spacer group. The quality of the imaging here was low due to dye bleaching and due to the utilisation of the hot stage at high temperatures. Furthermore, the quality of the

sample was fairly poor after washing due to the elastomer particles sticking together as well as the fact that not all of the PVA was removed, as seen by the PVA crystals, highlighted in red in Figure 104a, which crashed out of the outer fluid. PVA can also be seen on the surface of the particles in brightfield imaging. Photobleaching meant that it was difficult to track a nanoparticle throughout the heat/cool cycle and so few particles could be analysed. The aspect ratio of the highlighted particle, which is fused to the neighbouring microparticle, changed from 1.03 to 1.02 upon clearing, a negligible change. The aspect ratio returned to 1.03 upon cooling back to the nematic phase. It can be seen from the fluorescence imaging that nanoparticles remained located within the elastomer microparticles when heated through the phase transition into the isotropic phase and returned into the nematic phase, although further analysis such as defect location, cannot be determined here due to the imaging and sample quality. The location retention of the nanoparticles within the elastomer microparticles suggests that the polymer network of the liquid crystal elastomer held the nanoparticles in place. As mesogen alignment was lost when the microparticle passed into the isotropic phase, the elastic forces from the director field holding nanoparticles in place was also lost and so it must have been the elastomer network which preserved the nanoparticle location. Without the elastic forces holding nanoparticles in place in the isotropic phase, it would be expected that the nanoparticles would delocalise.[85]

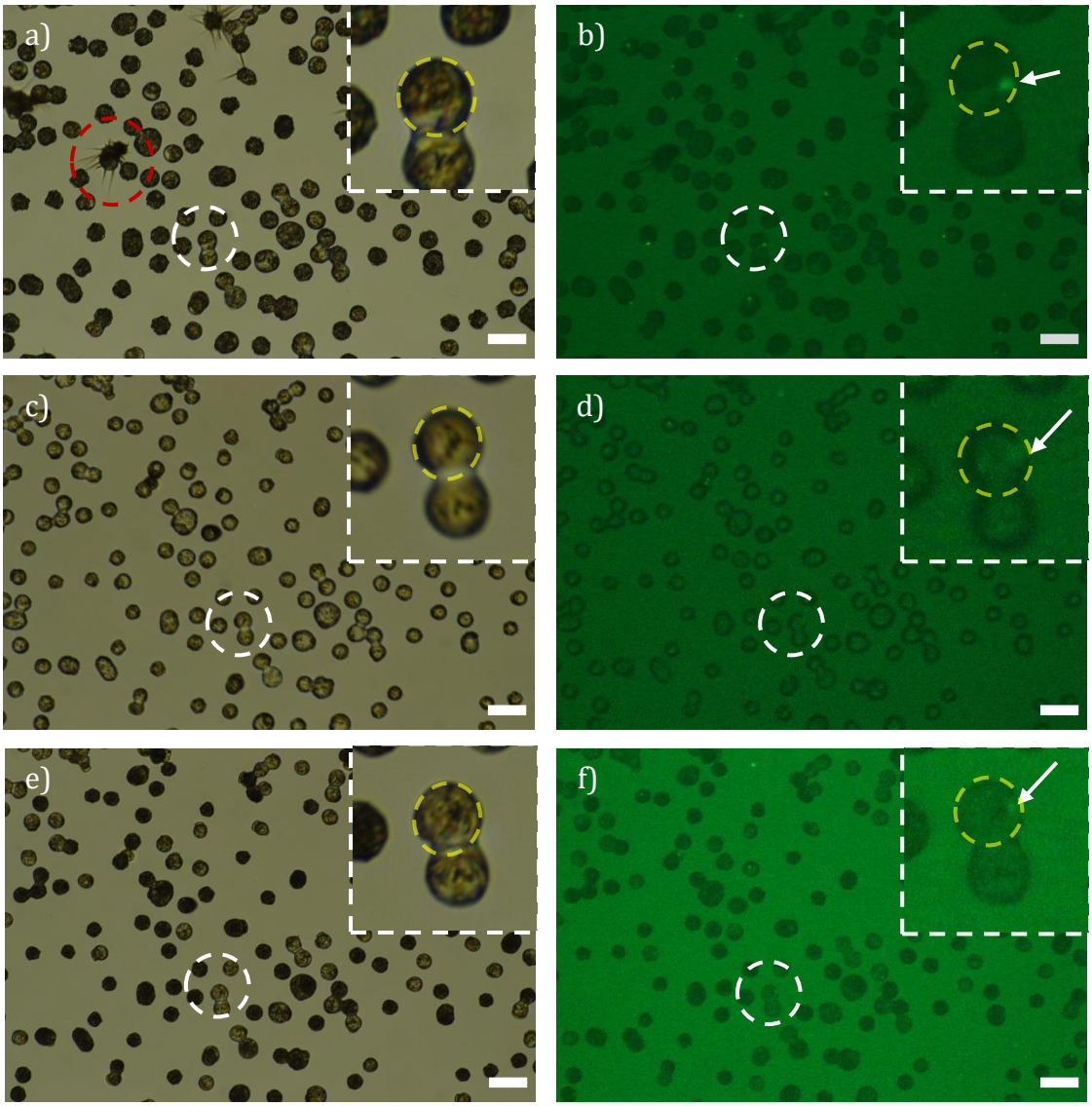

Figure 104: Brightfield (a, c & e) and fluorescence photomicrographs (b, d & f) of bipolar nematic **E3** microparticles from **E3-MF48** containing nanoparticles, at 25 °C before (a & b) and after (e & f) heating above their T_{NI} to 110 °C (c & d) and returning to the nematic phase at 25 °C. 200x magnification, scale bars 50 µm. Particle highlighted zoomed in by 3.8x, shown in top right corner. White arrows indicate nanoparticle locations. PVA crystals highlighted in red.

A second example of nanoparticle location preservation through clearing into the isotropic phase and cooling back into the nematic phase in **E3** particles is shown in Figure 105. The particles shown in the figure were imaged before heating to isotropy and after returning to the nematic phase. The highlighted particles show no movement of the nanoparticles within the elastomer microparticles before and after the temperature experiment, showing the location of the nanoparticles was preserved throughout. Again, problems imaging through crossed polarisers at high temperature through the hotstage meant the nematic texture could not be

observed. Similarly, photobleaching of the fluorescent nanoparticles made imaging challenging, however sufficient brightness persisted in the highlighted particles to determine their location, which was unchanged between the heat/cool cycle.

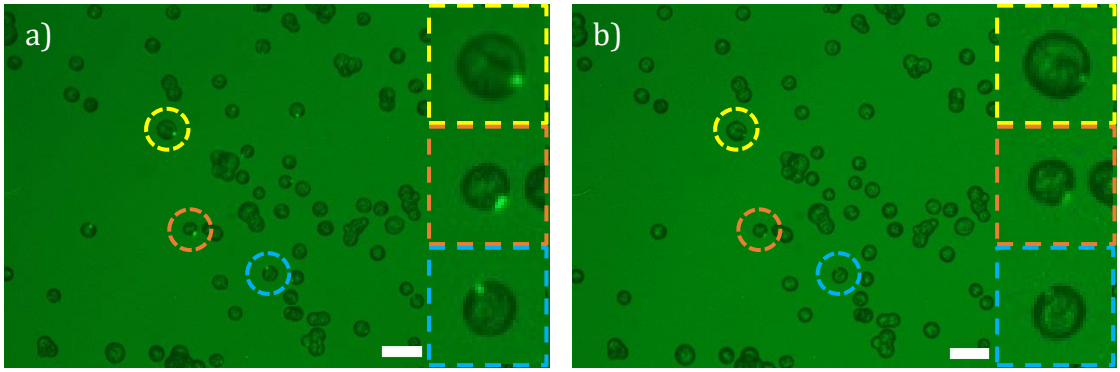

Figure 105: Fluorescence photomicrographs of bipolar nematic E**3** microparticles from **E3-MF34** containing nanoparticles at 70 °C before (a) and after (b) heating above their T_{NI} to 100 °C and returning to the nematic phase. 200x magnification, scale bars 50 µm. Highlighted particles zoomed by 3.3x, shown on the right-hand side of photomicrograph in corresponding colours.

Elastomer particles of **E1** containing nanoparticles were also investigated for their response to temperature. The nematic microparticles infiltrated with nanoparticles were heated at 10 °C/min from their nematic phase, 25 °C (Figure 106a & b), through their T_{NI}, at 116 °C, to 140 °C (Figure 106c & d), before returning to 25 °C (Figure 106e & f). Again, after washing the sample quality was low, with particles sticking together and fluorescence imaging difficult due to photobleaching. Very few particles could be analysed due the sample and imaging quality. However, it can be seen that upon clearing into the isotropic phase shape changes did occur, although much different to those seen in chapter 3 (section 3.3.1.2). The particles appear to adopt more irregular shapes than the expected elongation, including shapes similar to coffee beans and red blood cells. It is thought that, as the droplets and elastomer microparticles produced which contained nanoparticles already showed evidence of distortion and variation of their bipolar confinement, upon investigating the particles' shape change response to temperature the already distorted particles deformed in various, irregular ways due the shape deformation being closely linked to the nematic confinement. As a consequence of photobleaching, two highlighted particles were the only ones in

which the infiltrated nanoparticle could be followed through the heat/cool cycle. It was observed that, similar to in the **E3** elastomer particles, the nanoparticles' location persisted throughout the temperature experiment, including through the reversible shape change about the phase transition temperature. Despite the limitations to analysis of the microparticles' confinement texture, as far as we are aware this is the first actuation of nematic elastomer microparticles which contain nanoparticles.

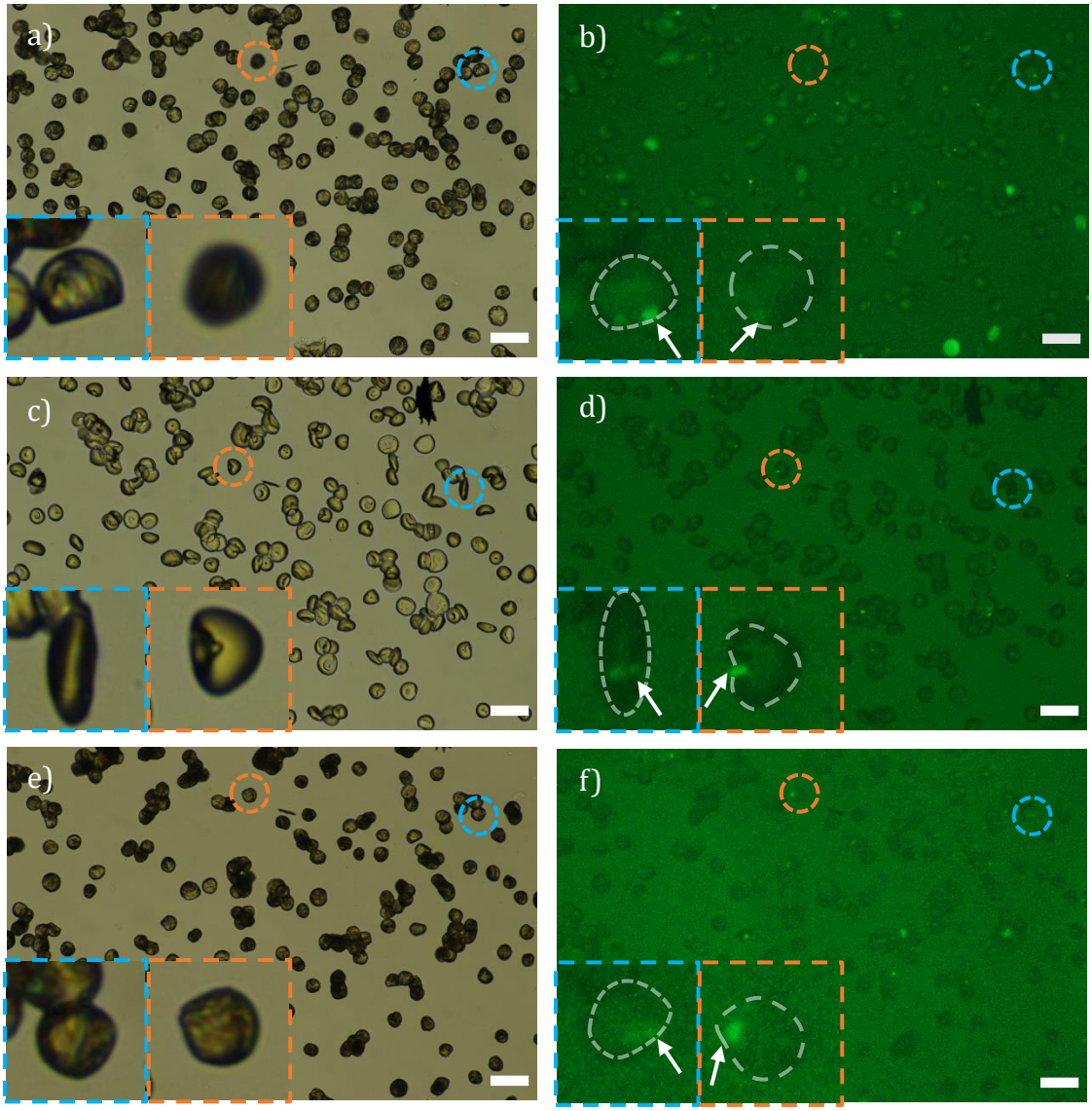

Figure 106: Brightfield (a, c & e) and fluorescence photomicrographs (b, d & f) of bipolar nematic **E1** microparticles from **E1-MF61** containing nanoparticles, at 25 °C before (a & b) and after (e & f) heating above their T_{NI} to 140 °C (c & d) and returning to the nematic phase at 30 °C. 200x magnification, scale bars 50 µm. Particles highlighted zoomed in by 5.2x, shown in top right corner. White arrows indicate nanoparticle locations.

A further example of nanoparticle location preservation throughout an actuation cycle of **E1** nematic elastomer microparticles is shown in Figure 107. Upon clearing, the aspect ratio changed by 55% from 1.15 to 1.78, before returning to 1.16 upon returning to the nematic phase. A 55% change in aspect ratio upon clearing is consistent with the values reported in the chapter 3 for **E1** systems without nanoparticles localised within them. POM imaging through crossed polarisers would have helped to elucidate the location of the nanoparticles with respect to the nematic configuration and defects, but unfortunately the setup did not allow for this. Although it is worth noting that, distortion at the particle seen in the brightfield imaging, may indicate that some contamination or degree of crystallisation was present within the elastomer microparticle.

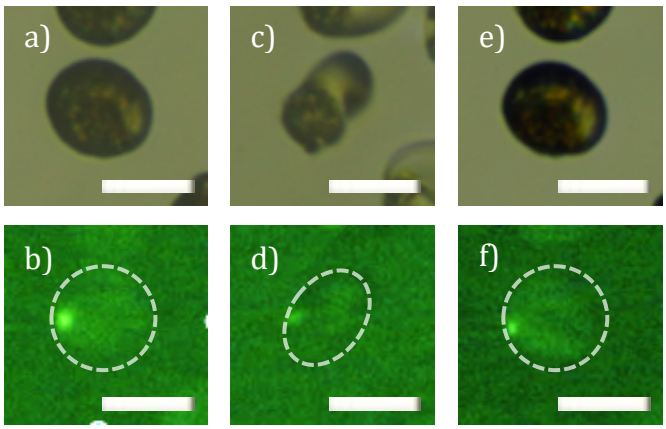

Figure 107: Brightfield (a, c & e) and fluorescence photomicrographs (b, d & f) of a bipolar nematic **E1** microparticle from **E1-MF45** containing one nanoparticle at 25 °C before (a & b) and after (e & f) heating above their T_{NI} to 140 °C (c & d) and returning to the nematic phase at 25 °C. 200x magnification, zoomed by 4.1x and cropped, scale bars 25 μm.

The results discussed here are preliminary and important for setting the foundation for future investigation of actuating nematic elastomer microparticles containing localised nanoparticles with better controlled confinement textures. Unfortunately, this particular area of research within this thesis was affected by a change in project emphasis due to the COVID-19 pandemic and hence, the time to carry out further actuation investigations was no longer available.

4.4 Conclusion

Polymer nanoparticles were dyed and suspended in organic solvent before being loaded into the inner phase of a microfluidic experiment containing nematic monomer, crosslinker and photoinitiator. Randomly oriented nanoparticles were observed in isotropic droplets until solvent evaporation yielded nematic droplets where the nanoparticles became localised at the surface. Where two nanoparticles were present, they were observed to generally localise at the droplet surface at a ~180° angle from each other, suggesting localisation into the bipolar defects present in the nematic droplets due to the elastic forces of the nematic system. Furthermore, POM imaging revealed that nanoparticles were localised at defect sites. Nanoparticle concentration investigations revealed that when several nanoparticles were introduced per droplet, utilising a 7 : 1 nanoparticle to droplet ratio, mesogen alignment was heavily affected and a defined nematic texture was lost. However at a 4 : 1 ratio, many droplets contained no more than two nanoparticles, whilst a fairly defined bipolar nematic configuration was retained, although some slight configuration distortion was observed local to the introduced nanoparticle. The infiltration rates of droplets with nanoparticles were orders of magnitude greater, with rates of up to 66% at a 4 : 1 ratio, when utilising the microfluidic method in comparison to post-production methods where less than 1% of droplets became infiltrated.

Upon polymerisation, the location of nanoparticles within droplets was preserved to produce nanoparticle containing nematic elastomer microparticles. However, the bipolar texture of elastomer microparticles containing nanoparticles became further distorted which meant that imaging was challenging resulting in difficulty determining the location of the topological defects with respect to the nanoparticles. Despite this, where the bipolar texture was clearer in a small sample of microparticles, it could be seen that nanoparticles did appear to still be localised within topological defects.

The temperature response of the synthesised elastomer microparticles was investigated. As far as we are aware, for the first time the actuation of nematic elastomer microparticles of **E1** containing a localised nanoparticle at the surface in response to temperature changes has been demonstrated, whilst the location of

the nanoparticle was preserved throughout the shape change. However, due to difficulty controlling confinement texture through nanoparticle addition, polymerisation and washing of the particles, the shape change was irregular, producing particles of shapes not previously seen in this thesis.

Although the results here were preliminary, they pave the way for future development of these **E1** and **E3** systems containing nanoparticles for possible applications in micromechanics, soft robotics, photonics or, for **E1**, as artificial muscle.[29,30,53,54] It is expected that a nanoparticle infiltrated **E2** system would show comparable results, given the proven actuation response of **E2**, discussed in the previous chapter.

5 Chiral Nematic Systems

For this section, data carried out in the group under my supervision has been assigned (†).

5.1 Overview

In this chapter, the optical and responsive properties of chiral nematic mixtures, films, droplets and microparticles were investigated. Monomers **M2** and **M3** were doped with CB15, molecular structure shown in Figure 6, which is neither liquid crystalline nor polymerisable. These systems were investigated with the aim of producing reflectors of tuneable colours with phase properties which allow for room temperature applications. Mixtures doped with CB15 were utilised so that upon polymerisation the dopant could be extracted and the effect on the properties of the elastomers could be studied.

Previous work in the group has demonstrated that chiral nematic mixtures and elastomer films of **M1** doped with chiral dopant CB15 can be produced where the pitch length could be tuned by altering CB15 concentration such that the wavelength of selective reflection lies within in the visible region therefore producing films in various colours across the spectrum. However, due to the high glass transition in these systems, to access properties like stress responsiveness, high temperatures had to be utilised. As pure **E2** and **E3** have lower glass transition temperatures (17.3 °C and 15.6 °C respectively) than **E1** (42.8 °C),[51] they were employed to produce CB15 doped mixtures with lower glass transitions.[51]

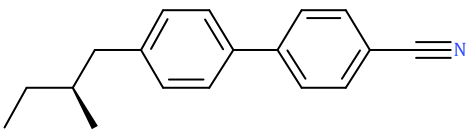

Figure 108: Molecular structure of chiral dopant CB15.

5.2 Chiral Nematic Mixtures and Elastomer Films

In order to assess the feasibility of whether CB15 doped **M2** and **M3** mixtures would be miscible and selectively reflect within the visible light spectrum contact preparations were made up. For the contact preparation the achiral liquid

crystalline material, in these cases **M2** or **M3**, were melted on a glass slide at 80 °C. A coverslip was placed on top. The material was then cooled into the nematic phase and a drop of the chiral dopant, CB15, was placed at the edge of the coverslip and allowed time to mix into the nematogen. As the dopant was placed in a specific area, as it moved through the liquid crystalline monomer it created a concentration gradient of chiral dopant in the nematogen. This meant that a chiral pitch gradient was also present within the samples. Figure 109 shows the photomicrographs from POM in reflection mode of the two contact preparations. Mixing was observed with a concentration gradient across the preparations. The colour of the observed reflection followed this concentration gradient with reflection wavelengths increasing with decreasing CB15 concentration. The resulting colours showed that not only could selective reflection in CB15 doped monomers **M2** and **M3** be tuned by dopant concentration control to be within the visible region of light, but also that the chiral nematic phase was stable at room temperature at the required CB15 concentrations which allowed for the selective reflection to occur within the visible region of light. Hence, mixtures of **M2** and **M3** were determined viable candidates for producing visible light selective reflecting chiral nematic mixtures, films, droplets and microparticles.

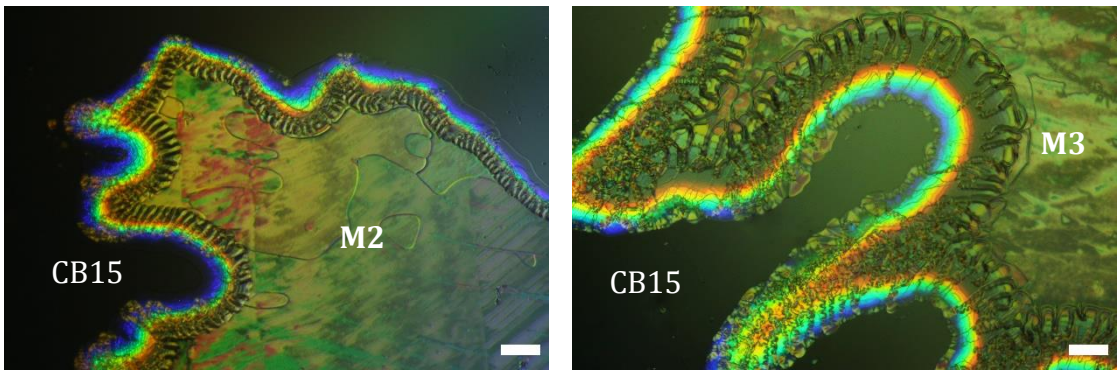

Figure 109: Photomicrographs, taken in reflection mode, of contact preparations of CB15 with: **M2** at 100x magnification, scale bar 100 µm (a)†, **M3** at 200x magnification, scale bar 50 µm.

To prepare elastomer films with selective reflection in the visible region, mixtures were made up of monomer **M2** and **M3** which had been doped with various concentrations of CB15. Mixtures of **M2** or **M3**, CB15, crosslinker 1,6-hexanediol diacrylate (10 mol% w.r.t monomer) and photoinitiator diphenyl(2,4,6-trimethylbenzoyl) phosphine oxide (2 mol% w.r.t monomer) were

prepared. The addition of the photoinitiator and crosslinker from preprepared chloroform stock solutions facilitated uniform mixing as the monomer and CB15 dissolved into the chloroform solution. The chloroform was evaporated at 100 °C before the mixtures were cooled to 80 °C in the isotropic phase and loaded into glass 25 µm planar alignment cells by capillary forces. The mixtures were cooled into the chiral nematic phase and through to room temperature for imaging under POM. Full experimental method can be found in the experimental chapter (section 7.4.1). The composition of each of the films as well as well as the optical properties obtained under POM in conjunction with a temperature controlled hot stage can be found in Table 17.

Table 6: Details of dopant concentration used to produce chiral nematic mixtures for polymerising into films, and their resulting selective reflection colours.

Identifier	CB15 (wt%)	Selective Reflection Colour
M2-CF1†	20	-
M2-CF2†	22	-
M2-CF3†	24	Red
M2-CF4†	26	Red
M2-CF5†	28	Orange
M2-CF6†	30	Yellow-Green
M2-CF7†	32	Green
M2-CF8†	34	Green
M2-CF9†	36	Blue-Green
M2-CF10†	38	Blue
M2-CF11†	40	Purple
M2-CF12†	42	-
M3-CF1	18	-
M3-CF2	23	-
M3-CF3	25	Red
M3-CF4	28	Orange
M3-CF5	30	Yellow
M3-CF6	33	Green
M3-CF7	35	Green
M3-CF8	38	Blue
M3-CF9	40	Purple
M3-CF10	43	-
M3-CF11	45	-

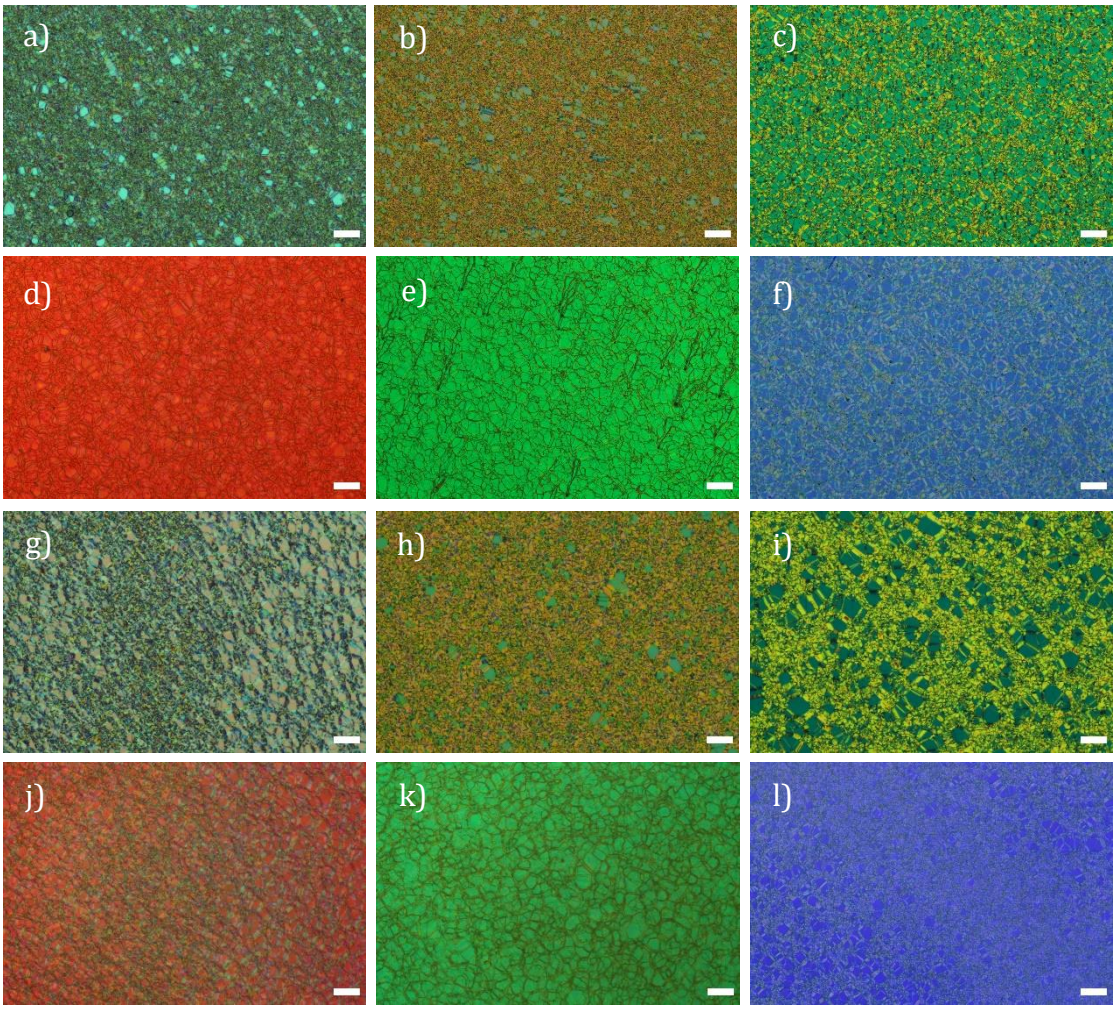

Figure 110: Polarised photomicrographs, taken in transmission mode (a – c & g – i) and reflection mode (d – f & j – l), of CB15 doped mixtures of **M2** and **M3** in alignment cells at 100x magnification, scale bars 100 µm. **M2-CF4** (a & d)†, **M2-CF7** (b & e)†, **M2-CF10** (c & f)†, **M3-CF3** (g & j), **M3-CF7** (h & k), **M3-CF8** (i & l).

Figure 110a – b & g – i show POM imaging in transmission mode at room temperature of some of the chiral nematic mixtures of **M2** and **M3** within alignment cells at various dopant concentrations. It can be seen that each mixture displayed textures with patches of uniform *Grandjean* alignment between the oily streaks which dominated the texture. The presence of *Grandjean* alignment is characteristic of an aligned chiral nematic phase, whereas the oily streaks suggest some deviation from this.

Figure 110d – f & j – l show photomicrographs taken in reflection mode at room temperature of some of the same chiral nematic mixtures which afforded red, green and blue selective reflection. Full data for all mixtures can be found in the experimental chapter (section 7.4.1). It was observed that the minimum

concentration to shorten the chiral pitch such that selective reflection entered the visible range from the infrared (IR) region was 24% CB15 for **M2** and 25% CB15 for **M3**. The maximum concentration required such that selective reflection shifts into the UV region from the visible region was >40% CB15 for both mixtures investigated. Hence, the full visible region of light could be accessed using a CB15 concentration range of ~15%.

Overall, it can be seen that an array of chiral nematic mixtures of CB15 and either **M2** or **M3** were produced which all displayed a well aligned chiral nematic phase, where all colours could be accessed at room temperature.

The chiral mixtures were then heated on a temperature controlled hotstage and imaged under POM to determine the T_{NI} of each mixture, which are plotted in blue in Figure 111, it can be seen that introducing CB15 to both monomers, **M2** and **M3,** reduced the nematic phase stability as a negative linear trend was observed. In the **M3** system for example the nematic to isotropic phase transition temperature decreased from 69.5 °C,[51] obtained by differential scanning calorimetry (DSC), for the pure monomer to 48 – 50 °C, obtained by POM, for the lowest concentration of CB15 investigated, 18%. CB15 is not liquid crystalline itself therefore acts as an impurity in the system, disrupting alignment and reducing phase stability as the CB15 concentration increases.

The mixtures within the alignment cells were photopolymerised 15 cm away from a 365 nm Omnicure LX500 LED UV source at 50% intensity for 10 minutes in the chiral nematic phase (35 °C for **M3-CF1**, 30 °C for **M3-CF2** or at room temperature for the remaining films). Optical properties of the elastomer films were recorded using POM (shown later in Figure 113) before the alignment cells were opened by submerging in liquid nitrogen and prising open with a scalpel blade. Further optical and thermal properties of the elastomer films was recorded using UV-Vis-NIR spectroscopy and DSC. The full polymerisation method and conditions can be found in the experimental chapter alongside optical and thermal properties of the elastomer films (section 7.4.1, Table 18).

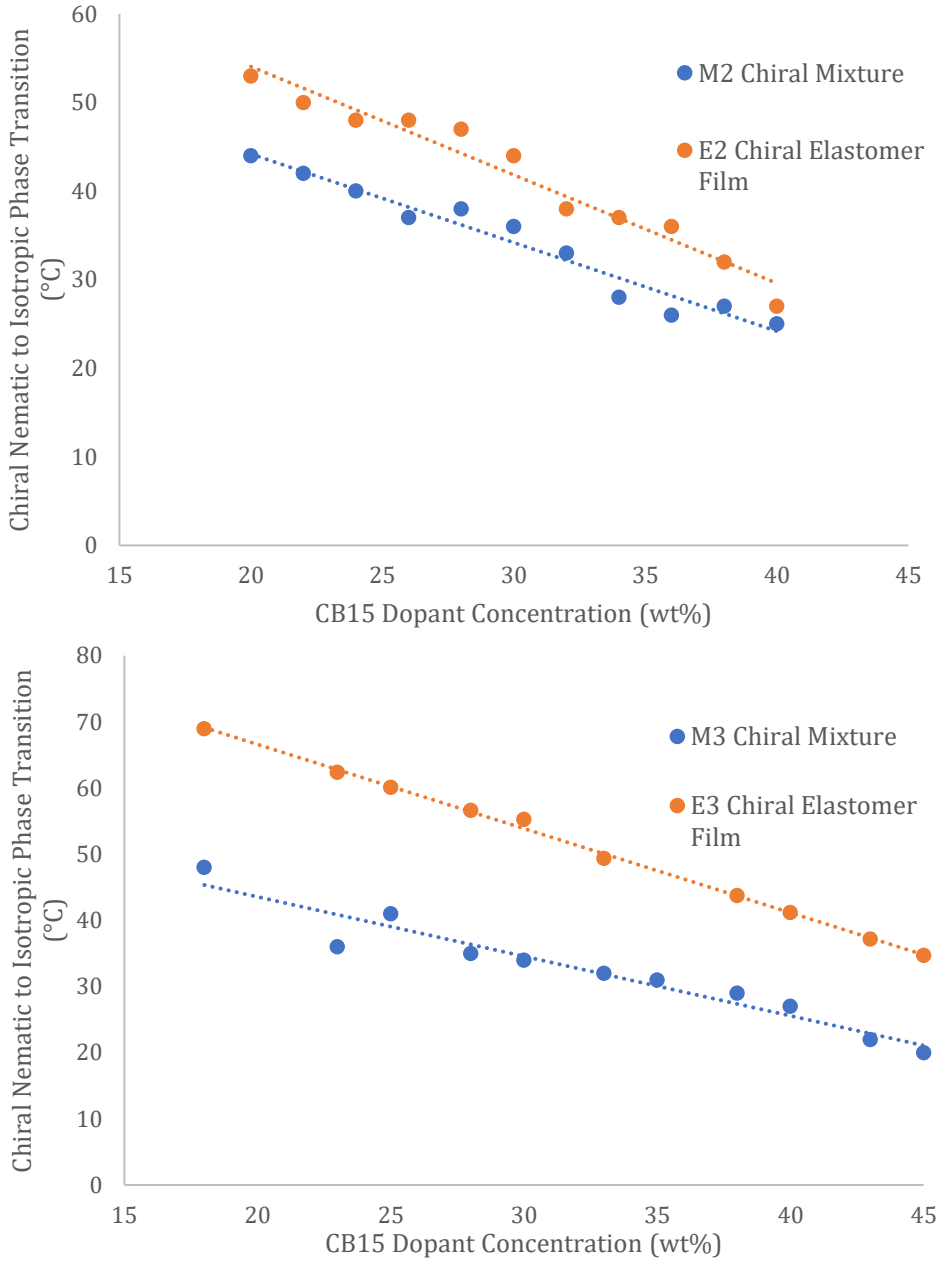

Figure 111: Graphs showing the effect of increasing CB15 concentration on the T_{NI} in chiral nematic mixtures and elastomer films of **M2** and **E2** (top)† and **M3** and **E3** (bottom).

The phase transition temperatures were plotted against CB15 concentration, displayed in Figure 111. For monomer mixtures and **E2** elastomer films, transition temperatures observed in POM on heating at 10 °C/min were plotted; for **E3** elastomer films onset phase transition temperatures were obtained by DSC and plotted. **E3-CF7** was later used for dopant washout so a DSC was not run, hence the missing data point. **E2** and **E3** have higher phase stability that **M2** and **M3**. The chiral nematic phase was stabilised in both mixtures as characterised by the increase in phase transition temperature between the chiral mixture and the chiral

elastomer. The increase in stability arose due to the elastomer backbone reducing the freedom of the mesogens, holding them in place.[3] However, negative gradients were found for all of the systems, showing that the pure monomer and pure elastomers had greater nematic phase stability than any CB15 doped mixtures and elastomers investigated. Furthermore, the trendline gradients for the graphs of T_{NI} against CB15 concentration plotted in Figure 111 were calculated and are reported in Table 7. It can be seen that for both monomer mixtures, **M2** and **M3**, the gradients were not as steep than their polymerised elastomer counterparts, observed only slightly in **E2** but more pronounced in **E3**. Increasing the CB15 concentration in the elastomer not only acted as a decrease in material purity, like in the chiral mixtures, but had a secondary effect of reducing the volume of polymer per volume of material so there was less of the stabilising effect of polymer chains supporting the chiral nematic alignment. Hence, the T_{NI} dropped off more rapidly compared to in a mixture where the dominating factor in reducing the phase transition was CB15 acting as an impurity. Also in Table 7 is a calculated intercept of the trendline, indicating where the T_{NI} for the pure monomer and elastomer would be according to the trendline equation. When compared to the actual T_{NI} of the pure monomer and elastomer, also reported in the table, it can be seen that these values are close but not the same. It is likely that this error stems from the fact that the T_{NI} of the pure material was measured by DSC, whereas the data which generated the plots in Figure 111 was recorded under POM.

Table 7: Shows the gradient, y-intercept and R^2 value of the trendlines produced from graphs of T_{NI} against CB15 dopant concentration for **M2**, **E2**, **M3** and **E3** shown in Figure 111. TNI of pure material data obtained previously in the group by DSC at a 10 °C/min heat/cool rate. Phase transition temperature taken from peak onset on heating; glass transition temperature taken from the midpoint on cooling.[51]

CB15 Doped Material	Trendline Gradient (Δ°C/wt%)	R^2	Trendline Intercept (°C)	T_{NI} of Pure Material (°C)
M2	-1.0	0.96	64	70.8
E2	-1.2	0.96	78	76.0
M3	-0.9	0.93	62	69.5
E3	-1.3	0.99	92	86.3

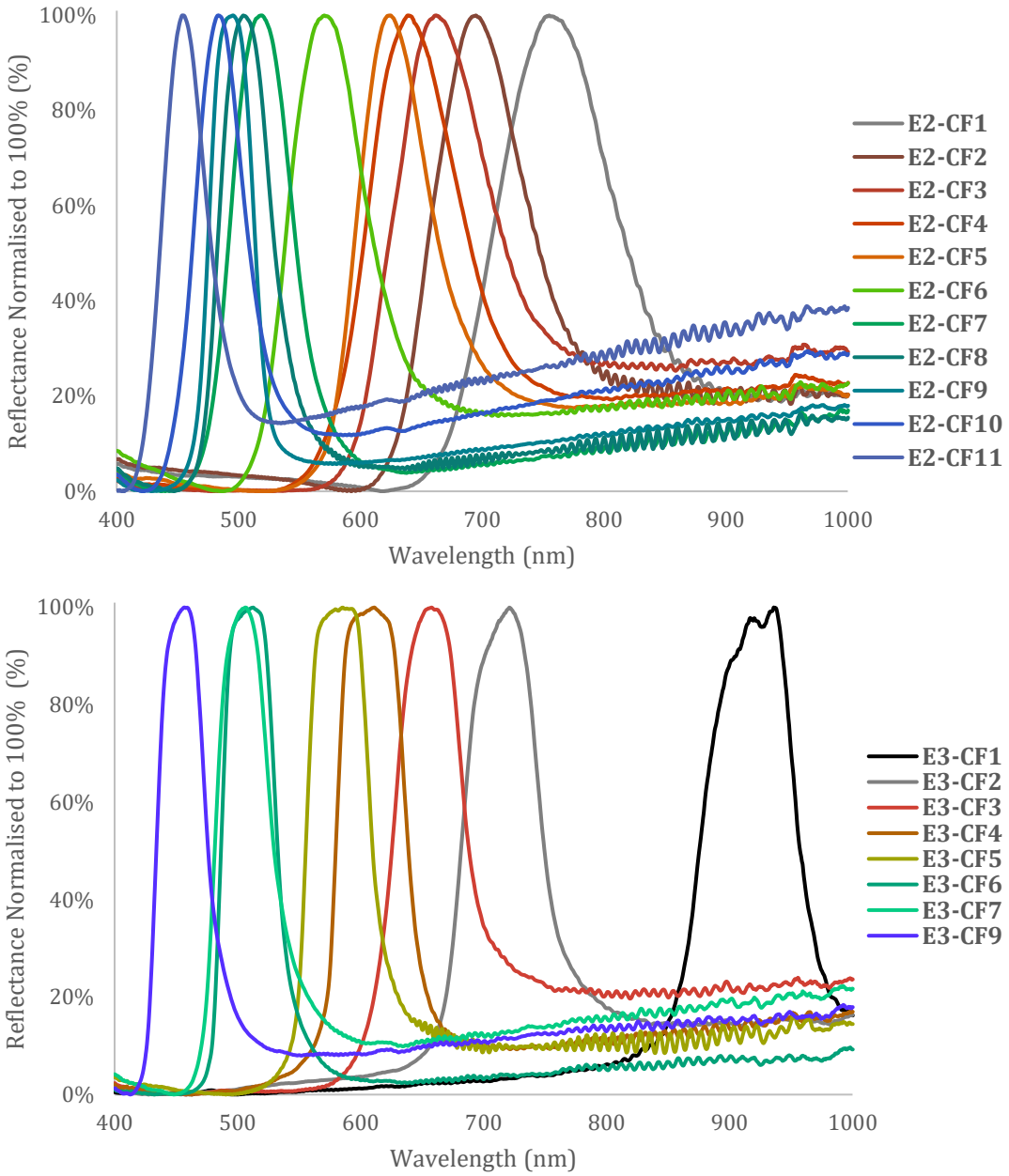

Figure 112: UV-Vis-NIR reflection spectra at room temperature for CB15 doped chiral nematic elastomers of **E2**† (top) and **E3** (bottom).

Figure 112 shows the UV-Vis-NIR spectra for the films which corresponds to the selective reflection colours, with examples shown in Figure 113, as well as λ_{max} values reported in the experimental chapter (section 7.4.1, Table 18). The alignment cells were opened so that the film was supported underneath by one half of the glass cell. The UV-Vis-NIR spectra were collected at room temperature in reflection mode to show the selective reflection bands of each **E2** and **E3** film from the UV regions, across the visible region and into the near IR (NIR) region.

Some periodicity can be seen in the baseline, particularly in the NIR region which is thought to be due to the mounting of the film on a glass half alignment cell and the refractive index differences of the materials.

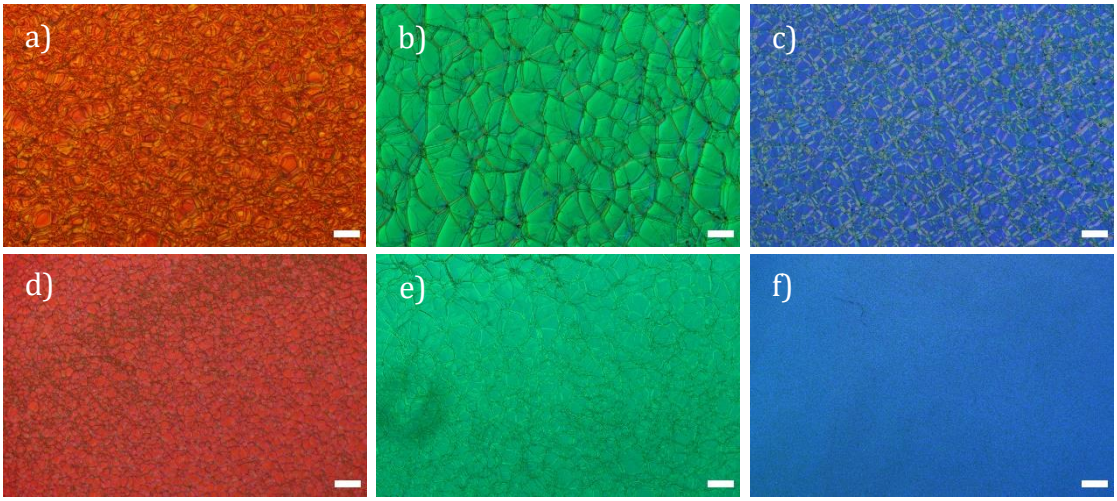

Figure 113: Photomicrographs, taken in reflection mode, of CB15 doped films of **E2** and **E3** in alignment cells at 100x magnification, scale bars 100 μm. **E2-CF4** (a)†, **E2-CF7** (b)†, **E2-CF10** (c)†, **E3-CF3** (d), **E3-CF7** (e), **E3-CF8** (f).

The minimum CB15 concentration to exhibit selective reflection in the visible region, the red films, for **E2** was 22% and 25% for **E3**; whilst the maximum, the blue films, was 40% for both elastomer systems investigated. In comparison to the mixtures these films were produced from, as seen in Figure 110d – f & j – l, there was a small blue-shift of some of the reflected colours. For example, when comparing the bright red selective reflection in Figure 110d with the polymerised counterpart in Figure 113a we can see the colour of the selective reflection shifted to more of an orange-red colour showing a slightly shorter wavelength of light was reflected. Upon polymerisation, as new bonds form small volume contraction occurs, leading to slight shrinkage of the film. The shrinking of the film in turn causes shortening of the chiral pitch which is observed as a small blue-shift.

The UV-Vis-NIR spectra and photomicrographs taken in reflection mode show that the chiral nematic elastomers produced of **E2** and **E3** both show facile tunability to reflect wavelengths of light of any colour. Not only this but any colour can be accessed at room temperature due to the excellent phase stability of the elastomer films. Selective reflection wavelength shifts with altering chiral dopant

concentration was exploited by van Delden and Feringa, like seen in **E2** and **E3**, to predict the enantiomeric excess (ee) using selective reflection colour. They mixed chiral compounds with various levels of ee into an achiral reactive mesogen mixture known as 'E7'. Due to the helical twisting power of the chiral mixtures, the chiral pitch was proportional to the ee and therefore selective reflection colours could be used to determine, the ee of the initial chiral mixture.[180] It may be possible that **E2** and **E3** mixtures could be candidates as molecular chirality indicators in chiral mixtures with similar helical twisting powers to CB15, given their visible selective reflection colours accessible at room temperature.

5.2.1 Chiral Imprinted Elastomer Films

In this section CB15 doped films of **E2**† and **E3** were washed with organic solvent to investigate the consequences of chiral removal on the properties of the nematic elastomers.

Alignment cells containing films **E2-CF1–11** and **E3-CF7** had been opened so that the films were allowed to stay on one side of the open glass alignment cell to act as a support for the film whilst it was washed with acetone five times. For these washes, ~1 mL acetone was washed over the elastomer film, using a pipette, swelling the elastomer film. The films swelled and became isotropic due to the loss of chiral nematic order, appearing black under crossed polarisers. The acetone was then dabbed up using paper roll to remove it as well as the CB15 which was released from the film matrix upon swelling and dissolution into the acetone. The remaining acetone was allowed to evaporate, at which point chiral nematic order returned and the films became birefringent again. Washing was repeated five times to ensure the CB15 was fully removed, which was confirmed by the loss of film volume, observed by cracking under imaging, as well as selective reflection changes discussed below.

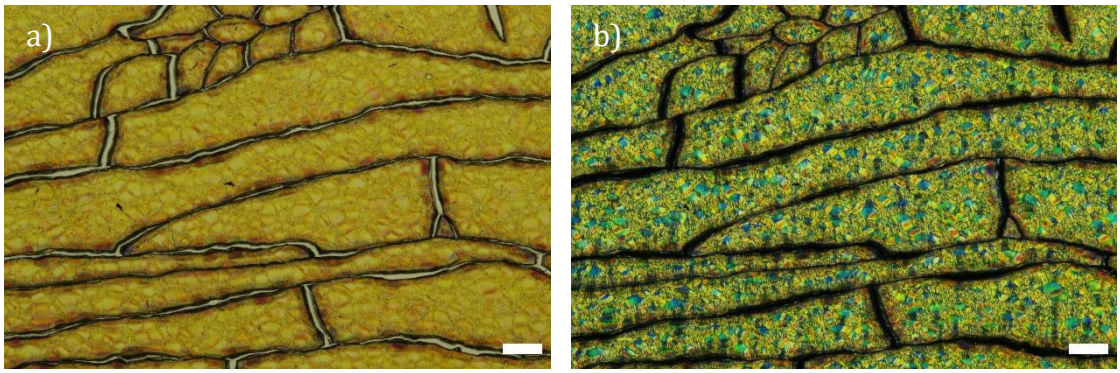

Figure 114: Brightfield (a) and polarised (b) photomicrographs of **WE2-CF4** at 100x magnification, scale bars 100 μm.†

Figure 114 shows **E2-CF4** elastomer film after acetone washes under brightfield and POM imaging, **WE2-CF4**. It can be seen that after the acetone washes, a chiral nematic phase returned as seen by the characteristic *Grandjean* texture under POM. Furthermore, large cracks can be seen across the film in the brightfield images, showing that as the CB15 was removed, cracking occurred due to volume reduction of the film.

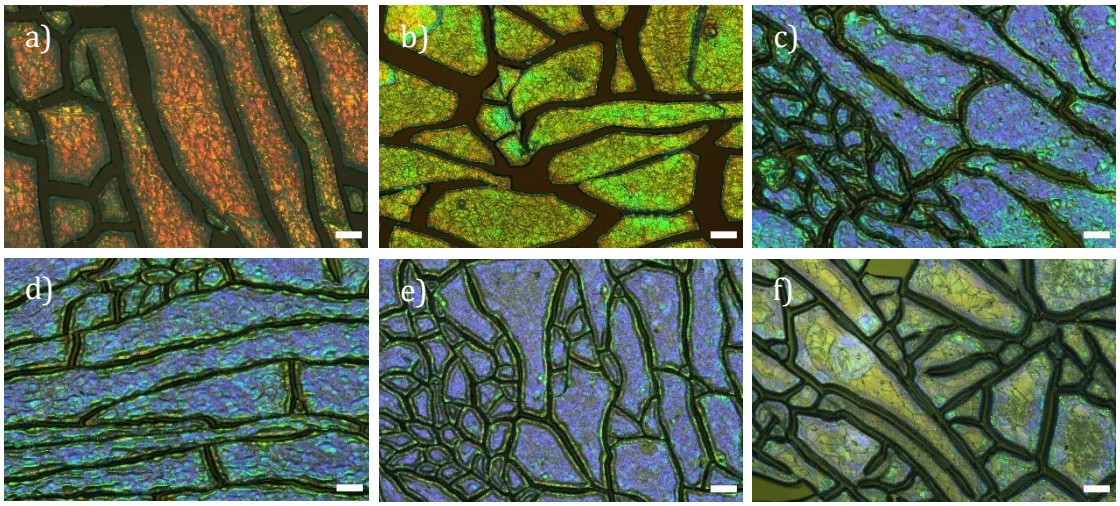

Figure 115: Photomicrographs, taken in reflection mode, of washed **E2** elastomer films at 100x magnification, scale bars 100 μm. **WE2-CF1** (a), **WE2-CF2** (b), **WE2-CF3** (c), **WE2-CF4** (d), **WE2-CF5** (e), **WE2-CF6** (f).†

Under reflectance imaging, it was observed that selective reflection colours which had blue-shifted from the pre-washed films, were present for **WE2-CF1–5**, photomicrographs taken in reflection mode can be seen in Figure 115. UV-Vis-NIR spectroscopy confirmed the blue-shift of the selective reflection with λ_{max} values

reported in the experimental chapter (section 7.4.1, Table 19), found from the spectra shown in Figure 116. In the UV-Vis-NIR spectra, it could be seen that generally the baseline shifted upwards after washing, this can be attributed to the degradation of quality of films post-wash which contained the large cracks seen in the imaging which allowed for greater reflectance. The sensitivity of the UV-Vis-NIR probe meant that λ_{max} values below ~400 nm could not be reported; hence the blue-shift effect meant a final λ_{max} could not be recorded for **WE2-CF6–11** however Figure 115f confirms it is not in the visible region by the observation of the loss of bright reflection colours as selective reflection shifted into the UV region, the colours seen in this photomicrograph are not sure to selective reflection, they are due to birefringence.

a)

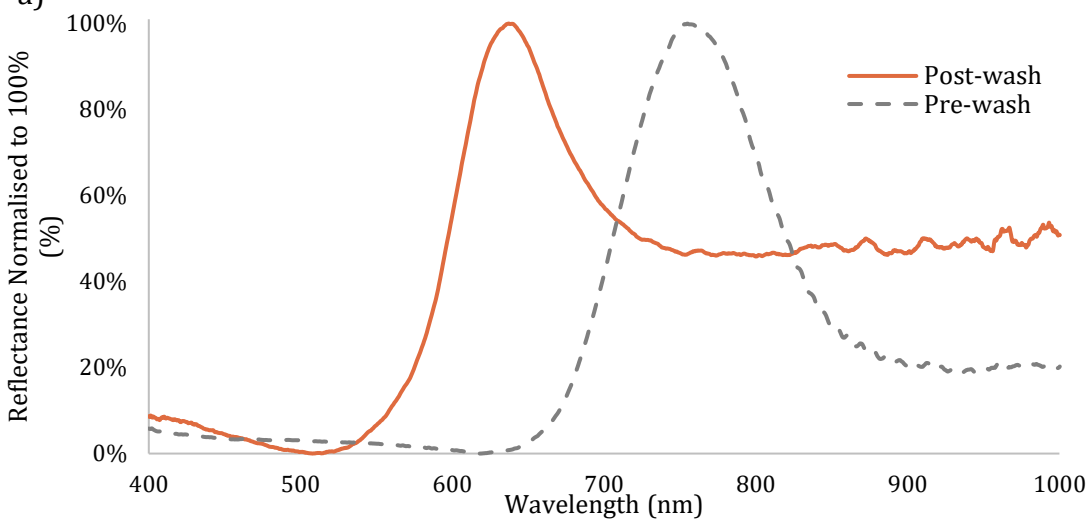
Reflectance Normalised to 100% (%)
100%
80%
60%
40%
20%
0%
400
500
600
700
800
900
1000
Wavelength (nm)
Post-wash
Pre-wash

b)

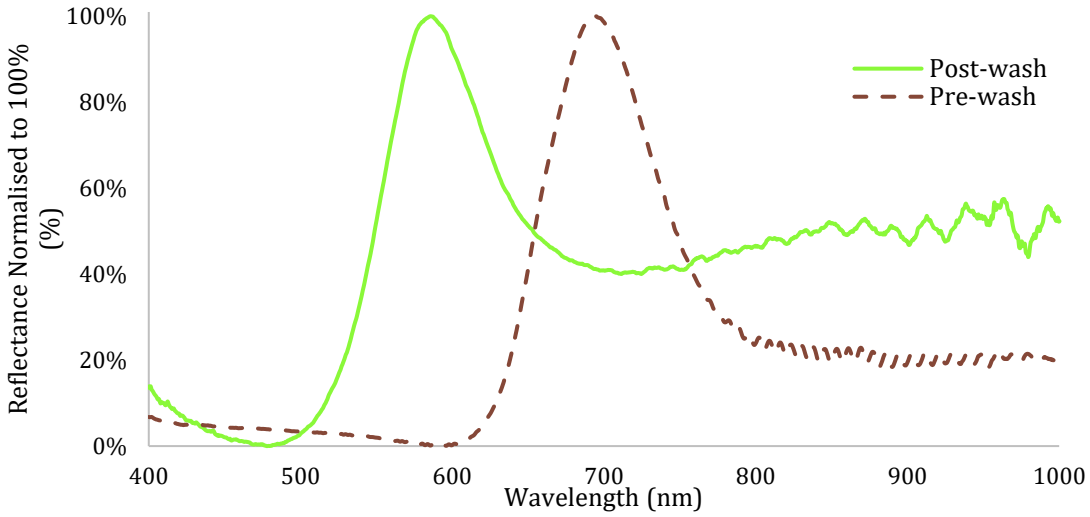
Reflectance Normalised to 100% (%)
100%
80%
60%
40%
20%
0%
400
500
600
700
800
900
1000
Wavelength (nm)
Post-wash
Pre-wash

c)

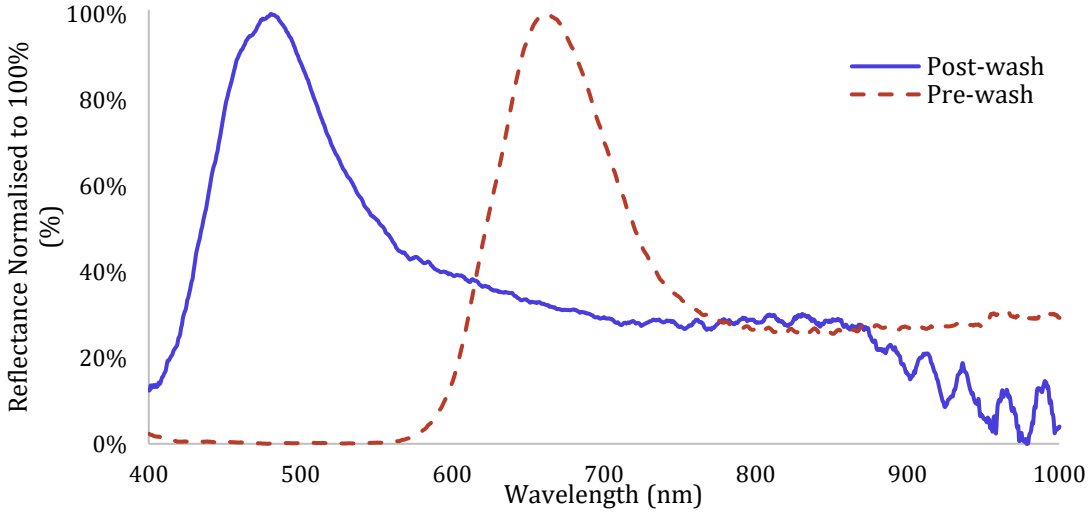
Reflectance Normalised to 100% (%)
100%
80%
60%
40%
20%
0%
400
500
600
700
800
900
1000
Wavelength (nm)
Post-wash
Pre-wash

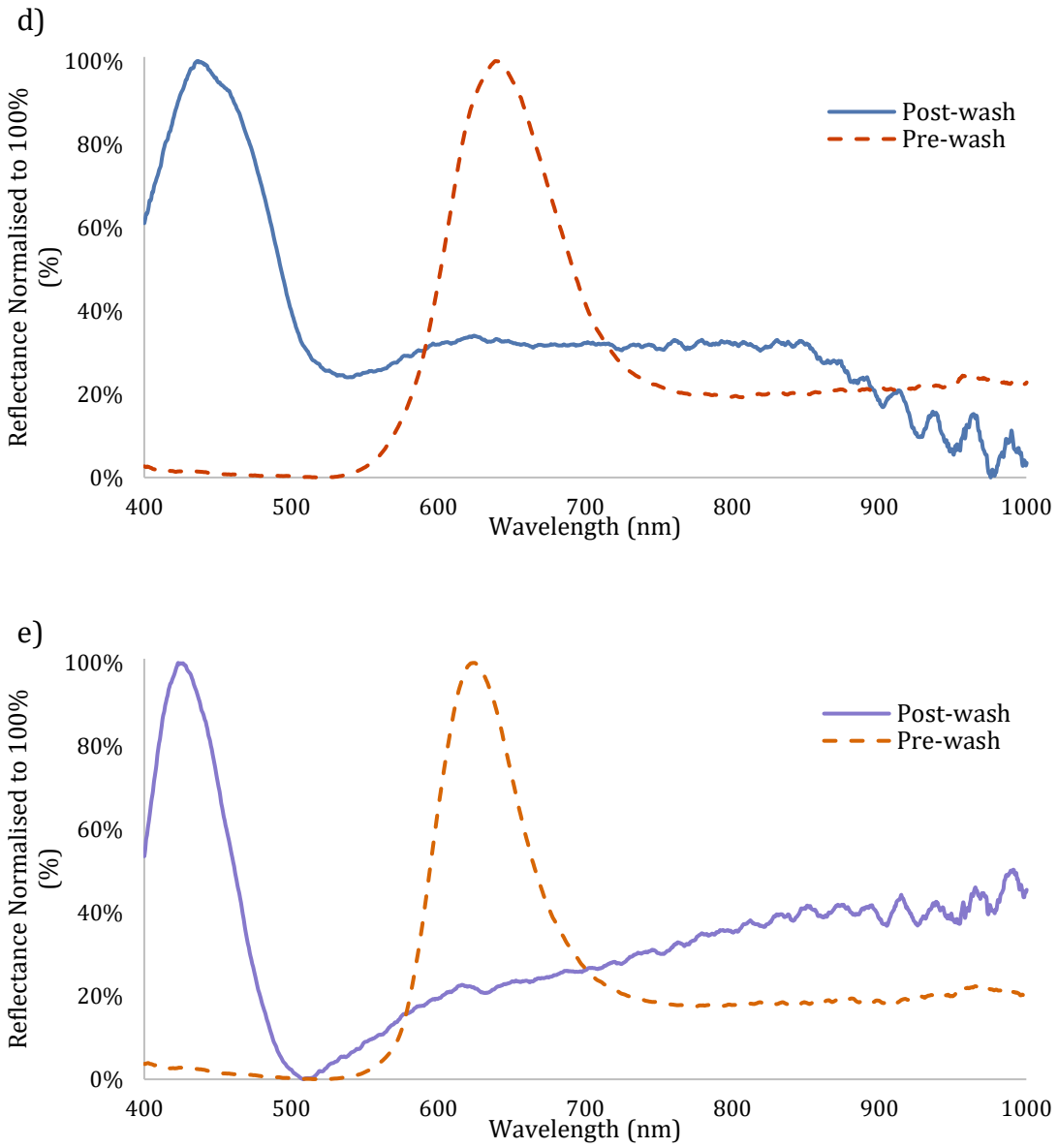

Figure 116: UV-Vis-NIR reflection spectra at room temperature for CB15 doped chiral nematic elastomer films and acetone washed elastomer films. **E2-CF1** & **WE2-CF1** (a), **E2-CF2** & **WE2-CF2** (b), **E2-CF3** & **WE2-CF3** (c), **E2-CF4** & **WE2-CF4** (d) and **E2-CF5** & **WE2-CF5** (e).†

For the acetone washed **E3** film, **WE3-CF7** on the other hand, a polydomain nematic phase was observed through crossed polarisers under POM and no bright selective reflection colours were seen in reflection mode shown in Figure 117. The bright green colour seen in Figure 113e was no longer observed and UV-Vis-NIR spectroscopy, shown Figure 118, confirmed that no selective reflection bands were present.

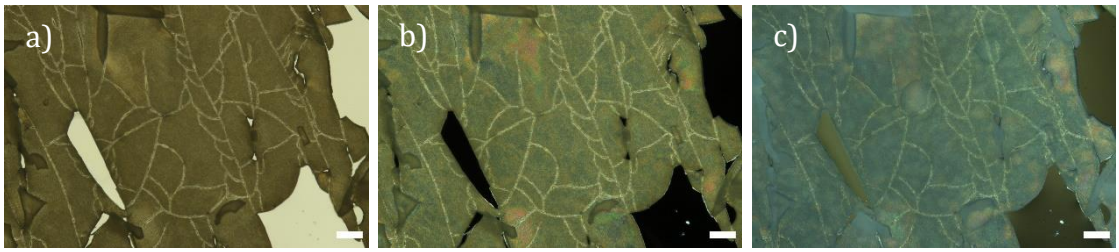

Figure 117: Brightfield (a), polarised (b) and reflection mode (c) photomicrographs of **WE3-CF7** at 100x magnification, scale bars 100 μm.

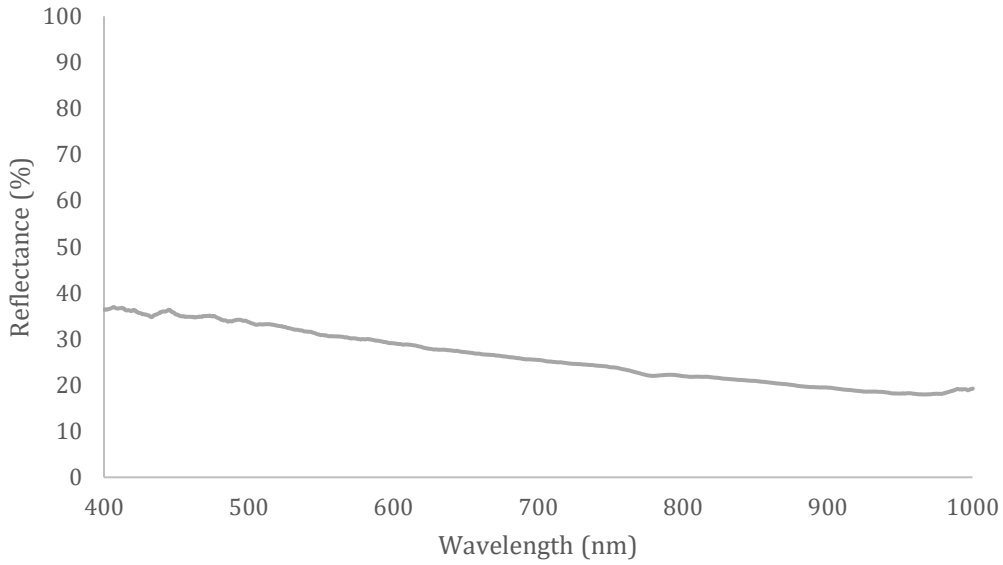

Figure 118: UV-Vis-NIR reflection spectra of **WE3-CF7** at room temperature.

These results indicate that the chiral superstructure had been imprinted on the elastomer films of **WE2**, as shown by the persistence of selective reflection, but had not been imprinted on the elastomer of **WE3**, as shown by the lack of selective reflection. Upon polymerisation and crosslinking, the elastomer matrix was produced within the chiral nematic environment, and thus the elastomer matrix itself possessed the helical superstructure due to coupling between the helical mesogen arrangement and polymer backbone. When the CB15 was washed out with acetone, the helices of the elastomer matrix persisted due to the crosslinking. This is known as chiral imprinting as the helical structure was imprinted into the polymer network after the chiral dopant was removed to produce a chemically achiral superstructure.[34,36] Because the **WE2** elastomer had a large degree of coupling between mesogen and elastomer backbone, the imprinted elastomer matrix held the mesogens in the helical arrangement, allowing for the chiral

nematic phase to still be observed, as well as selective reflection. However, as there was a lack of coupling between the mesogen and elastomer backbone in **WE3**, due to the long spacer group, the anisotropic mesogen alignment within the chiral superstructure was not imprinted into the elastomer matrix and hence when the chiral dopant was removed, no chiral superstructure persisted and thus no selective reflection or chiral nematic texture was observed post-wash, and nematic alignment was favoured.

The blue-shift in selective reflection observed in **WE2** was typical of dopant removal in chiral nematic elastomers due to the volume reduction, responsible for the cracking observed also. Further volume reduction may be attributed to removal of some non-polymerised monomer. The volume reduction resulted in compression of the imprinted helical pitch of the elastomer network. In turn this induced a shorter pitch in the mesogenic helices formed, by coupling to the elastomer backbone. Hence, shorter wavelengths of light were selectively reflected. This contraction in the helical pitch reduced the wavelength of the selectively reflected light as observed by the blue-shift.[34–38] When more CB15 was washed out, the volume reduced more and therefore the helical pitch reduced by a greater degree. Hence, as the concentration of CB15 increased, the change in λ_{max} also increased. For example, In **WE2-CF1** the λ_{max} decreased by 119 nm after washing CB15 from the 20% doped elastomer, whereas in **WE2-CF5** the λ_{max} decreased by 202 nm after washing CB15 from the 28% doped elastomer.

CB15 dopant was successfully washed out of elastomer films composed of **WE1**, using acetone previously in the group which, as with **WE2** investigated here, resulted in chiral imprinting of the films. This was due to the similar structure of **WE1** and **WE2**, where a short spacer of only 4-carbons long between the mesogen and elastomer backbone was found in both systems. Furthermore, selective reflection in **WE1** was found to blue-shift upon removal of the CB15 dopant, which occurred at a similar degree to those in **WE2**. Changes in λ_{max} were reported between 104 and 280 nm reported for dopant concentrations of 14 – 35%.

It was found that the helical superstructure imparted by the chiral dopant had imprinted on the elastomer upon polymerisation so when the dopant was washed out, the helices endured. Chiral imprinting is a known phenomenon fairly sparsely

reported in literature[34–38]. Noh and Park reported chiral imprinting of 'RMM727' elastomer films with CB15 at various concentrations from 20 – 31 wt% where selective reflection blue-shifted by a similar degree to **WE1** and **WE2**, ~189 – 208 nm depending on the initial concentration.[37,51]

The optical effects of chiral imprinting may lead to applications in drug delivery as indicators a chemical has been withdrawn from the elastomer, or even enantiomer separation in the chiral voids left behind by the dopant after it has been removed.[181,182] The **WE2** elastomer films reported in this chapter, and their pre-washed counterparts, have shown the ability to access tuneable selective reflection wavelengths at room temperature with good phase stabilities making real world applicability viable.

5.2.2 Responsiveness of Films

5.2.2.1 Temperature Response

The temperature response of some of the chiral elastomer films prepared was investigated by cutting a small sample of film and placing it in a droplet of PEG 200 on a microscope slide which was then covered with a coverslip. The mounted sample was then placed on a temperature controlled hot stage and the response monitored under POM in reflection mode.

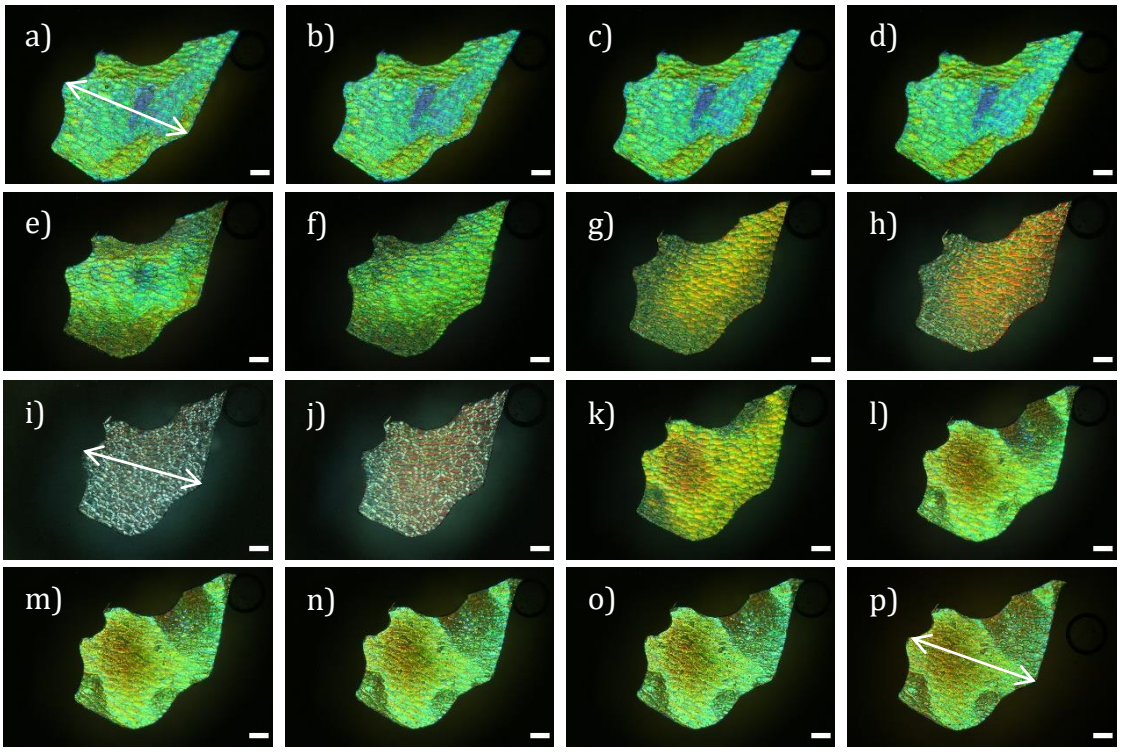

Figure 119: Polarised photomicrographs taken in reflection mode of a heat/cool cycle at 10 °C/min of a cut sample of **WE2-CF1** in PEG 200 taken at 100x magnification, scale bars 100 µm. Imaged at 25 °C (a), 35 °C (b), 45 °C (c), 55 °C (d), 65 °C (e), 75 °C (f), 85 °C (g), 85 °C (h), 90 °C (i), 85 °C (j), 75 °C (k), 65 °C (l), 55 °C (m), 45 °C (n), 35 °C (o) and 25 °C (p).† White arrows show dimension in which film was measured.

The temperature response of a sample of a free-standing film piece of **WE2-CF1** can be seen in Figure 119. Upon removal from the alignment cell and suspension in PEG 200 a blue-shift in the selective reflection was seen from red to green, possibly as a response of stress introduced by cutting the film, or also as a result of the film releasing away from the alignment cell surface. It can be seen that as the film was heated there was little response up until 75 – 85 °C where a red-shift occurred as the reflection of the film shifted from green through yellow to red shortly before passing the phase transition into the isotropic phase at >90 °C. The red-shift occurred as the chiral nematic system began to lose order, indicating an expansion of the chiral nematic pitch before the isotropic phase transition. Upon cooling, the colour of selective reflection returned to mostly green but domains of more of an orange colour did persist showing the selective reflection response to temperature was not fully reversible. This could be due to the fact that the film was cut at room temperature which was below the glass transition temperature of the

film (26.8 °C)† which could have introduced stresses which were not replicated after clearing and cooling back into the chiral nematic phase.

The width of the film indicated by the arrows in Figure 119a, i & p was measured at the start temperature of 25 °C to be 691 μm, close to clearing at 90 °C to be 633 μm and finally after cooling back to the start temperature of 25 °C to be 690 μm. This shows that, corresponding to the helix expansion, there was a contraction in the width of the film by 8% upon heating, which upon cooling did return to the initial dimensions of the film. Overall, the results indicate an actuation temperature response which was reversible. This is consistent with the findings of previous work in the group using washed out CB15 doped **E1** films, where a reversible shape change about the phase transition was observed. Again, this is due to the strong coupling between mesogen and polymer backbone in **E1** and **E2**, and hence the loss of order is transmitted to the elastomer network and results in a shape change. Varanytsia *et al* produced chiral nematic elastomer films from a reactive chiral mesogen, 'A*-60CB', and crosslinker which selectively reflected light in the visible region.[28] When the film was heated from the glassy state at 22.8 °C, to above the glass transition into the rubbery state at 74.4 °C a decrease in the top surface area of the film was observed from 23.64 mm^2 to 20.90 mm^2. To conserve volume the film thickness must have increased, increasing the chiral pitch and therefore red-shifting selective reflection of the film. In addition, Zhang *et al* produced chiral nematic elastomer films from a mixture of chiral and achiral mesogens with crosslinker to yield a chiral nematic main chain elastomer. When heated from 22 – 102 °C a dramatic shape change occurred, due to the main chain attachment of mesogen to the elastomer backbone, with the length of the film decreasing by 40%, although the system had a T_{NI} > 171 °C.[183]

However, there is a clear benefit in **E2** over **E1**, and even the elastomers produced by Zhang *et al* despite the much smaller actuation, in that the phase transition and actuation temperatures were lower and therefore more useful in real world applications.

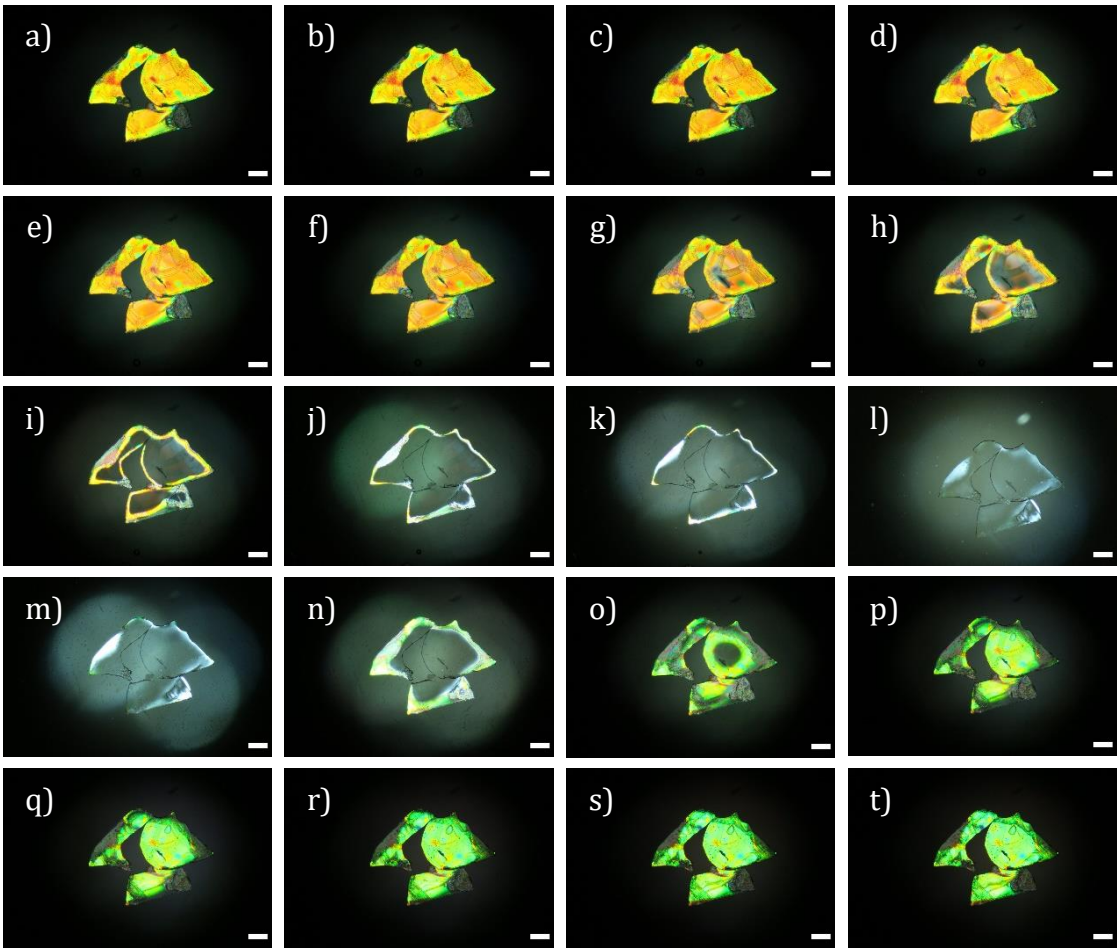

Figure 120: Polarised photomicrographs taken in reflection mode of the first heat/cool cycle at 10 °C/min of a cut sample of **E3-CF2** in PEG 200 taken at 100x magnification, scale bars 100 µm. Imaged at 25 °C (a), 34 °C (b), 46 °C (c), 53 °C (d), 64 °C (e), 69 °C (f), 72 °C (g), 74 °C (h), 77 °C (i), 83 °C (j), 89 °C (k), 100 °C (l), 86 °C (m), 78 °C (n), 69 °C (o), 60 °C (p), 53 °C (q), 40 °C (r), 31 °C (s) and 25 °C (t).

The temperature response of **E3-CF2** was also investigated and the photomicrographs for an initial heat/cool cycle can be seen in Figure 120. Again, upon removing from the alignment cell and suspending in PEG 200 a blue-shift occurred in the selective reflection from the IR region into orange. When the film was cut stresses were introduced which meant that the film was not fully flat or of constant thickness, this can be seen particularly around the edge of the film, where shorter wavelengths of light were reflected than the centre of the film. As the temperature increased there was little response up to clearing, which began at ~72 – 74 °C. Above these temperatures the film cleared into the isotropic phase. Contrary to **WE2-CF1**, no red-shift occurred just before the nematic to isotropic phase transition in the **E3** film due to decoupling caused by the long spacer. The dimensions of the film did not change upon clearing and hence the chiral pitch was

not expanded. Upon cooling the film did not return to the original orange colour, instead a shorter chiral pitch arose giving rise to green selective reflection. It is unclear why the chiral pitch contracted, however a second heat/cool cycle, shown in Figure 121a – o, showed that heating to clearing and back a second time did show a reversible change back to green. The film was left for 3 days after the second heat/cool cycle and imaged again, shown in Figure 121p, it can be seen that regions of the film had red-shifted to yield some yellow selective reflection suggesting that, if left long enough, the film may red-shift further to the starting colour of orange. Unfortunately, time constraints meant that this could not be investigated. The property of having the film return to a different colour to the starting colour seen in this film gives it a potential application as an indicator to show that a temperature change has occurred in the past, which could be useful in applications with temperature sensitive materials.

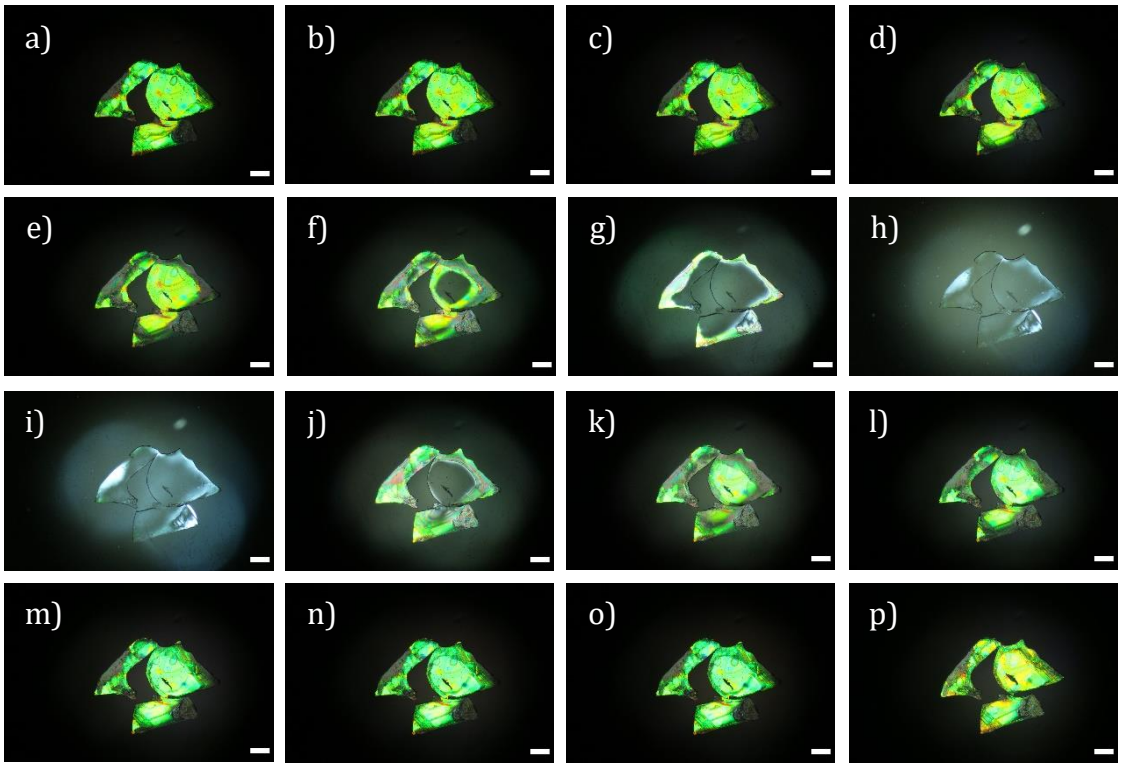

Figure 121: Polarised photomicrographs taken in reflection mode of the second heat/cool cycle at 10 °C/min of a cut sample of **E3-CF2** in PEG 200 taken at 100x magnification, scale bars 100 µm. Imaged at 30 °C (a), 40 °C (b), 50 °C (c), 60 °C (d), 70 °C (e), 78 °C (f), 87 °C (g), 100 °C (h), 90 °C (i), 76 °C (j), 68 °C (k), 56 °C (l), 40 °C (m), 30 °C (n), 25 °C (o) and after 3 days at RT (p).

In both temperature response investigations there was some discrepancy between the temperatures recorded on the hot stage, which were higher than expected, arising due to the need for the stage lid to be open during measurements to image in reflection mode, compared to the more accurate phase transition temperatures recorded by POM with a closed hot stage and by DSC as recorded in experimental tables. Overall, however, the transitions observed visually during microscopy are not equal to DSC transitions which can be measured from onset.

5.2.2.2 Pressure Response

The response of the films to mechanical strain in the form of pressure was also investigated. A small sample was cut and placed in a droplet of PEG 200 on a glass slide before covering with a coverslip. To investigate the response of selective reflection to pressure the slide was imaged on video under POM in reflection mode. Pressure was applied to the top of the cover slip by pushing a small spatula tip against it. All the while the video recorded the response of the film to the pressure and the recovery of the film afterwards.

Figure 122 shows screenshots from the video taken and photomicrographs of **WE2-CF1** under POM in reflection mode of before, during and after pressure was applied to the film. It can be seen that before the pressure was applied the film reflected orange wavelengths of light but when pressure was applied the colour shifted from orange through green to blue at the edge. This was due to the physical compressing of the chiral nematic helices, which as they became shorter, reflected shorter wavelengths and therefore the colour blue-shifted.[31–33] An area of the film remained orange on one side, likely due to uneven application of pressure to the surface of the film. The film did not recover back to the initial shape and colour even after 1 hour. The experiment was carried out at room temperature, slightly below the glass transition of **E2** (26.8 °C)† so when the film was compressed, stress induced mobility of the elastomer allowed for a deformation of shape. However as the film was below the glass transition temperature, when the stress was removed, the deformation imparted by the mechanical pressure was locked-in, likely until the film is heated above its glass transition[39] as seen in shape memory polymers.[184] It is expected that if this mechanical strain was imparted on the film above the

glass transition then it would act more like **E1** films which were compressed at 75 °C (higher than the T_g of **E1** of ~70 °C), which did return to their original state within seconds.

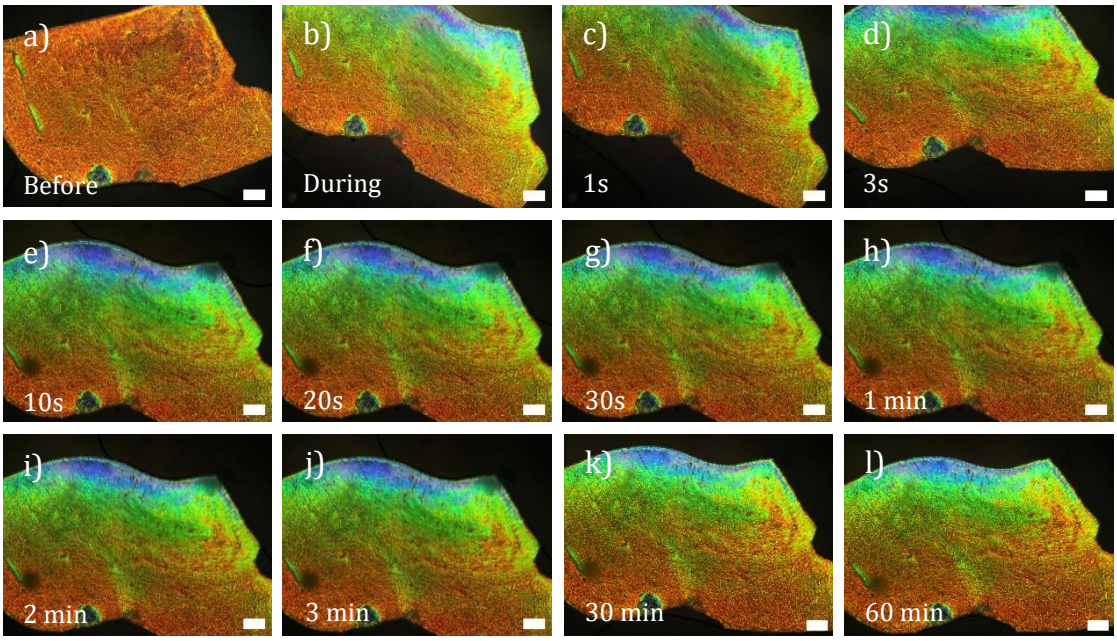

Figure 122: Screenshots from a video (a-j) and photomicrographs (k-l) taken under POM in reflection mode at room temperature of **WE2-CF1** before (a), during (b) and 1s (c), 3s (d), 10s (e), 20s (f), 30s (g), 1 min (h), 2 min (i), 3 min (j), 30 min (k) and 60 min (l) after applying pressure to the film with a spatula tip. Taken at 100x magnification, scale bars 100 μm.†

On the other hand, a sample of film **E3-CF4** was also investigated. Figure 123 shows the screenshots from the video taken before, during and after the application of pressure to the surface of the film. Initially the film mainly reflected an orange colour, however when pressure was applied it can be seen that the film shifted from orange to green through to blue as the helical pitch was compressed. The pitch length of the chiral helices immediately started recovering as seen by the red-shift which occurred after 1 second. The film then shifted back through green after ~10 seconds and through to the original orange colour after 10 – 15 minutes. Compared to the **E1** films investigated previously in the group at 75 °C which recovered within seconds, the recovery time for the **E3** elastomers was much slower on the order of minutes. Unlike in **E1** films, the mesogen and elastomer network were decoupled due to the longer spacer group, so the elasticity of the film had less of an influence in returning the chiral pitch to

pre-compression lengths. Wood *et al* produced a chiral nematic gel consisting of an achiral elastomer, produced from the reactive mesogen mixture known as 'E7', doped with a non-polymerisable chiral dopant, known as 'R5011'. The elastomer gel saw a blue-shift in selective reflection with stretching, and upon removal of the strain, the optical properties recovered within seconds.[185] However, others report relaxation times of ~15 minutes, for example the film produced by Varanytsia *et al* described in the previous section had a high glass transition temperature of ~70 °C meant that the film required heating to 75 °C to investigate the response to pressure. Upon stretching the selective reflection blue-shifted, however when the stress was removed it took ~15 minutes to return to the initial state of the film, similar to **E3** at room temperature.[28] Hence **E3** films could be strong contenders in applications as pressure sensors, despite relaxation time being an order of magnitude longer than in **E1**, and especially considering this was achieved at room temperature as opposed to the elevated temperatures of ~75 °C required in the materials investigated in some literature examples and **E1** materials previously investigated within the group.[28,39,51]

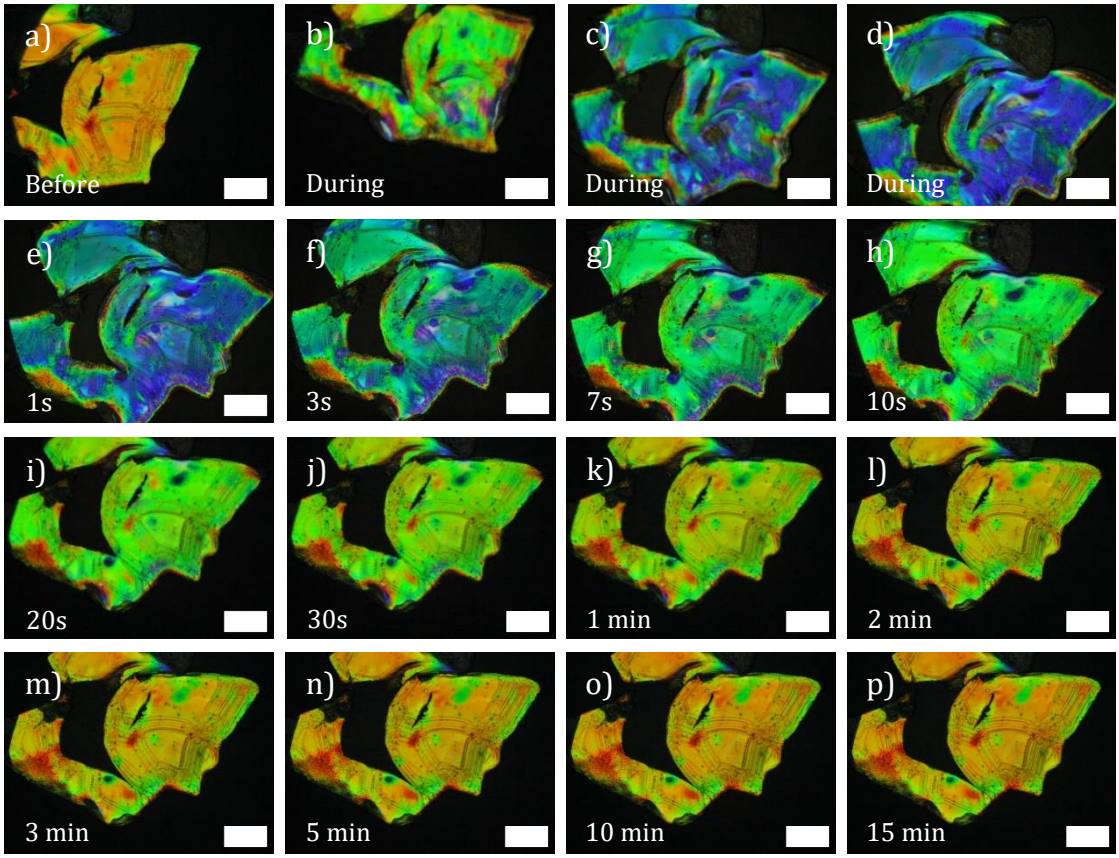

Figure 123: Screenshots from a video taken under POM in reflection mode at room temperature of **E3-CF4** before (a), during (b – d) and 1s (e), 3s (f), 7s (g), 10s (h), 20s (i), 30s (j), 1 min (k), 2 min (l), 3 min (m), 5 min (n), 10 min (o) and 15 min (p) after applying pressure to the film with a spatula tip. Taken at 200x magnification, scale bars 100 μm.

5.3 Radial Chiral Nematic Droplets

Chiral nematic droplets of **CM1–4** doped with chiral dopant CB15 as well as crosslinker 1,6 hexanediol diacrylate (10 mol%), and photoinitiator, diphenyl(2,4,6-trimethylbenzoyl) phosphine oxide (2 mol%), were produced by microfluidics, using the experimental parameters described fully in the experimental chapter (section 7.4.2, Table 21). Droplets of **M1** doped with CB15 were previously produced in the group and were also produced in this project. Due to the findings in this chapter for the chiral mixtures and films of **M2** and **M3** doped with CB15, droplets with these compositions were also investigated. In total droplets of 4 chiral mixtures were produced, details of this composition can be found in Table 8.

Table 8: Details the monomer and CB15 composition of chiral mixtures **CM1-4**.

Chiral Mixture	Monomer	CB15 (wt%)
CM1	**M1**	40
CM2	**M1**	30
CM3	**M3**	33
CM4	**M2**	28

The resulting droplets were characterised by POM which confirmed chiral nematic alignment as Maltese cross textures were observed under POM in all cases. Furthermore, in reflection mode it was seen that all chiral mixtures had selective reflection bands within the visible region of light as different colours were seen under reflectance mode imaging, depending on the monomer and CB15 concentration. The resulting droplet diameters, CV, and observations under brightfield, POM and reflection mode imaging for all experiments are reported in the experimental chapter (section 7.4.2, Table 21).

Figure 124 shows brightfield and polarised photomicrographs of droplets of each chiral mixture where the Maltese cross texture can be seen in all of the mixtures. As discussed in the introduction (section 1.4.3), the Maltese cross texture observed is typical of short-pitched chiral nematic microdroplets where mesogens are aligned parallel to the surface, promoted by the outer fluid composed of PVA in water. When the mesogens were aligned parallel to the surface, the helical axis ran perpendicular to the surface resulting in a central defect, hence radial alignment was observed.[62]

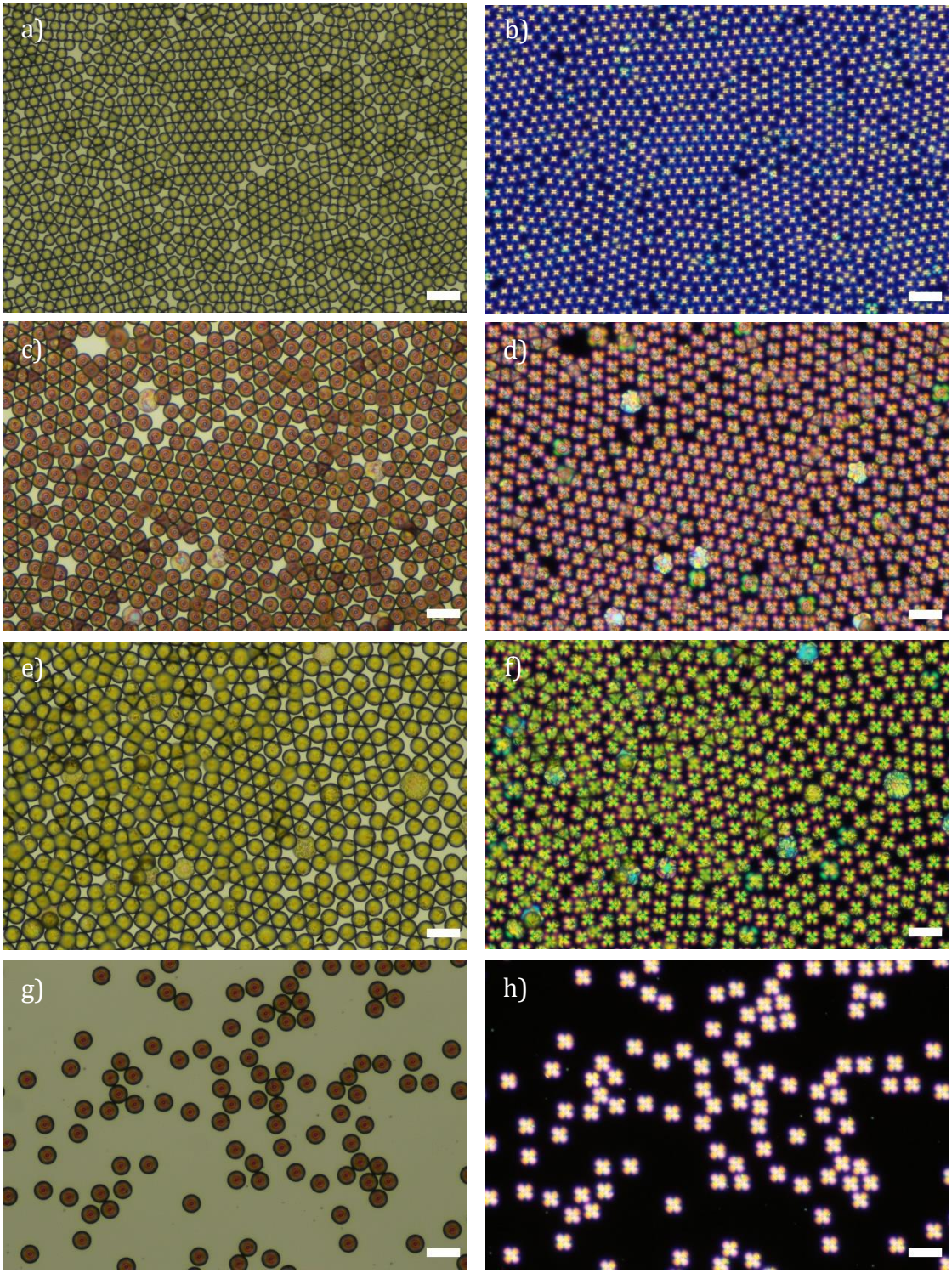

Figure 124: Brightfield (a, c, e, g) and polarised (b, d, f, h) photomicrographs, taken in transmission mode, of chiral nematic droplets of **CM1-MF86** (a, b), **CM2-MF76** (c, d), **CM3-MF91** (e, f) and **CM4-MFCG** (g, h)† taken at 200x magnification, scale bars 50 µm. Average diameters: 18 µm (a), 26 µm (c), 27 µm (e) and 29 µm (g).

Chiral nematic droplets were produced with diameters as small as 18 µm with CV of only 1.5% in **CM1-MF84** which still retained the chiral nematic texture and

ability to selectively reflect blue light. POM photomicrographs taken in reflection mode can be seen in Figure 125 which show the selective reflection colours of each chiral mixture. **CM1** reflected blue light, **CM2** red light, **CM3** green light and **CM4** red light. The narrow size distribution across almost all experiments allowed for hexagonally packed monolayers of chiral nematic droplets to be produced which allowed for cross-communication between droplets reflecting longer wavelengths of light, in chiral mixtures **CM2** and **CM4**, to be observed which demonstrates excellent alignment within the droplets, arising from their small size and low polydispersity.

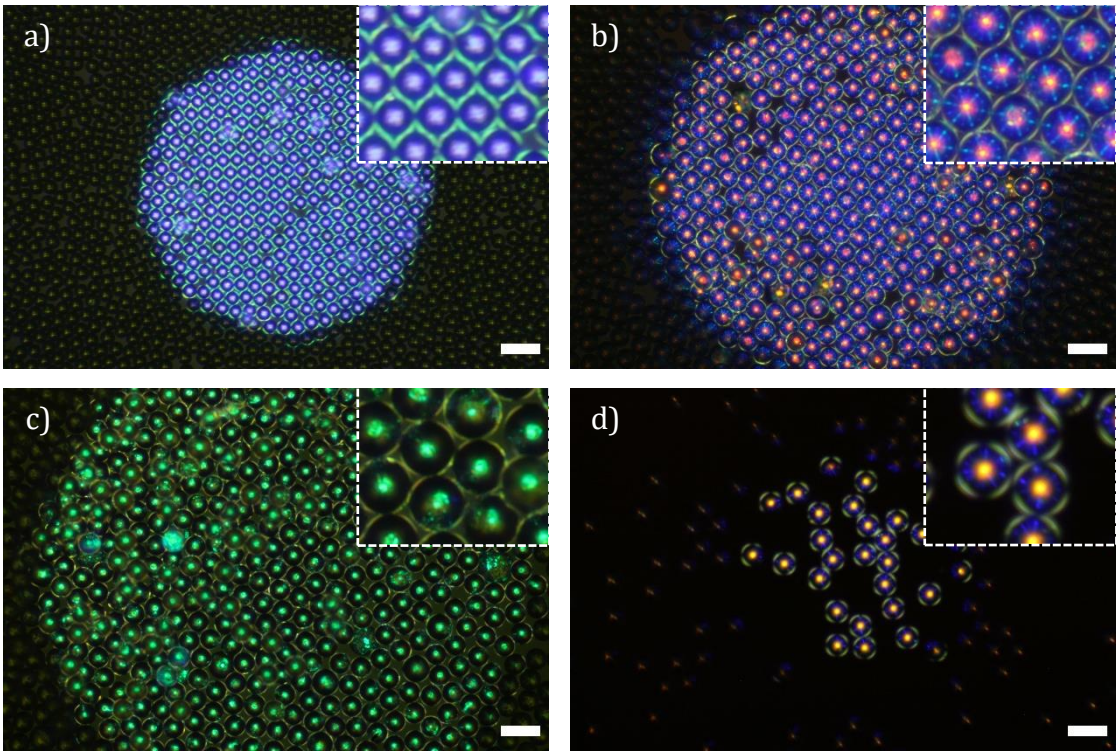

Figure 125: Polarised photomicrographs, taken in reflection mode, of chiral nematic droplets of **CM1-MF86** (a), **CM2-MF76** (b), **CM3-MF91** (c) and **CM4-MFCG** (d)† taken at 200x magnification, scale bars 50 μm. Cut outs in the top right corner of each photomicrograph show a section zoomed in by 2.7x. The field diaphragm was reduced to better resolve the imaging. Average diameters: 18 μm (a), 26 μm (b), 27 μm (c) and 29 μm (d).

Photonic cross-communication is described in section 1.4.3 and is observed as bright coloured reflection lines which appear to radiate out from the centre of droplets, examples can be seen in the zoomed in cut outs of Figure 125b & d which show droplets of **CM2** and **CM4**.

No cross-communication lines were seen between droplets of **CM1** and **CM3** however. This was because the wavelengths of light reflected during cross-communication must be shorter than the wavelength of selective reflection, as described by Braggs Law (section 1.2.2.3, Equation 7). As **CM1** and **CM3** were already shorter wavelength reflectors, the cross-communication lines were not within the visible region of light due to the blue-shift into the UV region.

On the other hand, in the longer wavelength reflectors, droplets of **CM2** and **CM4**, shown in Figure 125b & d, red central selective reflection spots were present and where a nearest neighbour was present, a shorter wavelength blue cross-communication line was observed. In Figure 125b a hexagonal close-packed arrangement means each droplet had six nearest neighbours giving rise to six cross-communication lines in each hexagonally close-packed droplet.

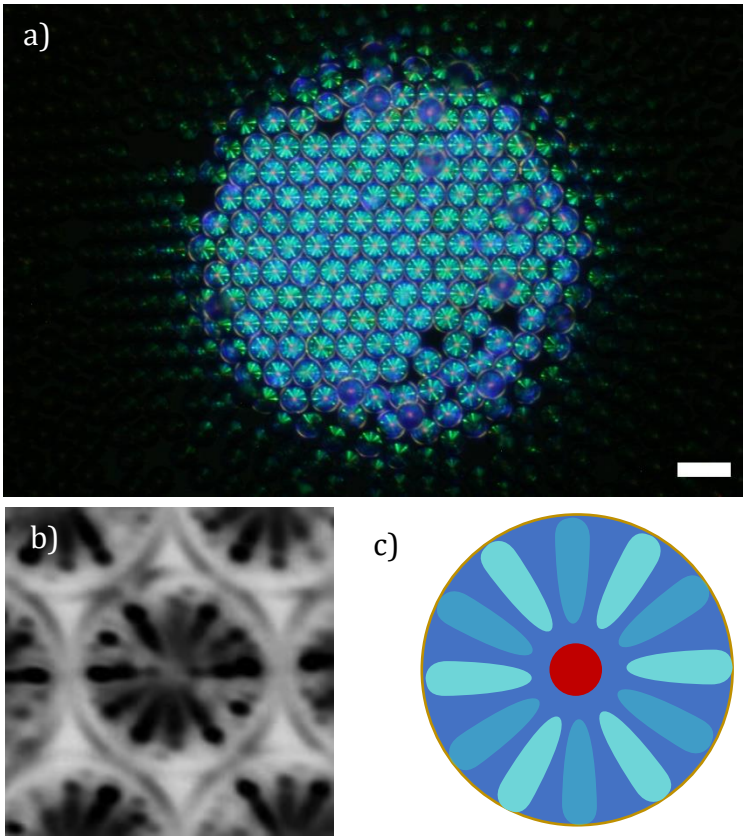

Figure 126: Polarised photomicrograph (a), taken in reflection mode with very bright illumination, of chiral nematic droplets of **CM2-MF93** to show droplet cross-communication. The field diaphragm was reduced to better resolve the imaging. Photomicrograph zoomed and processed to make cross-communication lines clearer (b) and a cartoon representation of the cross-communication lines (c). Average diameters: 27 µm (a).

Figure 126 shows a POM photomicrograph taken in reflection mode of **CM2** with the microscope lamp turned up extremely bright. Central red selective reflection spots were observed with blue-green cross communication lines but there were more than six cross-communication lines present. For clarity, the image was processed by separating the green colour channel, converting to greyscale and inverting the image colour allowing for the drawing of the cartoon representation seen in the same figure. As well as the six nearest neighbour cross-communication lines, six slightly dimmer cross-communication lines were present. Similar cross communication patterns were reported Fan *et al* and Noh *et al* where they are rationalised to be from the next nearest neighbour droplets.[64,66] Noh *et al* showed that cross-communication could be observed even further into the so called 'next next nearest neighbour'.[66] Figure 127 shows where nearest neighbours are in a hexagonally close-packed system. Whilst **CM2** was already known to give rise to photonic cross-communication with nearest neighbours in monodisperse samples, the observation of cross-communication with the next nearest neighbour had not been previously observed. Cross-communication relies on helix alignment, and therefore the higher quality the chiral nematic alignment in a droplet, the higher quality the cross-communication patterning within the sample. It is clear that the quality of the droplets, for example the small diameter of 27 μm and CV of only 1% produced here, using microfluidic parameters described in the experimental chapter (section 7.4.2, Table 21), has given rise to remarkably well aligned droplets of **CM2**, which in turn has promoted complex optical properties. The more complicated cross-communication patterns produced, the more complex the patterns, and therefore the more useful the systems in security applications. Specific numbers of droplets with specific placement within the close-packed structure have been reported showing how controllable patterning can be to produce unique cross-communication arrays.[64]

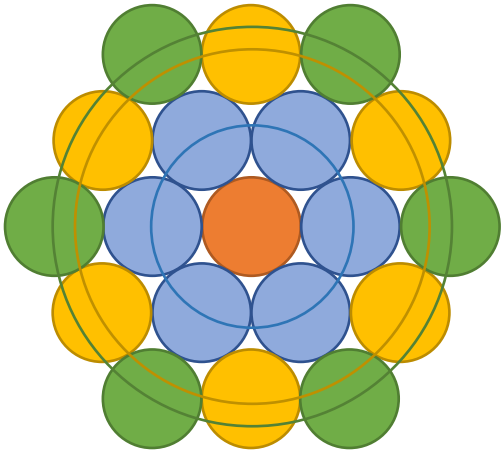

Figure 127: Cartoon representation to show a central hexagonally close-packed droplet (orange) surrounded by the nearest neighbour droplets (blue), the next nearest neighbour droplets (yellow) and the next next nearest neighbour droplets (green).

5.4 Radial Chiral Nematic Elastomer Microparticles

Droplets were photopolymerised at room temperature, in the chiral nematic phase, under an Omnicure LX500 365 nm UV lamp to yield crosslinked chiral nematic microparticles. Full experimental details can be found in the experimental chapter (section 7.4.3, Table 22).

Upon polymerisation, the chiral nematic phase remained for all chiral mixtures, resulting in elastomer microparticles which displayed Maltese cross textures under POM. POM photomicrographs in Figure 128 show the Maltese cross texture was retained albeit much less defined in elastomers **CE2** and **CE4**. Although it was difficult to see the Maltese cross, it was hidden underneath some surface distortion, as shown in the zoomed in sections of Figure 128d & h, when the sample was rotated with respect to the crossed polarisers, it could be seen that the isogyres which make up the Maltese cross rotated too. The presence of the Maltese cross under this distortion suggests that the chiral nematic alignment was still present on the inside of the particles.

The polymerisation conditions and resulting microparticle diameters and aspect ratios for each experiment can be found in the experimental chapter (section 7.4.3, Table 22). It can be seen that, compared to their droplet counterparts (section 7.4.2, Table 21) in many of the experiments there was some shrinkage of mean diameter by 0 – 2 μm. For example, in experiment **CE2-MF76** droplets reduced from 26 μm to 25 μm diameter microparticles. This is to be expected as

new bonds form in polymerisation, it is the same phenomena which caused the pitch contraction and small blue-shift at a similar degree to that seen in the chiral nematic films discussed earlier.[186] In spherical confinement, the shrinkage may cause some surface wrinkling which could explain the texture surface distortion, seen in the brightfield and POM imaging in Figure 128, particularly in (c) and (g). The distortion at the surface could have arisen due to the outside of the particle polymerising more rapidly than the inside as the most intense UV light hit the surface of the droplet. The distortion was not seen in **CE1** (Figure 128a & b), likely because these are much smaller, at 18 μm, compared to the shown for **CE2–4** which were 26 – 28 μm. The surface anchoring in smaller droplets and particles had a stronger effect throughout the whole sphere, promoting better overall alignment, than in their larger counterparts where the surface area to volume ratio was smaller and surface anchoring effects needed to penetrate further into the sphere.

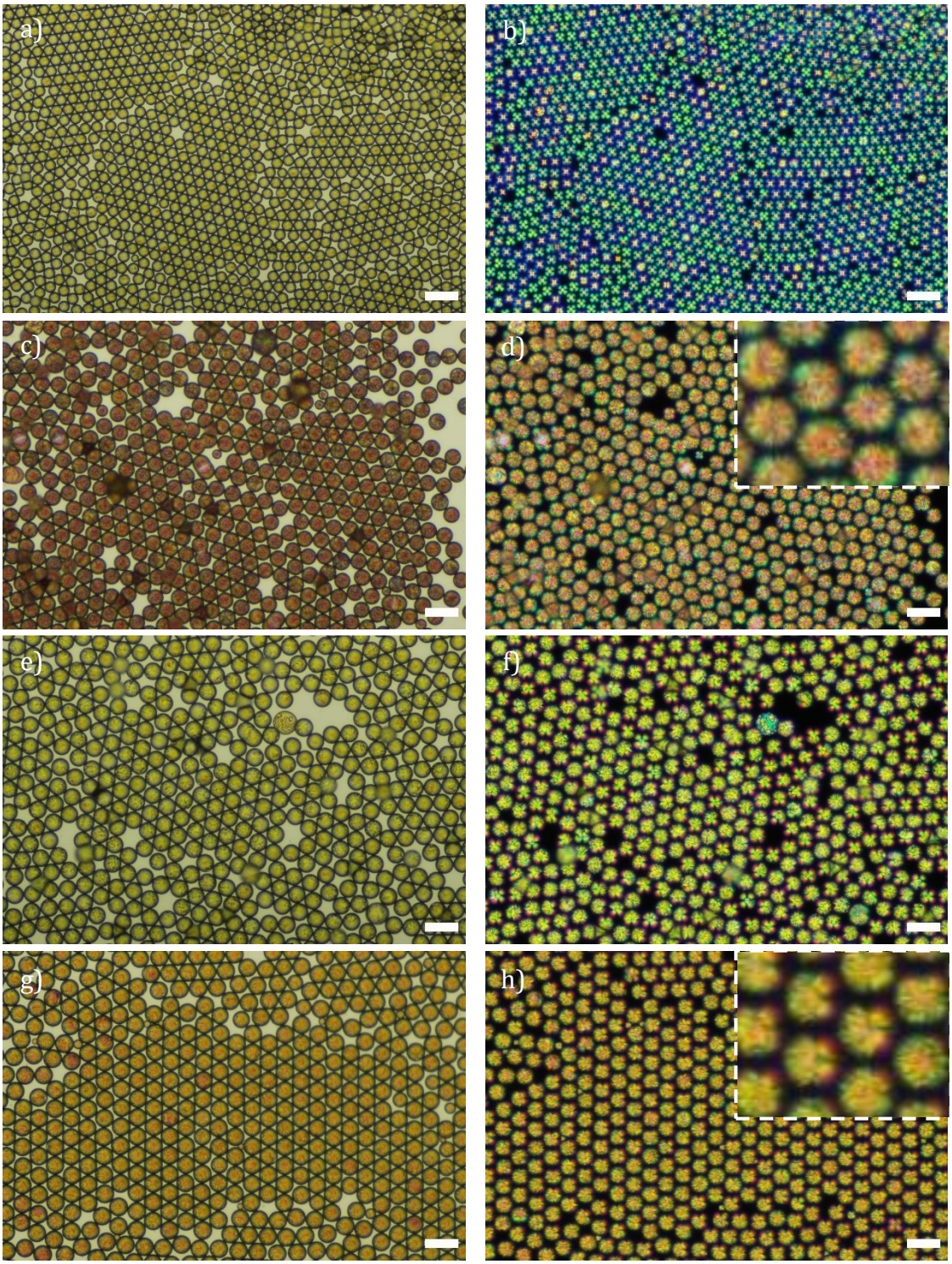

Figure 128: Brightfield (a, c, e, g) and polarised (b, d, f, h) photomicrographs, taken in transmission mode, of chiral nematic particles of **CE1-MF86** (a, b), **CE2-MF76** (c, d), **CE3-MF91** (e, f) and **CE4-MFCG** (g, h)† taken at 200x magnification, scale bars 50 µm. Zoomed in sections shown in the top right corner of photomicrographs zoomed by 3.3x. Average diameters: 17 µm (a), 25 µm (c), 27 µm (e) and 28 µm (g).

In addition, the aspect ratios of chiral nematic elastomer microparticles were measured and recorded in the experimental chapter (section 7.4.3, Table 22). It

can be seen that the aspect ratios of all the elastomer microparticles produced ranged from 1.00 – 1.02 with a CV of between 0.8 and 2.0. The aspect ratios show that there was no deformation of shape or elongation of particles upon polymerisation as observed in bipolar nematic particles of **E1** and **E2**. Furthermore, when the polymerisation was performed at the highest intensity possible with the setup, in comparison with the normal conditions of 50% intensity at 15 cm away, (investigated in **CE2-MF76**), no deformation from spherical was observed, as seen in the brightfield images in Figure 129. A particle geometry deformation was not promoted for the chiral nematic elastomers as the parallel aligned mesogens were organised in a radial helical arrangement so there was no overall director in the spherical system and hence no directional deformation could occur.

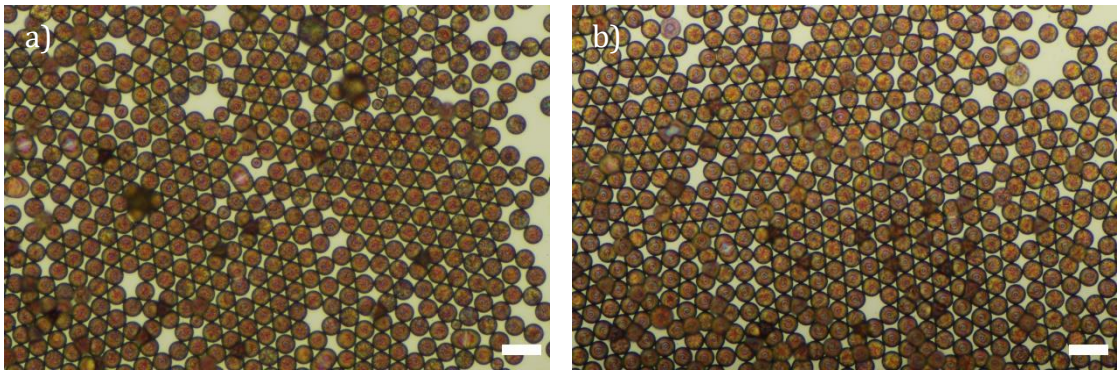

Figure 129: Brightfield photomicrographs of droplets of **M2-MF76** (a) and their polymerised counterparts **E2-MF76** (b). Average diameters: 26 μm (a) and 25 μm (b).

The chiral nematic elastomer particles were also imaged under POM in reflection mode to reveal their selective reflection properties, shown in Figure 130. It can be seen that whilst the selective reflection colours post-polymerisation of **CE1**, **CE2** and **CE3** remained similar, if not the same, as their droplet counterparts, **CE4** shifted from red to green. This could be a blue-shift due to shrinkage of the particles compressing the helix, although it is unclear why as such a dramatic blue-shift upon polymerisation was not observed for systems composed of monomers **M1** or **M3** or with the chiral film of the same composition as **CE4, E2-CF5**, which was orange. Speckling of the surface of the **CE4** microparticles, as well as some in **CE3** particles, can also be seen which suggested lower quality chiral nematic alignment in the particles.

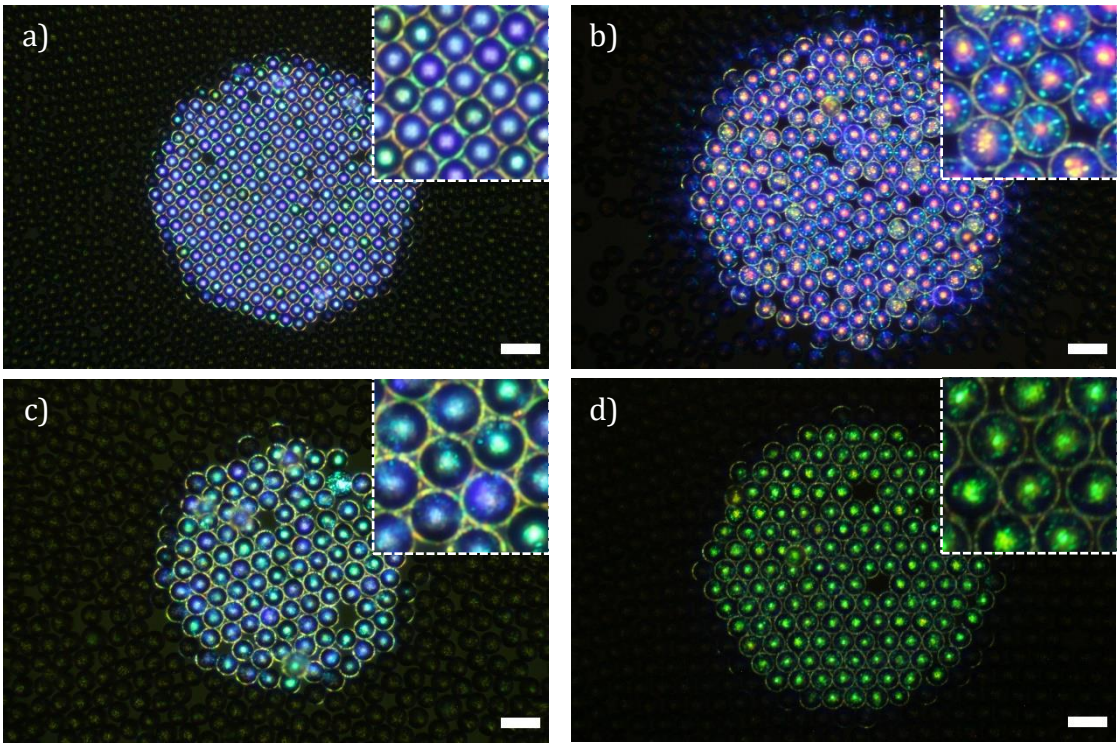

Figure 130: Polarised photomicrographs, taken in reflection mode, of chiral nematic droplets of **CE1-MF86** (a), **CE2-MF76** (b), **CE3-MF91** (c) and **CE4-MFCG** (d)† taken at 200x magnification, scale bars 50 μm. Cut outs in the top right corner of each photomicrograph show a section zoomed in by 2.7x. The field diaphragm was reduced to better resolve the imaging. Average diameters: 17 μm (a), 25 μm (b), 27 μm (c) and 28 μm (d).

The selective reflection of microparticles of **CE1-MF91** and **CE3-MF86** did have some particle-to-particle variation. Some particles had darker blue reflection than others, this could have been due to the samples receiving a gradient of UV intensity away from the central UV spot produced by the LED, then upon moving to the microscope the agitation mixed them up in the sample. This is reflected by the large range at which the T_{NI} of the sample was measured under POM at 52 – 62 °C as some particles may be less polymerised than others within the population.

Finally, photonic cross-coupling can be seen for in the sample of **CE2** elastomer microparticles, shown in Figure 130b, and more significantly it is still very clear and bright showing excellent retention of the droplets optical properties throughout and after polymerisation, as a result of high quality internal alignment. Previous work in the group found CB15 doped non-crosslinked 20 μm polymer particles also exhibited cross-communication post-polymerisation however it was not as pronounced as the results seen here in 26 μm **CE2-MF76** particles. As the particles were bigger, the quality of the internal alignment resulting in bright

cross-communication lines cannot be attributed to smaller particle size. Instead, as **CE2** particles were crosslinked, and those previously investigated were not, it is suggested that the crosslinking could have played an important role in preserving the optical properties of a droplet through polymerisation to a microparticle by maintaining better internal mesogen alignment.

Aβhoff *et al* produced chiral nematic elastomer microspheres from droplets which exhibited photonic cross-communication. Upon polymerisation, like in **CE2,** the cross-communication was preserved, however they reported a loss of the quality of the optical properties due to alignment disruption at polymerisation which was postulated to be due to preferential polymerisation at the central defect.[67] Whereas, Geng *et al* found that optical quality could be fully retained when utilising chiral nematic liquid crystal shells rather than fully polymerised spheres of elastomer particles which is to be expected due to high quality nematic alignment due to surface anchoring only needing to penetrate the surface of the shell and not the hollow insides.[22]

The results here show that **CE2** elastomer microparticles are excellent candidates for patterning applications, due to the level of optical quality retained upon polymerisation, whilst benefitting from the robustness of being a solid sphere compared to polymer shells. These findings give rise to a whole host of investigations which could be based on **CE2** microparticles. For example, Belmonte *et al* introduced reactive dye into chiral nematic microparticles capable of photonic cross-communication. The wavelength of reflected light from cross-communication activated the dyes to produce particles with multi-coloured reflective coatings.[187] **CE2** microparticles could be a good candidate for the investigation of reactive dye reflective coatings in the future.

5.4.1 Refractive Index Matching Chiral Nematic Elastomer Particles

In the preceding experiments the selective reflection colours of the chiral nematic droplets and particles produced were mostly only visible under microscopy. Whilst there was some colour seen in the dishes with the naked eye, it was very dim and washed out as shown in Figure 131b.

Refractive index matching of the dispersion medium with the chiral nematic polymer microparticles could allow for bright selective reflection colours of chiral nematic particle dispersions to be seen by the naked eye.[63] Refractive index matching the dispersion medium to the particles could improve the visibility of the reflection colours by reducing reflection loss at the interface between the elastomer microparticle and the outer fluid, and may act to reduce internal reflection within the microspheres. Typically, nematic systems have refractive indices of 1.4 – 1.8, with the average being ~1.6.[63,188,189] To improve the macroscopic optical properties of the **E1** chiral nematic elastomer particles collected, the dispersion medium was replaced with various solutions with different refractive indices in an attempt to match the refractive index of the particles with the dispersion medium, whilst not swelling the particles which may result in loss of chiral nematic alignment.

To replace the dispersion medium, first the PVA had to be removed so each dish was washed 15 – 20 times with MilliQ water by removing 2 mL of the outer fluid and replacing it with 2 mL MilliQ water, leaving it 30 minutes and then repeating. Once the particles were in MilliQ water, the same washing technique was used and repeated 2 – 3 times to replace the MilliQ water with the dispersion medium to be investigated. Initially MilliQ water, PEG 200, Glycerol, 85 wt% sugar water solution and resin were investigated with refractive indices ranging from 1.33 to ~1.60. It was found that glycerol and the sugar solution were the best refractive index matches from the selection which have refractive indices of 1.47 and 1.50 respectively. A facile way of altering the refractive index of a sugar solution is to change the sugar concentration, refractive indices for several concentrations can be found in Table 9, so different sugar solutions were investigated. Figure 131 shows the results of this investigation, it can be seen that when in 80 wt% sugar in water, the chiral nematic elastomer particles appeared the brightest blue without the aid of a microscope, suggesting that the refractive index of the **CE1** particles investigated is ~1.49, although the change in density of the outer fluid meant that some particles became buoyant in the medium. Imaging under POM (Figure 131g, h & i) showed that many particles survived the washing into water and then sugar water solutions, however some larger masses of chiral nematic material were observed, possibly due to poor polymerisation around the outer

edges of the dish where the UV lamp was less intense, coupled with washing and dish agitation.

Table 9: Refractive indices of sugar water solutions at different concentrations.[190]

Sugar Solution Concentration (wt%)	Refractive Index
70	1.4651
75	1.4774
80	1.4901
85	1.5033

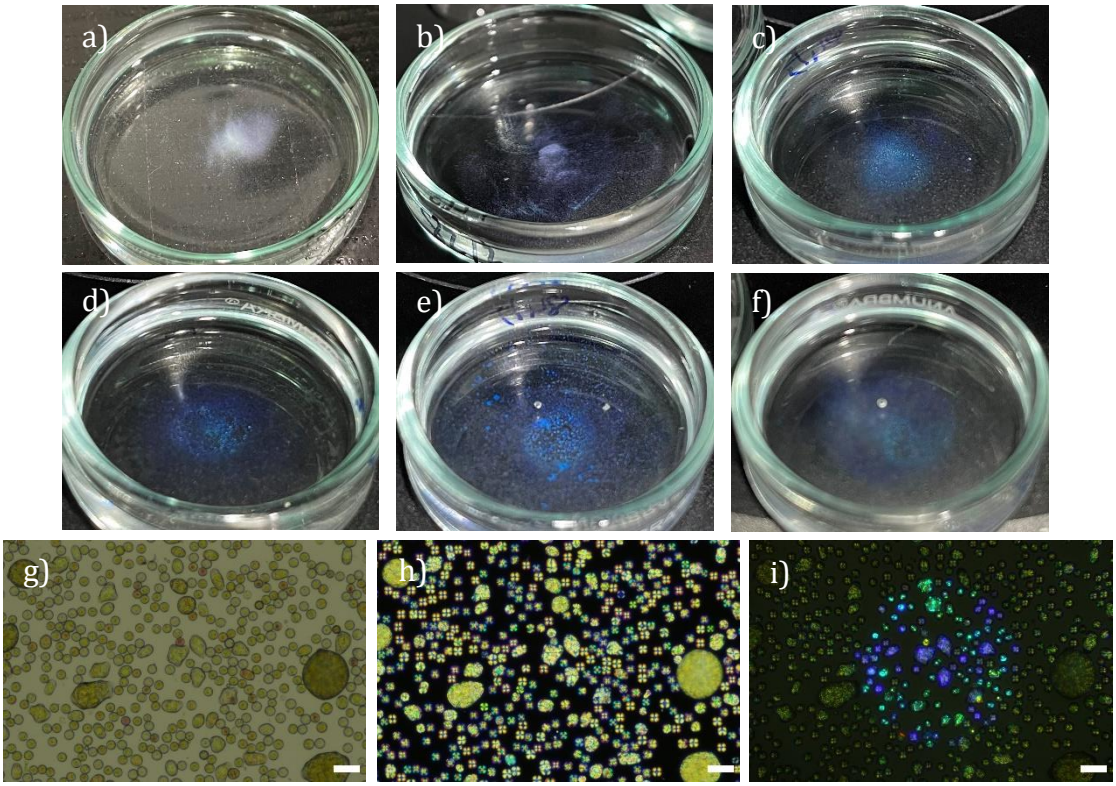

Figure 131: Photographs of Petri dishes containing chiral nematic elastomer particles of **CE1-MF82** (a & b) and **CE1-MF84** (c – f) where particles are in water (a), 3 wt% PVA in water (b), 70 wt% sugar in water (c), 75 wt% sugar in water (d), 80 wt% sugar in water (e) and 85 wt% sugar in water (f). Brightfield (g), polarised (h) and reflection (i) POM photomicrographs of particles in sugar water solution, 200x magnification, scale bars 50 µm.

5.4.2 CB15 Extraction from Chiral Nematic Elastomer Microparticles

Following the successful CB15 removal with acetone washes for chiral elastomer films, washing chiral nematic elastomer microparticles to remove CB15 was attempted for **CE2–4** microparticles prepared as described in the experimental

chapter (section 7.4.3.1). Again, dishes were washed 20 times with MilliQ water to remove all PVA using the same method used during refractive index matching. Then, dishes were replaced with 25, 50, 75 and 100 vol% acetone, ethanol or IPA twice.

Initially, the dispersion medium of **CE2-MF76** was replaced with ethanol, acetone and IPA to test the CB15 washing out capabilities of each solvent. It was found that IPA and ethanol did not swell the elastomer particles such that they would transition to the isotropic phase upon solvent addition. However, it was found that acetone did successfully swell the microparticles, which went into the isotropic phase, without compromising their spherical geometry. When the microparticles were washed back into MilliQ water from acetone, they became birefringent again showing some order had returned. In a further series of experiments, acetone was used in attempts to wash CB15 out of **CE2–4** in experiments **CE2-MF93**, **CE3-MF91** and **CE4-MFCG**.

CE2-MF93 and **CE4-MFCG** were washed with up to 75% acetone, which was when particles transitioned into the isotropic phase, as seen in Figure 132e and Figure 133e. In acetone some particles did fuse, although this was a minority, with most remaining spherical. Upon washing back to water, the integrity of most of the particles remained intact and birefringence returned. Figure 132h and Figure 133h show that polydomain textures returned in both cases, instead of the Maltese cross chiral nematic textures which were present pre-wash. A similar polydomain texture was seen in reflection mode (Figure 132i and Figure 133i) with the characteristic selective reflection central spots missing. The undefined textures after washing back into water suggests that the chiral nematic superstructure was lost, possibly indicating successful removal of CB15 as the chiral nematic texture seen pre-wash did not return. However, the fusing together of particles and loss of alignment could suggest that the crosslinking with the particles was not sufficient to maintain the integrity of the particles, or that polymerisation may have been incomplete in these samples.

On the other hand, **CE3-MF91** was washed with up to 50% acetone, where particles swelled and turned isotropic, however most of the particle's integrity was lost and the particles fused together, as seen in Figure 134d. Compared to **CE2** and

CE4 where the experiment was carried out at room temperature which was below the T_g of both systems (T_g **CE2** = ~45.5 °C[51], T_g **CE4** between 26.1 and 46.2 °C[†]), for **CE3** the particles were washed above their T_g (T_g **CE3** = -21.9 °C). It is expected **CE2** and **CE4** held their integrity better due to the fact the particles were in a glassy state. However, the fusing of particles could again indicate incomplete polymerisation as well as the observation of a polydomain texture through crossed polarisers and in reflection mode, shown in Figure 134.

Acetone was successfully used to remove CB15 from RMM727 particles by Noh and Park,[37] whereas Belmonte *et al* successfully removed a chiral dopant from chiral nematic polymer microparticles to produce chiral imprinted particles by washing particles with tetrahydrofuran,[187] so a future attempt at washing particles of **CE1–4** with tetrahydrofuran should be carried out as a continuation of this investigation.

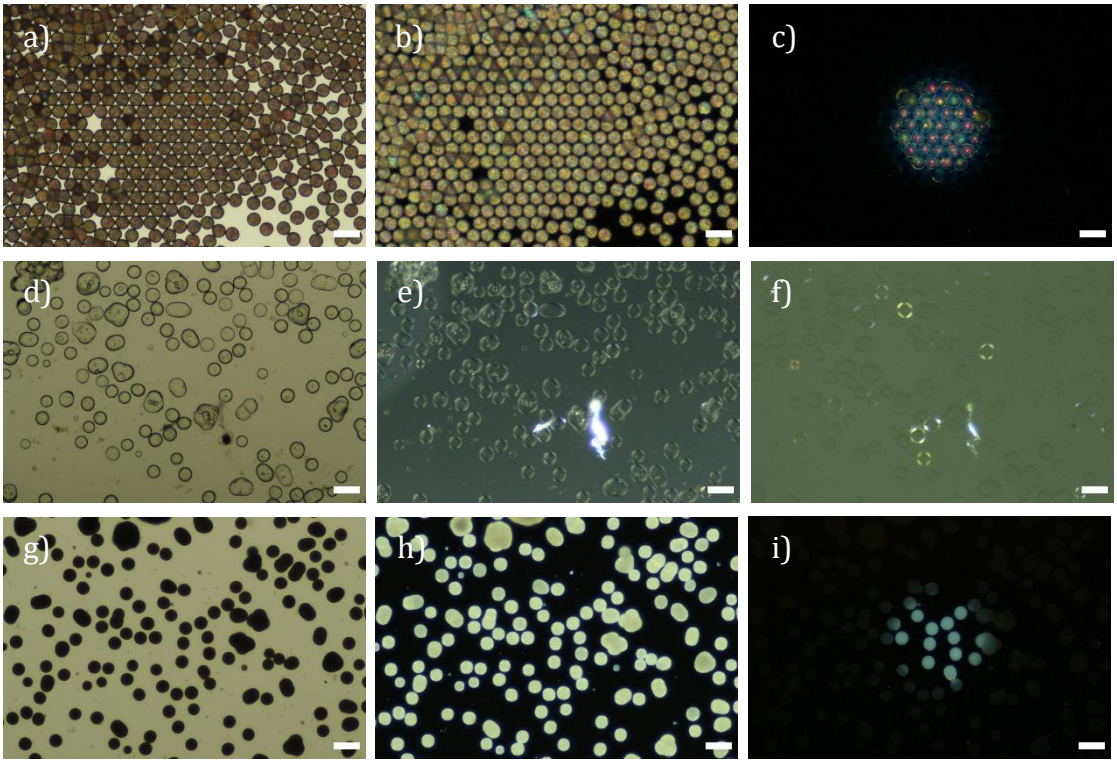

Figure 132: Brightfield (a, d, g) and polarised (b, e, h) and reflection mode (c, f, i) POM photomicrographs of chiral nematic elastomer microparticles of **CE2-MF76** pre-acetone wash in water (a – c), in 75% acetone (d – f) and post-acetone wash once returned to water (g – i). Taken at 200x magnification, scale bars 50 μm.

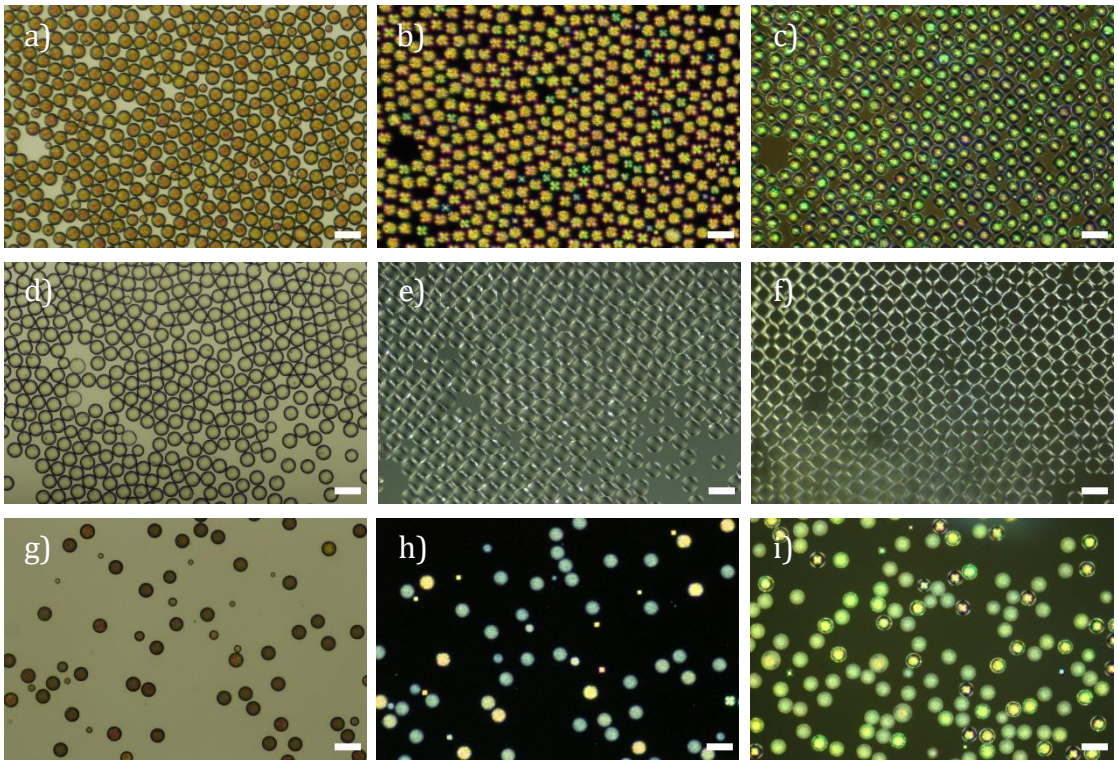

Figure 133: Brightfield(a, d, g) and polarised (b, e, h) and reflection mode (c, f, i) POM photomicrographs of chiral nematic elastomer microparticles of **CE4-MFCG** pre-acetone wash in water (a – c), in 75% acetone (d – f) and post-acetone wash once returned to water (g – i). Taken at 200x magnification, scale bars 50 μm.†

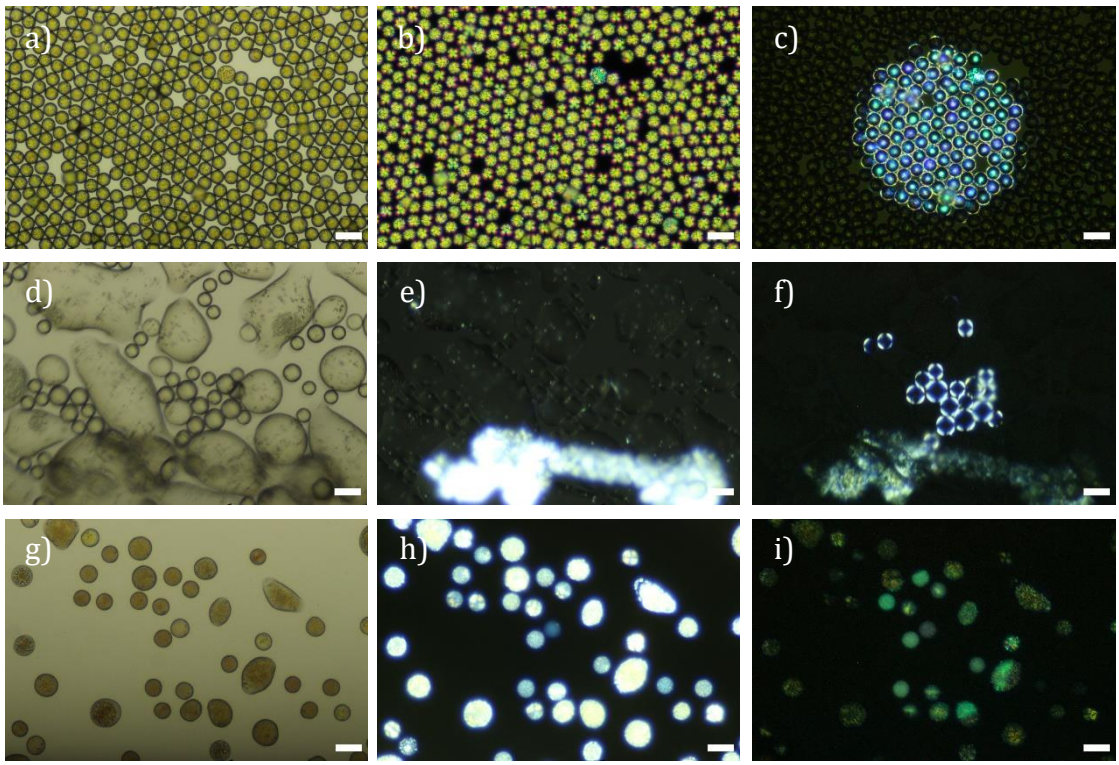

Figure 134: Brightfield(a, d, g) and polarised (b, e, h) and reflection mode (c, f, i) POM photomicrographs of chiral nematic elastomer microparticles of **CE3-MF91** pre-acetone wash in water (a – c), in 75% acetone (d – f) and post-acetone wash once returned to water (g – i). Taken at 200x magnification, scale bars 50 μm.

5.5 Conclusion

An array of novel CB15 doped mixtures and elastomer films made up of monomers **M2** and **M3** were produced which selectively reflected wavelengths of light within the visible region leading to brightly coloured mixtures and films upon imaging. Concentration control of CB15 fine-tuned selective reflection of the materials to produce reflection in all colours across the visible region. As expected, when introducing CB15 the phase stability was reduced, however it was improved with polymerisation.

The responsiveness of films to acetone washes and external stimuli, such as temperature and pressure, were investigated. Acetone washes swelled chiral films of **WE2** and **WE3**, allowing the CB15 to be removed. Upon drying of acetone **WE2** films remained chiral nematic and exhibited a selective reflection shift showing that the chiral helices were imprinted on the films, whereas **WE3** films lost selective reflection and appeared as achiral films showing imprinting had not occurred. Temperature response experiments yielded a reversible colour change of films **WE2** and a colour change response which was only partially reversible for **E3-CF4**. A pressure response investigation on films showed a fully reversible response in **E3-CF4**, however, **WE2** requires further investigation at above the glass transition temperature. The colour changing responses displayed in films of **WE2** and **E3-CF4** shows that they are good candidates for use as sensors in several scenarios. Whether this is indicating the presence of organic solvent, temperature or pressure.[65,191] Furthermore, the actuation response of the selective reflecting film of **WE2** could give rise to applications in soft robotics or self-cleaning coatings for example.[192]

Droplets and microparticles of chiral mixtures were produced from a selection of the mixtures which had been investigated as films. The droplets and microparticles exhibited planar radial alignment which led to selective reflection of specific colours. Low wavelength reflectors were able to exhibit photonic cross-communication due to their low polydispersity, spherical symmetry and the quality of the chiral nematic alignment. Photonic cross-communication in droplets of **CM2** showed more complex patterning than previously reported in polymer particles and upon polymerisation retained the optical properties remarkably well

for elastomer particles, lending itself for applications within security patterning.[22,66]

Further to this, dispersion medium exchanges led to refractive index matching of **CE1** elastomer microparticles using sugar water solutions, giving rise to a boost in the macroscopic optical properties of the particles. Dispersion medium exchanges to acetone were utilised in attempts to wash out CB15 from **CE2-4** microparticles, however this led to the loss of nematic texture in all cases and destruction of particles of **CE3**. Although unsuccessful, acetone washes lay the foundation for future work to investigate the removal of CB15 to produce imprinted chiral elastomer particles.

6 Conclusion

The main aims of this thesis revolved around the research of both nematic and chiral nematic systems for their response to various stimuli, whether that be polymerisation conditions, introduction of nanoparticles, temperature, or pressure. To achieve these aims various bipolar and chiral nematic systems were produced, characterised, and investigated resulting in impressive results, in some cases not previously observed within the field.

6.1 Bipolar Nematic Systems

Bipolar nematic droplets were produced from **M1**, **M2** and **M3** by a microfluidic method which yielded nematic droplets with small micrometre sized diameters and in extremely low dispersity, in many cases below 1% and on average at 1.8%. The droplet sizes and CVs were improvements upon previously reported results in the group and literature.[42,51,114,121] Additionally, the small, monodisperse particle sizes were significant to the quality of the internal alignment of droplets across the whole population, due to the size dependence of the elastic constants.

Upon photopolymerisation, crosslinked nematic elastomer microparticles were produced. Polymerisation conditions were altered to produce microparticles of different geometries. Specifically, microparticles of **E1** and **E2** were produced, reliably, in anisometric elongated spindle shaped geometries where the bipolar nematic alignment deformed into a twisted bipolar nematic alignment. The deformation happened instantly upon polymerisation, hence the production of the anisometric microparticles did not require additional synthesis steps as in the literature.[55–57,59] The actuation response of these particles was investigated. Elongated particles of **E1** and **E2** presented large, reversible, aspect ratio changes about their phase transition temperatures, comparable to the values reported previously in the group for **E1** microparticles. This property could give rise to applications in micromechanics, as sensors or in soft robotics.[29,145,146] Furthermore, anisotropic, directional wrinkling was induced on the surface of these particles upon polymerisation, which appeared to follow the nematic alignment within the elastomer particles. anisotropic wrinkling is particularly

difficult to achieve in isotropic polymer particles, and so the directionality of the wrinkling of anisotropic elastomer microparticles reported within this thesis is particularly significant. Controlled wrinkling could be useful in applications surrounding templating, micromechanics or microfluidics.[154,161] Particles of **E3** however did not exhibit geometry deformation, and wrinkling was also not observed, due to the comparatively long spacer group between mesogen and polymer backbone decoupling the anisotropy of the mesogen from the polymer matrix.

The polar orientation of droplets was manipulated using a magnetic field to produce populations of droplets where polar axes were aligned across the sample. Where droplets had been aligned using a magnetic field, they elongated in a common direction, along the director, as captured in noteworthy videos attached with this thesis showing striking arrays of commonly deforming droplets into uniform anisometric microparticles, this was another observation not previously reported in the literature. It was found that the anisometric particles of **E1** and **E2** could be aligned and rotated in synchrony using a magnetic field. As far as we are aware, this phenomenon has not previously been reported in literature for free liquid crystalline microparticles.

Bipolar nematic droplets were also infiltrated with nanoparticles using a microfluidic method combined with nanoparticle concentration control to carefully introduce nanoparticles so that the number entering droplets was tuneable. The nanoparticles were functionalised with fluorescent dye and suspended in organic solvent before introduction into the microfluidic inner phase. At high infiltration concentrations, with nanoparticle to droplet ratios of 6 : 1 or higher, the bipolar nematic alignment was interrupted to the extent that a polydomain configuration was observed, however at lower concentrations of 4 : 1 the nematic alignment of droplets was retained, with only a small degree of director distortion local to nanoparticles, and 1 – 2 nanoparticles were observed to be localised into bipolar defects. **E1** elastomer microparticles containing a nanoparticle underwent an actuation cycle upon heating and cooling, the nanoparticle remained in place throughout the reversible shape change about the phase transition temperature. In the literature, actuation of nanoparticle

containing nematic elastomer microparticles has not previously been reported, as far as we are aware.

6.1.1 Future Work for Bipolar Nematic Systems

To be able to better observe the surface morphology of **E2** and **E3** particles, the washing and drying methods should be re-evaluated to allow for SEM imaging to be performed. Optimising the washing step to create samples with less deterioration of sample quality could also allow for the actuation response of whole assemblies of spherical and anisometric **E1** and **E2** nematic elastomer microparticles to be observed.

To further progress on the nanoparticle infiltration research reported in this thesis, nanoparticle infiltration should be optimised further to produce populations of particles which contain exactly two nanoparticles, with one localised at each pole. The actuation response of these particles should also be investigated. Further to this, magnetic alignment of these particles should be attempted to allow for populations of ordered nanoparticle 'patches' in a population of nematic elastomer particles. Finally, surface functionalised nanoparticles of complimentary functionality, capable of non-covalent interactions, should be produced and introduced into microparticles with the aim of observing interactions between nanoparticle infiltrated nematic elastomer microparticles.

6.2 Chiral Nematic Systems

Chiral nematic mixtures of **M2** and **M3** were produced where different chiral dopant, CB15, concentrations were utilised to produce an array of mixtures where selective reflection of any colour in the visible region was accessible at room temperature. Upon polymerisation into films the selective reflection persisted, and the phase stability increased allowing for potential real-world usability.

The CB15 was washed out of doped **E2** and **E3** films using acetone washes. **WE3** exhibited a loss of the chiral nematic texture and therefore selective reflection, whereas **WE2** films retained the chiral nematic texture, despite the removal of the

chiral dopant as chiral imprinting had occurred. The helical structure was imprinted into the elastomer matrix, which in turn held the mesogens in place to selectively reflect wavelengths of visible light, albeit at a shorter wavelength.

The response of films to external stimuli was investigated and showed that, due to strong coupling between mesogen and elastomer backbone, **WE2** films exhibited a red-shift just before the phase transition temperature as nematic order was reduced about clearing. Whereas **E3** films did not exhibit any colour changing response to temperature upon clearing, although when cooled the film did not revert back to its original colour, instead a blue-shift had occurred. On the other hand, pressure response experiments showed that **E3** films exhibited a strong blue-shift response to pressure at room temperature which was reversible. However, **WE2** films did show a blue-shift that was not reversible, likely due to the experiment being performed below the films glass transition temperature. The responsiveness of the chiral nematic films to pressure and temperature make them candidates for use as sensors indicating, for example, the presence of organic solvent, temperature or pressure.[65,191]

Chiral nematic droplets and elastomer microparticles were also produced from mixtures of **M1**, **M2** and **M3** doped with CB15. Photonic cross-communication was observed in monolayers between longer-wavelength reflectors produced showing excellent internal mesogen alignment, likely due to the small droplet size and dispersity. Upon polymerisation, **CE2** elastomer microparticles retained the optical properties of their droplet counterparts to a remarkable degree, exhibiting strong cross-communication lines. lending to applications within security patterning.[22,66] Refractive index matching with sugar solutions of varying concentrations found that **CE1** particles had a refractive index of ~1.49 and allowed for bright blue selective reflection to be observed by the naked eye.

Finally, CB15 extraction from chiral nematic elastomer microparticles was attempted using acetone washes. The acetone swelled particles such that they entered the isotropic phase, and upon washing back into water birefringence returned. After several washes to remove CB15, it was found that radial textures could no longer be observed indicating that CB15 had likely been removed, however droplet merging suggested that the particles may not have been fully

polymerised. It is expected that microparticles which were fully polymerised, or with a greater degree of crosslinking may have survived washing to retain the chiral nematic texture throughout CB15 extraction, producing chiral imprinted elastomer microparticle capable of selective reflection.

6.2.1 Future Work for Chiral Nematic Systems

A clear follow up to the research reported for chiral nematic systems would be the extraction of chiral dopant from chiral nematic elastomer microparticles to produce chiral imprinted elastomer particles. In addition to acetone washes attempted in this thesis, and successfully used in literature, different solvents could be investigated, such as tetrahydrofuran.[187]

Finally, nanoparticle infiltration could be extended into chiral nematic systems. The microfluidic method utilised to infiltrate bipolar nematic droplets with nanoparticles, could be utilised to infiltrate chiral nematic droplets with nanoparticles also. It is expected that if magnetic nanoparticles were introduced, then contactless heating of the microparticles could be performed to investigate contactless temperature responsivity of the systems.

7 Experimental

7.1 General Information on Materials and Equipment

All chemicals were used as received without further purification, 1,6-hexanediol diacrylate, 4-cyano-4′-pentylbiphenyl, and (*S*)-4'-(2-methylbutyl)-4-cyanobiphenyl were purchased from Alfa Aesar; diphenyl(2,4,6-trimethylbenzoyl) phosphine oxide was purchased from Fluorochem; fluorescein isothiocyanate, polyethylene glycol with average molecular weights of 200 $gmol^{-1}$ and 87-89% hydrolysed polyvinyl alcohol with molecular weights of 13000-23000 and 87000-124000 $gmol^{-1}$ were purchased from Merck. Ultrapure water was obtained from either a Milli-Q Direct 16 or Sartorius Arium water purification system. KSRP-25/B111P1NSS Glass planar ITO alignment cells with a 25 µm gap were purchased from E.H.C. Co. N42 bar and ring neodymium magnets were obtained from Magnet Expert. Monomers **M1**, **M2** and **M3** were obtained from previous work within the group. Masses were obtained using a Mettler Toledo XPE205 DeltaRange analytical balance.

For microfluidic chips, round (ID: 0.70 mm; OD: 0.87 mm) and square (ID: 1.00 mm) borosilicate glass capillaries were purchased from CM Scientific. Capillaries were pulled using a Sutter P30 micropipette puller and the tips broken using an Ultrawave U100 ultrasonic water bath. In microfluidic experiments, the inner phase was loaded into a 250 µL Hamilton glass syringe and fitted into a Chemyx Fusion 400 syringe pump. The outer phase was loaded into a 20 mL Norm-Ject syringe and fitted into a Cole-Parmer Single-syringe 230 VAC syringe pump. Droplet production was monitored on either a Leica CM E or Swift SW380B microscope.

Polymerisations of films and droplets were performed under a 365 nm Omnicure LX500 LED UV light source. For imaging and polymerisations at elevated temperatures a Mettler Toledo FP82HT hot stage with a Mettler Toledo FP90 controller was employed.

Brightfield microscopy was performed on a Zeiss Axio Scope.A1 Pol microscope in either transmission or reflection mode. Polarised light optical microscopy was performed on a Zeiss Axio Scope.A1 Pol microscope in transmission mode. POM

photomicrographs were taken with a Canon 700D digital camera. Droplet and particle size measurements were taken using ImageJ software.

For post-production nanoparticle infiltration of droplets, the nanoparticles were either 1.0 μm amine modified or 0.5 μm sulfate modified crosslinked polystyrene fluorescent microspheres purchased from Sigma Aldrich. Agitation of samples with nanoparticles by shaker plate was performed using a Sky Line S-3 16L orbital shaker. For imaging during these experiments by fluorescence microscopy a Zeiss Axio Scope.A1 microscope with a CooLED pE-300^{White} light source in reflection mode, fitted with filter set 38 HE (excitation 470/40, beam splitter FT495, emission BP 525/50) was used. Fluorescence photomicrographs were taken with a Zeiss AxioCam ICm1 camera. Fluorescence images were coloured green and overlaid with greyscale brightfield images in transmission mode using Zeiss ZEN 3.0 blue edition software.

For microfluidic nanoparticle infiltration of droplets, the nanoparticles were Polybead 1.0 μm amine modified crosslinked polystyrene microspheres purchased from Polysciences. Nanoparticles were modified with fluorescent dye and imaged by fluorescence microscopy using a Zeiss Axio Scope.A1 Pol microscope with a Colibri 5 light source in reflection mode, fitted with filter set 38 HE (excitation 470/40, beam splitter FT495, emission BP 525/50). Fluorescence photomicrographs were taken with a Canon 700D digital camera. Images were processed using ImageJ software.

Differential scanning calorimetry was performed on a Mettler Toledo DSC1, calibrated against an indium standard, using STARe software. Selective reflection was characterised using an Avantes Avaspec 2048 UV-Vis-NIR spectrometer with Avasoft software. Scanning electron microscopy was performed on a JEOL JSM-7800F. Scanning electron microscopy samples were dried in a Thermo Scientific Vacutherm vacuum oven, mounted on aluminium stubs using carbon wafers and sputter coated with gold using a Quorum Technologies Q150RES sputter coater.

Nanoparticle suspensions were centrifuged using a Hettich Universal 320 R centrifuge and resuspended using a Fisherbrand ZX3 vortex mixer and a Fisherbrand FB15047 ultrasonic water bath.

7.2 Microfluidic Chip Building

Round glass capillaries (ID: 0.70 mm; OD: 0.87 mm) were pulled on a glass pipette puller and then placed in an ultrasonic bath to produce a droplet tip diameter of ~15 - 30 μm and collection tip diameter of ~180 - 240 μm by varying sonication time. The lengths of droplet and collection tips were cut to 22 mm and 19 mm respectively and inserted into a square glass capillary (L: 25 mm; ID: 1.00 mm) mounted on a glass microscope slide. The round tip capillaries were aligned in 3-dimensions ~45 – 140 μm apart and glued into place. Syringe needles (23G) were cut, glued over openings and fitted with PTFE tubing.[51]

7.3 Bipolar Nematic Systems

7.3.1 Bipolar Nematic Droplets

7.3.1.1 4-Cyano-4′-pentylbiphenyl (5CB)

Bipolar droplets of 5CB were produced by a suspension method and by microfluidics.[51,85]

Method 1: In the suspension method, 5CB (8.8 μL) was added to a water/glycerol solution (90 vol%, 4.4 mL) in a small glass vial. The suspension was transferred to petri dishes for imaging under POM. The resulting mixture was agitated by rapid manual shaking (1 min) to yield bipolar droplets with a high polydispersity. Average droplet diameters and observations by brightfield and POM imaging for each experiment are shown in Table 10.

Table 10: Droplet sizes of 5CB produced by the suspension method.

Identifier	Mean Droplet Diameter (μm)	Observations & Notes
5CB-SM1	27 (CV: 73.9%)	Very polydisperse droplets. Bipolar nematic alignment. Nanoparticles added post-production.
5CB-SM2	25 (CV: 108.4%)	Very polydisperse droplets. Bipolar nematic alignment. Nanoparticles added post-production.

Method 2: A solution of 5CB (15 mg) in chloroform (97.5 vol% w.r.t 5CB) was prepared. A solution of PVA (87-89% hydrolysed) in MilliQ water (3 wt%) was flowed as an outer fluid through the square capillary and the 5CB solution was co-flowed through the droplet tip of a microfluidic chip. Droplets of 5CB in chloroform were collected through the collection tip into petri dishes. The chloroform was allowed to evaporate yielding droplets which displayed a nematic phase at room temperature (~20 °C), as seen by baseball textures under POM. Experimental parameters for individual experiments are shown in Table 11.

Table 11: Details of microfluidic parameters and resulting droplet sizes of 5CB.

Identifier	PVA Molecular Weight ($gmol^{-1}$)	Tip Sizes (µm)	Flow Rates (µL/hr)	Mean Droplet Diameter (µm)	Solvent Evaporation (hr)	Observations & Notes
5CB-MF11	87-124000	20/200	Outer:16000 Inner: 140	Isotropic: 63 (CV: 9.5%) Nematic: 30 (CV: 13.8%)	20	Polydisperse droplets. Bipolar nematic alignment, baseball textures observed. Nanoparticles added post-production.
5CB-MF14	13-23000	25/200	Outer: 13000 Inner: 140	Isotropic: 63 (CV: 1.9%) Nematic: 26 (CV: 1.9%)	90	Monodisperse droplets. Bipolar nematic alignment, baseball textures observed. Nanoparticles added post-production.

*7.3.1.2 4''-(Acryloyloxybutyl) 2,5-di(4'-butyloxybenzoyloxy)benzoate (**M1**), 4''-(Acryloyloxybutyl 2,5-di(4'-heptyloxybenzoyloxy)benzoate (**M2**) and 11''-(Acryloyloxyundecyl) 2,5-di(4'-butyloxybenzoyloxy)benzoate (**M3**)*

A solution of monomer **M1**, **M2** or **M3** (15 mg), 1,6-hexanediol diacrylate (10 mol% w.r.t monomer) and diphenyl(2,4,6-trimethylbenzoyl) phosphine oxide (2 mol% w.r.t monomer) in chloroform (97.5 vol% w.r.t monomer) was prepared. A solution of PVA (13-23000 $gmol^{-1}$, 87-89% hydrolysed) in MilliQ water (3 wt%) was flowed as an outer fluid through the square capillary and the monomer solution was co-flowed through the droplet tip. Droplets of the monomer mixture in chloroform were collected through the collection tip into petri dishes. The chloroform was allowed to evaporate yielding either droplets which displayed a nematic phase at room temperature (~20 °C),[51] as seen by baseball textures under POM, or if **M1** or **M2** droplets were left, crystallised droplets. Observations under brightfield and POM imaging, as well as full experimental parameters are shown in Table 12.

To prevent droplet crystallisation droplets were polymerised as soon as the bipolar texture formed (**M1-MF22**).

In **M1-MF23** droplets were collected in glass vials (10 x 35, 16 x 66, 20 x 42 and 23 x 57 mm) instead of petri dishes, resulting in longer solvent evaporation times due to decreased surface area to volume ratios compared to dishes. To shorten solvent evaporation, in **M1**-**MF36**, the droplet concentration within petri dishes was lowered by only collecting only 1 – 2 mL of the microfluic droplet mixture in 40 mm petri dishes where additional outer fluid (3 mL) was added. Solvent evaporation was reduced to 3 – 5 hours and as soon as the nematic texture formed, droplets were polymerised to prevent crystallisation and retain the bipolar alignment. This collection method to reduce solvent evaporation was used in all the experiments using **M1** and **M2** monomers which followed **M1-MF36**.

Table 12: Details of microfluidic parameters and resulting droplet sizes and POM observations of **M1**, **M2** and **M3** droplets.

Identifier	Tip Sizes (μm)	Flow Rates (μL/hr)	Mean Droplet Diameter (μm)	Solvent Evaporation (hr)	Observations & Notes
M1-MF2	20/200	Outer: 15000 Inner: 140	Isotropic: 91 (CV: 3.8%) Nematic: 36 (CV: 1.4%)	22	Monodisperse droplets. Bipolar nematic alignment, baseball textures observed. Nanoparticles added post-production.
M1-MF3	20/190	Outer: 15000 Inner: 150	Isotropic: 50 (CV: 8.3%) Nematic: 22 (CV: 3.1%)	20	Slightly polydisperse droplets. Bipolar nematic alignment, baseball textures observed. Some contamination on the surface of droplets. Nanoparticles added post-production.
M1-MF5	20/200	Outer: 15000 Inner: 140	Isotropic: 91 (CV: 1.7%) Nematic: 38 (CV: 9.2%)	20	Fairly polydisperse droplets. Bipolar nematic alignment, baseball texture observed. Some contamination on the surface of droplets. Nanoparticles added post-production.
M1-MF7	15/190	Outer: 15000 Inner: 140	Isotropic: 32 (CV: 49.4%) Nematic: 18 (CV: 47.8%)	20	Droplets were very polydisperse and had smaller droplets, possible of contamination, on the surface.
M1-MF8	25/200	Outer: 15000 Inner: 140	Isotropic: N/A Nematic: N/A	N/A	Chip blocked – no droplets collected.
M1-MF9	25/180	Outer: 15000 Inner: 140	Isotropic: 69 (CV: 2.2%) Nematic: N/A	19	Droplets crystallised upon solvent evaporation, hence no nematic diameter data.
M1-MF10	25/200	Outer: 15000 Inner: 140	Isotropic: 79 (CV: 1.1%) Nematic: N/A	19	Droplets crystallised upon solvent evaporation, hence no nematic diameter data.

M1-MF12	20/200	Outer: 15000 Inner: 140	Isotropic: 72 (CV: 2.2%) Nematic: N/A	21	Droplets crystallised upon solvent evaporation, hence no nematic diameter data.
M1-MF13	20/200	Outer: 15000 Inner: 140	Isotropic: 61 (CV: 1.9%) Nematic: N/A	20	Droplets crystallised upon solvent evaporation, hence no nematic diameter data.
M1-MF15	20/200	Outer: 15000 Inner: 140	Isotropic: 59 (CV: 1.5%) Nematic: N/A	22	Droplets crystallised upon solvent evaporation, hence no nematic diameter data.
M1-MF16	30/200	Outer: 15000 Inner: 140	Isotropic: 71 (CV: 1.9%) Nematic: N/A	13	Droplets crystallised upon solvent evaporation, hence no nematic diameter data.
M1-MF17	20/200	Outer: 15000 Inner: 140	Isotropic: 51 (CV: 1.2%) Nematic: N/A	22	Droplets crystallised upon solvent evaporation, hence no nematic diameter data.
M1-MF22	25/200	Outer: 15000 Inner: 140	Isotropic: 71 (CV: 1.1%) Nematic: 29 (CV: 1.1%)	8	Imaged as soon as nematic texture formed. Monodisperse droplets. Bipolar nematic alignment, baseball texture observed. Solvent evaporation faster in larger dishes. Polymerisation straight away prevented crystallisation.
M1-MF23	20/200	Outer: 15000 Inner: 140	Isotropic: 58 (CV: 4.4%) Nematic: 28 (CV: 1.1%)	65 – 162+	Droplets collected in various vials with different surface area to volume ratios to vary solvent evaporation length. Solvent evaporation extended in all cases. Monodisperse droplets. Bipolar nematic alignment, baseball texture observed.
M1-MF24	30/200	Outer: 15000 Inner: 140	Isotropic: 104 (CV: 1.9%) Nematic: 40 (CV: 1.9%)	16 – 22	Outer fluid added and removed from dishes to alter droplet to PVA solution volume ratio to change solvent evaporation length. Monodisperse droplets. Bipolar nematic alignment, baseball texture observed.
M1-MF40	20/190	Outer: 16000 Inner: 140	Isotropic: 69 (CV: 1.4%) Nematic: 29 (CV: 1.5%)	4 – 5	Outer fluid added to small volume of droplets to shorten solvent evaporation. Monodisperse droplets. Bipolar nematic alignment, baseball texture observed.

M1-MF52	20/210	Outer: 18000 Inner: 140	Isotropic: 57 (CV: 15.2%) Nematic: 25 (CV: 20.3%)	4 – 5+	Polydisperse droplets caused by jetting during the experiment. Bipolar nematic alignment, baseball texture observed.
M1-MF57	25/220	Outer: 16000 Inner: 140	Isotropic: 72 (CV: 1.1%) Nematic: N/A	4 – 10	Outer fluid added and removed from dishes to alter droplet to PVA solution volume ratio to change solvent evaporation length. Solvent evaporation monitored overnight. Where outer fluid was quadrupled evaporation reduced to 4 hrs, where it was halved evaporation took 10 hrs. Crystallisation began after 30 – 60 minutes. Monodisperse droplets although some stuck to the bottom of the dish. Bipolar nematic alignment, baseball texture observed.
M1-MF59	15/200	Outer: 16000 Inner: 140	Isotropic: 64 (CV: 8.5%) Nematic: 26 (CV: 10.0%)	3	Polydisperse droplets caused by chip blockage and jetting during the experiment. Bipolar nematic alignment, baseball texture observed.
M1-MF60	25/220	Outer: 16000 Inner: 140	Isotropic: 96 (CV: 2.2%) Nematic: 38 (CV: 2.3%)	13	Three times number of droplets collected, outer fluid removed from dishes to change solvent evaporation length. Solvent evaporation monitored overnight. Where droplet number quadrupled, per dish solvent evaporation took 13 hrs and droplets crystallised after 1 hr. Mostly monodisperse, unknown nematic texture (out of focus) however were birefringent.
M1-MF63	15/200	Outer: 16000 Inner: 140	Isotropic: 67 (CV: 2.0%) Nematic: 27 (CV: 1.6%)	4 – 5+	Solvent evaporation decreased by 2.5 – 4x dilution of dish with outer fluid. Monodisperse droplets. Bipolar nematic alignment, baseball texture observed.

M1-MF64	15/200	Outer: 16000 Inner: 140	Isotropic: 69 (CV: 1.3%) Nematic: 26 (CV: 1.3%)	3 – 6	Solvent evaporation decreased by 2.5x – 4x dilution of dish with outer fluid. Monodisperse droplets although some stuck to bottom of dish. Bipolar nematic alignment, baseball texture observed.
M1-MF66	15/200	Outer: 16000 Inner: 140	Isotropic: 65 (CV: 0.8%) Nematic: 27 (CV: 1.0%)	3 – 4	Solvent evaporation decreased by 2.5x – 4x dilution of dish with outer fluid. Monodisperse droplets. Bipolar nematic alignment, baseball texture observed.
M1-MF67	15/200	Outer: 16000 Inner: 140	Isotropic: 82 (CV: 0.9%) Nematic: 33 (CV: 1.3%)	3 – 5	Solvent evaporation decreased by 2.5x – 4x dilution of dish with outer fluid. Monodisperse droplets. Bipolar nematic alignment, baseball texture observed. Chip blocked during collection of dishes 6 of 10 causing polydispersity so dishes discarded.
M1-MF68	20/200	Outer: 16000 Inner: 140	Isotropic: 75 (CV: 1.1%) Nematic: 29 (CV: 0.9%)	3 – 5	Solvent evaporation decreased by 2.5x – 4x dilution of dish with outer fluid. Monodisperse droplets. Bipolar nematic alignment, baseball texture observed.
M1-MF69	25/200	Outer: 16000 Inner: 140	Isotropic: 66 (CV: 1.3%) Nematic: 26 (CV: 1.7%)	3 – 5	Solvent evaporation decreased by 2.5x – 4x dilution of dish with outer fluid. Monodisperse droplets. Bipolar nematic alignment, baseball texture observed.
M1-MF70	15/200	Outer: 16000 Inner: 140	Isotropic: 66 (CV: 1.1%) Nematic: 28 (CV: 1.0%)	3 – 5	Solvent evaporation decreased by 2.5x – 4x dilution of dish with outer fluid. Monodisperse droplets. Bipolar nematic alignment, baseball texture observed. Chip blocked during collection of dishes 5 of 8 causing polydispersity so dishes discarded.

M1-MF71	30/210	Outer: 16000 Inner: 140	Isotropic: 82 (CV: 1.3%) Nematic: 33 (CV: 1.0%)	3 – 5	Solvent evaporation decreased by 2.5x – 4x dilution of dish with outer fluid. Monodisperse droplets. Bipolar nematic alignment, baseball texture observed.
M1-MF72	20/200	Outer: 16000 Inner: 140	Isotropic: 58 (CV: 1.2%) Nematic: 25 (CV: 0.9%)	4 – 5	Solvent evaporation decreased by 2.5x – 4x dilution of dish with outer fluid. Monodisperse droplets. Bipolar nematic alignment, baseball texture observed.
M1-MF81	15/200	Outer: 16000 Inner: 140	Isotropic: 74 (CV: 1.2%) Nematic: 31 (CV: 1.4%)	3 – 5	Solvent evaporation decreased by 2.5x – 4x dilution of dish with outer fluid. Monodisperse droplets. Bipolar nematic alignment, baseball texture observed.
M1-MF83	15/200	Outer: 16000 Inner: 140	Isotropic: 68 (CV: 0.8%) Nematic: 27 (CV: 1.2%)	4 – 5	Solvent evaporation decreased by 2.5x – 4x dilution of dish with outer fluid. Monodisperse droplets. Bipolar nematic alignment, baseball texture observed. Droplets polar axes aligned using neodymium magnets.
M1-MF85	15/200	Outer: 16000 Inner: 140	Isotropic: 56 (CV: 1.4%) Nematic: 22 (CV: 1.7%)	3 – 5	Solvent evaporation decreased by 2.5x – 4x dilution of dish with outer fluid. Monodisperse droplets. Bipolar nematic alignment, baseball texture observed. Droplets polar axes aligned using neodymium magnets.
M1-MF90	10/200	Outer: 16000 Inner: 125	Isotropic: N/A Nematic: N/A	N/A	Chip blocked – no droplets collected.
M1-MF92	15/210	Outer: 16000 Inner: 140	Isotropic: 75 (CV: 36.4%) Nematic: 29 (CV: 15.2%)	3 – 5	Solvent evaporation decreased by 2.5x – 4x dilution of dish with outer fluid. Polydisperse droplets caused by chip blockage and jetting during the experiment. Bipolar nematic alignment not present, swirled texture observed possibly due to contamination.
M1-MF94	20/210	Outer: 16000 Inner: 140	Isotropic: 89 (CV: 2.2%) Nematic: 36 (CV: 1.7%)	3 – 5	Solvent evaporation decreased by 2.5x – 4x dilution of dish with outer fluid. Monodisperse droplets. Bipolar nematic alignment, although texture much less defined than usual, possible contamination.

M1-MF97	15/200	Outer: 16000 Inner: 140	Isotropic: 58 (CV: 1.9%) Nematic: 23 (CV: 1.8%)	3 – 5	Solvent evaporation decreased by 2.5x – 4x dilution of dish with outer fluid. Monodisperse droplets. Bipolar nematic alignment, baseball texture observed. Droplets polar axes aligned using neodymium magnets.
M2-MF20	25/200	Outer: 16000 Inner: 140	Isotropic: 69 (CV: 3.8%) Nematic: N/A	17	Droplets crystallised upon solvent evaporation, hence no nematic diameter data.
M2-MF74	15/200	Outer: 16000 Inner: 140	Isotropic: 49 (CV: 29.8%) Nematic: 18 (CV: 7.9%)	3 – 5	Solvent evaporation decreased by 2.5x – 4x dilution of dish with outer fluid. Polydisperse droplets caused by chip blockage during the experiment. Bipolar nematic alignment, baseball texture observed.
M2-MF75	15/200	Outer: 16000 Inner: 140	Isotropic: 69 (CV: 1.5%) Nematic: 29 (CV: 1.9%)	4 – 5	Solvent evaporation decreased by 2.5x – 4x dilution of dish with outer fluid. Monodisperse droplets, although some stuck to the bottom of the dish. Bipolar nematic alignment, baseball texture observed.
M2-MF77	15/200	Outer: 16000 Inner: 140	Isotropic: 65 (CV: 1.4%) Nematic: 28 (CV: 1.5%)	3 – 4	Solvent evaporation decreased by 2.5x – 4x dilution of dish with outer fluid. Monodisperse droplets. Bipolar nematic alignment, baseball texture observed.
M2-MF78	25/200	Outer: 16000 Inner: 140	Isotropic: 71 (CV: 6.4%) Nematic: 26 (CV: 20.7%)	3 – 5	Solvent evaporation decreased by 2.5x – 4x dilution of dish with outer fluid. Polydisperse droplets caused by chip blockage during the experiment. Bipolar nematic alignment, baseball texture observed.
M2-MF80	30/210	Outer: 16000 Inner: 140	Isotropic: 72 (CV: 0.8%) Nematic: 29 (CV: 1.2%)	4 – 6	Solvent evaporation decreased by 2.5x – 4x dilution of dish with outer fluid. Monodisperse droplets. Bipolar nematic alignment, baseball texture observed.
M2-MF88	25/200	Outer: 16000 Inner: 140	Isotropic: 79 (CV: 1.3%) Nematic: 33 (CV: 0.9%)	3 – 5	Solvent evaporation decreased by 2.5x – 4x dilution of dish with outer fluid. Monodisperse droplets. Bipolar nematic alignment, baseball texture observed. Droplets polar axes somewhat aligned using neodymium magnets.

M2-MF89	25/180	Outer: 16000 Inner: 140	Isotropic: 71 (CV: 1.2%) Nematic: 30 (CV: 2.6%)	3 – 5	Solvent evaporation decreased by 2.5x – 4x dilution of dish with outer fluid. Monodisperse droplets. Bipolar nematic alignment, baseball texture observed. Droplets polar axes aligned using neodymium magnets, better than in **M2-MF88**.
M3-MF19	20/200	Outer: 16000 Inner: 140	Isotropic: 64 (CV: 1.0%) Nematic: 26 (CV: 1.3%)	13	Monodisperse droplets. Bipolar nematic alignment, baseball texture observed.
M3-MF21	30/200	Outer: 16000 Inner: 140	Isotropic: 81 (CV: 1.2%) Nematic: 34 (CV: 1.4%)	17	Monodisperse droplets. Bipolar nematic alignment, baseball texture observed. Nanoparticles added post-production.
M3-MF25	25/200	Outer: 16000 Inner: 140	Isotropic: 78 (CV: 0.9%) Nematic: 32 (CV: 1.3%)	20	Monodisperse droplets. Bipolar nematic alignment, baseball texture observed. Nanoparticles added post-production.
M3-MF26	25/200	Outer: 19000 Inner: 130	Isotropic: 117 (CV: 1.9%) Nematic: 45 (CV: 9.2%)	17	Polydisperse droplets caused by chip blockage during the experiment. Bipolar nematic alignment, baseball texture observed.
M3-MF27	25/200	Outer: 16000 Inner: 140	Isotropic: 73 (CV: 1.6%) Nematic: 29 (CV: 2.1%)	18	Monodisperse droplets. Bipolar nematic alignment, baseball texture observed.
M3-MF31	20/200	Outer: 15000 Inner: 140	Isotropic: N/A Nematic: N/A	N/A	Chip blocked – no droplets collected.
M3-MF49	30/200	Outer: 16000 Inner: 140	Isotropic: 80 (CV: 1.5%) Nematic: 32 (CV: 1.6%)	17	Monodisperse droplets. Bipolar nematic alignment, baseball texture observed for most droplets. However, some droplets had an undefined texture.

M3-MF73	20/200	Outer: 16000 Inner: 140	Isotropic: 51 (CV: 1.3%) Nematic: 22 (CV: 12.8%)	17	Polydisperse droplets caused by chip blockage during the experiment. Bipolar nematic alignment, baseball texture observed for most droplets. However, some undefined droplets with contamination at the surface were present.
M3-MF87	15/190	Outer: 16000 Inner: 140	Isotropic: 47 (CV: 2.1%) Nematic: 19 (CV: 1.5%)	17	Monodisperse droplets. Bipolar nematic alignment, baseball texture observed. Droplets polar axes aligned using neodymium magnets.

7.3.1.3 Magnetic Field Alignment of Bipolar Nematic Droplets

Droplets were prepared as described in 7.3.1.2 and a magnetic field was applied either during solvent evaporation to isotropic droplets, or afterwards to nematic droplets. Dishes containing droplets were positioned between the poles of magnets by being placed on top of either three stacked N42 bar magnets or a diametrically magnetised N42 ring magnet. The solvent was allowed to evaporate from the isotropic droplets, and the nematic droplets were swirled in the magnetic field. The droplets were imaged under POM. A population of nematic droplets where the polar axes were aligned across the whole population was produced where the polar axes direction was parallel with the magnetic field.

7.3.2 Nanoparticle Infiltration of Bipolar Nematic Microdroplets

7.3.2.1 Nanoparticle Infiltration by Post-production Methods of Bipolar Nematic Microdroplets

Several methods of nanoparticle addition for infiltration into bipolar droplets by post-production methods have been employed.

In method A, nanoparticles were added using a glass syringe, in high nanoparticle to droplet ratios, to collection dishes. The collection dishes contained isotropic monomer droplets after the microfluidic experiment had been carried out, but before solvent evaporation had taken place. Samples were taken by Pasteur pipette and loaded onto glass slides before imaging under the fluorescence microscope.

In method B, the suspension method was utilised to produce droplets. Nanoparticles, initially in a high nanoparticle to droplet ratio and then in a 2 : 1 ratio, were suspended in vials of water/glycerol solution (90 vol%). The nanoparticle suspension was used as the dispersion medium in the suspension method to produce nematic 5CB droplets as described in section 7.3.1.1.[85] Samples were taken by Pasteur pipette and loaded onto glass slides before imaging under the fluorescence microscope.

In method C, 5CB droplets were produced by microfluidics. Nanoparticles were added to collection dishes containing nematic droplets after complete solvent

evaporation in ratios of 2, 4 or 8 nanoparticles per nematic droplet. Samples were taken by Pasteur pipette and loaded onto glass slides before imaging under the fluorescence microscope.

In method D, nematic monomer droplets were produced by microfluidics. After complete solvent evaporation, the droplet and PVA/water solution was transferred into a glass vial (16 x 66 mm) to which nanoparticles were added. The suspensions were agitated on an orbital shaker (**M3-MF21**: 300 rpm, 1 hr; **M3-MF25a**: 300 rpm, 0.5 – 2 hr; **M3-MF25b**: 200 rpm, 0.5 – 2 hr). Samples were taken by Pasteur pipette and loaded onto glass slides before imaging under the fluorescence microscope.

Table 13 shows nanoparticle size, functionality and ratio to liquid crystal droplets in each individual experiment, as well as the method of nanoparticle infiltration.

Table 13: Details of the type, ratio and post-production method of addition of crosslinked polystyrene nanoparticles to nematic microdroplets.

Identifier	Nanoparticle Diameter (μm)	Nanoparticle Surface Groups	Nanoparticle : Droplet Ratio	Nanoparticle Addition Method	Observations & Notes
M1-MF2a	0.5	Sulfate	Excess (0.01 wt%)	A	Average number of nanoparticles within droplets unknown due to lack of fluorescence microscopy equipment.
M1-MF2b	0.5	Sulfate	Excess (0.01 wt%)	A	Average number of nanoparticles within droplets unknown due to lack of fluorescence microscopy equipment.
M1-MF3a	0.5	Sulfate	Excess (0.01 wt%)	A	Dye leaching prevented the ability to determine average number of nanoparticles in droplets.
M1-MF3b	1.0	Amine	Excess (0.01 wt%)	A	Dye leaching prevented the ability to determine average number of nanoparticles in droplets.
M1-MF5a	1.0	Amine	Excess (0.01 wt%)	A	Dye leaching prevented the ability to determine average number of nanoparticles in droplets.
M1-MF5b	1.0	Amine	Excess (0.01 wt%)	A	Dye leaching prevented the ability to determine average number of nanoparticles in droplets.
M1-MF5c	1.0	Amine	Excess (0.01 wt%)	A	Dye leaching prevented the ability to determine average number of nanoparticles in droplets.
M1-MF5d	1.0	Amine	Excess (0.01 wt%)	A	Dye leaching prevented the ability to determine average number of nanoparticles in droplets.
M1-MF5e	1.0	Amine	Excess (0.01 wt%)	A	Dye leaching prevented the ability to determine average number of nanoparticles in droplets.
5CB-SM1a	1.0	Amine	Excess (0.01 wt%)	B	Too many nanoparticles infiltrated droplets to determine average number of nanoparticles in droplets.
5CB-SM1b	0.5	Sulfate	Excess (0.01 wt%)	B	Too many nanoparticles infiltrated droplets to determine average number of nanoparticles in droplets.
5CB-SM2a	1.0	Amine	2 : 1	B	Too few droplets infiltrated to determine average number of nanoparticles in droplets.
5CB-SM2b	0.5	Sulfate	2 : 1	B	Too few droplets infiltrated to determine average number of nanoparticles in droplets.

5CB-MF11a	1.0	Amine	2 : 1	C	Too few droplets infiltrated to determine average number of nanoparticles in droplets.
5CB-MF11b	0.5	Sulfate	2 : 1	C	Too few droplets infiltrated to determine average number of nanoparticles in droplets.
5CB-MF11c	0.5	Sulfate	4 : 1	C	Too few droplets infiltrated to determine average number of nanoparticles in droplets.
5CB-MF11d	1.0	Amine	4 : 1	C	Too few droplets infiltrated to determine average number of nanoparticles in droplets.
5CB-MF14a	1.0	Amine	2 : 1	C	Too few droplets infiltrated to determine average number of nanoparticles in droplets.
5CB-MF14b	1.0	Amine	4 : 1	C	Too few droplets infiltrated to determine average number of nanoparticles in droplets.
5CB-MF14c	1.0	Amine	8 : 1	C	Too few droplets infiltrated to determine average number of nanoparticles in droplets.
M3-MF21a	1.0	Amine	4 : 1	D	Too few droplets infiltrated to determine average number of nanoparticles in droplets.
M3-MF21b	0.5	Sulfate	4 : 1	D	Too few droplets infiltrated to determine average number of nanoparticles in droplets.
M3-MF25a	1.0	Amine	4 : 1	D	Too few droplets infiltrated to determine average number of nanoparticles in droplets.
M3-MF25b	1.0	Amine	4 : 1	D	Too few droplets infiltrated to determine average number of nanoparticles in droplets.

7.3.2.2 Nanoparticle Infiltration During Production of Bipolar Nematic Microdroplets by Microfluidic Method

FITC modified polystyrene nanoparticles were prepared as described in section 7.4.3.1. Bipolar microdroplets containing nanoparticles were produced using **M1**, **M2** and **M3**. A solution of monomer (15 mg), 1,6-hexanediol diacrylate (10 mol% w.r.t monomer) and diphenyl(2,4,6-trimethylbenzoyl) phosphine oxide (2 mol% w.r.t monomer) in chloroform (97.5 vol% w.r.t monomer) was prepared. FITC modified 1.0 µm polystyrene nanoparticle suspension in chloroform (2 : 1 ratio: 2.5 x 10^{-3} %w/v, 62 µL, 4 : 1 ratio: 2.5 x 10^{-3} %w/v, 124 µL; 8 : 1 ratio: 5 x 10^{-3} %w/v, 124 µL) was added to the monomer solution.[125] The resulting suspension was vortexed at 3000 rpm for 1 minute. A solution of PVA (13-23000 $gmol^{-1}$, 87-89% hydrolysed) in MilliQ water (3 wt%) was flowed as an outer fluid and the monomer solution was co-flowed through the droplet tip. Droplets of the nanoparticle and monomer mixture in chloroform were collected through the collection tip into petri dishes. For **M1** and **M2** 1 – 2 mL of the microfluic droplet mixture was collected in 40 mm petri dishes where additional outer fluid (3 mL) was then added. For **M3**, 3 - 4 mL microfluidic droplet mixture was collected in 40 mm petri dishes. The chloroform was allowed to evaporate to yield droplets which displayed a nematic phase at room temperature (~20 °C). Details of the imaging under POM and fluorescence imaging can be found in Table 14, alongside experimental parameters for individual experiments, droplet sizes, infiltration rates and the average number of nanoparticles found per isotropic droplet.

Table 14: Details of microfluidic experiment parameters to incorporate 1 µm FITC modified nanoparticles with amine surface groups, resulting droplet sizes and nanoparticle : droplet ratio for microfluidic nanoparticle infiltration of droplets of **M1**, **M2** & **M3**. *Nanoparticle : droplet ratio estimated using expected droplet diameter; **calculated from nanoparticle containing isotropic droplets only.

Identifier	Tip Sizes (µm)	Flow Rates (µL/hr)	Nanoparticle : Droplet Ratio*	Mean Droplet Diameter (µm)	Solvent Evaporation (hr)	% Droplets Infiltrated / Average Number of Nanoparticles per Droplet**	Observations & Notes
M1-MF36	20/200	Outer: 16000 Inner: 140	4 : 1	Isotropic: 66 (CV: 2.2%) Nematic: 27 (CV: 1.0%)	3 - 6	28% / 1.04	Monodisperse droplets. Bipolar nematic alignment, baseball texture observed, slight distortion.
M1-MF41	30/220	Outer: 16000 Inner: 140	6 : 1	Isotropic: 48 (CV: 0.7%) Nematic: 22 (CV: 3.9%)	3 - 4	N/A	Monodisperse droplets with grainy nematic alignment. Some droplets with deformed geometry and ill-defined texture, possible premature polymerisation. Nanoparticles not observed due to photobleaching.
M1-MF42	25/200	Outer: 15000 Inner: 140	8 : 1	Isotropic: 66 (CV: 1.2%) Nematic: 28 (CV: 2.4%)	3 - 4	N/A	Droplets monodisperse with grainy nematic alignment. Some droplets crystallised. Nanoparticles not observed due to photobleaching.
M1-MF43	20/200	Outer: 16000 Inner: 140	6 : 1	Isotropic: 47 (CV: 1.9%) Nematic: 20 (CV: 3.6%)	4 - 5	45% / 1.69	Monodisperse droplets with grainy nematic alignment. Some droplets with deformed geometry and ill-defined texture, possible premature polymerisation.

M1-MF44	30/220	Outer: 16000 Inner: 140	6 : 1	Isotropic: 62 (CV: 1.7%) Nematic: 25 (CV: 8.6%)	4	36% / 1.81	Monodisperse droplets with grainy nematic alignment. Some droplets with deformed geometry and ill-defined texture, possible premature polymerisation. Some droplets crystallised.
M1-MF45	20/220	Outer: 16000 Inner: 140	8 : 1	Isotropic: 28 (CV: 1.4%) Nematic: 29 (CV: 4.2%)	3 - 5	72% / 2.61	Monodisperse droplets with grainy nematic alignment. Some droplets with deformed geometry and ill-defined texture, possible premature polymerisation.
M1-MF46	20/210	Outer: 16000 Inner: 140	7 : 1	Isotropic: 62 (CV: 1.0%) Nematic: 27 (CV: 3.2%)	4 - 5	72% / 3.19	Monodisperse droplets with grainy nematic alignment. Some droplets with deformed geometry and ill-defined texture, possible premature polymerisation.
M1-MF47	20/210	Outer: 16000 Inner: 140	7 : 1	Isotropic: 54 (CV: 1.1%) Nematic: 25 (CV: 1.3%)	3 - 5	73% / 2.57	Monodisperse droplets with grainy nematic alignment. Some droplets with deformed geometry and ill-defined texture, possible premature polymerisation.
M1-MF56	20/220	Outer: 18000 Inner: 140	4 : 1	Isotropic: 97 (CV: 2.0%) Nematic: 38 (CV: 1.9%)	3 - 6	91% / 2.70	Monodisperse droplets. Bipolar nematic alignment, baseball textures observed, slight distortion. Some large domains of droplets which had stuck to the bottom of the dish.
M1-MF58	25/220	Outer: 17000 Inner: 140	4 : 1	Isotropic: 53 (CV: 19.8%) Nematic: 25 (CV: 23.8%)	3 - 7	41% / 1.48	Polydisperse droplets due to jetting. Bipolar nematic alignment, baseball textures observed, slight distortion.

M1-MF61	15/220	Outer: 16000 Inner: 140	4 : 1	Isotropic: 50 (CV: 1.6%) Nematic: 20 (CV: 1.5%)	3+	67% / 1.54	Monodisperse droplets. Bipolar nematic alignment, baseball textures observed, slight distortion.
M2-MF35	20/180	Outer: 16000 Inner: 140	6 : 1	Isotropic: 118 (CV: 1.5%) Nematic: 18 (CV: 0.8)	4 - 5	65% / 2.67	Monodisperse droplets. Bipolar nematic alignment, baseball texture observed, slight distortion. Some droplets crystallised.
M2-MF38	20/200	Outer: 16000 Inner: 140	6 : 1	Isotropic: 48 (CV: 1.2%) Nematic: 21 (CV: 1.9%)	4 - 5	N/A	Monodisperse droplets. Bipolar nematic alignment, baseball textures. observed. Some large domains of droplets which had stuck to the bottom of the dish. Nanoparticles not observed due to photobleaching.
M3-MF28	20/180	Outer: 16000 Inner: 140	1 : 5	Isotropic: 78 (CV: 2.0%) Nematic: 30 (CV: 1.5%)	17	2% / 1.33	Monodisperse droplets. Bipolar nematic alignment, baseball texture observed.
M3-MF29	30/230	Outer: 19000 Inner: 140	2 : 1	Isotropic: 136 (CV: 2.0%) Nematic: 54 (CV: 7.5%)	17	49% / 1.28	Slightly polydisperse droplets due to chip blockage. Bipolar nematic alignment, baseball texture observed.
M3-MF30	20/190	Outer: 16000 Inner: 140	2 : 1	Isotropic: 70 (CV: 1.7%) Nematic: 28 (CV: 1.2%)	18	N/A	Monodisperse droplets. Bipolar nematic alignment, baseball texture observed. Some droplets stuck to bottom of dish. Nanoparticles not observed due to photobleaching.

M3-MF32	25/200	Outer: 15000 Inner: 140	2 : 1	Isotropic: 58 (CV: 1.1%) Nematic: 23 (CV: 2.8%)	18	20% / 1.05	Monodisperse droplets. Bipolar nematic alignment, baseball texture observed.
M3-MF33	25/200	Outer: 16000 Inner: 140	4 : 1	Isotropic: 71 (CV: 1.8%) Nematic: 30 (CV: 1.4%)	21	69% / 1.82	Monodisperse droplets. Bipolar nematic alignment, baseball texture observed, slight distortion.
M3-MF34	20/190	Outer: 15000 Inner: 140	8 : 1	Isotropic: 52 (CV: 1.7%) Nematic: 22 (CV: 2.1%)	19	53% / 3.49	Monodisperse droplets. Bipolar nematic alignment, baseball texture observed, slight distortion.
M3-MF37	30/220	Outer: 17500 Inner: 140	4 : 1	Isotropic: 66 (CV: 3.2%) Nematic: 29 (CV: 31.5%)	18	N/A	Polydisperse droplets due to jetting and droplet merging. Bipolar nematic alignment, baseball texture observed, slight distortion. Some droplets stuck to the bottom of the dish. Nanoparticles not observed due to photobleaching.
M3-MF39	20/200	Outer: 16000 Inner: 140	4 : 1	Isotropic: 55 (CV: 0.8%) Nematic: 24 (CV: 1.0%)	18	N/A	Monodisperse droplets. Bipolar nematic alignment, baseball texture observed, slight distortion. Nanoparticles not observed due to photobleaching.
M3-MF48	20/200	Outer: 16000 Inner: 140	7 : 1	Isotropic: 57 (CV: 1.9%) Nematic: 25 (CV: 1.8%)	17	78% / 2.48	Monodisperse droplets. Grainy texture, poor alignment.

M3-MF53	30/210	Outer: 18000 Inner: 140	4 : 1	Isotropic: 69 (CV: 3.7%) Nematic: 27 (CV: 3.7%)	18	71% / 1.70	Monodisperse droplets. Grainy texture, poor alignment.
M3-MF55	20/200	Outer: 18000 Inner: 140	4 : 1	Isotropic: 60 (CV: 1.9%) Nematic: 24 (CV: 3.8%)	17	63% / 1.47	Monodisperse droplets. Bipolar nematic alignment, baseball texture observed, slight distortion.
M3-MF95	20/210	Outer: 16000 Inner: 140	4 : 1	Isotropic: 107 (CV: 6.4%) Nematic: 43 (CV: 10.9%)	18	66% / 1.88	Polydisperse droplets due to chip blockage. Bipolar nematic alignment, baseball texture observed, slight distortion.
M3-MF96	25/210	Outer: 16000 Inner: 140	4 : 1	Isotropic: 65 (CV: 1.1%) Nematic: 27 (CV: 1.2%)	17	60% / 1.56	Monodisperse droplets. Bipolar nematic alignment, baseball texture observed, slight distortion.
5CB-MF50	20/220	Outer: 13000 Inner: 180	7 : 1	Isotropic: 45 (CV: 15.2%) Nematic: 23 (CV: 22.5%)	17	62% / 2.08	Polydisperse droplets due to chip blockage. Distorted nematic texture, slightly grainy.
5CB-MF51	30/230	Outer: 17000 Inner: 140	6 : 1	Isotropic: 63 (CV: 1.6%) Nematic: 25 (CV: 4.7%)	18	74% / 1.92	Monodisperse droplets. Bipolar nematic alignment, baseball texture observed, slight distortion.
5CB-MF54	20/210	Outer: 28000 Inner: 140	4 : 1	Isotropic: 75 (CV: 13.4%) Nematic: 24 (CV: 40.5%)	19	56% / 1.62	Very polydisperse droplets due to chip blockage, jetting and droplet merging. Bipolar nematic alignment, baseball texture observed, slight distortion.

7.3.3 Photopolymerisation of Bipolar Nematic Droplets into Bipolar Nematic Elastomer Microparticles

Droplets of **M1**, **M2** and **M3** were produced as described in sections 7.3.1 and 7.3.2 and photopolymerised at various temperatures within the nematic phase by irradiating 6 - 40 cm away from a 365 nm Omnicure LX500 LED UV source at varying intensities for up to 60 minutes to yield crosslinked bipolar microparticles.

In some experiments droplets were polymerised in the isotropic phase (**M1**: >85.6 °C; **M2**: >70.8 °C; **M3**: >69.5 °C)[51] to yield crosslinked polydomain microparticles.

Microparticles were washed by heating to 80 °C for 1 hr before replacing the PVA/water solution with MilliQ water. Washing with water was repeated a minimum of 4 times before replacing the water with PEG 200 for imaging at high temperatures.[51] (Experiments **EX-MF19** – **EX-MF40**)

Alternatively, microparticles were washed at room temperature by removing and replacing 2 mL of the outer fluid with 2 mL MilliQ water. The microparticles were left for 30 – 60 minutes before washing was repeated 15 – 20 times. For imaging at high temperatures dishes were replaced with 25, 50, 75 vol% PEG 200 in water once each before replacing with 100% PEG 200 six times. (Experiments **EX-MF41** – **EX-MF97**)

Table 15 shows the polymerisation parameters, resulting particle dimensions and imaging observations from each individual experiment for the polymerisation of droplets which did not contain any nanoparticles, whereas Table 16 shows these details for the polymerisation of droplets which did contain nanoparticles.

Table 15: Experimental parameters used for polymerisation of microdroplets, resulting mean particle length, width and aspect ratios and observations under POM.

Identifier	Intensity (%) Distance (cm) Temperature (°C) Time (min)	Mean Particle Length (µm), Width (µm) & Mean Aspect Ratio	Observations & Notes
E1-MF22	50% 30 cm 55 °C 30 min	L: 32 (CV: 7.1%) W: 28 (CV: 4.5%) AR: 1.17 (CV: 11.1%)	Slightly elongated irregularly shaped particles with bipolar alignment. Washed with MilliQ water at 80°C and exchanged to PEG 200. Reversible shape change about T_{NI}.
E1-MF23	50% 30 cm 55 °C 30 min	L: 28 (CV: 3.1%) W: 27 (CV: 3.3%) AR: 1.03 (CV: 2.0%)	Mostly round particles with bipolar alignment. Some particles crystallised prior to polymerisation.
E1-MF40	50% 30 cm 55 °C 20 min	L: 30 (CV: 4.0%) W: 27 (CV: 4.9%) AR: 1.14 (CV: 8.8%)	Slightly elongated irregularly shaped particles with bipolar alignment. Wrinkling at surface. Washed with MilliQ water at 80°C and exchanged to PEG 200. Reversible shape change about T_{NI}.
E1-MF52	50% 30 cm 55 °C 20 min	L: 28 (CV: 6.0%) W: 24 (CV: 5.6%) AR: 1.19 (CV: 10.1%)	Slightly elongated irregularly shaped particles with bipolar alignment. Some wrinkling at surface. Washed with MilliQ water at RT and exchanged to PEG 200. Reversible shape change about T_{NI}. T_{NI} = ~125 °C.
	50% 35 cm 55 °C 20 min	L: 31 (CV: 5.3%) W: 24 (CV: 4.5%) AR: 1.31 (CV: 9.2%)	Elongated irregularly shaped particles with bipolar alignment. Some wrinkling at surface. Washed with MilliQ water at RT and exchanged to PEG 200. Reversible shape change about T_{NI}. T_{NI} = ~125 °C.
	50% 40 cm 55 °C 20 min	L: 32 (CV: 8.0%) W: 23 (CV: 4.3%) AR: 1.38 (CV: 10.9%)	Elongated irregularly shaped particles with bipolar alignment. Some wrinkling at surface. Washed with MilliQ water at RT and exchanged to PEG 200. Reversible shape change about T_{NI}. T_{NI} = ~125 °C.

E1-MF59	50% 40 cm 55 °C 20 min	L: 26 (CV: 24.8%) W: 22 (CV: 22.2%) AR: 1.17 (CV: 12.1%)	Elongated irregularly shaped particles with bipolar alignment. Some wrinkling at surface. Washed with MilliQ water at RT and dried for SEM imaging.
E1-MF63	50% 40 cm RT °C 20 min	L: 27 (CV: 2.2%) W: 25 (CV: 2.6%) AR: 1.07 (CV: 2.5%)	Close to spherical particles with bipolar alignment. Slight surface wrinkling. Washed with MilliQ water at RT and either exchanged with PEG 200 or dried for SEM imaging. Reversible shape change about T_{NI}. T_{NI} = ~120 °C.
	50% 40 cm 55 °C 20 min	L: 34 (CV: 4.2%) W: 22 (CV: 2.2%) AR: 1.55 (CV: 4.3%)	Elongated, mainly spindle shaped, particles with bipolar alignment. Some surface wrinkling. Washed with MilliQ water at RT and either exchanged with PEG 200 or dried for SEM imaging. When heated back to polymerisation temperature, no change in wrinkling. When heated to isotropic, wrinkling lost Reversible shape change about T_{NI}. T_{NI} = ~120 – 125 °C.
	50% 40 cm 107 °C 15 min	L: 26 (CV: 1.9%) W: 25 (CV: 2.4%) AR: 1.02 (CV: 1.4%)	Droplets polymerised in isotropic phase. Polydomain spherical particles. No wrinkling. Washed with MilliQ water at RT and either exchanged with PEG 200 or dried for SEM imaging. No shape change about T_{NI}. T_{NI} = ~120 – 125 °C.
E1-MF64	7% 30 cm 55 °C 30 min	L: 28 (CV: 5.1%) W: 24 (CV: 3.1%) AR: 1.15 (CV: 5.6%)	Slightly elongated irregularly shaped particles with bipolar alignment. Wrinkling at surface. Washed with MilliQ water at RT and either exchanged with PEG 200 or dried for SEM imaging.
	50% 30 cm 55 °C 20 min	L: 32 (CV: 3.7%) W: 22 (CV: 2.8%) AR: 1.42 (CV: 3.2%)	Elongated, mainly spindle shaped but some irregularity, particles with bipolar alignment. Surface wrinkling. Washed with MilliQ water at RT and either exchanged with PEG 200 or dried for SEM imaging.
	100% 30 cm 55 °C 20 min	L: 34 (CV: 4.2%) W: 22 (CV: 2.7%) AR: 1.55 (CV: 5.6%)	Elongated, mainly spindle shaped, particles with bipolar alignment. Surface wrinkling. Washed with MilliQ water at RT and either exchanged with PEG 200 or dried for SEM imaging.

E1-MF66	100% 6 cm RT 10 min	L: 35 (CV: 2.7%) W: 22 (CV: 2.3%) AR: 1.60 (CV: 3.0%)	Elongated spindle shaped particles with bipolar alignment. Polymerised on microscope. Wrinkling at surface. Washed with MilliQ water at RT and either exchanged with PEG 200 or dried for SEM imaging. Reversible shape change about T_{NI}. T_{NI} = ~120 °C.
	100% 6 cm 55 °C 10 min	L: 34 (CV: 2.8%) W: 23 (CV: 2.6%) AR: 1.53 (CV: 4.0%)	Elongated spindle shaped particles with bipolar alignment. Polymerised on microscope. Wrinkling at surface. Washed with MilliQ water at RT and either exchanged with PEG 200 or dried for SEM imaging. Reversible shape change about T_{NI}. T_{NI} = ~120 °C.
	100% 6 cm 107 °C 10 min	L: 28 (CV: 0.9%) W: 28 (CV: 0.8%) AR: 1.01 (CV: 0.5%)	Droplets polymerised in isotropic phase. Polydomain spherical particles 1 µm larger than droplets. No wrinkling. Washed with MilliQ water at RT and either exchanged with PEG 200 or dried for SEM imaging. No shape change about T_{NI}. T_{NI} = ~120 – 125 °C.
E1-MF67	7% 30 cm 80 °C 30 min	L: 34 (CV: 13.7%) W: 33 (CV: 15.3%) AR: 1.03 (CV: 1.9%)	Droplets polymerised in isotropic phase. Polydomain spherical particles. No wrinkling. Some particles fused together before or during polymerisation.
	50% 30 cm 80 °C 20 min	L: 40 (CV: 12.4%) W: 37 (CV: 11.9%) AR: 1.07 (CV: 6.0%)	Droplets polymerised in isotropic phase. Polydomain spherical particles. No wrinkling. Some particles fused together before or during polymerisation increasing average particle dimensions larger than droplet.
	100% 30 cm 80 °C 10 min	L: 32 (CV: 1.0%) W: 32 (CV: 1.7%) AR: 1.02 (CV: 1.4%)	Droplets polymerised in isotropic phase. Polydomain spherical particles. No wrinkling.
	100% 6 cm 80 °C 10 min	L: 36 (CV: 12.9%) W: 34 (CV: 11.9%) AR: 1.06 (CV: 6.5%)	Droplets polymerised in isotropic phase. Polydomain spherical particles. No wrinkling. Some particles fused together before or during polymerisation.

E1-MF68	7% 30 cm 70 °C 40 min	L: 31 (CV: 6.7%) W: 28 (CV: 4.9%) AR: 1.09 (CV: 8.9%)	Slightly elongated irregularly shaped particles with bipolar alignment. Wrinkling at surface. Some droplets crystallised prior to polymerisation. Washed with MilliQ water at RT and either exchanged with PEG 200 or dried for SEM imaging. Reversible shape change about T_{NI}. T_{NI} = ~125 °C.
	50% 30 cm 70 °C 20 min	L: 38 (CV: 3.2%) W: 25 (CV: 4.5%) AR: 1.54 (CV: 5.8%)	Elongated, mainly spindle shaped but some irregularity, particles with bipolar alignment. Wrinkling at surface. Some droplets crystallised prior to polymerisation. Washed with MilliQ water at RT and exchanged with PEG 200. Reversible shape change about T_{NI}. T_{NI} = ~120 °C.
	100% 30 cm RT 10 min	L: 35 (CV: 7.2%) W: 25 (CV: 4.0%) AR: 1.41 (CV: 9.2%)	Elongated spindle shaped with bipolar alignment. Wrinkling at surface. Some droplets crystallised prior to polymerisation. Washed with MilliQ water at RT and exchanged with PEG 200. Reversible shape change about T_{NI}. T_{NI} = ~120 °C.
	100% 30 cm 70 °C 10 min	L: 33 (CV: 13.4%) W: 26 (CV: 8.3%) AR: 1.30 (CV: 18.9%)	Some elongated spindle shaped particles and some rounder with bipolar alignment. Wrinkling at surface. Some droplets crystallised prior to polymerisation. Washed with MilliQ water at RT and exchanged with PEG 200. Reversible shape change about T_{NI}. T_{NI} = ~120 °C.
E1-MF69	7% 30 cm RT 40 min	L: 26 (CV: 3.5%) W: 25 (CV: 3.0%) AR: 1.03 (CV: 1.3%)	Spherical particles with bipolar alignment. Wrinkling at surface. Washed with MilliQ water at RT and exchanged with PEG 200. Reversible shape change about T_{NI}. T_{NI} = ~120 – 125 °C.
	50% 30 cm RT 20 min	L: 27 (CV: 5.2%) W: 24 (CV: 2.4%) AR: 1.12 (CV: 6.2%)	Slightly elongated particles with bipolar alignment. Wrinkling at surface. Washed with MilliQ water at RT and exchanged with PEG 200. Reversible shape change about T_{NI}. T_{NI} = ~120 °C.
	100% 30 cm RT 10 min	L: 29 (CV: 4.8%) W: 22 (CV: 3.3%) AR: 1.31 (CV: 7.5%)	Elongated particles with bipolar alignment. Wrinkling at surface. Washed with MilliQ water at RT and exchanged with PEG 200. Reversible shape change about T_{NI}. T_{NI} = ~120 – 125 °C.

E1-MF69 (cont.)	100% 6 cm RT 10 min	L: 31 (CV: 4.4%) W: 23 (CV: 3.7%) AR: 1.36 (CV: 6.2%)	Elongated particles with bipolar alignment. Polymerised on microscope. Wrinkling at surface. Washed with MilliQ water at RT and exchanged with PEG 200. Reversible shape change about T_{NI}. T_{NI} = ~120 °C.
E1-MF70	100% 6 cm RT 10 min	L: 37 (CV: 3.2%) W: 23 (CV: 2.0%) AR: 1.63 (CV: 4.3%)	Elongated spindle shaped particles with bipolar alignment. Polymerised on microscope. Wrinkling at surface.
E1-MF71	100% 6 cm RT 10 min	L: 43 (CV: 2.6%) W: 27 (CV: 2.2%) AR: 1.57 (CV: 3.3%)	Elongated spindle shaped particles with bipolar alignment. Polymerised on microscope. Wrinkling at surface. Washed with MilliQ water at RT and either exchanged with PEG 200 or dried for SEM imaging. Reversible shape change about T_{NI}. T_{NI} = ~120 – 125 °C.
E1-MF72	7% 30 cm RT 60 min	L: 25 (CV: 4.0%) W: 23 (CV: 3.3%) AR: 1.09 (CV: 4.4%)	Close to spherical particles with bipolar alignment. Some surface wrinkling. Washed with MilliQ water at RT and dried for SEM imaging.
	50% 30 cm RT 20 min	L: 29 (CV: 3.0%) W: 22 (CV: 2.3%) AR: 1.32 (CV: 4.4%)	Elongated particles with bipolar alignment. Slight wrinkling at surface. Washed with MilliQ water at RT and dried for SEM imaging.
	50% 30 cm 70 °C 20 min	L: 29 (CV: 5.3%) W: 22 (CV: 3.5%) AR: 1.36 (CV: 6.8%)	Elongated, irregularly shaped, particles with bipolar alignment. Wrinkling at surface. Washed with MilliQ water at RT and dried for SEM imaging.
	100% 6 cm 55 °C 10 min	L: 30 (CV: 1.9%) W: 21 (CV: 2.6%) AR: 1.46 (CV: 2.5%)	Elongated spindle shaped particles with bipolar alignment. Wrinkling at surface. Washed with MilliQ water at RT and dried for SEM imaging.

E1-MF72 (cont.)	100% 6 cm 107 °C 10 min	L: 24 (CV: 2.3%) W: 23 (CV: 2.4%) AR: 1.04 (CV: 1.7%)	Droplets polymerised in isotropic phase. Polydomain spherical particles. No wrinkling. Washed with MilliQ water at RT and either exchanged with PEG 200 or dried for SEM imaging.
	100% 30 cm RT 10 min	L: 28 (CV: 5.6%) W: 22 (CV: 3.7%) AR: 1.28 (CV: 7.8%)	Elongated particles with bipolar alignment. Wrinkling at surface. Washed with MilliQ water at RT and dried for SEM imaging.
E1-MF81	7% 30 cm RT 60 min	L: 32 (CV: 3.8%) W: 30 (CV: 2.9%) AR: 1.06 (CV: 5.8%)	Spherical particles with bipolar alignment. Wrinkling at surface. Washed with MilliQ water at RT and exchanged with PEG 200. Particles stuck together after washing and exchange with PEG 200.
	7% 30 cm 55 °C 45 min	L: 33 (CV: 5.9%) W: 30 (CV: 3.8%) AR: 1.13 (CV: 6.4%)	Slightly elongated, irregularly shaped, particles with bipolar alignment. Wrinkling at surface. Washed with MilliQ water at RT and exchanged with PEG 200. Reversible shape change about T_{NI}. T_{NI} = ~ 115 – 120 °C.
	100% 6 cm RT 10 min	L: 43 (CV: 3.8%) W: 26 (CV: 2.6%) AR: 1.67 (CV: 5.0%)	Elongated spindle shaped particles with bipolar alignment. Wrinkling at surface. Washed with MilliQ water at RT and exchanged with PEG 200. Reversible shape change about T_{NI}. T_{NI} = ~ 115 – 120 °C.
E1-MF83	100% 6 cm RT 10 min	L: 34 (CV: 5.4%) W: 22 (CV: 2.2%) AR: 1.54 (CV: 5.8%)	Elongated spindle shaped particles with bipolar alignment. Polymerised on microscope. Particles deformed in common direction due to droplet magnetic alignment.
E1-MF85	100% 6 cm RT 10 min	L: 28 (CV: 6.9%) W: 19 (CV: 5.2%) AR: 1.51 (CV: 4.5%)	Elongated spindle shaped particles with bipolar alignment. Polymerised on microscope. Particles deformed in common direction due to droplet magnetic alignment. Elongated particles aligned with magnetic field, when the field was rotate 90°, the particles also rotated 90° in 15 – 30 min.

E1-MF92	100% 6 cm RT 10 min	L: 26 (CV: 24.5%) W: 22 (CV: 23.4%) AR: 1.20 (CV: 6.8%)	Slightly elongated particles with undefined texture and alignment. Polymerised on microscope.
E1-MF94	100% 6 cm RT 10 min	L: 42 (CV: 7.1%) W: 36 (CV: 8.4%) AR: 1.25 (CV: 16.2%)	Mostly elongated, but irregularly shaped, particles with bipolar alignment. Polymerised on microscope. Wrinkling at surface. Some rotation of particles to align with magnetic field.
E1-MF97	100% 6 cm RT 10 min	L: 30 (CV: 3.6%) W: 19 (CV: 3.8%) AR: 1.57 (CV: 6.8%)	Elongated spindle shaped particles with bipolar alignment. Polymerised on microscope. Particles deformed in common direction due to droplet magnetic alignment. Elongated particles aligned with magnetic field in ~10 min, when the field was rotate 90°, the particles also rotated 90° in ~10 min. When magnetic field rotated 180°, particles did not rotate.
E2-MF74	100% 6 cm RT 10 min	L: 23 (CV: 4.0%) W: 15 (CV: 3.0%) AR: 1.53 (CV: 3.1%)	Elongated spindle shaped particles with bipolar alignment. Polymerised on microscope. Some very large particles due to droplet polydispersity.
E2-MF75	7% 30 cm RT 40 min	L: 30 (CV: 5.1%) W: 26 (CV: 4.7%) AR: 1.14 (CV: 8.3%)	Slightly elongated particles with bipolar alignment. Wrinkling at surface. Most particles stuck together. Washed with MilliQ water at RT and exchanged with PEG 200. Reversible shape change about T_{NI}. T_{NI} = ~90 °C.
	50% 30 cm RT 20 min	L: 33 (CV: 7.2%) W: 25 (CV: 4.5%) AR: 1.34 (CV: 9.7%)	Elongated particles with bipolar alignment. Wrinkling at surface. Some particles stuck together. Washed with MilliQ water at RT and exchanged with PEG 200. Reversible shape change about T_{NI}. T_{NI} = ~90 – 95 °C.
	100% 6 cm RT 10 min	L: 28 (CV: 4.7%) W: 25 (CV: 3.5%) AR: 1.55 (CV: 7.5%)	Elongated spindle shaped particles with bipolar alignment, some particles curled around in a crescent shape. Wrinkling at surface. Some particles stuck together. Washed with MilliQ water at RT and exchanged with PEG 200. Reversible shape change about T_{NI}. T_{NI} = ~90 – 95 °C.

E2-MF77	50% 30 cm RT 20 min	L: 29 (CV: 10.6%) W: 26 (CV: 6.5%) AR: 1.11 (CV: 17.3%)	Some elongated particles with bipolar alignment, most crystallised before or during polymerisation. Washed with MilliQ water at RT and exchanged with PEG 200. Reversible shape change about T_{NI}. T_{NI} = ~95 – 100 °C.
	50% 30 cm 55 °C 20 min	L: 33 (CV: 7.3%) W: 24 (CV: 3.8%) AR: 1.37 (CV: 10.7%)	Elongated irregular shaped particles with bipolar alignment, some crystallised before or during polymerisation. Wrinkling at surface. Washed with MilliQ water at RT and exchanged with PEG. Reversible shape change about T_{NI}. T_{NI} = ~105 °C.
	50% 30 cm 70 °C 20 min	L: 27 (CV: 4.6%) W: 26 (CV: 2.4%) AR: 1.05 (CV: 6.6%)	Droplets polymerised in isotropic phase. Polydomain spherical particles. Washed with MilliQ water at RT and exchanged with PEG 200.
	50% 30 cm 100 °C 20 min	L: 29 (CV: 7.4%) W: 28 (CV: 5.6%) AR: 1.05 (CV: 3.5%)	Droplets polymerised in isotropic phase. Polydomain spherical particles. Washed with MilliQ water at RT and exchanged with PEG 200. No reversible shape change about T_{NI}. T_{NI} = ~95 – 100 °C.
E2-MF78	50% 30 cm RT 20 min	L: 32 (CV: 6.6%) W: 26 (CV: 6.6%) AR: 1.25 (CV: 9.2%)	Slightly elongated irregularly shaped particles with bipolar alignment. Washed with MilliQ water at RT and exchanged with PEG 200. Reversible shape change about T_{NI}. T_{NI} = ~90 – 95 °C.
	50% 30 cm 55 °C 20 min	L: 34 (CV: 7.0%) W: 26 (CV: 3.1%) AR: 1.31 (CV: 8.2%)	Elongated particles with bipolar alignment. Washed with MilliQ water at RT and exchanged with PEG 200. Reversible shape change about T_{NI}. T_{NI} = ~90 °C.
	50% 30 cm 65 °C 20 min	L: 29 (CV: 4.0%) W: 28 (CV: 2.2%) AR: 1.05 (CV: 3.7%)	Droplets polymerised in isotropic phase. Polydomain spherical particles. Particles ~2 µm larger than droplets. Washed with MilliQ water at RT and exchanged with PEG 200. No reversible shape change about T_{NI}. T_{NI} = ~90 °C.

E2-MF78 (cont.)	50% 30 cm 70 °C 20 min	L: 31 (CV: 4.5%) W: 26 (CV: 8.3%) AR: 1.19 (CV: 9.7%)	Droplets polymerised in isotropic phase. Polydomain irregularly shaped particles.
E2-MF80	7% 30 cm RT 60 min	L: 35 (CV: 2.7%) W: 26 (CV: 2.6%) AR: 1.36 (CV: 3.6%)	Elongated irregularly shaped particles with bipolar alignment. Washed with MilliQ water at RT and exchanged with PEG 200. Particles stuck together after washing. Reversible shape change about T_{NI}. T_{NI} = ~90 °C.
	7% 30 cm 55 °C 45 min	L: 33 (CV: 7.0%) W: 26 (CV: 5.6%) AR: 1.26 (CV: 11.5%)	Elongated irregularly shaped particles with bipolar alignment. Washed with MilliQ water at RT and exchanged with PEG 200. Particles stuck together after washing.
	100% 6 cm RT 10 min	L: 42 (CV: 4.3%) W: 24 (CV: 3.2%) AR: 1.75 (CV: 7.0%)	Elongated spindle shaped particles with bipolar alignment. Polymerised on microscope. Washed with MilliQ water at RT and exchanged with PEG 200. Reversible shape change about T_{NI}. T_{NI} = ~90 – 95 °C.
	100% 30 cm RT 20 min	L: 34 (CV: 4.4%) W: 27 (CV: 2.9%) AR: 1.26 (CV: 5.6%)	Elongated particles with bipolar alignment. Washed with MilliQ water at RT and exchanged with PEG 200. Reversible shape change about T_{NI}. T_{NI} = ~90 °C.
E2-MF88	100% 6 cm RT 10 min	L: 44 (CV: 1.6%) W: 27 (CV: 2.0%) AR: 1.60 (CV: 3.2%)	Elongated spindle shaped particles with bipolar alignment, some particles curled around in a crescent shape. Polymerised on microscope. Particles deformed in common direction due to droplet magnetic alignment. Elongated particles aligned with magnetic field in ~15 min, when the field was rotate 90°, many of the particles also rotated 90° in ~45 min.
E2-MF89	100% 6 cm RT 10 min	L: 39 (CV: 3.1%) W: 25 (CV: 2.4%) AR: 1.54 (CV: 5.1%)	Elongated spindle shaped particles with bipolar alignment, some particles curled around in a crescent shape. Polymerised on microscope. Particles deformed in common direction due to droplet magnetic alignment. Elongated particles which were not in a monolayer aligned with magnetic field in ~15 min, when the field was rotate 90°, many of the particles also rotated 90° in ~15 min. When magnetic field rotated 180°, elongated spindle shaped particles did not rotate but curled crescent shaped ones did.

E3-MF19	50% 30 cm 55 °C 30 min	L: 27 (CV: 2.1%) W: 25 (CV: 1.4%) AR: 1.06 (CV: 2.2%)	Spherical particles with bipolar alignment. Washed with MilliQ water at 80°C and exchanged to PEG 200. Some particles stuck together after washing. No shape change about T_{NI}.
E3-MF49	50% 20 cm 45 °C 30 min	L: 32 (CV: 3.0%) W: 31 (CV: 1.4%) AR: 1.04 (CV: 2.6%)	Spherical particles with bipolar alignment. Some particles stuck together during or after polymerisation.
	50% 30 cm 45 °C 30 min	L: 32 (CV: 1.5%) W: 32 (CV: 1.3%) AR: 1.01 (CV: 1.0%)	Spherical particles with bipolar alignment. T_{NI} > 80 °C.
	50% 30 cm 70 °C 30 min	L: 31 (CV: 1.2%) W: 31 (CV: 1.7%) AR: 1.01 (CV: 1.4%)	Droplets polymerised in isotropic phase. Polydomain spherical particles. Some particles joined together.
E3-MF73	100% 6 cm 45 °C 10 min	L: 21 (CV: 2.1%) W: 20 (CV: 2.2%) AR: 1.04 (CV: 2.8%)	Spherical particles with bipolar alignment. Some particles stuck together during or after polymerisation.
E3-MF87	50% 30 cm 45 °C 30 min	L: 19 (CV: 2.0%) W: 19 (CV: 2.0%) AR: 1.03 (CV: 2.4%)	Spherical particles with bipolar alignment. Polymerised on microscope. Polar axes aligned because droplets were aligned magnetically prior to polymerisation. Inconclusive evidence that particles may have rotated in magnetic field.

Table 16: Experimental parameters used for polymerisation of microdroplets containing nanoparticles, resulting mean particle length, width and aspect ratios and observations under POM and fluorescence imaging.

Identifier	Intensity (%) Distance (cm) Temperature (°C) Time (min)	Mean Particle Length (µm), Width (µm) & Mean Aspect Ratio	Observations & Notes
E1-MF2	50% 15 cm 50 °C 20 min	L: 36 (CV: 1.0%) W: 35 (CV: 1.0%) AR: 1.01 (CV: 0.7%)	Spherical monodisperse bipolar nematic particles with bipolar alignment, some texture distortion.
E1-MF3	50% 15 cm 55 °C 20 min	L: 22 (CV: 4.3%) W: 22 (CV: 4.6%) AR: 1.02 (CV: 1.5%)	Spherical monodisperse particles with bipolar alignment, some texture distortion. Some surface contamination present.
E1-MF5	50% 15 cm 55 °C 20 min	L: 41 (CV: 5.6%) W: 35 (CV: 4.2%) AR: 1.17 (CV: 9.4%)	Irregularly shaped, elongated nematic particles.
E1-MF36	50% 30 cm 55 °C 20 min	L: 28 (CV: 15.1%) W: 26 (CV: 13.4%) AR: 1.06 (CV: 3.9%)	Close to spherical polydisperse nematic particles. Few nanoparticles visible due to photobleaching. Washed with MilliQ water at 80 °C and exchanged with PEG 200. Reversible shape change about T_{NI}.
E1-MF41	50% 40 cm 55 °C 20 min	L: 22 (CV: 4.3%) W: 20 (CV: 4.0%) AR: 1.09 (CV: 4.5%)	Close to spherical monodisperse nematic particles with grainy texture. Nanoparticles not visible due to photobleaching. Washed with MilliQ water at RT and exchanged with PEG 200. Reversible shape change about T_{NI}. Some droplets had crystallised prior to polymerisation.

E1-MF42	50% 40 cm 55 °C 20 min	L: 28 (CV: 2.1%) W: 26 (CV: 2.0%) AR: 1.10 (CV: 3.2%)	Slightly elongated monodisperse nematic particles with grainy texture. Nanoparticles not visible due to photobleaching. Washed with MilliQ water at RT and exchanged with PEG 200. Reversible shape change about T_{NI}.
E1-MF43	50% 40 cm 55 °C 20 min	L: 21 (CV: 3.7%) W: 20 (CV: 3.5%) AR: 1.06 (CV: 3.1%)	Close to spherical monodisperse nematic particles with grainy texture. Few nanoparticles visible due to photobleaching. Some particles had stuck together after polymerisation.
E1-MF44	50% 40 cm 55 °C 20 min	L: 31 (CV: 12.6%) W: 25 (CV: 8.5%) AR: 1.24 (CV: 10.0%)	Close to spherical monodisperse nematic particles with grainy texture. Few nanoparticles visible due to photobleaching. Washed with MilliQ water at RT and exchanged with PEG 200. Reversible shape change about T_{NI}. Some droplets had crystallised prior to polymerisation.
E1-MF45	50% 40 cm 55 °C 20 min	L: 30 (CV: 2.8%) W: 28 (CV: 2.4%) AR: 1.07 (CV: 3.8%)	Close to spherical monodisperse nematic particles with grainy texture. Nanoparticles visible under fluorescence imaging. Washed with MilliQ water at RT and exchanged with PEG 200. Reversible shape change about T_{NI} with nanoparticles held in place.
E1-MF46	50% 30 cm 55 °C 20 min	L: 28 (CV: 6.8%) W: 24 (CV: 3.9%) AR: 1.19 (CV: 9.7%)	Slightly elongated monodisperse nematic particles with grainy texture. Dust contamination present on particles. Nanoparticles visible under fluorescence imaging. Washed with MilliQ water at RT and exchanged with PEG 200. Reversible shape change about T_{NI} with nanoparticles held in place.
E1-MF47	50% 30 cm 55 °C 20 min	L: 25 (CV: 3.8%) W: 23 (CV: 2.8%) AR: 1.08 (CV: 4.7%)	Close to spherical monodisperse nematic particles with grainy texture. Nanoparticles visible under fluorescence imaging.
E1-MF56	50% 45 cm 55 °C 20 min	L: 41 (CV: 5.8%) W: 33 (CV: 4.2%) AR: 1.27 (CV: 7.3%)	Elongated monodisperse nematic particles. Nanoparticles location not visible under fluorescence imaging, however the elongated tips fluoresced in the microparticles.

E1-MF58	30% 40 cm 55 °C 30 min	L: 29 (CV: 18.2%) W: 24 (CV: 27.3%) AR: 1.25 (CV: 15.6%)	Polydisperse, irregularly shaped particles with some spindle shaped particles. Bipolar nematic alignment, some texture distortion. Nanoparticles location not visible under fluorescence imaging, however the elongated tips fluoresced in the microparticles. Many droplets crystallised before polymerisation. Washed with MilliQ water at RT and either exchanged with PEG 200 or dried for SEM imaging. Reversible shape change about T_{NI} with nanoparticles held in place.
	50% 40 cm 55 °C 20 min	L: 34 (CV: 33.2%) W: 24 (CV: 27.1%) AR: 1.42 (CV: 15.4%)	
E1-MF61	50% 40 cm 55 °C 20 min	L: 21 (CV: 3.5%) W: 18 (CV: 5.4%) AR: 1.17 (CV: 8.9%)	Elongated, irregularly shaped, polydisperse nematic particles. Nanoparticles visible under fluorescence imaging. Washed with MilliQ water at RT and either exchanged with PEG 200 or dried for SEM imaging. Reversible shape change about T_{NI} with nanoparticles held in place. Nanoparticles remained in place throughout shape change. T_{NI} = ~125 °C.
E2-MF38	50% 30 cm 55 °C 30 min	L: 22 (CV: 4.9%) W: 19 (CV: 3.9%) AR: 1.19 (CV: 7.5%)	Elongated, irregularly shaped, polydisperse nematic particles. Nanoparticles not visible due to photobleaching. Many droplets crystallised before polymerisation.
E3-MF28	50% 30 cm 55 °C 30 min	L: 30 (CV: 1.5%) W: 30 (CV: 1.9%) AR: 1.02 (CV: 1.4%)	Spherical, monodisperse bipolar nematic particles, some texture distortion. Few nanoparticles visible due to low infiltration ratio.
E3-MF33	50% 30 cm 45 °C 30 min	L: 30 (CV: 1.3%) W: 30 (CV: 2.1%) AR: 1.01 (CV: 1.5%)	Spherical, monodisperse bipolar nematic particles, some texture distortion some texture distortion. Nanoparticles visible under fluorescence microscopy. Washed with MilliQ water at 80 °C and exchanged with PEG 200. Many particles stuck together upon washing. No reversible shape change about T_{NI}, nanoparticles remained in place throughout heat/cool cycle.
E3-MF34	50% 30 cm 45 °C 20 min	L: 23 (CV: 3.5%) W: 22 (CV: 2.2%) AR: 1.05 (CV: 2.6%)	Spherical, monodisperse bipolar nematic particles. Nanoparticles visible under fluorescence microscopy. Washed with MilliQ water at 80 °C and exchanged with PEG 200. Some particles stuck together upon washing. No reversible shape change about T_{NI}, nanoparticles remained in place throughout heat/cool cycle.

E3-MF37	50% 30 cm 45 °C 30 min	L: 29 (CV: 3.0%) W: 28 (CV: 5.2%) AR: 1.05 (CV: 4.9%)	Spherical, polydisperse bipolar nematic particles, some texture distortion. Few nanoparticles visible due to photobleaching.
E3-MF39	50% 30 cm 45 °C 30 min	L: 25 (CV: 3.3%) W: 24 (CV: 3.3%) AR: 1.04 (CV: 3.0%)	Spherical, monodisperse bipolar nematic particles, some texture distortion. Few nanoparticles visible due to photobleaching. Washed with MilliQ water at 80 °C and exchanged with PEG 200. Some particles stuck together upon washing. No reversible shape change about $T_{NI.}$
E3-MF48	50% 30 cm 45 °C 30 min	L: 25 (CV: 1.4%) W: 24 (CV: 2.0%) AR: 1.04 (CV: 2.4%)	Spherical, monodisperse nematic particles with grainy texture. Nanoparticles visible under fluorescence microscopy. Washed with MilliQ water at RT and exchanged with PEG 200. Some particles stuck together upon washing. No reversible shape change about T_{NI}, nanoparticles remained in place throughout heat/cool cycle.
E3-MF53	50% 30 cm 45 °C 30 min	L: 28 (CV: 7.4%) W: 27 (CV: 7.7%) AR: 1.04 (CV: 2.3%)	Spherical, monodisperse nematic particles with grainy texture. Many nanoparticles visible under fluorescence microscopy. Washed with MilliQ water at RT and exchanged with PEG 200. No reversible shape change about T_{NI}, nanoparticles remained in place throughout heat/cool cycle although photobleaching made it difficult to observe them.
E3-MF55	50% 30 cm 45 °C 30 min	L: 26 (CV: 2.7%) W: 24 (CV: 1.7%) AR: 1.04 (CV: 2.3%)	Spherical, monodisperse bipolar nematic particles, some texture distortion. Nanoparticles visible under fluorescence microscopy, however photobleaching did occur. Washed with MilliQ water at RT and dried in the vacuum oven. Upon drying particles all stuck together so SEM could not be performed.
E3-MF95	100% 6 cm RT 10 min	L: 42 (CV: 30.0%) W: 41 (CV: 30.3%) AR: 1.03 (CV: 4.0%)	Spherical, polydisperse bipolar nematic particles, some texture distortion. Nanoparticles visible under fluorescence microscopy.
E3-MF96	100% 6 cm RT 10 min	L: 27 (CV: 2.7%) W: 26 (CV: 3.4%) AR: 1.03 (CV: 1.9%)	Spherical, monodisperse bipolar nematic particles, some texture distortion. Nanoparticles visible under fluorescence microscopy.

7.3.3.1 Magnetic Alignment of Nematic Elastomer Particles

Bipolar nematic elastomer particles were produced as described in section 7.3.3. Petri dishes of anisometric nematic **E1** and **E2** elastomer microparticles, as well as spherical **E3** elastomer microparticles, were placed between the poles a diametrically magnetised N42 ring magnet which was mounted on a microscope for imaging. Anisometric particles rotated so that their long axis was parallel with the magnetic field in ~10 -15 minutes. The magnet was then rotated 90° and the microparticles also rotated 90° to follow the magnetic field. The magnet was then rotated 180° and the elongated spindle shaped particles did not rotate 180°. It was inconclusive whether spherical **E3** particles rotated to align with the magnetic field.

7.3.3.2 Scanning Electron Microscopy of Nematic Elastomer Particles

Bipolar nematic elastomer particles were produced as described in section 7.3.3. To prepare samples for SEM **E1**, **E2** and **E3** microparticles were washed with MilliQ water at room temperature by removing and replacing 2 mL of the outer fluid with 2 mL MilliQ water. The microparticles were left for 30 – 60 minutes before washing was repeated 15- 20 times before removing the water with a syringe. Dishes were transferred to a vacuum oven where the microparticles were dried under vacuum at 35 °C for 3 days. **E1** samples dried and retained their shape, whereas **E2** and **E3** particles stuck together, rendering them unsuitable for SEM. **E1** samples were then mounted on aluminium stubs using adhesive carbon discs and sputter coated with a conductive gold coating.

7.4 Chiral Nematic Systems

For this section, data carried out in the group under my supervision has been assigned (†).

7.4.1 Chiral Nematic Films

Solutions of **M2**† or **M3**, CB15 (at various concentrations w.r.t monomer detailed in Table 17), 1,6-hexanediol diacrylate (10 mol% w.r.t monomer) and

diphenyl(2,4,6-trimethylbenzoyl) phosphine oxide (2 mol% w.r.t monomer) in chloroform were prepared. The solutions were heated to 100 °C and the chloroform was allowed to evaporate. The resulting mixtures were cooled to 80 °C and loaded into 25 μm planar alignment cells before allowing to cool to room temperature. The mixtures were imaged under POM, observations detailed in Table 17, and then photopolymerised in the chiral nematic phase (20 – 35 °C) by irradiating 15 cm away from a 365 nm Omnicure LX500 LED UV source at 50% intensity for 10 minutes to yield crosslinked chiral nematic elastomer films which were images were imaged under POM. Alignment cells were immersed in liquid nitrogen and opened using a scalpel to release the elastomer films. The resulting chiral nematic films were characterised by UV-Vis-NIR spectroscopy, DSC and imaged under POM again. The polymerisation conditions to produce the films and resulting characterisation data can be found in Table 18.

Table 17: Details of dopant concentration used to produce chiral nematic mixtures to be polymerised into films, and their resulting selective reflection colours and T_{NI}.

Identifier	CB15 (wt%)	Selective Reflection Colour	T_{NI} (°C)
M2-CF1†	20	-	44
M2-CF2†	22	-	42
M2-CF3†	24	Red	40
M2-CF4†	26	Red	37
M2-CF5†	28	Orange	38
M2-CF6†	30	Yellow-Green	36
M2-CF7†	32	Green	33
M2-CF8†	34	Green	28
M2-CF9†	36	Blue-Green	26
M2-CF10†	38	Blue	27
M2-CF11†	40	Purple	25
M2-CF12†	42	-	<25
M3-CF1	18	-	48-50
M3-CF2	23	-	36-38
M3-CF3	25	Red	41-44
M3-CF4	28	Orange	35-37
M3-CF5	30	Yellow	34-36
M3-CF6	33	Green	32-34
M3-CF7	35	Green	31-35
M3-CF8	38	Blue	29-30
M3-CF9	40	Purple	27-30
M3-CF10	43	-	22-24
M3-CF11	45	-	20-22

Table 18: Details of dopant concentration, selective reflection colour and λ_{max}, T_{NI} and T_g obtained by POM, DSC and UV-Vis-NIR spectroscopy for **E2** and **E3** CB15 doped chiral nematic elastomers. *Collected by POM for **E2** and DSC for **E3**; **missing T_g values were not measured.

Identifier	CB15 (wt%)	Polymerisation Temperature (°C)	Selective Reflection Colour	λ_{max} (nm)	T_{NI}* (°C)	T_g** (°C)
E2-CF1†	20	RT	-	756	53	46.2
E2-CF2†	22	RT	Red	695	50	-
E2-CF3†	24	RT	Red	662	48	-
E2-CF4†	26	RT	Orange-Red	639	48	-
E2-CF5†	28	RT	Orange	625	47	-
E2-CF6†	30	RT	Green	571	44	-
E2-CF7†	32	RT	Green	518	38	-
E2-CF8†	34	RT	Blue-Green	504	37	-
E2-CF9†	36	RT	Blue-Green	496	36	-
E2-CF10†	38	RT	Blue	484	32	26.1
E2-CF11†	40	RT	Purple	454	27	-
E2-CF12†	42	RT	-	-	<25	-
E3-CF1	18	35	-	936	69.0	-9.3
E3-CF2	23	30	-	721	62.4	-10.9
E3-CF3	25	RT	Red	658	60.1	-12.9
E3-CF4	28	RT	Orange	611	56.6	-15.5
E3-CF5	30	RT	Yellow	586	55.3	-16.7
E3-CF6	33	RT	Green	513	49.4	-21.9
E3-CF7	35	RT	Green	506	-	-
E3-CF8	38	RT	Blue	-	43.7	-25.7
E3-CF9	40	RT	Purple	456	41.2	-26.2
E3-CF10	43	RT	-	-	37.2	-29.9
E3-CF11	45	RT	-	-	34.7	-31.1

7.4.1.1 Chiral Dopant Removal from Chiral Nematic Elastomer Films

Films **E2-CF1–11**† and **E3-CF7** were produced as described in section 7.4.1. The films were washed with acetone (5 x 1 mL) and dabbed with paper roll to remove the chiral dopant. The acetone washed films were characterised by UV-Vis-NIR spectroscopy and imaged under POM. The resulting λ_{max} values after dopant removal are reported in Table 19.

Table 19: Details of λ_{max} collected by UV-Vis-NIR spectroscopy after washing CB15 out of doped **E2** and **E3** elastomer films.

Identifier	λ_{max} (nm)
WE2-CF1†	637
WE2-CF2†	585
WE2-CF3†	480
WE2-CF4†	436
WE2-CF5†	423
WE2-CF6†	Not observable at ~>400 nm
WE2-CF7†	Not observable at ~>400 nm
WE2-CF8†	Not observable at ~>400 nm
WE2-CF9†	Not observable at ~>400 nm
WE2-CF10†	Not observable at ~>400 nm
WE2-CF11†	Not observable at ~>400 nm
WE3-CF7	Selective reflection lost

7.4.2 Chiral Nematic Microdroplets

Chiral mixtures (**CM1**, **2**, **3** & **4**) were prepared. a solution of monomer, CB15, 1,6-hexanediol diacrylate (10 mol% w.r.t monomer) and diphenyl(2,4,6-trimethylbenzoyl) phosphine oxide (2 mol% w.r.t monomer) in chloroform (97.5 vol% w.r.t monomer + CB15) was prepared. The monomer and CB15 composition of each chiral mixture is detailed in Table 20.

Table 20: Details of the monomer and CB15 composition of chiral mixtures, also containing crosslinker 1,6-hexanediol diacrylate at 10 mol% w.r.t monomer, photoinitiator diphenyl(2,4,6-trimethylbenzoyl) phosphine oxide at 2 mol% w.r.t monomer and chloroform at 97.5 vol% w.r.t monomer + CB15.

Identifier	Monomer	Mass of Monomer added (mg)	CB15 added (wt% w.r.t monomer)
CM1	**M1**	9.0	40
CM2	**M1**	10.5	30
CM3	**M3**	10	33
CM4	**M2**	10.8	28

A solution of PVA (13-23000 $gmol^{-1}$, 87-89% hydrolysed) in MilliQ water (3 wt%) was flowed as an outer fluid through the square capillary and the monomer

solution was co-flowed through the droplet tip. Droplets of the monomer solution in chloroform were collected through the collection tip into a petri dish.[51] The chloroform was allowed to evaporate to yield droplets which displayed a chiral nematic phase at room temperature (~20 °C), as seen by Maltese cross textures under POM. Experimental parameters for individual experiments are shown in Table 21.

Table 21: Details of microfluidic parameters and resulting droplet sizes and POM observations of CB15 doped chiral mixtures of **M1**, **M2** or **M3**.

Identifier	Tip Sizes (µm)	Flow Rates (µL/hr)	Mean Droplet Diameter (µm)	Solvent Evaporation (hr)	Observations & Notes
CM1-MF1	25/190	Outer: 15000 Inner: 140	Isotropic: 62 (CV 1.4%) Chiral Nematic: 25 (CV 3.0%)	22	Droplets with blue selective reflection. Maltese cross chiral nematic texture under POM.
CM1-MF4	25/200	Outer: 15000 Inner: 140	Isotropic: 78 (CV 1.4%) Chiral Nematic: 32 (CV 1.7%)	67	Droplets with blue selective reflection. Maltese cross chiral nematic texture under POM.
CM1-MF6	25/190	Outer: 15000 Inner: 140	Isotropic: 65 (CV 1.0%) Chiral Nematic: 28 (CV 8.0%)	20	Droplets with blue selective reflection. Maltese cross chiral nematic texture under POM.
CM1-MF18	25/220	Outer: 16000 Inner: 150	Isotropic: 91 (CV 0.8%) Chiral Nematic: 36 (CV 0.9%)	13	Droplets with blue selective reflection. Maltese cross chiral nematic texture under POM.
CM1-MF79	15/240	Outer: 16000 Inner: 140	Isotropic: 63 (CV 1.6%) Chiral Nematic: 26 (CV 0.9%)	17	Droplets with blue selective reflection. Maltese cross chiral nematic texture under POM.
CM1-MF82	25/200	Outer: 16000 Inner: 140	Isotropic: 64 (CV 0.9%) Chiral Nematic: 26 (CV 1.2%)	17	Droplets with blue selective reflection. Maltese cross chiral nematic texture under POM.

CM1-MF84	15/200	Outer: 16000 Inner: 140	Isotropic: 42 (CV 1.6%) Chiral Nematic: 18 (CV 1.5%)	17	Droplets with blue selective reflection. Maltese cross chiral nematic texture under POM.
CM1-MF86	15/200	Outer: 16000 Inner: 140	Isotropic: 41 (CV 2.2%) Chiral Nematic: 18 (CV 2.1%)	17	Droplets with blue selective reflection. Maltese cross chiral nematic texture under POM.
CM2-MF76	20/190	Outer: 16000 Inner: 140	Isotropic: 67 (CV 1.1%) Chiral Nematic: 26 (CV 2.3%)	17	Droplets with red selective reflection. Maltese cross chiral nematic texture under POM. Cross-communication between droplets observed.
CM2-MF93	20/210	Outer: 16000 Inner: 140	Isotropic: 67 (CV 1.3%) Chiral Nematic: 27 (CV 1.0%)	17	Droplets with red selective reflection. Maltese cross chiral nematic texture under POM. Cross-communication between droplets observed.
CM3-MF91	15/220	Outer: 16000 Inner: 140	Isotropic: 68 (CV 1.0%) Chiral Nematic: 27 (CV 2.1%)	17	Droplets with green selective reflection. Maltese cross chiral nematic texture under POM.
CM4-MFCG†	20/180	Outer: 16000 Inner: 140	Isotropic: 63 (CV 1.5%) Chiral Nematic: 29 (CV 1.5%)	18	Droplets with red selective reflection. Maltese cross chiral nematic texture under POM. Cross-communication between droplets observed.

7.4.3 Photopolymerisation of Chiral Nematic Droplets into Chiral Nematic Elastomer Microparticles

Droplets of **CM1**, **CM2**, **CM3** and **CM4** were produced as described in section 7.4.2 and were photopolymerised in the chiral nematic phase (20 - 25 °C) by irradiating 6 – 15 cm away from a 365 nm Omnicure LX500 LED UV source at 50 – 100% intensity for 10 – 30 minutes to yield crosslinked chiral nematic elastomer microparticles.[51] Table 22 shows the parameters used in each individual experiment for polymerisation of droplets.

Table 22: Experimental data for elastomer particles of **CE1-4** including polymerisation conditions (intensity, distance, temperature and time), mean droplet diameters and aspect ratios, CV and observations under POM.

Identifier	Intensity (%) Distance (cm) Temperature (°C) Time (min)	Mean Particle Diameter (µm) and Aspect Ratio	Observations
CE1-MF1	50% 15 cm RT 20 min	23 (CV: 2.5%) AR: 1.02 (CV: 1.6%)	Particles with blue selective reflection. Maltese cross texture chiral nematic texture under POM with surface bubbles obscuring texture.
CE1-MF4	50% 15 cm RT 20 min	32 (CV: 2.2%) AR: 1.01 (CV: 1.1%)	Particles with blue selective reflection. Maltese cross texture chiral nematic texture under POM.
CE1-MF6	50% 15 cm RT 20 min	26 (CV: 4.5%) AR: 1.02 (CV: 1.8%)	Particles with blue selective reflection. Maltese cross texture chiral nematic texture under POM. Attempted refractive index matching with quinoline, particles merged together.
CE1-MF18	50% 15 cm RT 30 min	36 (CV: 1.4%) AR: 1.0 (CV: 1.0%)	Particles with blue selective reflection. Maltese cross texture chiral nematic texture under POM. T_{NI} (POM) = 40 – 42 °C.
CE1-MF79	50% 15 cm RT 20 min	24 (CV: 2.1%) AR: 1.02 (CV: 0.8%)	Particles with blue selective reflection. Maltese cross texture chiral nematic texture under POM with surface distortion on few particles.
CE1-MF82	100% 15 cm RT 20 min	26 (CV: 1.0%) AR: 1.01 (CV: 1.2%)	Particles with blue selective reflection. Maltese cross texture chiral nematic texture under POM with surface distortion on some particles. Some speckling on the surface seen in reflection mode suggesting some distortion to mesogen alignment. Attempted refractive index matching with resin, glycerol, 85 wt% sugar solution and PEG 200. Glycerol and 85% sugar solutions produced the brightest blue reflection.

CE1-MF84	100% 15 cm RT 20 min	17 (CV: 1.7%) AR: 1.02 (CV: 1.4%)	Particles with blue selective reflection. Maltese cross texture chiral nematic texture under POM. Attempted refractive index matching with glycerol and sugar solutions. The brightest blue reflection was seen in 80% sugar solution.
CE1-MF86	100% 15 cm RT 20 min	17 (CV: 1.3%) AR: 1.01 (CV: 1.2%)	Particles with blue and green selective reflection. Maltese cross texture chiral nematic texture under POM. Attempted refractive index matching with 75 wt% sugar solution in a vial, particles less dense than sugar solution so floated.
CE2-MF76	50% 15 cm RT 20 min	25 (CV: 1.4%) AR: 1.01 (CV: 1.0%)	Particles with red selective reflection, slight cross-communication observed. Maltese cross texture chiral nematic texture under POM with a lot of surface distortion. Attempted washing out CB15 with ethanol, acetone and IPA. IPA and ethanol did not swell particles. Acetone swelled particles which went isotropic and became birefringent again upon returning to water.
	100% 6 cm RT 10 min	25 (CV: 1.5%) AR: 1.01 (CV: 1.7%)	
CE2-MF93	50% 15 cm RT 20 min	26 (CV: 1.9%) AR: 1.01 (CV: 1.1%)	Particles with red selective reflection, slight cross-communication observed. Maltese cross texture chiral nematic texture under POM with a lot of surface distortion. Speckling on the surface in reflection mode suggests poor mesogen alignment. Attempted washing out CB15 with ethanol and acetone. Acetone swelled particles which went isotropic and became polydomain upon returning to water.
	50% 15 cm RT 30 min	27 (CV: 2.0%) AR: 1.02 (CV: 2.0%)	
	100% 15 cm RT 20 min	27 (CV: 2.7%) AR: 1.02 (CV: 1.4%)	

CE3-MF91	100% 15 cm RT 20 min	27 (CV: 2.5%) AR: 1.02 (CV: 1.2%)	Particles with green and blue selective reflection. Maltese cross texture chiral nematic texture under POM with surface distortion on some particles. Some speckling on the surface seen in reflection mode suggesting some distortion to mesogen alignment. Attempted washing out CB15 with acetone solutions – particles merged together. T_{NI} (POM) = 52 – 62 °C.
CE4-MFCG†	100% 30 cm RT 30 min	28 (CV: 3.8%) AR: 1.01 (CV: 1.0%)	Particles with green selective reflection. Maltese cross texture chiral nematic texture under POM with surface distortion on many particles. Some speckling on the surface seen in reflection mode suggesting some distortion to mesogen alignment. Attempted washing out CB15 with acetone solutions but upon return to water particles were polydomain. T_{NI} (POM) = 50 – 55 °C.

7.4.3.1 Chiral Dopant Removal from Chiral Nematic Elastomer Particles

CE2-MF93, **CE3-MF91** and **CE4-MFCG**† microparticles were produced as described in section 7.4.3. The chiral nematic elastomer microparticles were washed by removing and replacing 2 mL of the outer fluid with 2 mL MilliQ water. The microparticles were left for 30 – 60 minutes before washing was repeated 15 – 20 times. The outer fluid was then replaced with 25, 50, 75 (**CE2** and **CE4** only) vol% acetone in water. Microparticles were imaged by POM showing that the particles in acetone had transitioned to the isotropic phase at 75% acetone for **CE2** and **CE4** particles, and 50% for **CE3** particles. The particles were returned to water *via* washes with 50 (**CE2** and **CE4** only) and 25 vol% acetone in water until microparticles were washed with MilliQ water 3 times. The resulting microparticles were then imaged again under POM showing the acetone washed particles had become birefringent again Some particles of **CE2** and **CE4** and the majority of **CE3** particles had merged together post-acetone and water washes. Dopant removal was also attempted using ethanol, however particles in 100% ethanol remained birefringent suggesting particle swelling had not occurred.

7.5 Surface Modification and Dispersion Medium Exchange of Nanoparticles

7.5.1 Surface Modification of Nanoparticles to Covalently Bind Fluorescent Dye

1.0 μm amine modified crosslinked polystyrene nanoparticles in water (2.5 %w/v, 0.2 mL) was transferred to a 1.5 mL Eppendorf centrifuge tube. MilliQ water was added to the nanoparticle suspension (0.8 mL) and the suspension was vortexed at 3000 rpm for 1 minute. The suspension medium was centrifuged (5000 rpm, 10 minutes) and the supernatant replaced with sodium bicarbonate buffer (0.1M). The nanoparticles were resuspended by alternating vortexing at 3000 rpm for 1 minute and sonication for 1 minute. The suspension medium was replaced four times. Fluorescein isothiocyanate (47.70 mg, 0.133 mmol) was added to dimethylformamide (1.0 mL). The FITC solution (100 μL) was added to the buffered nanoparticle suspension and the reaction mixture was vortexed (500 rpm) for 16 hours in the dark at room temperature. The resulting suspension was centrifuged (5000 rpm, 10 minutes) and the supernatant replaced with MilliQ

water before resuspending nanoparticles by alternating vortexing at 3000 rpm for 1 minute and sonication for 1 minute. Washing with MilliQ water was repeated six times until unbound FITC was removed.[169–171]

The resulting nanoparticles had a concentration of 0.5 %w/v and were fluorescently active, with an appropriate level of brightness, upon imaging by fluorescence microscopy.

7.5.2 Nanoparticle Dispersion Medium Exchange from Water to Chloroform

FITC tagged 1.0 μm amine modified crosslinked polystyrene nanoparticles in water (100 μL) was transferred to a 1.5 mL Eppendorf centrifuge tube. MilliQ water was added to the nanoparticle suspension (0.90 mL) and the suspension was vortexed at 3000 rpm for 1 minute. The suspension medium was centrifuged (5000 rpm, 10 minutes) and the supernatant replaced with an IPA in water solution (25 vol%) before resuspension by alternating vortexing at 3000 rpm for 1 minute and sonication for 1 minute. The suspension medium was then replaced four more times with IPA concentrations of 50% (5000 rpm, 5 minutes), 75% (5000 rpm, 3 minutes) and twice at 100% (5000 rpm, 3 minutes). The resulting nanoparticles were imaged by fluorescence microscopy, confirming successful suspension in IPA.

The suspension of FITC tagged 1.0 μm amine modified crosslinked polystyrene nanoparticles in IPA (50 μL for 2 : 1 & 4 : 1 ratio, 100 μL for 8 : 1 ratio) was transferred to a 1.5 mL Eppendorf centrifuge tube containing chloroform (0.9 mL). The resulting suspension was vortexed at 3000 rpm for 1 minute and sonicated for 1 minute. The resulting nanoparticles were imaged by fluorescence microscopy, confirming successful suspension in chloroform with no evidence of dye leaching.

The resulting nanoparticle suspension had calculated concentration of either 2.5×10^{-3} %w/v for those used in 2 : 1 & 4 : 1 ratios, or 5×10^{-3} %w/v for those used in an 8 : 1 ratio. However, errors propagate through loss of nanoparticles when removing and replacing supernatant throughout surface modification and

dispersion medium exchange and therefore this concentration is only approximate.

8 References

1 P. J. Collings, *Liquid Crystals: Nature's Delicate Phase of Matter*, Princeton University Press, 1990.

2 F. Hessel and H. Finkelmann, *Polym. Bull.*, 1986, **15**, 349–352.

3 P. J. Collings and M. Hird, *Introduction to Liquid Crystals: Chemistry and Physics*, CRC Press, 1997.

4 T. C. Lubensky, *Phys. Rev. A*, 1970, **2**, 2497–2514.

5 S. Chandras, D. Krishnam and N. V. Madhusud, *Mol. Cryst. Liq. Cryst.*, 1969, **8**, 45–69.

6 M. N. Krakhalev, O. O. Prishchepa, V. S. Sutormin and V. Y. Zyryanov, *Liq. Cryst.*, 2016, **44**, 1–9.

7 M. N. Krakhalev, O. O. Prishchepa, V. S. Sutormin and V. Y. Zyryanov, *Opt. Mater. (Amst).*, 2019, **89**, 1–4.

8 D. Dunmur, M. Kaczmarek and T. Sluckin, in *Handbook of Liquid Crystals, Volume 2: Physical Properties and Phase Behaviour of Liquid Crystals*, eds. J. W. Goodby, P. J. Collings, T. Kato, C. Tschierske, H. F. Gleeson and P. Raynes, Wiley VCH, 2nd edn., 2014.

9 F. Ahmad, M. Jamil, J. W. Lee and Y. J. Jeon, *Liq. Cryst.*, 2015, **42**, 233–239.

10 S. Candau, P. Le Roy and F. Debeauvais, *Mol. Cryst. Liq. Cryst.*, 1973, **23**, 283–297.

11 F. C. Frank, *Discuss. Faraday Soc.*, 1958, **25**, 19.

12 Optical Properties – Birefringence in Nematics, http://www.doitpoms.ac.uk/tlplib/liquid_crystals/birefringence_nematics.php, (accessed 17 August 2022).

13 D. L. Thomsen, P. Keller, J. Naciri, R. Pink, H. Jeon, D. Shenoy and B. R. Ratna, *Macromolecules*, 2001, **34**, 5868–5875.

14 M. Yamahara, M. Nakamura, N. Koide and T. Sasaki, *Liq. Cryst.*, 2007, **34**, 381–387.

15 J. Stöhr and M. G. Samant, *J. Electron Spectros. Relat. Phenomena*, 1999, **98–99**, 189–207.

16 M. R. Wilson and D. J. Earl, *J. Mater. Chem.*, 2001, **11**, 2672–2677.

17 H. Lu, Z. Song, J. Zhang and G. Lv, *Liq. Cryst.*, 2014, **41**, 615–620.

18 M. Shlens, M. R. Stoltz and A. Benjamin, *West. J. Med.*, 1975, **122**, 367–370.

19 Introduction to Liquid Crystals, http://www-g.eng.cam.ac.uk/CMMPE/lcintro2.html, (accessed 18 June 2019).

20 The Hirst Lab, http://hirstlab.ucmerced.edu/?attachment_id=46, (accessed 17 August 2022).

21 H. Goto, *J. Mater. Chem.*, 2009, **19**, 4914–4921.

22 Y. Geng, J. Noh, I. Drevensek-Olenik, R. Rupp, G. Lenzini and J. P. F. Lagerwall, *Sci. Rep.*, 2016, **6**, 26840.

23 A. Taugerbeck and C. J. Booth, in *Handbook of Liquid Crystals, Volume 3: Nematic and Chiral Nematic Liquid Crystals*, eds. J. W. Goodby, C. Tschierske, P. Raynes, H. Gleeson, T. Kato and P. J. Collings, Wiley VCH, 2014, vol. 3, pp. 1–63.

24 P. Xie and R. Zhang, *J. Mater. Chem.*, 2005, **15**, 2529.

25 T. Ganicz and W. Stańczyk, *Materials (Basel).*, 2009, **2**, 95–128.

26 C. Pugh and V. Percec, in *Chemical Reactions on Polymers*, eds. J. L. Benham and J. F. Kinstle, American Chemical Society, Washinton, D.C., 1988, pp. 97–118.

27 S. Krause, F. Zander, G. Bergmann, H. Brandt, H. Wertmer and H. Finkelmann, *Comptes Rendus Chim.*, 2009, **12**, 85–104.

28 A. Varanytsia, H. Nagai, K. Urayama and P. Palffy-Muhoray, *Sci. Rep.*, 2015, **5**, 17739.

29 C. Ohm, M. Brehmer and R. Zentel, *Adv. Mater.*, 2010, **22**, 3366–3387.

30 S. Petsch, B. Khatri, S. Schuhladen, L. Köbele, R. Rix, R. Zentel and H. Zappe, *Smart Mater. Struct.*, 2016, **25**, 085010.

31 H. Finkelmann, S. T. Kim, A. Muñoz, P. Palffy-Muhoray and B. Taheri, *Adv. Mater.*, 2001, **13**, 1069–1072.

32 K. Ku, K. Hisano, K. Yuasa, T. Shigeyama, N. Akamatsu, A. Shishido and O. Tsutsumi, *Molecules*, 2021, **26**, 1–11.

33 M. Kishino, N. Akamatsu, R. Taguchi, S. Kubo, K. Hisano, O. Tsutsumi and A. Shishido, *J. Appl. Phys.*, 2021, **129**, 164701.

34 J. D. Marty, H. Gornitzka and M. Mauzac, *Eur. Phys. J. E*, 2005, **17**, 515–520.

35 C. D. Hasson, F. J. Davis and G. R. Mitchell, *Chem. Commun.*, 1998, **1**, 2515–2516.

36 C. D. Hasson, F. J. Davis and G. R. Mitchell, *Mol. Cryst. Liq. Cryst. Sci. Technol. Sect. A. Mol. Cryst. Liq. Cryst.*, 1999, **332**, 155–162.

37 K. G. Noh and S. Y. Park, *Mater. Horizons*, 2017, **4**, 633–640.

38 Y. Sawa, K. Urayama and T. Takigawa, *J. Phys. Conf. Ser.*, 2009, **184**, 0–6.

39 K. Ku, K. Hisano, S. Kimura, T. Shigeyama, N. Akamatsu, A. Shishido and O. Tsutsumi, *Appl. Sci.*, 2021, **11**, 5037.

40 E. Tjipto, K. D. Cadwell, J. F. Quinn, A. P. R. Johnston, N. L. Abbott and F. Caruso, *Nano Lett.*, 2006, **6**, 2243–2248.

41 K. Davey, PhD thesis, University of York, 2015.

42 A. Fernández-Nieves, G. Cristobal, V. Garcés-Chávez, G. C. Spalding, K. Dholakia and D. A. Weitz, *Adv. Mater.*, 2005, **17**, 680–684.

43 C. Melton, S. Riahinasab, A. Keshavarz, B. Stokes and L. Hirst, *Nanomaterials*, 2018, **8**, 146.

44 X. Wang, E. Bukusoglu and N. L. Abbott, *Chem. Mater.*, 2017, **29**, 53–61.

45 O. D. Lavrentovich, *Liq. Cryst.*, 1998, **24**, 117–126.

46 A. Katariya Jain and R. R. Deshmukh, in *Liquid Crystals and Display Technology*, eds. M. S. Ghamsari and I. Carlescu, IntechOpen, 1st edn., 2020.

47 D. S. Miller, X. Wang and N. L. Abbott, *Chem. Mater.*, 2014, **26**, 496–506.

48 R. J. Carlton, J. T. Hunter, D. S. Miller, R. Abbasi, P. C. Mushenheim, L. N. Tan and N. L. Abbott, *Liq. Cryst. Rev.*, 2013, **1**, 29–51.

49 M. C. D. Carter, D. S. Miller, J. Jennings, X. Wang, M. K. Mahanthappa, N. L. Abbott and D. M. Lynn, *Langmuir*, 2015, **31**, 12850–12855.

50 O. O. Prischepa, A. V. Shabanov and V. Y. Zyryanov, *Mol. Cryst. Liq. Cryst.*, 2005, **438**, 1705–1714.

51 J. Taylor, PhD thesis, Lancaster University, 2019.

52 C. Ohm, C. Serra and R. Zentel, *Adv. Mater.*, 2009, **21**, 4859–4862.

53 T. Hessberger, L. B. Braun, C. A. Serra and R. Zentel, *J. Vis. Exp.*, 2018, e57715.

54 C. M. Spillmann, J. Naciri, M. S. Chen, A. Srinivasan and B. R. Ratna, *Liq. Cryst.*, 2006, **33**, 373–380.

55 H. S. Ansell, D. S. Kim, R. D. Kamien, E. Katifori and T. Lopez-Leon, *Phys. Rev. Lett.*, 2019, **123**, 157801.

56 Y.-K. Kim, J. Noh, K. Nayani and N. L. Abbott, *Soft Matter*, 2019, **15**, 6913–6929.

57 X. Wang, E. Bukusoglu, D. S. Miller, M. A. Bedolla Pantoja, J. Xiang, O. D. Lavrentovich and N. L. Abbott, *Adv. Funct. Mater.*, 2016, **26**, 7343–7351.

58 X. Liu, X. Pan, M. G. Debije, J. P. A. Heuts, D. J. Mulder and A. P. H. J. Schenning, *Soft Matter*, 2020, **16**, 4908–4911.

59 X. Liu, M. G. Debije, J. P. A. Heuts and A. P. H. J. Schenning, *Chem. – A Eur. J.*, 2021, **27**, 14168–14178.

60 J. E. Marshall, S. Gallagher, E. M. Terentjev and S. K. Smoukov, *J. Am. Chem. Soc.*, 2014, **136**, 474–479.

61 M. Humar and I. Muševič, *Opt. Express*, 2010, **18**, 26995.

62 G. Cipparrone, A. Mazzulla, A. Pane, R. J. Hernandez and R. Bartolino, *Adv. Mater.*, 2011, **23**, 5773–5778.

63 E. Beltran-Gracia and O. L. Parri, *J. Mater. Chem. C*, 2015, **3**, 11335–11340.

64 J. Fan, Y. Li, H. K. Bisoyi, R. S. Zola, D. Yang, T. J. Bunning, D. A. Weitz and Q. Li, *Angew. Chemie Int. Ed.*, 2015, **54**, 2160–2164.

65 D. A. Paterson, X. Du, P. Bao, A. A. Parry, S. A. Peyman, J. A. T. Sandoe, S. D. Evans, D. Luo, R. J. Bushby, J. C. Jones and H. F. Gleeson, *Mol. Syst. Des. Eng.*, 2022, 607–621.

66 J. Noh, H.-L. Liang, I. Drevensek-Olenik and J. P. F. Lagerwall, *J. Mater. Chem. C*, 2014, **2**, 806–810.

67 S. J. Aβhoff, S. Sukas, T. Yamaguchi, C. A. Hommersom, S. Le Gac and N. Katsonis, *Sci. Rep.*, 2015, **5**, 14183.

68 A. Cardellini, M. Fasano, M. Bozorg Bigdeli, E. Chiavazzo and P. Asinari, *J. Phys. Condens. Matter*, 2016, **28**, 483003.

69 M. Škarabot, A. V. Ryzhkova and I. Muševič, *J. Mol. Liq.*, 2018, **267**, 384–389.

70 K. P. Zuhail, S. Čopar, I. Muševič and S. Dhara, *Phys. Rev. E*, 2015, **92**, 52501.

71 M. Nikkhou, M. Škarabot and I. Muševič, *Eur. Phys. J. E*, 2015, **38**, 23.

72 M. Škarabot, M. Ravnik, S. Žumer, U. Tkalec, I. Poberaj, D. Babič, N. Osterman and I. Muševič, *Phys. Rev. E*, 2008, **77**, 031705.

73 S. Alama, L. Bronsard and X. Lamy, *Phys. Rev. E*, 2016, **93**, 12705.

74 S. B. Chernyshuk and B. I. Lev, *Phys. Rev. E*, 2011, **84**, 11707.

75 S. Kulkarni, S. Kumar and P. Thareja, *J. Mol. Liq.*, 2021, **336**, 116241.

76 I. Muševič, M. Škarabot, U. Tkalec, M. Ravnik and S. Žumer, *Science*, 2006, **313**, 954–958.

77 M. Škarabot, M. Ravnik, S. Žumer, U. Tkalec, I. Poberaj, D. Babič, N. Osterman and I. Muševič, *Phys. Rev. E*, 2007, **76**, 51406.

78 M. Ravnik, M. Škarabot, S. Žumer, U. Tkalec, I. Poberaj, D. Babič, N. Osterman and I. Muševič, *Phys. Rev. Lett.*, 2007, **99**, 247801.

79 A. C. Pawsey and P. S. Clegg, *Soft Matter*, 2015, **11**, 3304–3312.

80 M. A. Gharbi, S. Manet, J. Lhermitte, S. Brown, J. Milette, V. Toader, M. Sutton and L. Reven, *ACS Nano*, 2016, **10**, 3410–3415.

81 O. D. Lavrentovich, *Proc. Natl. Acad. Sci.*, 2011, **108**, 5143–5144.

82 D. Pires, J.-B. Fleury and Y. Galerne, *Phys. Rev. Lett.*, 2007, **98**, 247801.

83 E. Karatairi, B. Rožič, Z. Kutnjak, V. Tzitzios, G. Nounesis, G. Cordoyiannis, J. Thoen, C. Glorieux and S. Kralj, *Phys. Rev. E*, 2010, **81**, 41703.

84 H. Yoshida, Y. Tanaka, K. Kawamoto, H. Kubo, T. Tsuda, A. Fujii, S. Kuwabata, H. Kikuchi and M. Ozaki, *Appl. Phys. Express*, 2009, **2**, 121501.

85 F. Mondiot, X. Wang, J. J. de Pablo and N. L. Abbott, *J. Am. Chem. Soc.*, 2013, **135**, 9972–9975.

86 M. Rahimi, T. F. Roberts, J. C. Armas-Pérez, X. Wang, E. Bukusoglu, N. L. Abbott and J. J. de Pablo, *Proc. Natl. Acad. Sci.*, 2015, **112**, 5297–5302.

87 E. Bukusoglu, X. Wang, Y. Zhou, J. A. Martínez-González, M. Rahimi, Q. Wang, J. J. de Pablo and N. L. Abbott, *Soft Matter*, 2016, **12**, 8781–8789.

88 Y. Lee, P. J. Johnson, P. T. Robbins and R. H. Bridson, *Eur. J. Pharm. Biopharm.*, 2013, **83**, 168–173.

89 T. Nisisako, T. Torii and T. Higuchi, *Chem. Eng. J.*, 2004, **101**, 23–29.

90 A. Mazzulla, G. Cipparrone, R. J. Hernandez, A. Pane and R. Bartolino, *Mol. Cryst. Liq. Cryst.*, 2013, **576**, 15–22.

91 Y. Zhang, A. McMullen, L.-L. Pontani, X. He, R. Sha, N. C. Seeman, J. Brujic and P. M. Chaikin, *Nat. Commun.*, 2017, **8**, 21.

92 J. Kim, R. J. Larsen and D. a Weitz, *J. Am. Chem. Soc.*, 2006, **128**, 14374–14377.

93 X. Liu, Y. Xu, J. P. A. Heuts, M. G. Debije and A. P. H. J. Schenning, *Macromolecules*, 2019, **52**, 8339–8345.

94 L. B. Braun and R. Zentel, *Liq. Cryst.*, 2019, **46**, 2023–2041.

95 M. Patel, A. N. P. Radhakrishnan, L. Bescher, E. Hunter-Sellars, B. Schmidt-Hansberg, E. Amstad, S. Ibsen and S. Guldin, *Soft Matter*, 2021, **17**, 947–954.

96 A. Sattari, P. Hanafizadeh and M. Hoorfar, *Adv. Colloid Interface Sci.*, 2020, **282**, 102208.

97 D. Wenzlik, C. Ohm, C. Serra and R. Zentel, *Soft Matter*, 2011, **7**, 2340.

98 F. H. Winslow and W. Matreyek, *Ind. Eng. Chem.*, 1951, **43**, 1108–1112.

99 P. J. Dowding and B. Vincent, *Colloids Surfaces A Physicochem. Eng. Asp.*, 2000, **161**, 259–269.

100 J. H. Kim, T. Y. Jeon, T. M. Choi, T. S. Shim, S.-H. Kim and S.-M. Yang, *Langmuir*, 2014, **30**, 1473–1488.

101 C. Serra, N. Berton, M. Bouquey, L. Prat and G. Hadziioannou, *Langmuir*, 2007, **23**, 7745–7750.

102 S. Omi, K. Katami, A. Yamamoto and M. Iso, *J. Appl. Polym. Sci.*, 1994, **51**, 1–11.

103 G. M. Whitesides, *Nature*, 2006, **442**, 368–373.

104 D. van Swaay, T.-Y. D. Tang, S. Mann and A. de Mello, *Angew. Chemie Int. Ed.*, 2015, **54**, 8398–8401.

105 S. L. Anna, N. Bontoux and H. A. Stone, *Appl. Phys. Lett.*, 2003, **82**, 364–366.

106 T. Fu, Y. Ma, D. Funfschilling, C. Zhu and H. Z. Li, *Chem. Eng. Sci.*, 2010, **65**, 3739–3748.

107 B. E. Rapp, in *Microfluidics: Modelling, Mechanics and Mathematics*, Elsevier, 2017, pp. 243–263.

108 Utilizing Microfluidics for Optimizing Stem Cell Therapies, https://bme240.eng.uci.edu/students/06s/bmosadeg/microback.htm, (accessed 3 September 2022).

109 S. Sharma, M. Srisa-Art, S. Scott, A. Asthana and A. Cass, in *Microfluidic Diagnostics: Methods and Protocols*, eds. G. Jenkins and C. D. Mansfield, Humana, 2013, pp. 207–230.

110 A. M. Ibrahim, J. I. Padovani, R. T. Howe and Y. H. Anis, *Micromachines*, 2021, **12**, 590.

111 E. K. Fleischmann, C. Ohm, C. Serra and R. Zentel, *Macromol. Chem. Phys.*, 2012, **213**, 1871–1878.

112 O. Sartipzadeh, S. M. Naghib, A. Seyfoori, M. Rahmanian and F. S. Fateminia, *Mater. Sci. Eng. C*, 2020, **109**, 110606.

113 M. L. Cordero, F. Gallaire and C. N. Baroud, *Phys. Fluids*, 2011, **23**, 094111.

114 C. Cramer, P. Fischer and E. J. Windhab, *Chem. Eng. Sci.*, 2004, **59**, 3045–3058.

115 A. S. Utada, L. Chu, D. R. Link, C. Holtze and D. A. Weitz, *MRS Bull.*, 2007, **32**, 702–708.

116 C. A. Serra, I. U. Khan, Z. Chang, M. Bouquey, R. Muller, I. Kraus, M. Schmutz, T. Vandamme, N. Anton, C. Ohm, R. Zentel, A. Knauer and M. Köhler, *J. Flow Chem.*, 2013, **3**, 66–75.

117 E.-K. Fleischmann, F. R. Forst, K. Köder, N. Kapernaum and R. Zentel, *J. Mater. Chem. C*, 2013, **1**, 5885.

118 R. S. Kularatne, H. Kim, J. M. Boothby and T. H. Ware, *J. Polym. Sci. Part B Polym. Phys.*, 2017, **55**, 395–411.

119 E.-K. Fleischmann, H.-L. Liang, N. Kapernaum, F. Giesselmann, J. Lagerwall and R. Zentel, *Nat. Commun.*, 2012, **3**, 1178.

120 C. Ohm, N. Kapernaum, D. Nonnenmacher, F. Giesselmann, C. Serra and R. Zentel, *J. Am. Chem. Soc.*, 2011, **133**, 5305–5311.

121 D. Rudhardt, A. Fernández-Nieves, D. R. Link and D. A. Weitz, *Appl. Phys. Lett.*, 2003, **82**, 2610–2612.

122 A. Fernández-Nieves, *Soft Matter*, 2006, **2**, 105–108.

123 A. S. Utada, E. Lorenceau, D. R. Link, P. D. Kaplan, H. A. Stone and D. A. Weitz, *Science*, 2005, **308**, 537–541.

124 R. Wei, L. Zhou, Y. He, X. Wang and P. Keller, *Polymer (Guildf).*, 2013, **54**, 5321–5329.

125 D. Ditter, P. Blümler, B. Klöckner, J. Hilgert and R. Zentel, *Adv. Funct. Mater.*, 2019, **29**, 1902454.

126 T. Hessberger, L. B. Braun and R. Zentel, *Adv. Funct. Mater.*, 2018, **28**, 1800629.

127 Y. Yuan, P. Keller and I. I. Smalyukh, *Soft Matter*, 2021, **17**, 3037–3046.

128 Z. Bradač, S. Kralj and S. Žumer, *Phys. Rev. E*, 2002, **65**, 021705.

129 X. Chen, B. D. Hamlington and A. Q. Shen, *Langmuir*, 2008, **24**, 541–546.

130 S. Haseloh, P. van der Schoot and R. Zentel, *Soft Matter*, 2010, **6**, 4112.

131 R. Wei and X. Hua, *Mol. Cryst. Liq. Cryst.*, 2017, **643**, 83–96.

132 M.-P. Van, C. C. L. Schuurmans, C. W. M. Bastiaansen and D. J. Broer, *RSC Adv.*, 2014, **4**, 62499–62504.

133 T. Seki, D. Yamaoka, T. Takeshima, Y. Nagashima, M. Hara and S. Nagano, *Mol. Cryst. Liq. Cryst.*, 2017, **644**, 52–60.

134 L. Liu and P. R. Onck, *J. Mech. Phys. Solids*, 2019, **123**, 247–266.

135 D. J. Broer, *Curr. Opin. Solid State Mater. Sci.*, 2002, **6**, 553–561.

136 L. Cai, F. Bian, H. Chen, J. Guo, Y. Wang and Y. Zhao, *Chem*, 2021, **7**, 93–136.

137 N. Tanjeem, M. B. Minnis, R. C. Hayward and C. W. Shields, *Adv. Mater.*, 2022, **34**, 2105758.

138 M. Caggioni, A. V. Bayles, J. Lenis, E. M. Furst and P. T. Spicer, *Soft Matter*, 2014, **10**, 7647–7652.

139 M. Caggioni, J. Lenis, A. V. Bayles, E. M. Furst and P. T. Spicer, *Langmuir*, 2015, **31**, 8558–8565.

140 S. Li, J. Zhao, P. Lu and Y. Xie, *Chinese Sci. Bull.*, 2010, **55**, 114–119.

141 L. Metselaar, I. Dozov, K. Antonova, E. Belamie, P. Davidson, J. M. Yeomans and A. Doostmohammadi, *Phys. Rev. E*, 2017, **96**, 022706.

142 P. S. Drzaic, *Liq. Cryst.*, 1999, **26**, 623–627.

143 O. O. Prishchepa, V. Y. Zyryanov, A. P. Gardymova and V. F. Shabanov, *Mol. Cryst. Liq. Cryst.*, 2008, **489**, 84–93.

144 T. Lopez-Leon and A. Fernandez-Nieves, *Colloid Polym. Sci.*, 2011, **289**, 345–359.

145 D. Sun, J. Zhang, H. Li, Z. Shi, Q. Meng, S. Liu, J. Chen and X. Liu, *Polymers (Basel).*, 2021, **13**, 1889.

146 L. Tan, A. C. Davis and D. J. Cappelleri, *Adv. Funct. Mater.*, 2021, **31**, 2007125.

147 A. M. Martinez, L. M. Cox, J. P. Killgore, N. J. Bongiardina, R. D. Riley and C. N. Bowman, *Soft Matter*, 2021, **17**, 467–474.

148 Y. Ebata, A. B. Croll and A. J. Crosby, *Soft Matter*, 2012, **8**, 9086.

149 Haixia Mei, Yaoyu Pang, Se Hyuk Im and Rui Huang, in *2008 11th Intersociety Conference on Thermal and Thermomechanical Phenomena in Electronic Systems*, IEEE, 2008, pp. 762–769.

150 J. Liu, Y. Liu, Y. Xue, Y. Ren, X. Fan, R. Wang, H. Zhang, B. Zhang and Q. Zhang, *J. Mater. Sci.*, 2019, **54**, 5852–5864.

151 W. Li, Y. Liu and J. Leng, *ACS Appl. Mater. Interfaces*, 2021, **13**, 23074–23080.

152 N. R. Visaveliya, C. W. Leishman, K. Ng, N. Yehya, N. Tobar, D. M. Eisele and J. M. Köhler, *Adv. Mater. Interfaces*, 2017, **4**, 1700929.

153 M. S. Krieger and M. A. Dias, *Phys. Rev. E*, 2019, **100**, 022701.

154 D. Yang and L. H. He, *Smart Mater. Struct.*, 2014, **23**, 045012.

155 P. Plucinsky and K. Bhattacharya, *J. Mech. Phys. Solids*, 2017, **102**, 125–150.

156 S. Yeom, H. Kim, K. Kim, C. W. Joo, H. Cho, H. Cho, S. Choi, W. J. Lee, Y. S. Jung, B.-H. Kwon and J.-H. Na, *Opt. Express*, 2020, **28**, 26519.

157 A. Agrawal, P. Luchette, P. Palffy-Muhoray, S. L. Biswal, W. G. Chapman and R. Verduzco, *Soft Matter*, 2012, **8**, 7138.

158 F. L. L. Visschers, M. Hendrikx, Y. Zhan and D. Liu, *Soft Matter*, 2018, **14**, 4898–4912.

159 S. H. Kang, J.-H. Na, S. N. Moon, W. Il Lee, P. J. Yoo and S.-D. Lee, *Langmuir*, 2012, **28**, 3576–3582.

160 L. A. Mihai and A. Goriely, *J. Mech. Phys. Solids*, 2020, **144**, 104101.

161 M. Li, D. Joung, B. Hughes, S. D. Waldman, J. A. Kozinski and D. K. Hwang, *Sci. Rep.*, 2016, **6**, 30463.

162 P. G. de Gennes and J. Prost, *The Physics of Liquid Crystals: No. 83 (International Series of Monographs on Physics)*, Oxford University Press, 2nd ed., 1994.

163 M. Winkler, A. Kaiser, S. Krause, H. Finkelmann and A. M. Schmidt, *Macromol. Symp.*, 2010, **291**, 186–192.

164 A. Kaiser, M. Winkler, S. Krause, H. Finkelmann and A. M. Schmidt, *J. Mater. Chem.*, 2009, **19**, 538–543.

165 J. M. Haberl, A. Sánchez-Ferrer, A. M. Mihut, H. Dietsch, A. M. Hirt and R. Mezzenga, *Adv. Funct. Mater.*, 2014, **24**, 3179–3186.

166 L. Cmok, M. Vilfan, S. Gyergyek and M. Čopič, *Liq. Cryst.*, 2021, **48**, 1815–1826.

167 T. Kimura, M. Yamato, W. Koshimizu, M. Koike and T. Kawai, *Langmuir*, 2000, **16**, 858–861.

168 A. Rešetič, J. Milavec, B. Zupančič, V. Domenici and B. Zalar, *Nat. Commun.*, 2016, **7**, 13140.

169 Introduction to Amine Modification, https://www.thermofisher.com/uk/en/home/references/molecular-probes-the-handbook/fluorophores-and-their-amine-reactive-derivatives/introduction-to-amine-modification.html, (accessed 21 November 2019).

170 L. Danos, Personal Conversation, 2019.

171 N. Chekina, D. Horák, P. Jendelová, M. Trchová, M. J. Bene, M. Hrubý, V. Herynek, K. Turnovcová and E. Syková, *J. Mater. Chem.*, 2011, **21**, 7630–7639.

172 Bangs Laboratories, TechNote 205, https://www.bangslabs.com/sites/default/files/imce/docs/TechNote 205 Web.pdf, (accessed 18 March 2019).

173 Bangs Laboratories, TechNote 203, https://www.bangslabs.com/sites/default/files/imce/docs/TechNote 203 Web.pdf, (accessed 18 March 2019).

174 L. Song, E. J. Hennink, I. T. Young and H. J. Tanke, *Biophys. J.*, 1995, **68**, 2588–2600.

175 A. P. Demchenko, *Methods Appl. Fluoresc.*, 2020, **8**, 022001.

176 A. Londoño-Hurtado, J. C. Armas-Pérez, J. P. Hernández-Ortiz and J. J. de Pablo, *Soft Matter*, 2015, **11**, 5067–5076.

177 J. Shechter, N. Atzin, A. Mozaffari, R. Zhang, Y. Zhou, B. Strain, L. M. Oster, J. J. de Pablo and J. L. Ross, *Langmuir*, 2020, **36**, 7074–7082.

178 S. Şengül, N. Aydoğan and E. Bukusoglu, *J. Colloid Interface Sci.*, 2022, **608**, 2310–2320.

179 Z. Sumer and A. Striolo, *Mol. Syst. Des. Eng.*, 2020, **5**, 449–460.

180 R. A. van Delden and B. L. Feringa, *Angew. Chemie Int. Ed.*, 2001, **40**, 3198–3200.

181 C. Binet, S. Ferrère, A. Lattes, E. Laurent, J.-D. Marty, M. Mauzac, A.-F. Mingotaud, G. Palaprat and M. Weyland, *Anal. Chim. Acta*, 2007, **591**, 1–6.

182 Y. Chen and K. D. Shimizu, *Org. Lett.*, 2002, **4**, 2937–2940.

183 P. Zhang, M. G. Debije, L. T. de Haan and A. P. H. J. Schenning, *ACS Appl. Mater. Interfaces*, 2022, **14**, 20093–20100.

184 D. J. D. Davies, A. R. Vaccaro, S. M. Morris, N. Herzer, A. P. H. J. Schenning and C. W. M. Bastiaansen, *Adv. Funct. Mater.*, 2013, **23**, 2723–2727.

185 S. M. Wood, F. Castles, S. J. Elston and S. M. Morris, *RSC Adv.*, 2016, **6**, 31919–31924.

186 H. J. Seo, S. S. Lee, J. Noh, J.-W. Ka, J. C. Won, C. Park, S.-H. Kim and Y. H. Kim, *J. Mater. Chem. C*, 2017, **5**, 7567–7573.

187 A. Belmonte, T. Bus, D. J. Broer and A. P. H. J. Schenning, *ACS Appl. Mater. Interfaces*, 2019, **11**, 14376–14382.

188 Cholesteric liquid crystals (CLC) and their photonic properties, https://www.cheric.org/files/research/ip/p201402/p201402-501.pdf, (accessed 27 July 2022).

189 M. T. Brannum, A. M. Steele, M. C. Venetos, L. S. T. J. Korley, G. E. Wnek and T. J. White, *Adv. Opt. Mater.*, 2019, **7**, 1–7.

190 R. C. Weast, M. J. Astle and W. H. Beyer, *Handbook of Chemsitry and Physics*, CRC Press, Boca Raton, FL, 65th edn., 1984.

191 D. J. Mulder, A. P. H. J. Schenning and C. W. M. Bastiaansen, *J. Mater. Chem. C*, 2014, **2**, 6695–6705.

192 L. T. J. Korley and T. H. Ware, *J. Appl. Phys.*, 2021, **130**, 220401.